

02751470  
CONTRACT NUMBER: NAS 9-14722

DRL NUMBER: T-707

DRD NUMBER: MA-559T

REPORT: MDC E1478

# DEVELOPMENT OF S-BAND ANTENNA INTERFACE DESIGN SHUTTLE ANTENNA RADOME TECHNOLOGY TEST PROGRAM

(NASA-CR-151470) SHUTTLE ANTENNA RADOME  
TECHNOLOGY TEST PROGRAM. VOLUME 2:  
DEVELOPMENT OF S-BAND ANTENNA INTERFACE  
DESIGN Final Report (McDonnell-Douglas  
Astronautics Co.) 191 p HC A09/MF A01

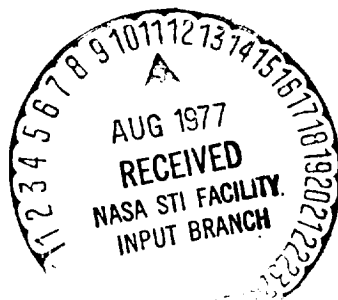
N77-28355

Unclas

G3/32 39233

## VOLUME II FINAL REPORT

MCDONNELL DOUGLAS ASTRONAUTICS COMPANY - EAST



MCDONNELL DOUGLAS



CORPORATION



**DISTRIBUTION LIST**

NASA Lyndon B. Johnson Space Center  
R&T Procurement Branch  
Attn: George Gaffney, Mail Code BC73(27)  
Houston, Texas 77058  
One Copy

NASA Lyndon B. Johnson Space Center  
Technical Library Branch  
Attn: Retha Shirkey, Mail Code JM6  
Houston, Texas 77058  
Four Copies

NASA Lyndon B. Johnson Space Center  
Technical Utilization Office  
Attn: John T. Wheeler, Mail Code AT3  
Houston, Texas 77058  
One Copy

NASA Lyndon B. Johnson Space Center  
Electromagnetic Systems Branch  
Attn: H. Dean Cubley, Mail Code EE3  
Houston, Texas 77058  
Eleven Copies

**DEVELOPMENT OF S-BAND ANTENNA INTERFACE DESIGN  
SHUTTLE ANTENNA RADOME TECHNOLOGY TEST PROGRAM**

**REPORT MDC E1478  
15 JUNE 1977  
VOLUME II**

THIS PAGE INTENTIONALLY LEFT BLANK



CONTRACT NUMBER: NAS 9-14722

DRL NUMBER: T-707

DRD NUMBER: MA-559T

REPORT: MDC E1478

COPY NO. 19

---

# DEVELOPMENT OF S-BAND ANTENNA INTERFACE DESIGN

## SHUTTLE ANTENNA RADOME TECHNOLOGY TEST PROGRAM

---

15 JUNE 1977

REPORT MDC E1478

### VOLUME II FINAL REPORT

Prepared By E. A. Kuhlman L. C. Baranowski  
E. A. Kuhlman L. C. Baranowski  
Program Manager Thermodynamics

Approved By R. A. Stacy  
R. A. Stacy  
Branch Chief Electronics

Approved By G. G. McKee  
G. G. McKee  
Director, Avionics Engineering

**MCDONNELL DOUGLAS ASTRONAUTICS COMPANY - EAST**

Saint Louis, Missouri 63166 (314) 232-0232

**MCDONNELL DOUGLAS**



**CORPORATION**



**ABSTRACT**

The effects of TPS contamination on the Space Shuttle Orbiter S-band Quad antenna due to multiple mission buildup are discussed. A test fixture was designed, fabricated and exposed to ten cycles of simulated ground and flight environments. Radiation pattern and impedance tests were performed to measure the effects of these contaminants. The degradation in antenna performance was attributed to the silicone waterproofing in the TPS tiles rather than exposure to the contaminating sources used in the test program.

Validation of the accuracy of an analytical thermal model developed in the first part of this contract is discussed. Thermal vacuum tests with a test fixture (also designed and fabricated in the first part of this contract) and a representative S-band Quad antenna were conducted to evaluate the predictions of the analytical thermal model for two orbital heating conditions and entry from each orbit. The results show that the accuracy of predicting the test fixture thermal responses is largely dependent on the ability to define the boundary and ambient conditions. When the test conditions were accurately included in the analytical model, the predictions were in excellent agreement with measurements.

THIS PAGE INTENTIONALLY LEFT BLANK

**DEVELOPMENT OF S-BAND ANTENNA INTERFACE DESIGN**  
**SHUTTLE ANTENNA RADOME TECHNOLOGY TEST PROGRAM**

**REPORT MDC E1478**  
**15 JUNE 1977**  
**VOLUME II**

**CONTENTS**

LIST OF FIGURES . . . . .	viii
LIST OF TABLES. . . . .	xii
SUMMARY . . . . .	1-1
CONCLUSIONS . . . . .	2-1
RECOMMENDATIONS . . . . .	3-1
INTRODUCTION. . . . .	4-1
MULTIPLE MISSION ANTENNA PERFORMANCE ASSESSMENT . . . . .	5-1
Test fixture . . . . .	5-1
Design. . . . .	5-2
TPS. . . . .	5-4
Structure simulation . . . . .	5-6
Antenna mounting assembly. . . . .	5-6
Fabrication . . . . .	5-6
Instrumentation . . . . .	5-8
Thermal Environment Simulation . . . . .	5-8
Facility description. . . . .	5-9
Test configuration. . . . .	5-10
Test environments . . . . .	5-12
Ascent . . . . .	5-12
Orbital. . . . .	5-14
Entry. . . . .	5-14
Test procedure. . . . .	5-17
Ground environments simulation . . . . .	5-21
Test setup description. . . . .	5-21
Test environments . . . . .	5-21
Dust . . . . .	5-21
Salt fog . . . . .	5-23
Humidity . . . . .	5-23
Test procedure. . . . .	5-23
Electrical performance testing . . . . .	5-23
Test setup description. . . . .	5-23
Data acquisition. . . . .	5-23
Test results . . . . .	5-28
Thermal environments verification . . . . .	5-28
Ground environments verification. . . . .	5-34
Electrical performance. . . . .	5-34
Physical observations . . . . .	5-36
THERMAL VACUUM TESTING. . . . .	6-1
Test Fixture . . . . .	6-1
Structure . . . . .	6-1
Antenna . . . . .	6-4

PRECEDING PAGE BLANK NOT FILMED

**DEVELOPMENT OF S-BAND ANTENNA INTERFACE DESIGN**  
**SHUTTLE ANTENNA RADOME TECHNOLOGY TEST PROGRAM**

**REPORT MDC E1478**  
**15 JUNE 1977**  
**VOLUME II**

Instrumentation . . . . .	6-7
Thermal environments . . . . .	6-9
Temperature . . . . .	6-16
Pressure. . . . .	6-17
Test facility. . . . .	6-20
Temperature simulation equipment. . . . .	6-20
Pressure simulation equipment . . . . .	6-27
Data acquisition system . . . . .	6-27
Test procedure . . . . .	6-27
Thermal control . . . . .	6-27
Pressure control. . . . .	6-29
Pretest . . . . .	6-29
Orbit temperature . . . . .	6-30
Entry temperature . . . . .	6-30
Entry pressure. . . . .	6-31
Post test . . . . .	6-32
Test results . . . . .	6-32
Temperature simulation. . . . .	6-32
Pressure simulation . . . . .	6-41
Thermal response. . . . .	6-41
Discussion. . . . .	6-53
REFERENCES. . . . .	7-1
APPENDIX A	
REFERENCE RADIATION PATTERNS IN RECTANGULAR COORDINATES. . . . .	A-1
APPENDIX B	
RADIATION PATTERNS IN RECTANGULAR COORDINATE FOR TEST 4. . . . .	B-1

**LIST OF PAGES**

Title
iii thru xii
1-1 thru 1-2
2-1 thru 2-2
3-1 thru 3-2
4-1 thru 4-2
5-1 thru 5-80
6-1 thru 6-61
7-1 thru 7-2
A-1 thru A-16
B-1 thru B-16

**LIST OF FIGURES**

**FIGURE**

1	Test Sequence. . . . .	5-2
2	MMAPA Test Fixture . . . . .	5-3
3	ARMSEF Facility Adapter. . . . .	5-4
4	Typical TPS/Structure Configuration. . . . .	5-5
5	Photo of MMAPA Test Fixture. . . . .	5-7
6	Thermocouple Locations . . . . .	5-8
7	NASA-JSC Radiant Heat Test Facility. . . . .	5-9
8	Thermal Test Configuration . . . . .	5-11
9	Ascent TPS Surface Temperature History . . . . .	5-12
10	Ascent Local Static Pressure History . . . . .	5-13
11	Orbital TPS Surface Temperature History. . . . .	5-14
12	Entry TPS Surface Temperature. . . . .	5-15
13	Entry Local Static . . . . .	5-16
14	One-Dimensional Thermal Model of MMAPA Test Fixture. . . . .	5-17
15	Structural Temperature for Ascent and Hot and Cold Orbits. . .	5-18
16	Backside Structural Temperature for Entry From Hot and Cold Orbits. . . . .	5-18
17	Calibration for Ascent Heating - Tests 1-5 . . . . .	5-19
18	Calibration for Entry From Hot Orbit - Tests 1-5 . . . . .	5-20
19	Ground Environments Simulation Cabinet . . . . .	5-22
20	Test Setup For Radiation Pattern Measurements. . . . .	5-24
21	Gain Reference Configuration . . . . .	5-25
22	Test Setup for Impedance Measurements. . . . .	5-26
23	Conversion From Peak Linear to Circular Gain . . . . .	5-27
24	Antenna Pattern Coordinate System. . . . .	5-28
25	Ascent Heating Repeatability - Tests 1-5 . . . . .	5-29
26	Ascent Pressure Simulation - Tests 1-10. . . . .	5-30
27	Hot Orbit Temperature History Test 1 . . . . .	5-31
28	Hot Orbit Pressure History Test 1. . . . .	5-31
29	Calibration for Cold Orbit . . . . .	5-31
30	Cold Orbit Temperature Histories - Tests 6-10. . . . .	5-32
31	Cold Orbit Pressure Histories - Tests 6-10 . . . . .	5-33
32	Entry Heating Repeatability - Tests 1-5 . . . . .	5-37
33	Entry Pressure Histories - Tests 1-10. . . . .	5-38
34	Backside Temperature Histories During Entry From Hot Orbit - Test 1 (T/C 1-10) . . . . .	5-39
35	Backside Temperature Histories During Entries From Hot Orbit - Tests 1-5 (T/C 8 only). . . . .	5-40
36	Backside Temperature Histories During Entry From Cold Orbit - Test 6 (T/C 1-10). . . . .	5-41
37	Backside Temperature Histories During Entries From Cold Orbit - Tests 6-10 (T/C 8 only). . . . .	5-42
38	Pattern Regions Used For Antenna Performance Analysis. . . . .	5-44
39	Reference Radiation Patterns (1.8 GHz) . . . . .	5-45
40	Reference Radiation Patterns (2.1 GHz) . . . . .	5-46
41	Reference Radiation Patterns (2.3 GHz) . . . . .	5-47

LIST OF FIGURES (CONT.)

FIGURE

42	Radiation Patterns - Test 4 (1.8 GHz). . . . .	5-48
43	Radiation Patterns - Test 4 (2.1 GHz). . . . .	5-49
44	Radiation Patterns - Test 4 (2.3 GHz). . . . .	5-50
45	Axial Ratio Changes - 1.8 GHz. . . . .	5-51
46	Axial Ratio Changes - 2.1 GHz. . . . .	5-52
47	Axial Ratio Changes - 2.3 GHz. . . . .	5-53
48	Circular Gain Variations Caused By Axial Ratio Changes-1.8 GHz .	5-54
49	Circular Gain Variations Caused By Axial Ratio Changes-2.1 GHz .	5-55
50	Circular Gain Variations Caused By Axial Ratio Changes-2.3 GHz .	5-56
51	Linear Gain Changes - 1.8 GHz. . . . .	5-58
52	Linear Gain Variations - 2.1 GHz . . . . .	5-59
53	Linear Gain Changes - 2.3 GHz. . . . .	5-60
54	Circular Gain Variations Caused by Axial Ratio and Linear Gain Changes - 1.8 GHz. . . . .	5-62
55	Circular Gain Variations Caused by Axial Ratio and Linear Gain Changes - 2.1 GHz. . . . .	5-63
56	Circular Gain Variations Caused by Axial Ratio and Linear Gain Changes - 2.3 GHz. . . . .	5-64
57	Reference Impedance (1.7 - 1.9 GHz). . . . .	5-65
58	Reference Impedance (2.0 - 2.4 GHz). . . . .	5-66
59	Impedance - Test 5 (1.7 - 1.9 GHz) . . . . .	5-67
60	Impedance - Test 5 (2.0 - 2.4 GHz) . . . . .	5-68
61	VSWR (Magnitude and Angle) and Mismatch Loss-1.7 to 1.9 GHz. . .	5-69
61	VSWR (Magnitude and Angle) and Mismatch Loss- 1.7 to 1.9 GHz (cont.) . . . . .	5-70
62	VSWR (Magnitude and Angle) and Mismatch Loss - 2.0 to 2.4 GHz. .	5-71
62	VSWR (Magnitude and Angle) and Mismatch Loss - 2.0 to 2.4 GHz (cont.) . . . . .	5-72
62	VSWR (Magnitude and Angle) and Mismatch Loss - 2.0 to 2.4 GHz (cont.) . . . . .	5-73
63	VSWR (Magnitude and Angle) and Mismatch Loss - 2.2 GHz . . . . .	5-74
64	Impedance - Tests 1-10 (1.7 - 1.9 GHz) . . . . .	5-75
65	Impedance - Tests 1-10 (2.0 - 2.4 GHz) . . . . .	5-76
65	Impedance - Tests 1-10 (2.0 - 2.4 GHz)(cont.) . . . . .	5-77
65	Impedance - Tests 1-10 (2.0 - 2.4 GHz)(cont.) . . . . .	5-78
66	Test Fixture After Test 5. . . . .	5-79
67	Test Fixture After Test 6. . . . .	5-80
68	Thermal Test Fixture Prior to Installation in Test Chamber . . .	6-2
69	Thermal Test Fixture - Design Details. . . . .	6-3
70	Antenna Installation in Test Fixture - Top View. . . . .	6-4
71	Antenna Installation in Test Fixture - Bottom View . . . . .	6-5
72	Test Fixture with Antenna - Bottom View. . . . .	6-6
73	Antenna with Dust Cover Installed. . . . .	6-7
74	Test Fixture Thermocouple Locations. . . . .	6-10
75	Antenna Thermocouple Locations and Nodal Array - Top View. . . .	6-11
76	Antenna Thermocouple Locations and Nodal Array - Side View B-B .	6-12



**LIST OF FIGURES (CONT.)**

**FIGURE**

77	Antenna Thermocouple Locations and Nodal Array - Side View C-C. . . . .	6-12
78	Skin-Stringer Panel Thermocouple Installation. . . . .	6-13
79	TG-15000 Insulation Thermocouple Installation. . . . .	6-14
80	Cabin Wall Panel Thermocouple Installation . . . . .	6-15
81	HRSI Bondline Temperatures For Orbital Representation. . . . .	6-16
82	Thermal Model Nodal Distribution - TPS/Structure/Insulation. .	6-17
83	Entry TPS Surface Heating Environment - Hot Orbit. . . . .	6-18
84	Entry HRSI Bondline Thermal Response - Hot and Cold Orbits. . . . .	6-18
85	Entry Pressure Environment . . . . .	6-19
86	Thermal Vacuum Test Setup. . . . .	6-21
87	NASA-JSC Space Chamber E with Test Fixture Support Structure .	6-22
88	Thermal Vacuum Test Installation . . . . .	6-23
89	Thermal Environment Control Configuration. . . . .	6-24
90	Heater Control Units . . . . .	6-25
91	Environment Control and Data Acquisition Systems . . . . .	6-26
92	Environmental Control Schematic. . . . .	6-28
93	Calculated HRSI Bondline Temperature Histories - Entry From Hot Orbit . . . . .	6-30
94	Calculated HRSI Bondline Temperature Histories - Entry From Cold Orbit. . . . .	6-31
95	Simulation of Hot Orbit. . . . .	6-32
96	Test Simulation of Entry - Hot Orbit . . . . .	6-33
97	Test Simulation of Cold Orbit. . . . .	6-34
98	Test Simulation of Entry - Cold Orbit. . . . .	6-35
99	Symmetry of Orbital Heating - Hot Orbit. . . . .	6-35
100	Symmetrical Structural Thermal Responses - Hot Orbit . . . . .	6-36
101	Symmetry of Entry Heating - Hot Orbit. . . . .	6-37
102	Symmetrical Structural Thermal Responses - Entry (Hot Orbit). . . . .	6-38
103	Surface Temperature Distribution - Hot Orbit . . . . .	6-39
104	Grid Heating Uniformity - Entry From Hot Orbit . . . . .	6-39
105	Cabin Wall Temperature - Hot Orbit . . . . .	6-40
106	Cabin Wall Temperature - Entry From Hot Orbit. . . . .	6-40
107	Cabin Wall Temperature - Cold Orbit. . . . .	6-40
108	Cabin Wall Temperature - Entry From Cold Orbit . . . . .	6-41
109	Entry Pressure History - Hot Orbit . . . . .	6-42
110	Entry Pressure History - Cold Orbit. . . . .	6-43
111	Outboard Structural Skin Temperatures - Entry From Hot Orbit . . . . .	6-44
112	Inboard Structural Skin Temperatures - Entry From Hot Orbit . . . . .	6-45
113	Antenna Flange Temperatures - Entry From Hot Orbit . . . . .	6-46
114	Antenna Element Temperatures - Entry From Hot Orbit. . . . .	6-47
115	Structural Skin Temperature Distribution - Entry From Cold Orbit. . . . .	6-49

LIST OF FIGURES (CONT.)

FIGURE

116	Insulation Temperatures - Entry From Hot Orbit . . . . .	6-50
117	Outboard Structural Skin Temperatures - Hot Orbit. . . . .	6-51
118	Inboard Structural Skin Temperatures - Hot Orbit . . . . .	6-51
119	Antenna Flange Temperatures - Hot Orbit. . . . .	6-52
120	Antenna Element Temperatures - Hot Orbit . . . . .	6-52
121	Insulation Temperatures - Hot Orbit. . . . .	6-53
122	Outboard Structural Skin Temperatures - Cold Orbit . . . . .	6-55
123	Inboard Structural Skin Temperatures - Cold Orbit. . . . .	6-55
124	Antenna Flange Temperatures - Cold Orbit . . . . .	6-56
125	Antenna Element Temperatures - Cold Orbit . . . . .	6-56
126	Insulation Temperatures - Cold Orbit . . . . .	6-57
127	Outboard Structural Skin Temperatures - Entry From Cold Orbit. . . . .	6-57
128	Inboard Structural Skin Temperatures - Entry From Cold Orbit .	6-58
129	Antenna Flange Temperatures - Entry From Cold Orbit. . . . .	6-59
130	Antenna Element Temperatures - Entry From Cold Orbit . . . . .	6-60
131	Insulation Temperatures - Entry From Cold Orbit. . . . .	6-61
132	Standard Gain Horn Reference Level - 1.8 GHz . . . . .	A-2
133	Reference Radiation Patterns - 1.8 GHz . . . . .	A-3
134	Standard Gain Horn Reference Level - 2.1 GHz . . . . .	A-7
135	Reference Radiation Patterns - 2.1 GHz . . . . .	A-8
136	Standard Gain Horn Reference Level - 2.3 GHz . . . . .	A-12
137	Reference Radiation Patterns - 2.3 GHz . . . . .	A-13
138	Standard Gain Horn Level For Test 4 - 1.8 GHz. . . . .	B-2
139	Radiation Patterns For Test 4 - 1.8 GHz. . . . .	B-3
140	Standard Gain Horn Level For Test 4 - 2.1 GHz. . . . .	B-7
141	Radiation Patterns For Test 4 - 2.1 GHz. . . . .	B-8
142	Standard Gain Horn Level For Test 4 - 2.3 GHz. . . . .	B-12
143	Radiation Patterns For Test 4 - 2.3 GHz. . . . .	B-13

LIST OF TABLES

I	Total TPS Thickness Over S-Band Quad Antenna . . . . .	5-5
II	Ground Environments Test Sequences . . . . .	5-43
III	Maximum Increase and Decrease in Circular Gain Caused by Axial Ratio Changes. . . . .	5-57
IV	Standard Gain Horn Pattern Level (-dB) . . . . .	5-61
V	Thermal Test Fixture Instrumentation Locations . . . . .	6-8



**SUMMARY**

The design, fabrication and testing of a test fixture used to assess TPS contamination and antenna performance are discussed. The test fixture design was based on the TPS and thermal-structure requirements for the lower Space Shuttle S-band Quad antenna. The test fixture was sized to permit testing in either a 2x2 ft channel nozzle plasma facility or a radiant heat facility. The TPS surface of the test fixture was subjected to select ground environments (dust, salt fog and humidity) followed by simulated flight environments (ascent, orbit and entry heating, and solar UV) in a radiant heat facility. The effects of the simulated environments were then measured by comparing the post test radiation patterns and impedance of an S-band antenna mounted in the test fixture with pretest data. Ten test cycles were performed. The test results indicate that the effects of the test environments do not cause any significant degradation in the electrical performance of the TPS. At 1.8 and 2.3 GHz the gain either stayed essentially unchanged or was increased slightly. However, at 2.1 GHz the gain in two planes ( $\phi = 45^\circ$  and  $90^\circ$ ) was reduced 1 dB consistently. Since the gain reduction was observed after the first thermal test and before the first exposure to the ground environment, it is attributed to burning of the silicone resin used for waterproofing the TPS tiles rather than the contaminants added during testing. The impedance changes over the entire frequency range (1.7 to 2.4 GHz) were, in general, insignificant.

Thermal analyses and the tests to validate an analytical thermal model are discussed. The analyses results using the analytical thermal model developed in the first part of the contract were updated to include revised ascent and heating rate histories and TPS thicknesses. The updated results were then used as the basis for specifying test parameters for two thermal tests using the test fixture which was designed and fabricated during the first part of the contract. The test results initially showed antenna and structural temperatures to be 17 to 22 K (30 to 40°F) lower than predicted. Revised boundary conditions, based on measured data, which bring the predicted results into good agreement with test results are discussed.

**DEVELOPMENT OF S-BAND ANTENNA INTERFACE DESIGN**  
**SHUTTLE ANTENNA RADOME TECHNOLOGY TEST PROGRAM**

**REPORT MDC E1478**  
**15 JUNE 1977**  
**VOLUME II**

THIS PAGE INTENTIONALLY LEFT BLANK

## **CONCLUSIONS**

The conclusions reached from the test results obtained during this program are:

### **1. Multiple Mission Antenna Performance Assessment**

- a. The thermal test fixture designed and fabricated for assessment of multiple mission TPS contamination provided a good representation of the Shuttle Orbiter S-band Quad antenna installation.
- b. The contamination from the simulated Shuttle ground and flight environments did not result in significant degradation in the electrical performance of the Shuttle TPS for the ten mission cycles considered. However, the tests showed that a surface deposit does build up. Therefore, the negative finding does not preclude measurable degradation after more mission cycles.
- c. The test results indicate that burning of the silicone waterproofing material in the TPS tiles during the first flight (thermal) environment exposure resulted in about 1 dB gain reduction at 2.1 GHz. Since the gain reduction occurred at only one of the three test frequencies, some degree of frequency dependence is implied.

### **2. Thermal Vacuum Testing**

- a. The agreement between predicted and measured results is excellent when the analytical thermal model is an accurate representation of the test fixture and environment. Therefore, the analytical thermal methods used are considered valid for making accurate flight predictions.
- b. Backside convective heat transfer should be included in the analytical model when the pressure is near ambient and the test model is not sealed. (Note: This is not only applicable to test models but should also be applicable to flight analysis.)
- c. A thermal test fixture should be designed to minimize support or side structure affects and/or instrumented to identify boundary conditions which deviate from the ideal adiabatic boundary condition. This would permit the modification of the input parameters so that the flight responses could be more closely obtained at critical points in the test fixture.
- d. It is difficult to accurately model sections of flight hardware because of the edge effects which occur when the surrounding thermal-structure is not present.
- e. Equipment thermal models should allow for transverse gradients in substrate backup materials.

**DEVELOPMENT OF S-BAND ANTENNA INTERFACE DESIGN**  
**SHUTTLE ANTENNA RADOME TECHNOLOGY TEST PROGRAM**

**REPORT MDC E1478**  
**15 JUNE 1977**  
**VOLUME II**

- f. Future antenna models may be simplified in terms of how the antenna is represented, i.e., if small differences in temperature are anticipated, fewer nodes should be used.



**RECOMMENDATIONS**

The work during this program leads to the following recommendations for future consideration:

- a. Tests should be run at higher frequencies (e.g., C-band and/or Ku-band) where the effects of entry heating on the Shuttle TPS waterproofing silicone could be expected to be more severe than at S-band frequencies.
- b. In future thermal vacuum tests, the test fixture should be instrumented to permit evaluation of the test environment and subsequent modification of test input parameters to achieve thermal responses at critical test points consistent with predicted flight responses.
- c. A thermal test fixture should be designed to minimize support or side structure effects and/or instrumented to identify boundary conditions which deviate from the assumed boundary conditions. This would permit modification of the input parameters so that the flight responses could be more closely obtained at critical points in the test fixture.

**DEVELOPMENT OF S-BAND ANTENNA INTERFACE DESIGN**  
**SHUTTLE ANTENNA RADOME TECHNOLOGY TEST PROGRAM**

**REPORT MDC E1478**  
**15 JUNE 1977**  
**VOLUME II**

THIS PAGE INTENTIONALLY LEFT BLANK

## **INTRODUCTION**

The objectives of this program were: (1) to assess the effects of TPS (thermal protection system) contamination on the Space Shuttle Orbiter S-band Quad antenna performance, and (2) to validate the accuracy of the analytical thermal model developed in the first part of this contract for use in support of the S-band Quad antenna design.

The first task consisted of: (1) designing a test fixture based on actual Shuttle TPS materials and support structure representative of the thermal mass of the Shuttle structure and antenna mounting hardware, (2) preparing engineering drawings of the test fixture for use in fabricating it at NASA-JSC, (3) preparing a test plan for a series of 10 test cycles involving simulation of selected ground and flight environments and antenna performance measurements, (4) monitoring preparation and testing as required to verify that inputs and outputs were consistent with task objectives, and (5) analyzing and evaluating results relative to the test objectives.

The second task consisted of: (1) incorporating the latest Shuttle design data into the thermal analysis program (developed in the first part of this contract) and updating the analysis output to provide data for thermal vacuum test control parameters and comparison with test results, (2) preparing a test plan for two tests involving simulation of flight thermal/pressure environments using the test fixture which was designed and fabricated during the first part of this contract, (3) monitoring preparation and testing as required to verify that inputs and outputs were consistent with task objectives, and (4) analyzing data and evaluating results relative to test objectives.

A test fixture for the first task, based on actual Shuttle TPS and thermally representative structure and antenna mounting hardware, was designed and detailed engineering drawings prepared and delivered. The test fixture was sized to permit testing in either a 2x2 ft channel nozzle plasma facility or a radiant heat facility, although testing was performed in the latter.

A test plan for the first task, multiple mission antenna performance assessment (MMAPA), was prepared and delivered. It provided the requirements for NASA-JSC preparation by specifying test parameters, general procedures, and data acquisition requirements. The plan was based on subjecting the test fixture to simulated Shuttle environments which could reasonably be suspect as a cause of contamination permanently attached to the TPS surface which, in turn, could degrade the performance of the antenna beneath the TPS. Testing included simulation of ground environments (dust, salt fog and humidity), simulation of flight environments (ascent, orbit and entry heating, and solar UV), and electrical measurements (radiation patterns and impedance) to measure the effects of exposure to these environments.

Ten test cycles were performed to obtain the effects of multiple mission buildup because the contamination occurring over a single mission cycle was not expected to be particularly significant. The radiation pattern and impedance data from each test were compared with the reference data to obtain a measure of

the electrical performance changes of the TPS.

The thermal analysis program, developed during the first part of this contract, was modified for current TPS thickness and rerun with the latest Shuttle heating/pressure data applicable to the lower S-band Quad antenna location. The revised calculations included temperature histories of the TPS surface and inner and outer bondline, structural skin and antenna. These results were used as the test inputs of both the MMAPA tests, to evaluate TPS contamination effects, and the thermal vacuum tests to validate the analytical thermal model of the antenna installation.

A test plan for the second task, thermal vacuum testing, was also prepared and delivered. It provided the requirements for NASA-JSC preparation by specifying test parameters, general procedures, and data acquisition requirements. Testing consisted of simulating the effects of the Shuttle flight thermal/pressure environments (orbit and entry) and measuring the resulting structural and antenna temperatures. For this test, the major input consists of heating a thin stainless steel sheet at the outer TPS bondline to simulate two flight environments. The measured response temperatures were then compared with those predicted by the analytical thermal model to evaluate the accuracy of the predictions.

Mr. E. A. Kuhlman, Program Manager, was responsible for the overall technical direction of this program. Other members of the McDonnell Douglas Astronautics Company-EAST (MDAC-EAST) engineering staff who contributed to this program were L. C. Baranowski, J. L. Conlee, D. A. Hartbauer and H. W. Kipp. Mr. Baranowski performed the analytical thermal analyses, coordinated test preparation and testing, and analyzed the thermal test data.

Mr. H. D. Cubley of the Antenna System Section of the Electromagnetic Systems Branch, NASA Lyndon B. Johnson Space Center, Houston, Texas was the technical monitor for this program.

The units used for the physical quantities defined in the text of this report are given in both the International System of Units (SI) and the U.S. customary units in the text. U.S. customary units are used in the drawings, graphs and tables.

This report is designated as Volume II in anticipation of additional work related to the work reported in Volume I.

The task numbers used in the text correspond to the tasks given in the Statement of Work, Exhibit "A", of Contract NAS 9-14772, Modification No. S/A-2, dated 1 July 1976.

**MULTIPLE MISSION ANTENNA PERFORMANCE ASSESSMENT**

The objective of this task (Task 2.3.1) was to determine the effects of TPS contamination on the performance of the S-band Quad antennas located on the lower surface of the Space Shuttle Orbiter. The TPS covers these antenna apertures and serves as a radome in addition to providing thermal protection from ascent and entry heating. Therefore, the build up of contamination on the surface of the TPS over a number of Shuttle flights could affect the antenna pattern (e.g., shape, gain and axial ratio, etc.) and impedance.

The environments, which are considered potential sources for TPS contamination, are certain ground environments (i.e., dust, salt fog and humidity) which can contribute to a deposit on the TPS tile surfaces and which, in turn, could be converted to a permanent deposit by one or more of the flight environments (i.e., ascent, orbital and entry heating, and solar ultra violet (UV) light). RCS exhaust deposits during orbit were also considered. A preliminary study (by MDAC-WEST under contract to Rockwell) indicated that a film of monomethyl hydrazine (MMH) nitrate and water, one micron thick, could be expected. However, even though evaporation can be significantly slower by solar UV, complete evaporation of the RCS exhaust film should occur in the early part of entry when the temperature range is in the 422 to 574 K (300 to 570°F) range. Therefore, an RCS exhaust film was eliminated as a TPS contamination candidate for this program.

To accomplish the above objective, a test fixture representative of the Shuttle thermal-structure and TPS at the S-band Quad antenna location was designed, fabricated, and subjected to simulated ground and space flight environments. The electrical performance of the TPS was obtained by measuring the radiation pattern and impedance of an S-band antenna mounted in the test fixture. Figure 1 shows a block diagram of the testing sequence. This sequence was repeated ten times to simulate the build up of the contamination from multiple Shuttle flights. It should be noted that the ground environments test was omitted prior to the first flight environments test. The results of each of the ten electrical tests were then compared with pretest reference data to assess the effects of the contamination.

This section describes the test fixture, the test facilities and configuration of the various environmental simulations, the electrical performance measurements, and discusses the test results.

**Test Fixture**

The Multiple Mission Antenna Performance Assessment (MMAPA) test fixture was designed to represent a section of Space Shuttle Orbiter TPS, skin-stringer structure, and mounting assembly for the S-band Quad antenna. The test fixture was designed for testing at NASA-JSC in either a plasma or a radiant heating facility. Preliminary studies of the test fixture requirements indicated that the flexibility of testing in either heating facility could be achieved without significant additional design effort or cost penalty. Since the plasma facility

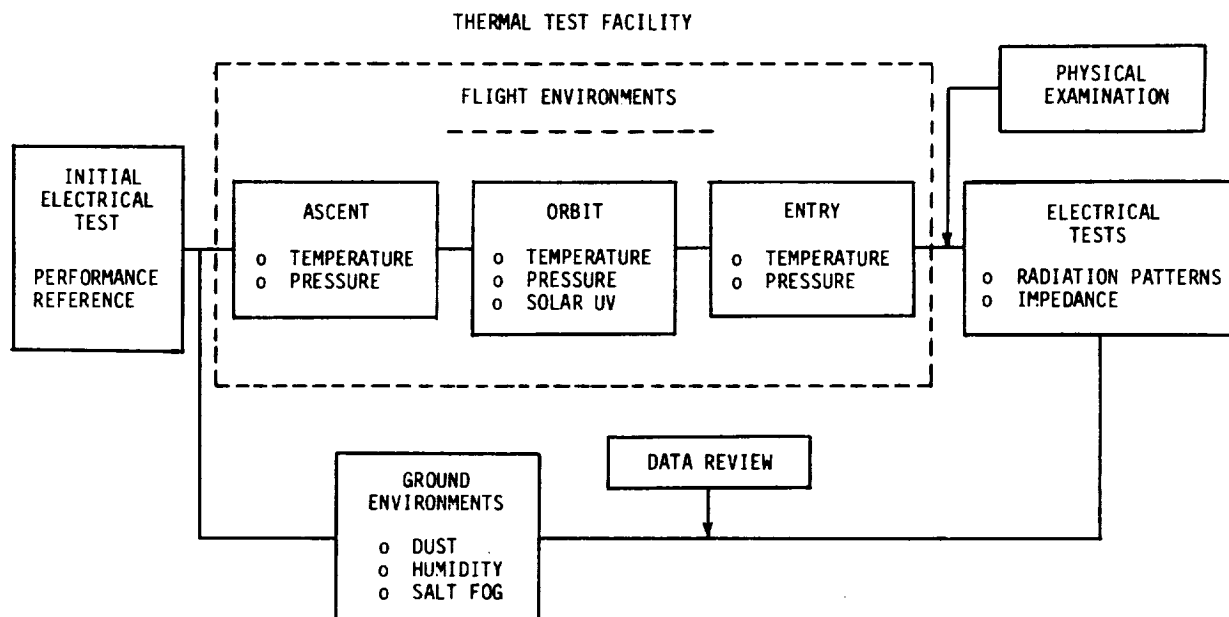


**FIGURE 1 TEST SEQUENCE**

requirements (e.g., size, differential pressure, etc.) were the most limiting factor, they served as the primary design guidelines in the test fixture design effort. A detailed drawing (SK1472201) of the test fixture design with dimensions, materials, and process specification was prepared and delivered to NASA-JSC for fabrication.

**Design.** - A sketch of the MMAPA test fixture is shown in figure 2. The design was based on the requirements for testing in the 2x2 feet channel nozzle fixture of the NASA-JSC 10 MW ARMSEF plasma facility. However, the same test fixture design can be used for testing in a radiant heat facility equally well. The test fixture has a TPS surface 45.7 x 45.7 cm (18.0 x 18.0 in.). This is adequate to mount an S-band antenna with a flange diameter of 31.750 cm (12.500 in.). Testing in a radiant heat facility requires only that guard insulation be placed appropriately around the sides of the test fixture and adjacent to the TPS. Testing in the ARMSEF facility requires an adapter assembly (figure 3) which would be attached to a standard test panel holder assembly (NASA-JSC drawing SED 36112527). The adapter assembly includes the necessary guard insulation around the test fixture. The design of the adapter assembly allows it to stay attached to the channel nozzle while the MMAPA test fixture can be removed for electrical testing and ground environment exposure. The MMAPA test fixture consists of three primary components: TPS, simulated structure, and antenna mounting assembly.

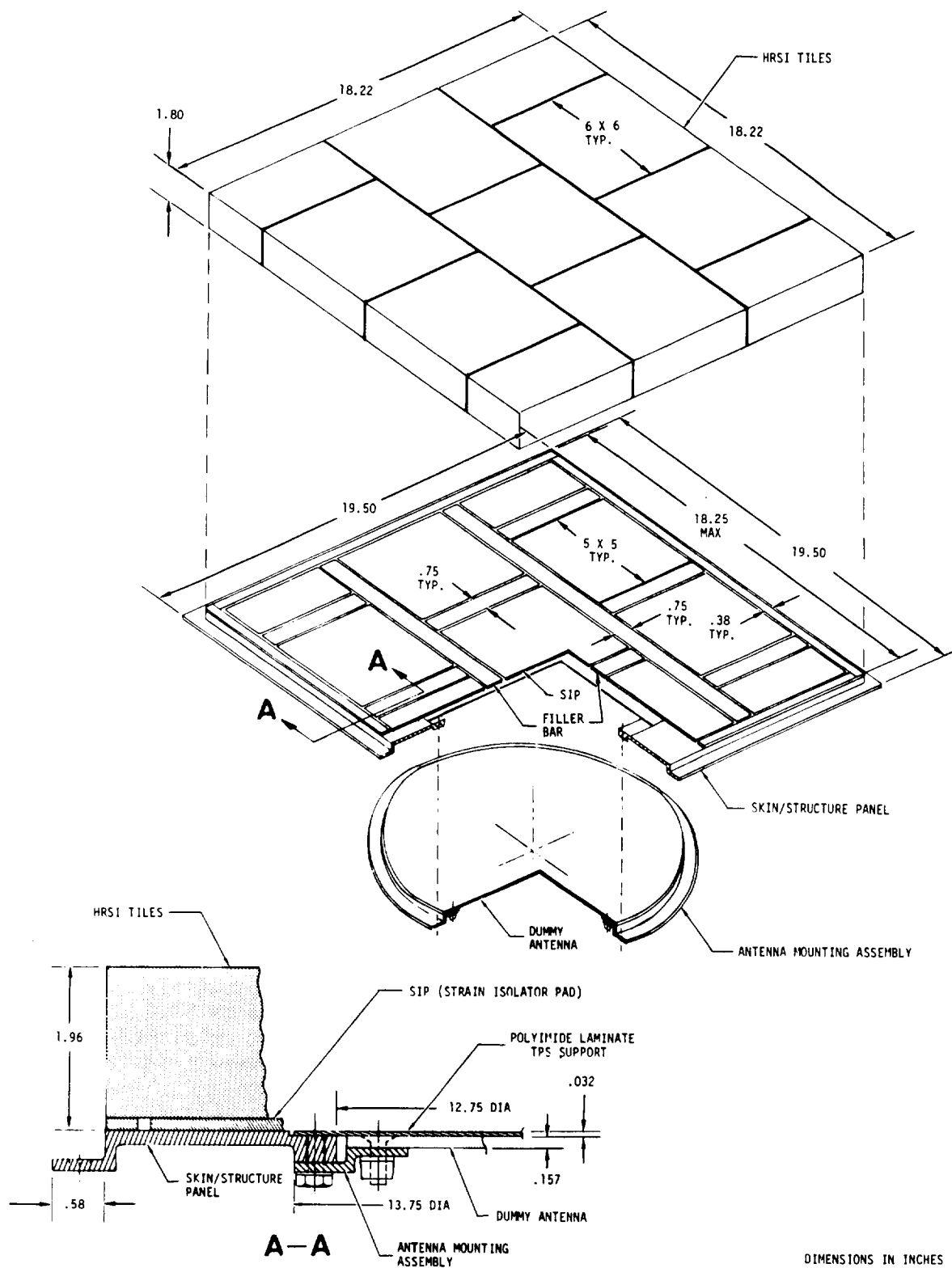


**FIGURE 2 MMAPA TEST FIXTURE**

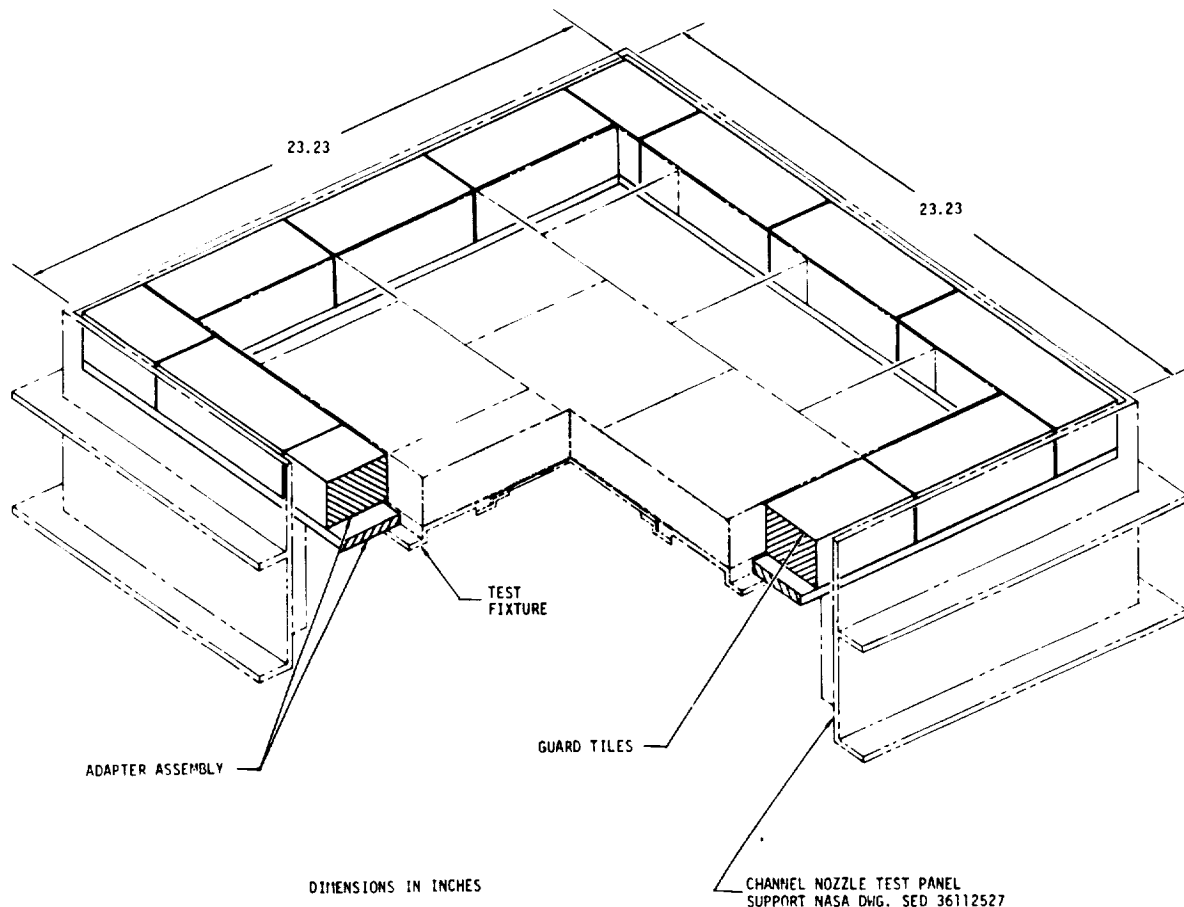


FIGURE 3 ARMSEF FACILITY ADAPTER

TPS: In the area of the lower S-band Quad antennas, the Shuttle TPS (figure 4) consists of HRSI (High Temperature Reusable Surface Insulation), SIP (Strain Isolator Pad) and a bonding adhesive. The HRSI is bonded to the SIP and the SIP to the skin with RTV-560. The thickness of the HRSI is dependent upon the local heat input. The HRSI is not continuous but is cut into tiles nominally 15.2 x 15.2 cm (6.0 x 6.0 in.). The tile rows are normally offset 7.6 cm (3.0 in.) in a transverse direction to eliminate long longitudinal gaps and, thus, minimize heating due to plasma gas flow in the gaps. The gap width between tiles is  $1.27 \pm 0.51$  mm ( $0.050 \pm 0.020$  in.).



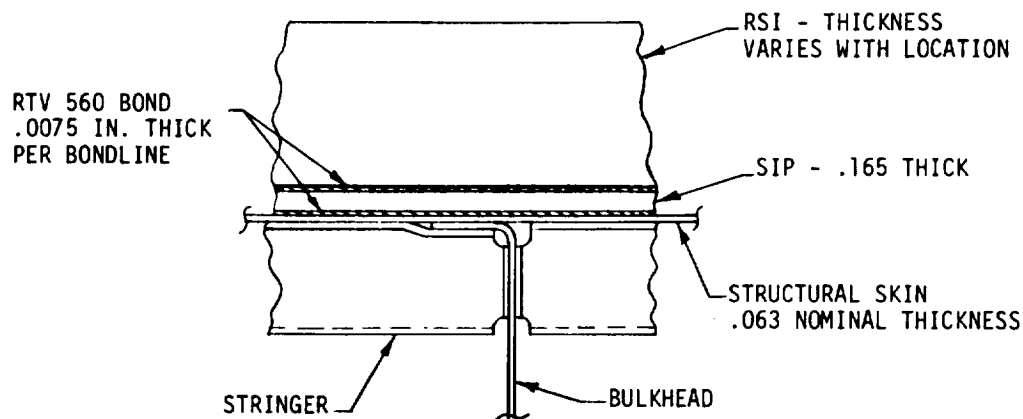


FIGURE 4 TYPICAL TPS/STRUCTURE CONFIGURATION

The HRSI tiles for the MMAPA test fixture are LI-900 insulation with a RCG (reaction cured glass) surface coating. The tiles were fabricated to the Shuttle specification in effect at the time of the order. Nominal tile sizes were used except in the corners where 7.6 x 15.2 cm (3.0 x 6.0 in.) tiles were used to accommodate the offset tile pattern (figure 2). The tile thickness selected for the test fixture was 4.572 cm (1.800 in.), the numerical average of tile thickness (table I) over the S-band Quad antenna taken at 5.08 cm (2.00 in.) intervals. The average tile thickness determined by numerical integration and the tile thickness profile over the antenna aperture was 0.178 mm (0.007 in.) less, which is well within the tile fabrication tolerance (+0.000/-0.025 in.) specified for the purchased tiles. The tile thickness data was supplied by Rockwell and was current as of 22 July 1976.

TABLE I  
TOTAL TPS THICKNESS  
OVER S-BAND QUAD ANTENNA

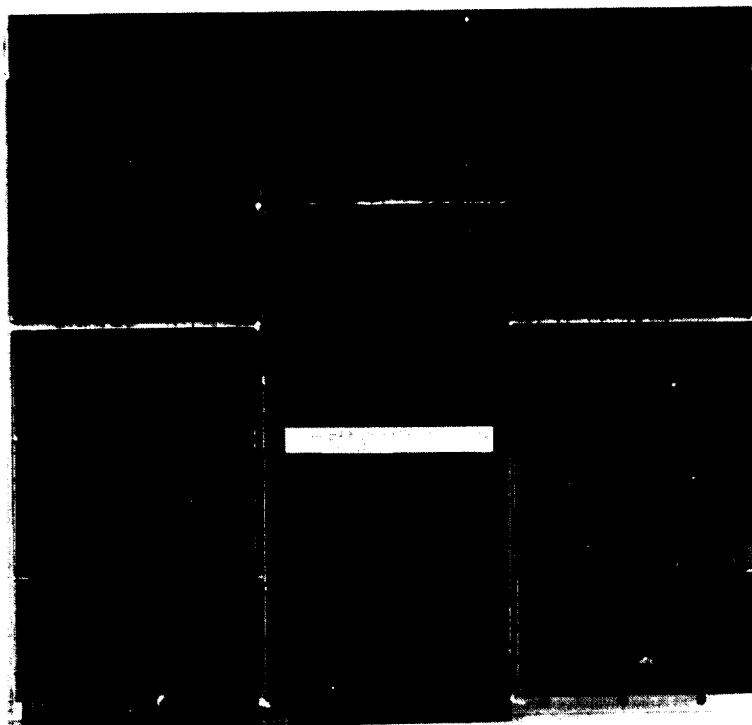
$X_0 = 556$	
$Y_0$	T(IN.)
88	1.7316
90	1.7710
92	1.8205
94	1.8818
96	1.9579
98	2.0518
100	2.1675
102	2.3099

The SIP is a layer of needle felted nomex 4.191 mm (0.165 in.) thick. The SIP configuration (figure 2) consists of individual pads under each tile and filler bar strips under the tile gaps. Nominally the SIP pads are 12.70 x 12.70 cm (5.00 x 5.00 in.) or 2.54 cm (1.00 in.) less than the tile dimension. The pads are bonded to the HRSI tile first and then the tile-SIP assembly is bonded to the structural skin. The outer surface of the filler bar is coated with RTV-560, 0.254 mm (0.010 in.) thick. This results in a rubber coating on the filler bar which serves as a waterproofing seal at the gaps between the tiles. The filler bars are bonded in place before the tile-SIP assemblies are bonded to the skin.

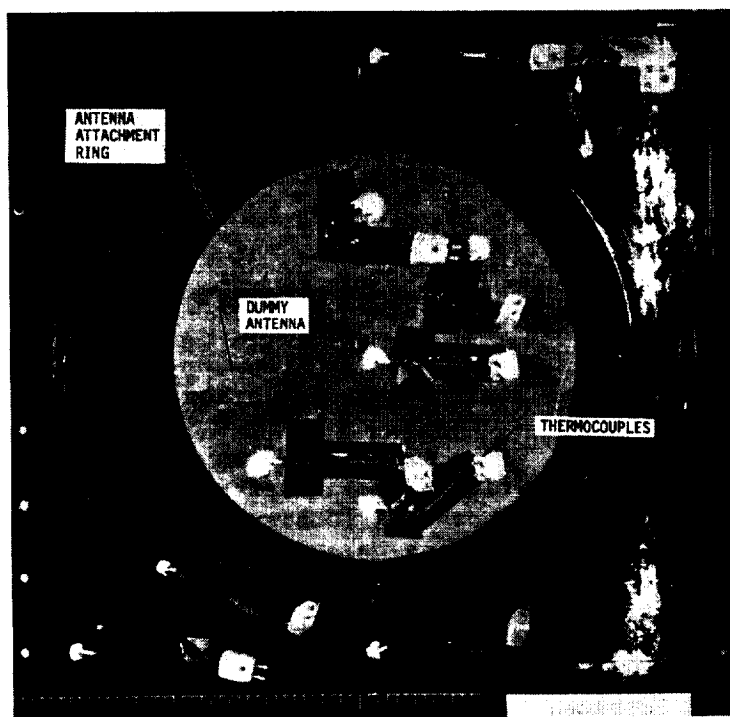
**Structure simulation:** The test fixture was designed to simulate the thermal mass of the shuttle structure in the region of the lower S-band Quad antenna. The skin-stringer structure was modeled with a simple flat plate because only the thermal mass was considered important to create the proper thermal environment for the TPS. This approach also simplified fabrication of the test fixture. The structure simulation was based on Rockwell drawings (Nos. V070-320124 and V070-320127) which give the details of the applicable structure and antenna mounting assembly details. After the test fixture design was completed and fabrication started, new drawings (Nos. V070-320780 and V070-742530) were received which show the antenna mounting fixture design has been revised. However, cursory review of the changes did not indicate any significant impact.

**Antenna mounting assembly:** The antenna mounting assembly (figure 2) was designed to permit removal of the antenna from the backside of the test fixture. This approach was necessary in order to avoid exposure of the antenna to the test environments since its performance served as a test reference. Normally the antenna would be mounted from the front (external) side and covered with TPS, thus, supporting the TPS in the same manner as the adjacent skin. To accomplish this change in mounting approach, a thin layer of laminant is inserted over the antenna aperture opening to provide a bonding surface for the TPS. A polyamide quartz cloth laminate 0.813 mm (0.032 in.) thick was used because of its superior electrical characteristics compared to other fiberglass type materials. The test fixture skin/structure panel (figure 2, cross-section A-A) was milled out to make the laminate flush with the adjacent panel surface in order to provide a smooth bonding surface for the TPS. The antenna is held in place with a circular ring which contains the necessary fasteners for the antenna. This permitted the antenna to be easily removed and replaced with a dummy antenna (i.e., a circular metal plate) during the various environmental tests.

**Fabrication.** - The MMAPA test fixture panel and associated hardware were fabricated by the NASA-JSC Technical Services machine shop. There were no significant deviations from the drawing supplied by MDAC. The TPS tiles were purchased from Lockheed to the Shuttle specification in effect at the time of the order. The tiles and the SIP were bonded to the test fixture panel by Rockwell representatives using current Shuttle bonding procedures. Figure 5 shows the completed test fixture. Figure 5(a) shows the TPS surface and figure 5(b) shows the test fixture backside with thermocouples attached.



(a) TOP VIEW



(b) BOTTOM VIEW

FIGURE 5 PHOTO OF MMAPA TEST FIXTURE

Instrumentation. - The MMAPA test fixture instrumentation consisted of ten thermocouples on the backside of the test fixture. The thermocouple locations are shown in figure 6. The primary purpose of these thermocouples (Type K, Chromel/Alumel) is to verify that the TPS bondline temperature limits were not exceeded. Thermocouples extending to the TPS surface were not used because of their effects on the antenna radiation patterns and/or impedance (ref. 2) during the antenna performance testing.

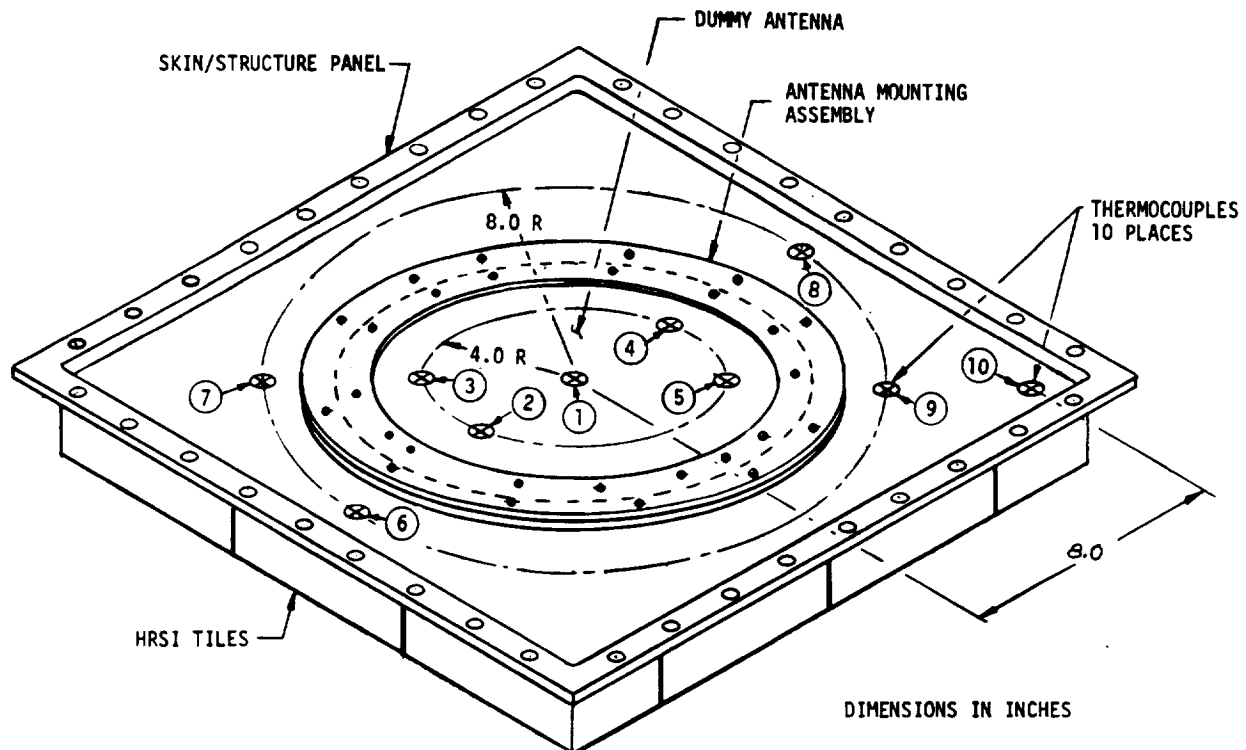


FIGURE 6 THERMOCOUPLE LOCATIONS

#### Thermal Environment Simulation

Each thermal test sequence (figure 1) simulated the Shuttle flight thermal environments consisting of ascent, orbital (abbreviated) and entry heating and pressures. The ascent and entry heating were simulated by a radiant heater. The orbital temperatures were obtained with a solar UV source for the hot orbit (i.e., where the TPS over the antenna is continuously illuminated by the sun) tests and a cold plate for the cold orbit (i.e., where solar illumination is absent) tests. The solar UV source also provided a polymerization source for any volatile deposits on the TPS tile surface. This could significantly reduce the evaporation rate of these deposits, thereby holding them on the TPS surface for possible carbonization during entry heating. (Note: this can be a significant problem

for optical coating systems.) The thermal environment simulation was performed in a continuous sequence inside a vacuum chamber because of the TPS insulation conductivity dependence on pressure. The heat flux and pressure histories used for the ascent and entry environments were obtained from Rockwell through the NASA-JSC Thermal Technology Branch. Resulting surface temperature histories were calculated using these environments in the thermal model described in reference 1 with an updated TPS thickness.

The environments simulated were those applicable to Space Shuttle in the area of the lower S-band Quad antennas located at  $X_0 = 556$ ,  $Y_0 = +95.62$ , and  $Z_0 = 294.65$ .

Facility description. - The MMAPA thermal tests were conducted in the NASA-JSC radiant heat facility located in Building 13. This facility (figure 7) consists of a graphite heater and control, a vacuum chamber and a data acquisition system (not shown). Additional equipment used for the MMAPA tests included a solar UV source and a cold plate.

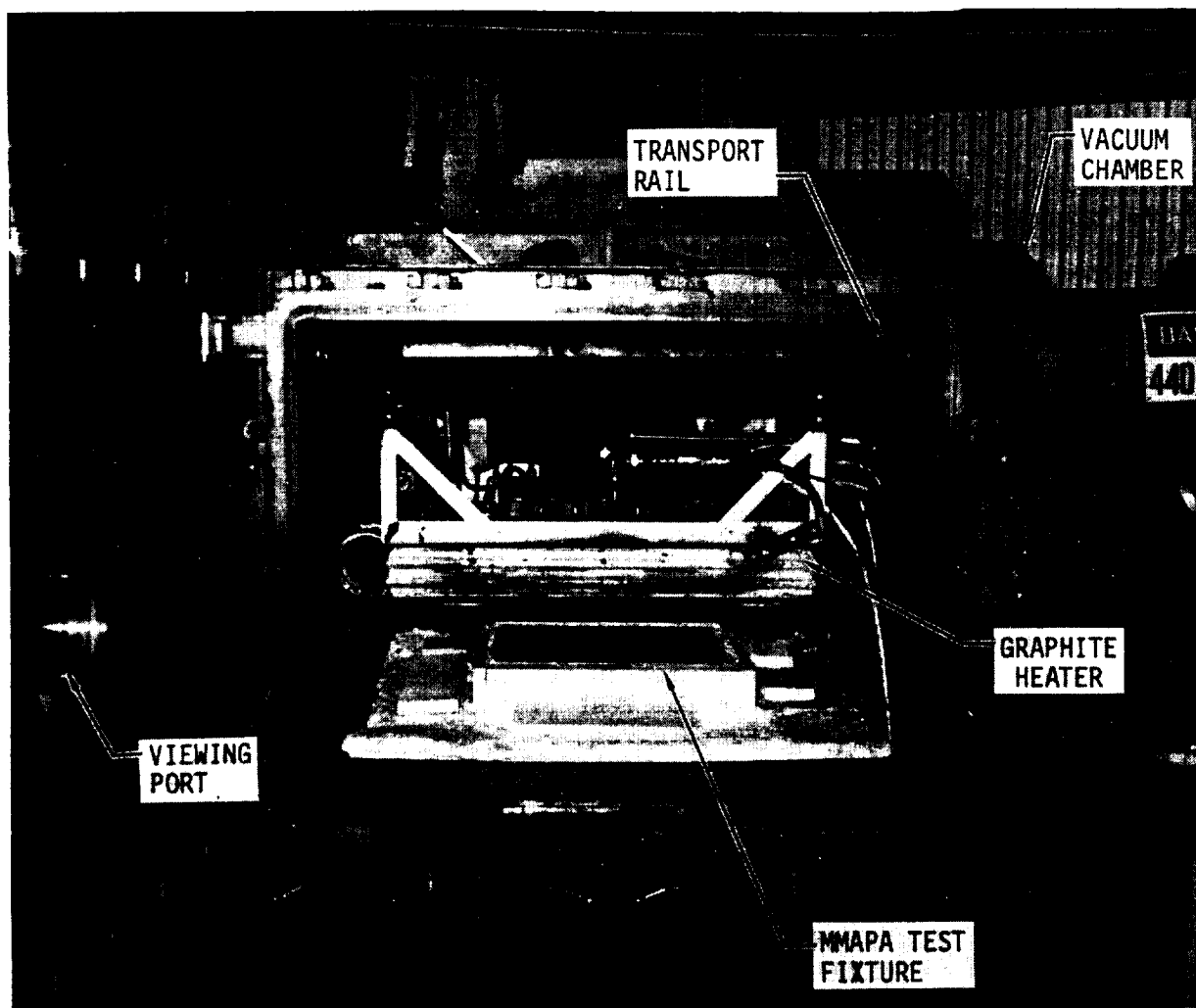


FIGURE 7 NASA-JSC RADIANT HEAT TEST FACILITY

The graphite heater assembly (figure 7) is a controllable radiant heat source capable of attaining maximum temperatures of 1644 K (2500°F) on the surface of a test specimen. The heater can be controlled to the desired temperature manually or automatically by a Data Trak system within  $\pm 2\%$ . The heater consists of an array of graphite elements, operated in a nitrogen purged enclosure, which heat a susceptor plate. The susceptor plate, a sheet of refractory metal, forms part of the enclosure and provides a test area of approximately 61 x 61 cm (24 x 24 in.). The heater assembly is suspended from an overhead rail assembly and can be moved to an alternate position manually. The range of movement permits testing at two positions.

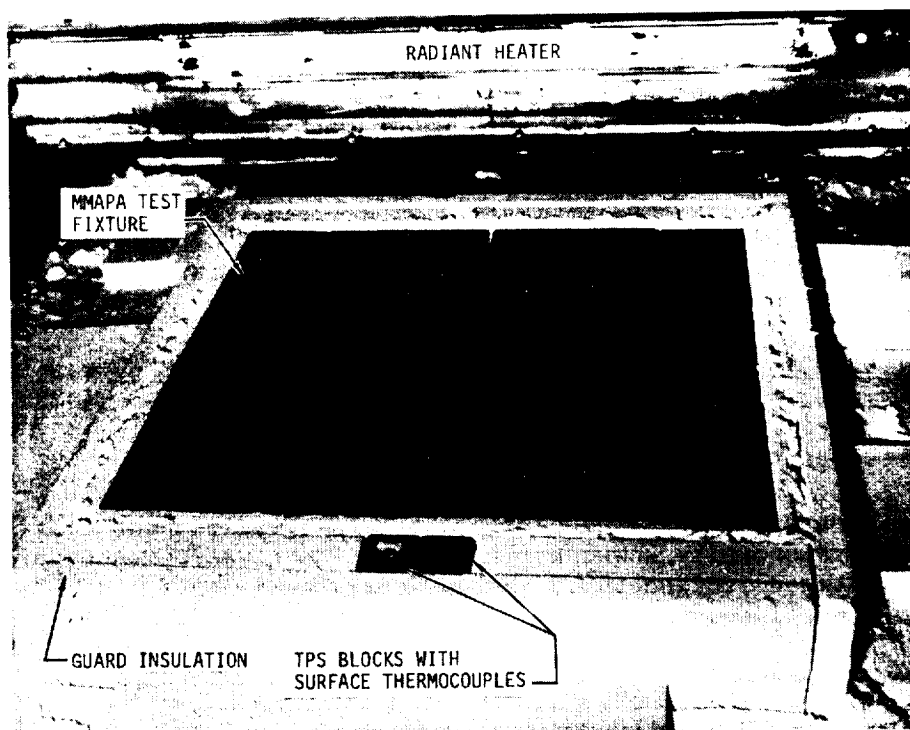
The vacuum chamber is a boilerplate pressure vessel from the Apollo program. The pressure can be controlled manually or automatically by a Data Trak system from sea level (ambient) to 93.3 Pa (0.7 torr). Pressure is measured by baratron or standard pressure transducer systems.

The data acquisition system consisted of a magnetic tape recorder with 50 channels capacity at a minimum speed of 100 samples/second/channel and 16 channels of real time strip chart plots. The magnetic tape can be processed after the test to provide tabulated data and/or data plots in the desired engineering units.

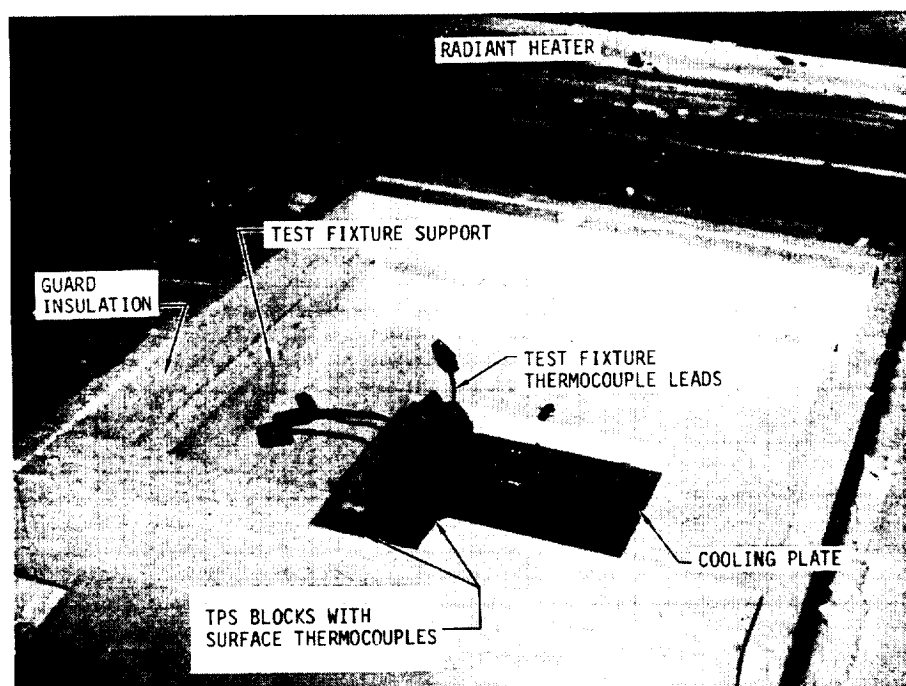
The solar UV source consists of a 4 kW xenon lamp. The lamp output (beam) entered the vacuum chamber through a quartz window in the access door (figure 7). It was deflected to the test specimen by a front face mirror attached to the heater assembly. The one-solar-constant spot size was limited to an area 19.1 x 19.1 cm (7.5 x 7.5 in.). The small spot size necessitated moving the illuminated region periodically to obtain illumination of the entire TPS surface area. The illuminated area was changed by moving the mirror and/or the lamp position.

The cold plate consisted of a nitrogen cooled plate. This plate was attached to the side of the heater assembly and, thus, was moved over the test specimen by the heater transport mechanism.

Test configuration. - The test configuration for the thermal test sequence is shown in figure 8. The MMAPA test fixture (figure 8(a)) was both surrounded and supported in place by guard insulation (LI-900 blocks and Fiberfrax) to minimize side heating and protect the test fixture edges. Two small TPS HRSI blocks with surface thermocouples were used to monitor the surface temperature since thermocouples were excluded from the test fixture TPS surface. Figure 8(b) shows the test setup with the test fixture removed. The test fixture support, backside cooling plate and thermocouple leads can be seen. The respective thermocouple locations on the test fixture are shown in figure 6. The cooling plate was held at about 294 K (70°F), nominal tap water temperature, to provide a radiation heat sink which would prevent the TPS bondline temperature from exceeding design limits.



(a) WITH TEST FIXTURE IN PLACE



(b) WITH TEST FIXTURE REMOVED

FIGURE 8 THERMAL TEST CONFIGURATION

The position of the test setup in the vacuum chamber permitted the heater to be moved from over the test specimen surface and replaced by a mirror for a solar UV environment or a cold plate for a dark space environment without opening the vacuum chamber.

Several of the test fixture TPS tile gaps exceeded the nominal limits. Therefore, to avoid excessive heating at the bottom of the gaps, the oversize gaps were filled with LI-900 fluff insulation equal to about 1/3 of the tile thickness.

Test environments. - Two thermal test environment sequences were used for the MMAPA tests. One included simulation of ascent, hot orbital flight, and entry from a hot orbit. The other included simulation of ascent, cold orbital flight and subsequent entry.

Ascent: The ascent TPS surface temperature history is shown in figure 9. The local static pressure is shown in figure 10. The lowest pressure for the MMAPA tests was limited to about 93.3 Pa (0.7 torr) because of the test facility vacuum chamber limitations.

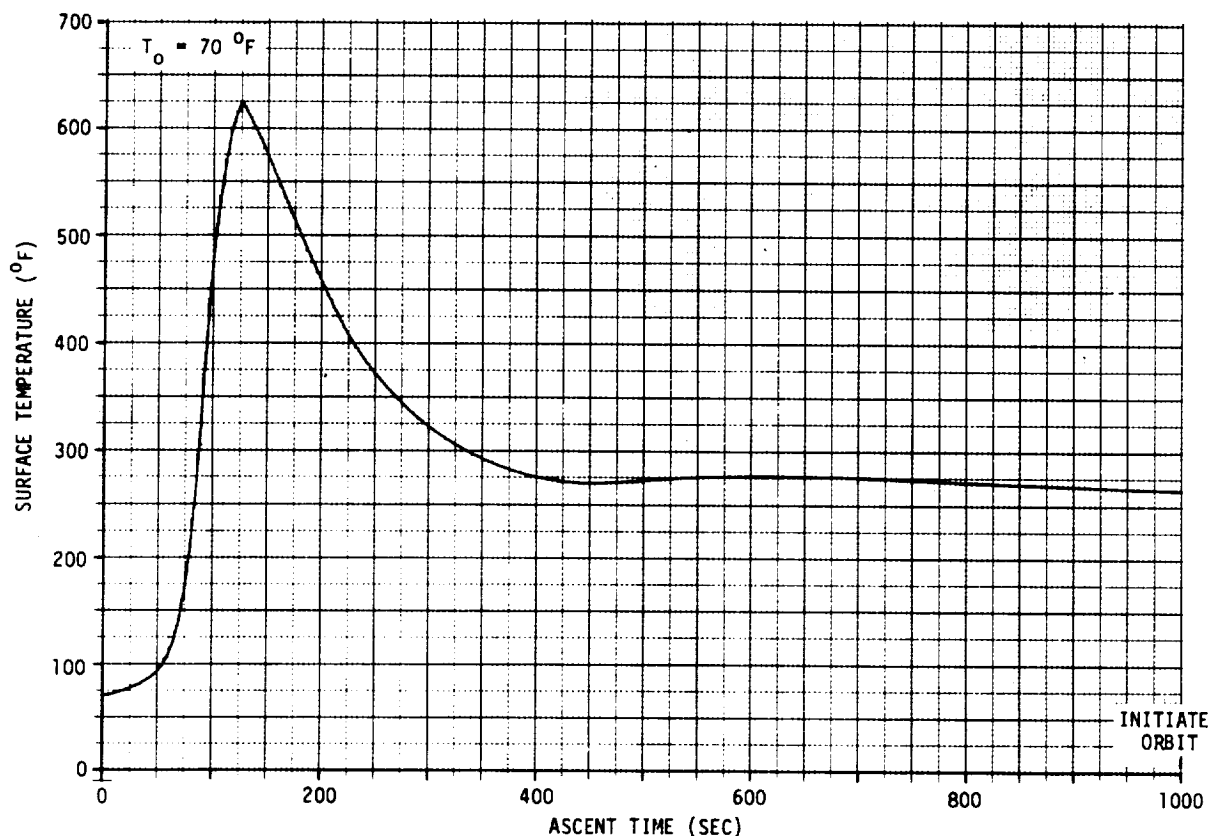


FIGURE 9 ASCENT TPS SURFACE TEMPERATURE HISTORY



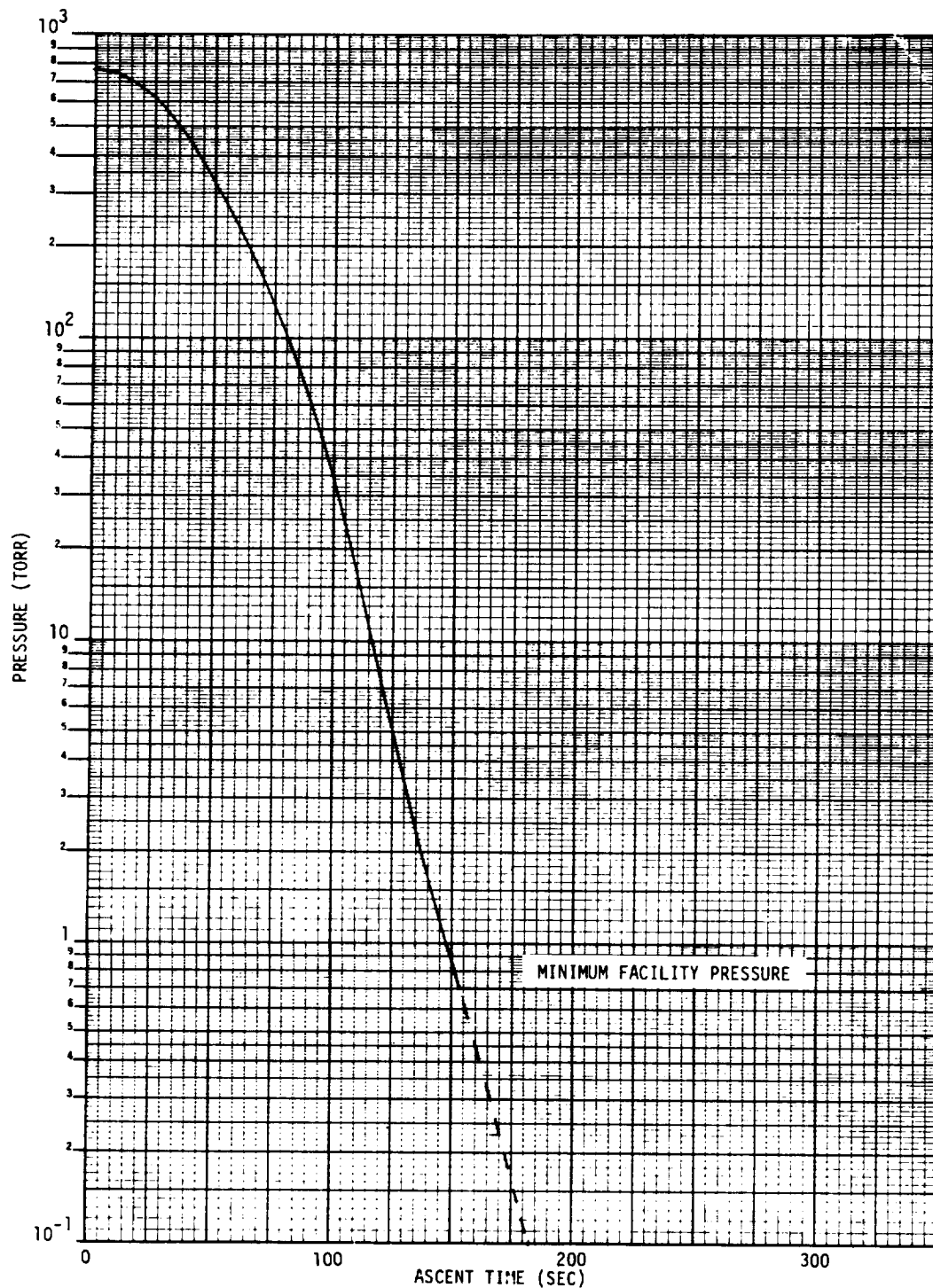


FIGURE 10 ASCENT LOCAL STATIC PRESSURE HISTORY

Orbital: The orbital TPS surface temperature history for both hot and cold orbital environments is shown in figure 11. The hot orbit was simulated for the first five tests and the cold orbit for the last five tests, with the option of continuing the hot orbit simulation if a significant trend of degradation in the electrical performance of the antenna was detected in the first five tests. The orbital test time was also limited to permit completion of a complete thermal test cycle within a 58 ksec (16 hr) period (i.e., a two-shift period).

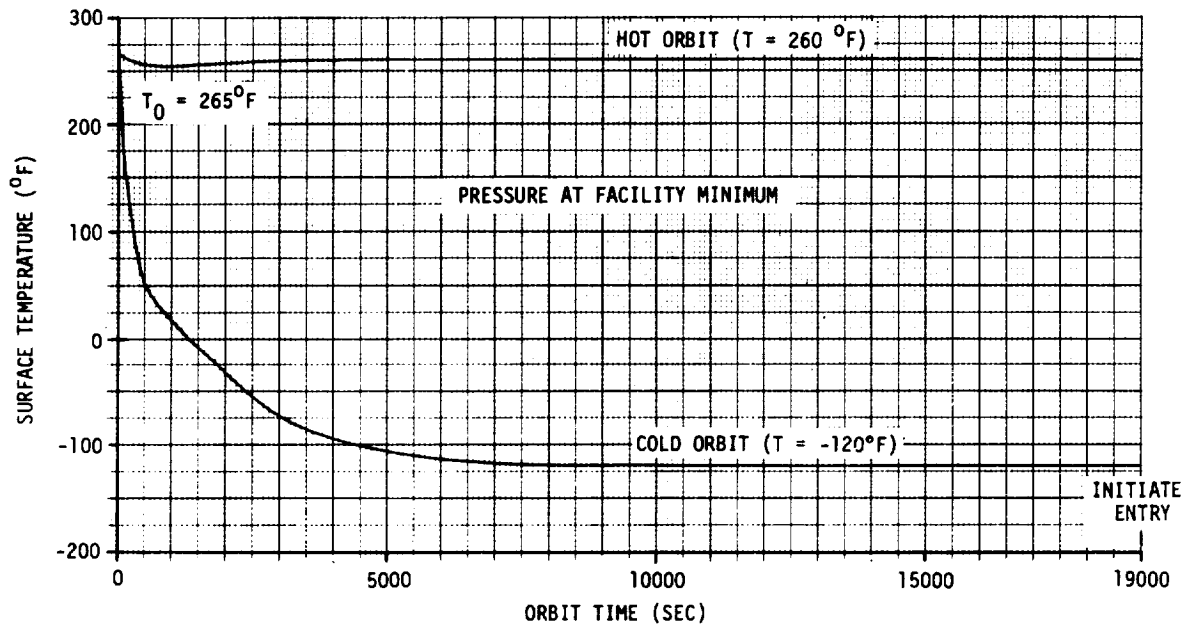


FIGURE 11 ORBITAL TPS SURFACE TEMPERATURE HISTORY

The hot orbit temperature level and simulated solar UV were obtained using a solar UV source. Because of the UV source spot size limitation (i.e., for one solar constant intensity), the MMAPA test fixture TPS surface was illuminated for 7.2 ksec (2 hrs) in each quadrant and 7.2 ksec (2 hrs) in the middle. However, during the fifth test cycle the solar UV exposure was increased from 36 to 72 ksec (10 to 20 hrs) to determine if any time dependence could be detected.

The cold orbit environment was obtained with a liquid nitrogen cooled plate placed directly over the test fixture.

Entry: The entry TPS surface temperature histories for entry from both hot and cold orbital environments are shown in figure 12. It may be noted that after about 200 sec, the TPS surface temperature is independent of the initial temperature. The entry local static pressure is shown in figure 13. The test pressure was modified slightly to remove minor pressure variations in the flight pressure history which were not considered important to meeting test objectives.

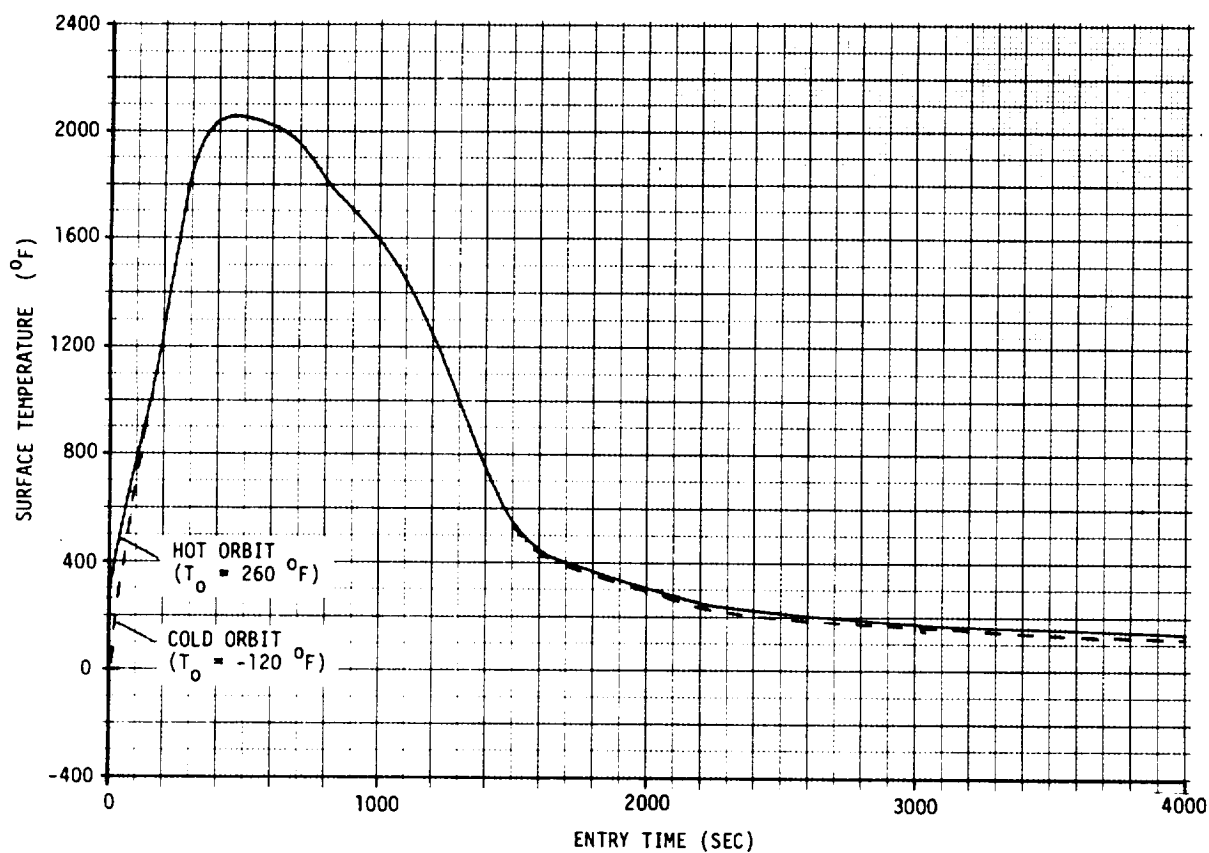


FIGURE 12 ENTRY TPS SURFACE TEMPERATURE

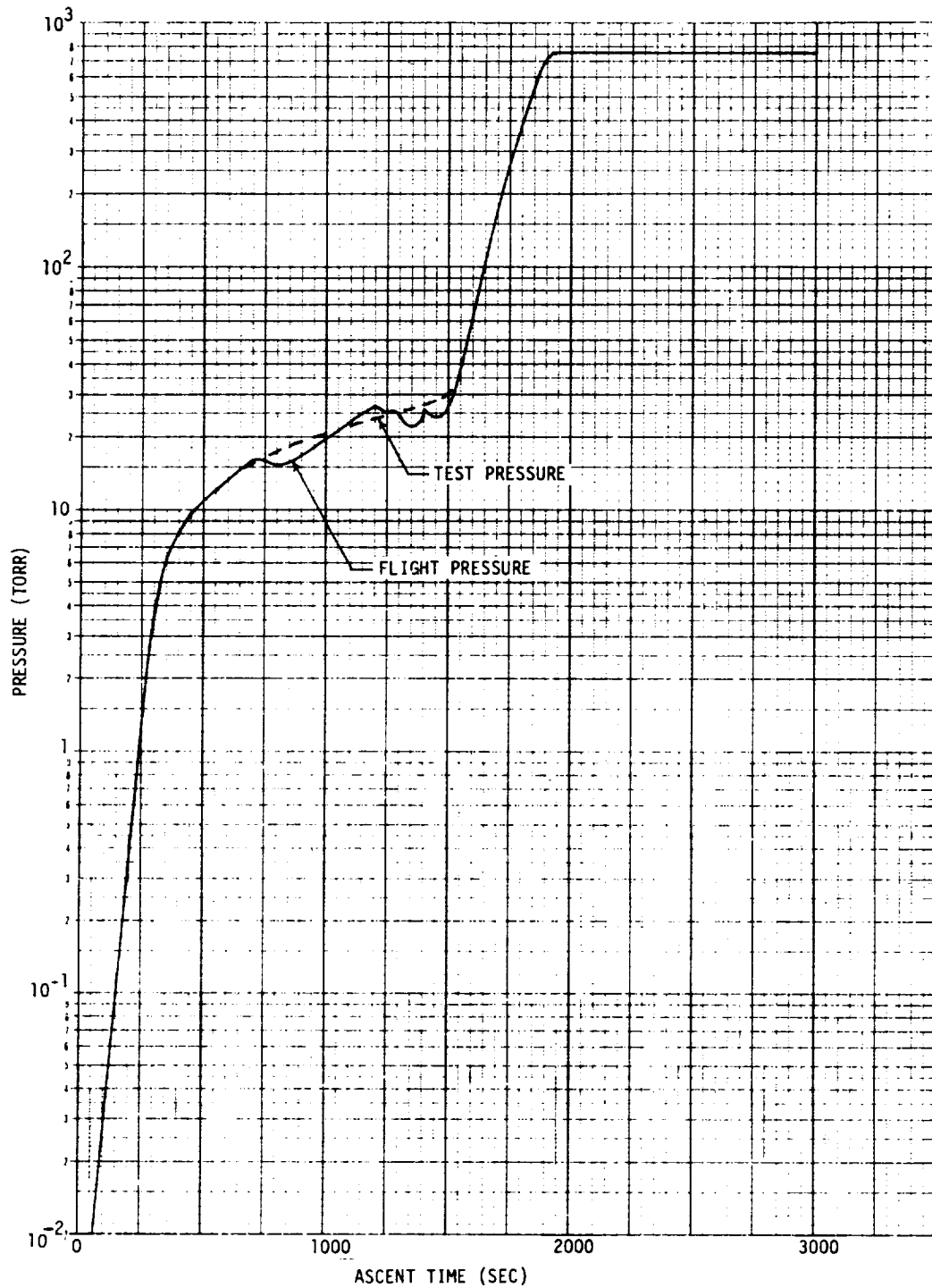


FIGURE 13 ENTRY LOCAL STATIC PRESSURE HISTORY

Test procedure. - The flight environments were simulated in a continuous sequence in the thermal test facility. This approach not only provided a more realistic sequence of events, but also improved the overall efficiency of testing by reducing the number of times the test fixture had to be handled.

The thermal environments were monitored by measuring the backside temperature of the MMAPA test fixture, the TPS surface temperature adjacent to the test fixture surface, the radiant heater susceptor plate temperature and local pressure.

The backside temperature of the MMAPA test fixture was measured to verify that the inner and outer TPS bondline temperatures did not exceed design limits. Calculations, based on a one-dimensional analytical thermal model of the test fixture (figure 14), were made to determine the respective bondline and structural skin temperatures. Figures 15 and 16 show the predicted structural skin temperature histories for ascent through both hot and cold orbits and entry from each. It may be noted that (1) the skin temperature rise during ascent (figure 15) is insignificant and (2) the temperature at the end of the orbit influences the backside entry magnitude (figure 16). The predicted skin temperature histories may deviate from the measured temperatures since the thermal model did not account for the partial blockage of the backside cooling plate by a layer of insulation as shown in figure 8(b).

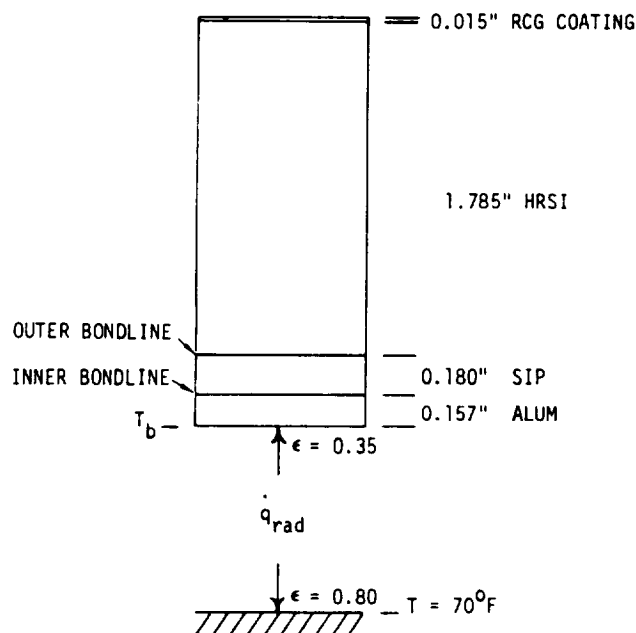


FIGURE 14 ONE-DIMENSIONAL THERMAL MODEL OF MMAPA TEST FIXTURE

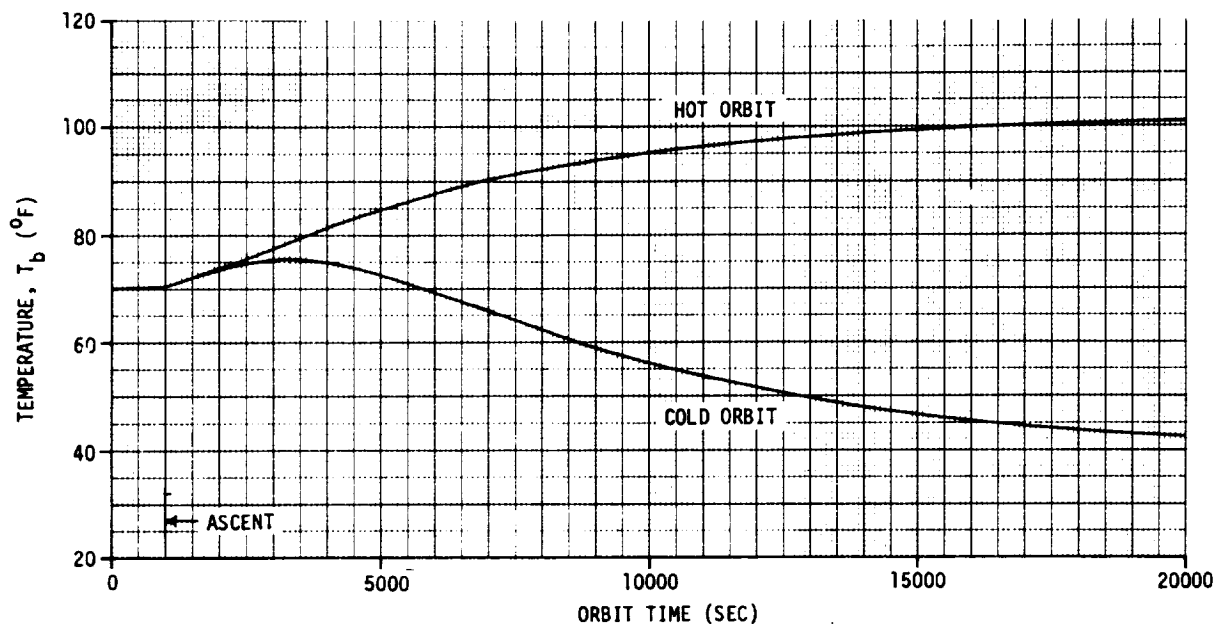


FIGURE 15 STRUCTURAL TEMPERATURE FOR ASCENT AND HOT AND COLD ORBITS

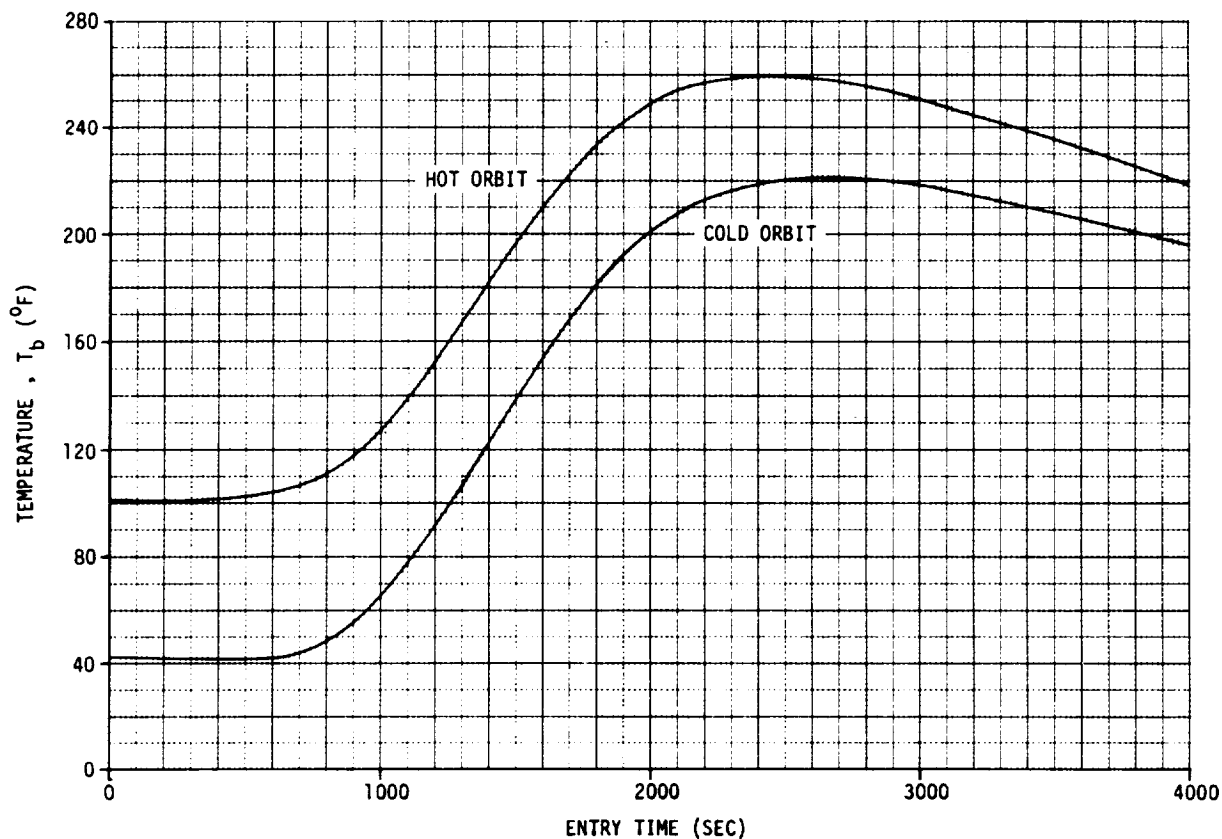


FIGURE 16 BACKSIDE STRUCTURAL TEMPERATURE FOR ENTRY FROM HOT AND COLD ORBITS

Several calibration runs were made to establish the radiant heater control temperature histories for the respective heating conditions. To obtain an equivalent TPS surface temperature measurement, the test fixture was replaced by an instrumented TPS block (i.e., an HRSI block with a surface thermocouple) located at the midpoint of the test fixture position and a suitable insulation to fill in the remaining space. This arrangement permitted indirect measurement of the peak surface temperature in the middle of the test fixture and was used to determine the relationship between the TPS surface temperature and the radiant heater susceptor plate temperature. Using that relationship, the susceptor plate temperature was adjusted to obtain the desired TPS surface temperature. Thereafter, the susceptor plate temperature was controlled by the Data Trak system. The instrumented TPS blocks just outside the test fixture boundary (figure 8), designated "L" and "D", indicated the temperature at the test fixture edges. Comparison of the edge and center temperatures shows the temperature gradient over the test fixture surface.

The ascent heating simulation calibration data is shown in figure 17. The fast surface temperature rise time was achieved by preheating the heater susceptor plate before moving it over the test fixture. The temperatures following the temperature peak were lower than desired, but this deviation is not considered an important factor.

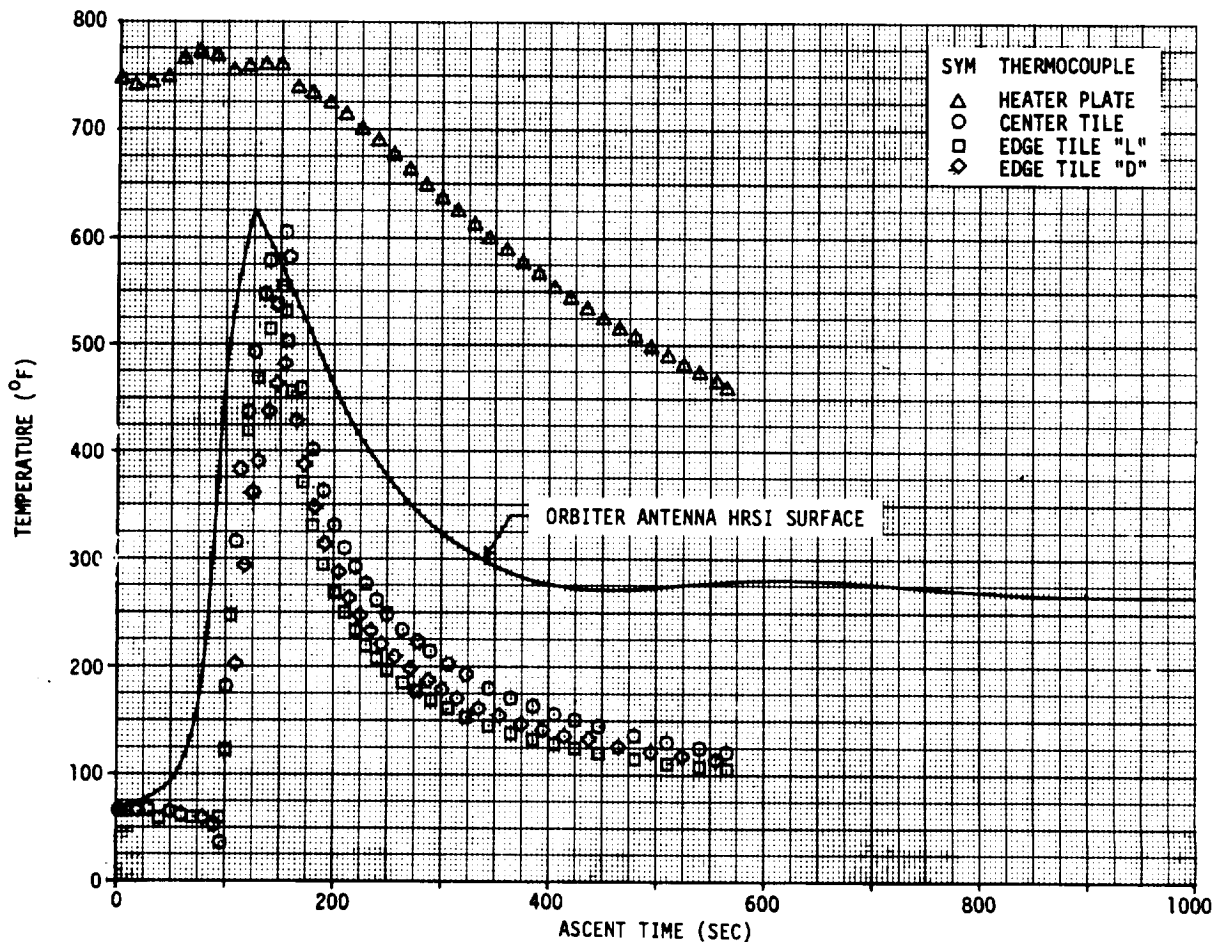


FIGURE 17 CALIBRATION FOR ASCENT HEATING - TESTS 1-5

For the hot orbit simulation tests, the solar UV source also served as the TPS heating source. Calibration tests results showed that a surface equilibrium temperature of about 389 K (240°F) was reached in about 7.2 ksec (2 hrs) at the center of the illumination spot. Because of the limited spot size, the instrument TPS blocks just beyond the edge of the test fixture did not measure the edge surface temperature with acceptable accuracy.

The entry heating simulation calibration data is shown in figure 18. The small time shift is due to the lack of preheating to the initial temperature shown by the calculated entry temperature history (figure 12). However, the measured temperatures follow the slope of calculated temperature history very closely. The surface temperature after 1300 sec is slightly high due to the lack of convective cooling which would be present in an actual entry.

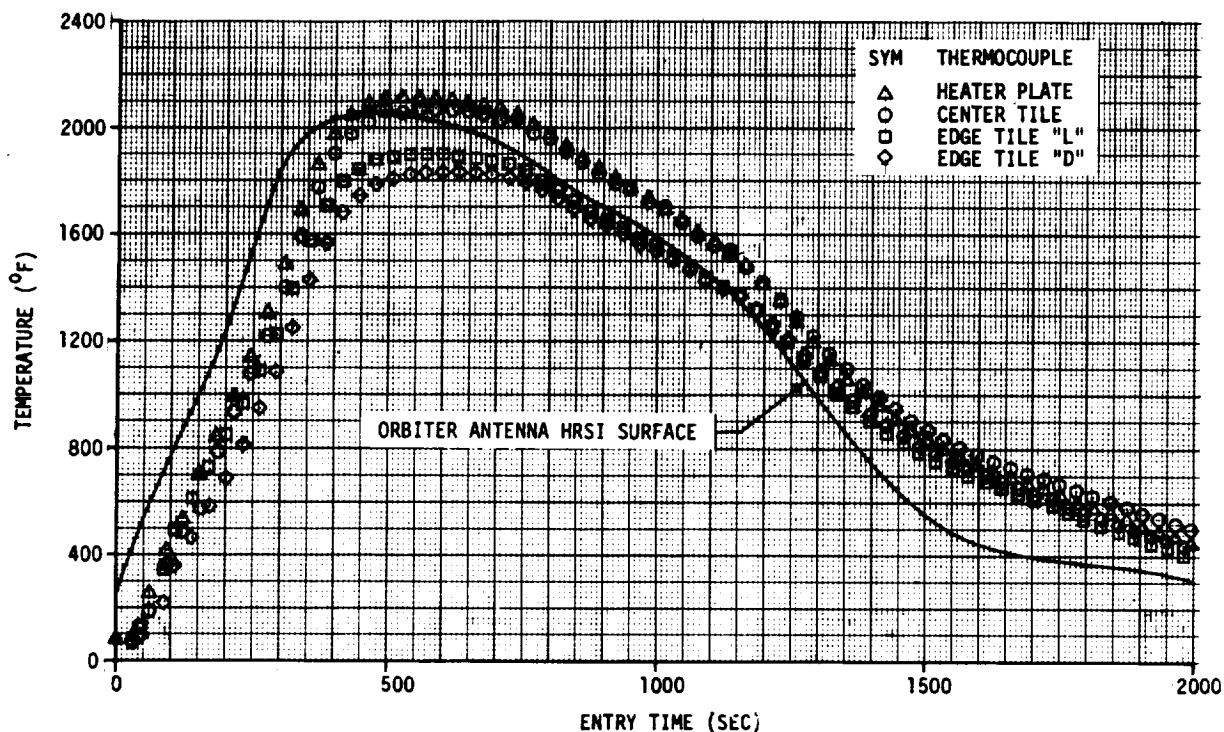


FIGURE 18 CALIBRATION FOR ENTRY FROM HOT ORBIT - TESTS 1-5



### Ground Environment Simulation

The ground environmental test consisted of simulating those ground environments which could contribute to the deposit of contaminants on the Space Shuttle TPS surface while on the ground after entry, or during prelaunch operations. The environments of primary interest were dust, salt fog and humidity. Dust, particularly that from the side of a runway, contains a variety of materials (e.g., oil, metals, rubber, carbon, etc.), which combined with salt fog and high humidity form a tightly bound deposit on the TPS surface. The subsequent ascent, orbital and entry thermal environments could then contribute to a permanent film fixed on the TPS surface. While the TPS surface contamination for a single mission cycle may be negligible that from a number of missions could build up and result in significant RF degradation which is of concern.

Test setup description. - The ground environments simulation cabinet (figure 19) consisted of: (1) an existing metal container (internal dimensions of 76.2 x 156.2 x 96.5 cm (30 x 61.5 x 38.0 in.)); (2) an instrument fan; (3) a shallow pan for water; (4) a hygrometer; and (5) two small ports added to the container walls to admit dust and salt fog. An existing rail inside the container provided a convenient mounting bracket for the fan and a support for the test fixture. The hygrometer was mounted in front of an existing port at one corner of the container. The port for admitting the dust was placed above the test fixture position and the port for the salt fog in the end above the fan. Figure 19 also shows the test fixture transport box with the dummy antenna and antenna mounting ring inside.

Test environments. - The ground environments used for the tests are subjective because there are no specifications which cover the type of contamination considered in this test program. Therefore, the test environment exposure dosages were determined experimentally prior to the start of testing. The methods for obtaining and controlling the respective environments are described below.

**Dust:** The dust environment of interest is that which simulates the results of gusting dust clouds or long exposure to airborne dust particles which could settle on the TPS surface and form a tightly bound surface deposit or film.

The dust for the MMAPA tests was taken from the side of an Ellington Air Force Base runway. To obtain the desired particle size, the dust sample was placed in a ball mill and milled for about 20 hours. This reduced the particle size to the proper range, about like flour, and mixed the constituents thoroughly.

A small shop vacuum cleaner was used to create a dust cloud in the test chamber above the test fixture. The vacuum cleaner output port was placed over a small hole in the chamber top (i.e., the chamber acts as the vacuum bag) and measured dust quantity (3.5 gm) dumped into the intake. This technique gave a reasonably uniform dust deposit and was superior to other methods that were tried.

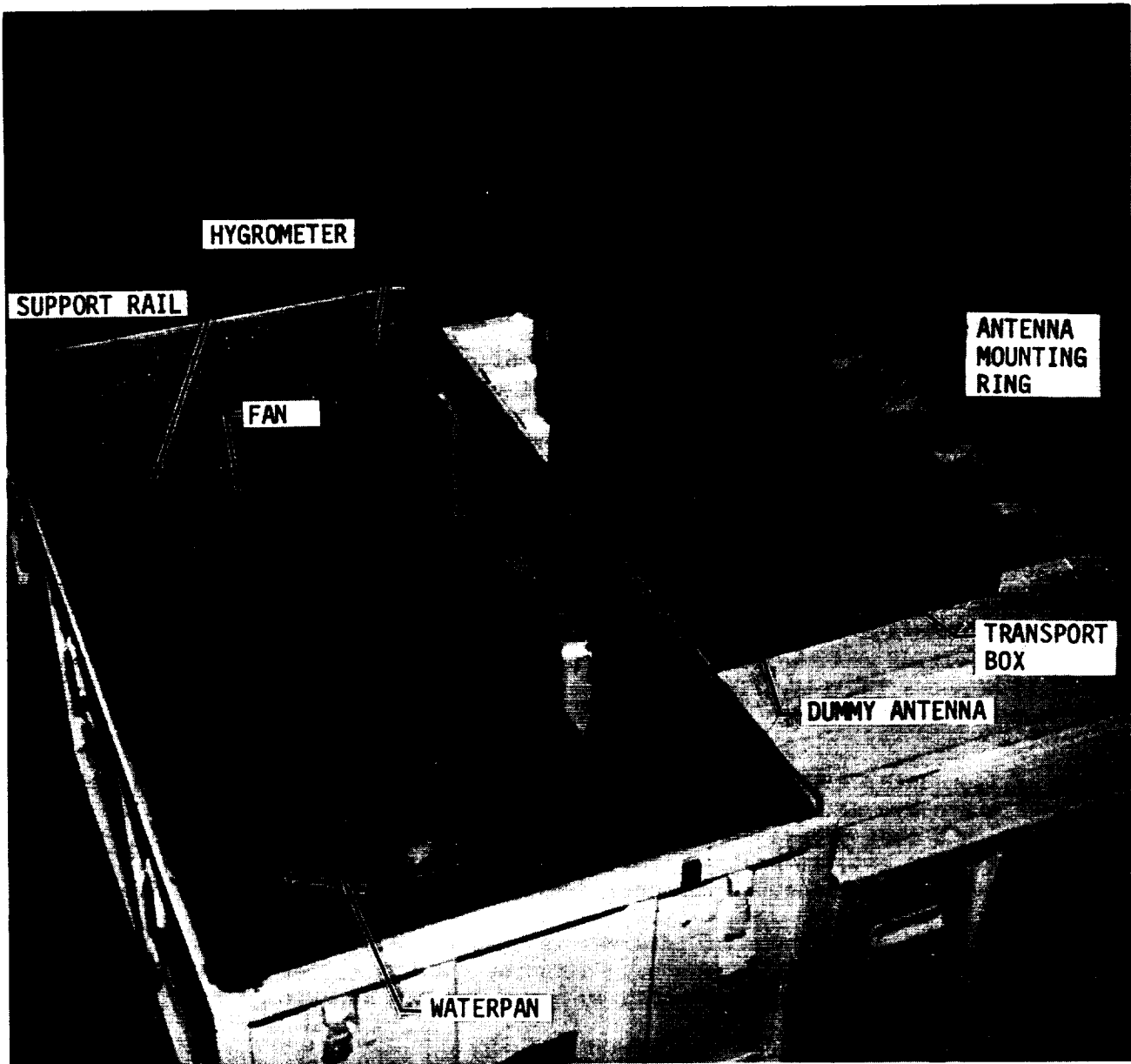


FIGURE 19 GROUND ENVIRONMENTS SIMULATION CABINET

Glass witness plates (2 x 2 in. glass plates used to mount photographic slides) were used to monitor the dust deposit density and uniformity. The relative density was measured by a standard laboratory device used to measure light transmission. For the MMAPA tests, the measurements included the effects of both the dust and salt fog residue. Pretest experiments indicated that a coating with a realistic appearance resulted in a 30% drop in light transmission through the witness plate.

**Salt fog:** The salt fog environment was created by spraying a fine mist of salt water above the test fixture. The salt water was a 5% solution per MIL-STD-810C. The mist was obtained with a pressurized laboratory atomizer. Pretest experiments determined that a 5 sec operation of the atomizer was sufficient to obtain the equivalent of several hours of salt fog exposure.

**Humidity:** The high humidity environment was easily achieved by the air flow from the fan over the shallow pan of water. With the test chamber closed, a relative humidity of 98 to 100% was obtained in 30 to 40 minutes. Starting with dry air, only 30.0 cm<sup>3</sup> (1.83 in.<sup>3</sup>) of water was required to obtain saturation. Since the test cabinet was essentially air tight, the high humidity could be maintained for long periods without replenishment of the water supply.

Test procedure. - Following each electrical test (except Test 10) the test fixture was placed in the ground environments simulation cabinet. The respective environments were then introduced in the following sequence:

1. Humidity (3.6 ksec (1 hr) exposure)
2. Dust (3.5 gm introduced by dust cloud over test fixture)
3. Humidity (57.6 ksec (16 hr) exposure)
4. Salt fog (5 sec spray over test fixture)
5. Repeat dust exposure of step (2).

#### Electrical Performance Testing

The electrical performance testing consisted of radiation pattern and impedance measurements after each thermal test cycle. This provided data which was compared with pretest data to evaluate changes in pattern shape, gain, axial ratio and antenna impedance.

Test setup description. - The radiation patterns and impedance were measured in the NASA-JSC anechoic chamber antenna pattern range. Major equipment components included a Watkins Johnson frequency synthesizer (a frequency and power stable signal generator), a Scientific-Atlanta (S-A) receiver, and S-A polar and rectangular recorders. Figure 20 shows the MMAPA test fixture mounted in a 3 x 3 m (10 x 10 ft) ground for pattern measurements. A standard gain horn was mounted on the backside of the ground plane (figure 21) for use in reestablishing a reference level before each test set. The test antenna was supplied by Rockwell and is representative of the Shuttle S-band Quad antenna. Figure 22 shows the test setup for the impedance measurement measurements. The back side of the antenna installation was covered with a plastic vacuum bag to keep the polyimide laminate which supported the TPS over the antenna in intimate contact with the antenna aperture. This procedure was used for both the pattern and impedance measurements to ensure that the position of TPS over the antenna remained stationary.

Data acquisition. - The radiation patterns were measured in both polar and rectangular coordinates. Rectangular plots are more useful than polar plots for analysis because the magnitude scale is expanded by a factor of about 3. Pat-

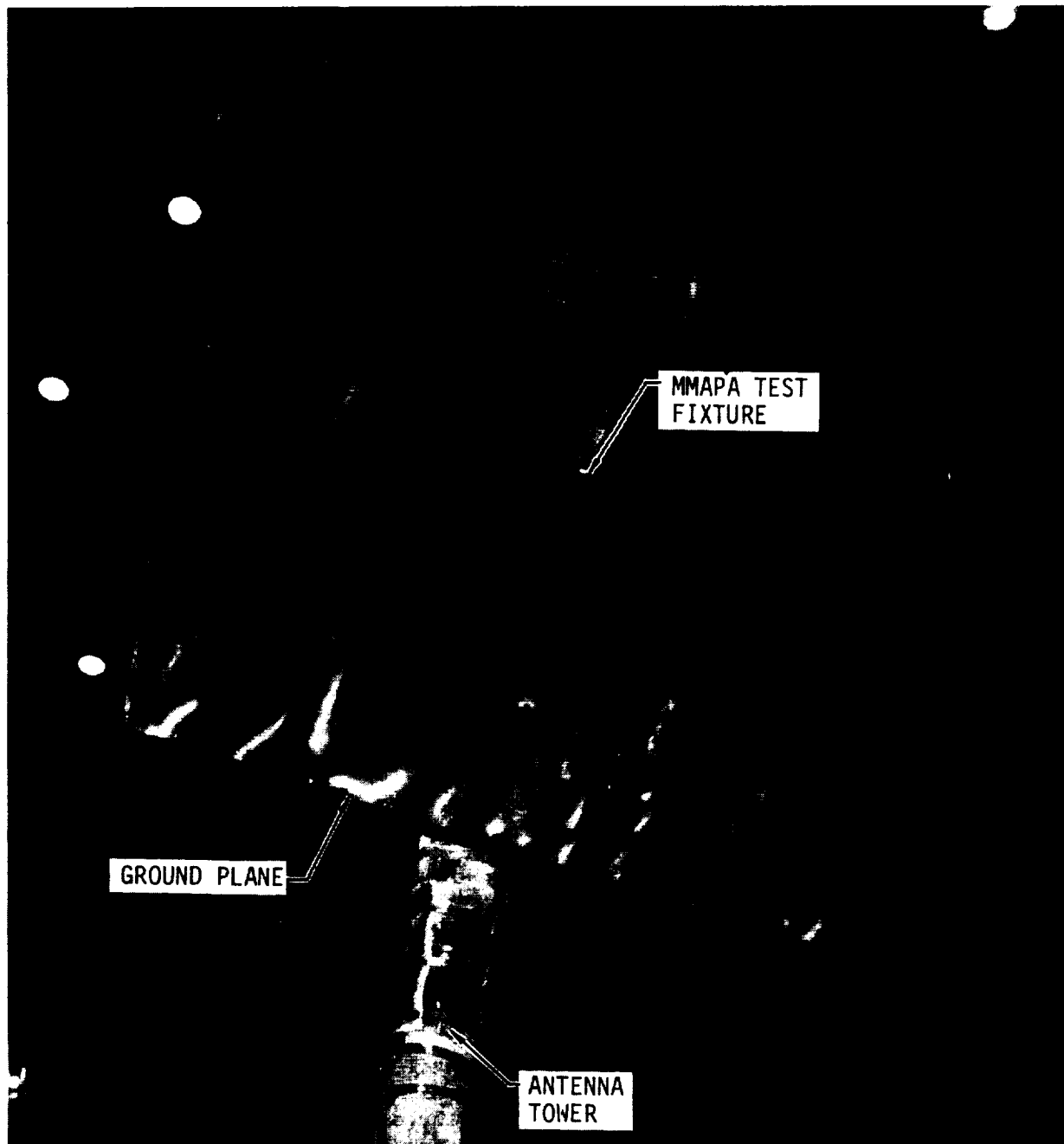
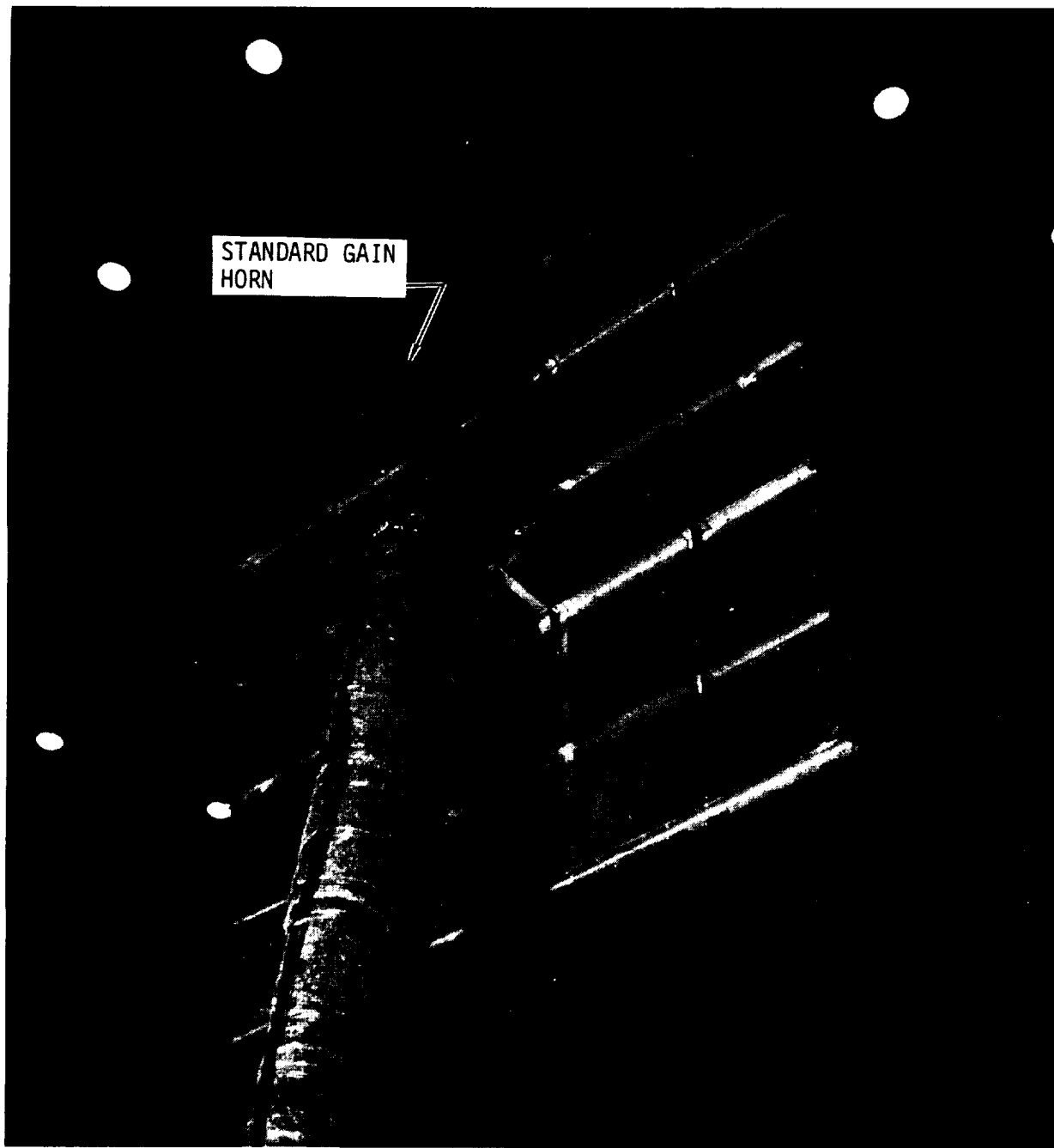


FIGURE 20 TEST SETUP FOR RADIATION PATTERN MEASUREMENTS



**FIGURE 21 GAIN REFERENCE CONFIGURATION**

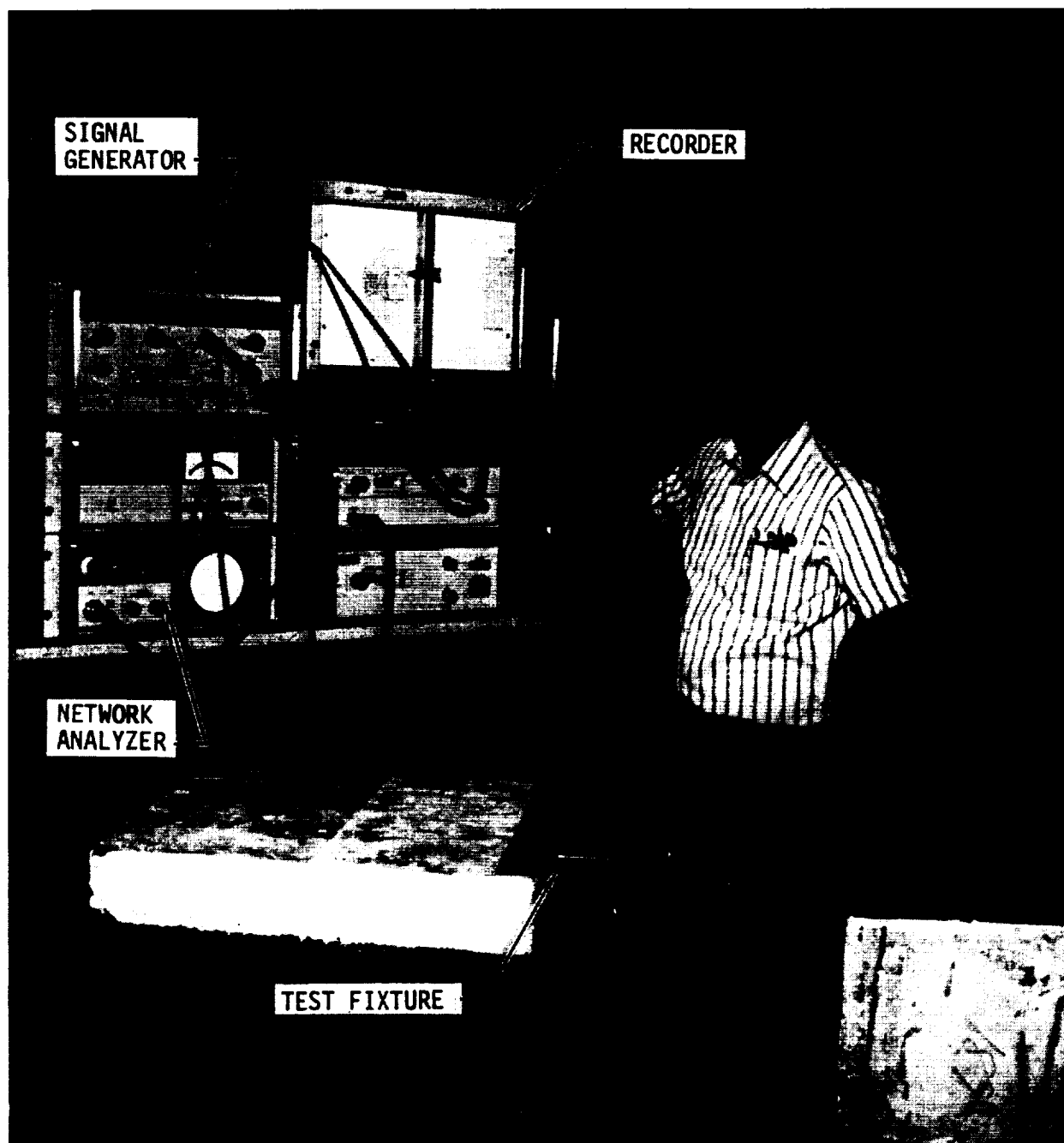
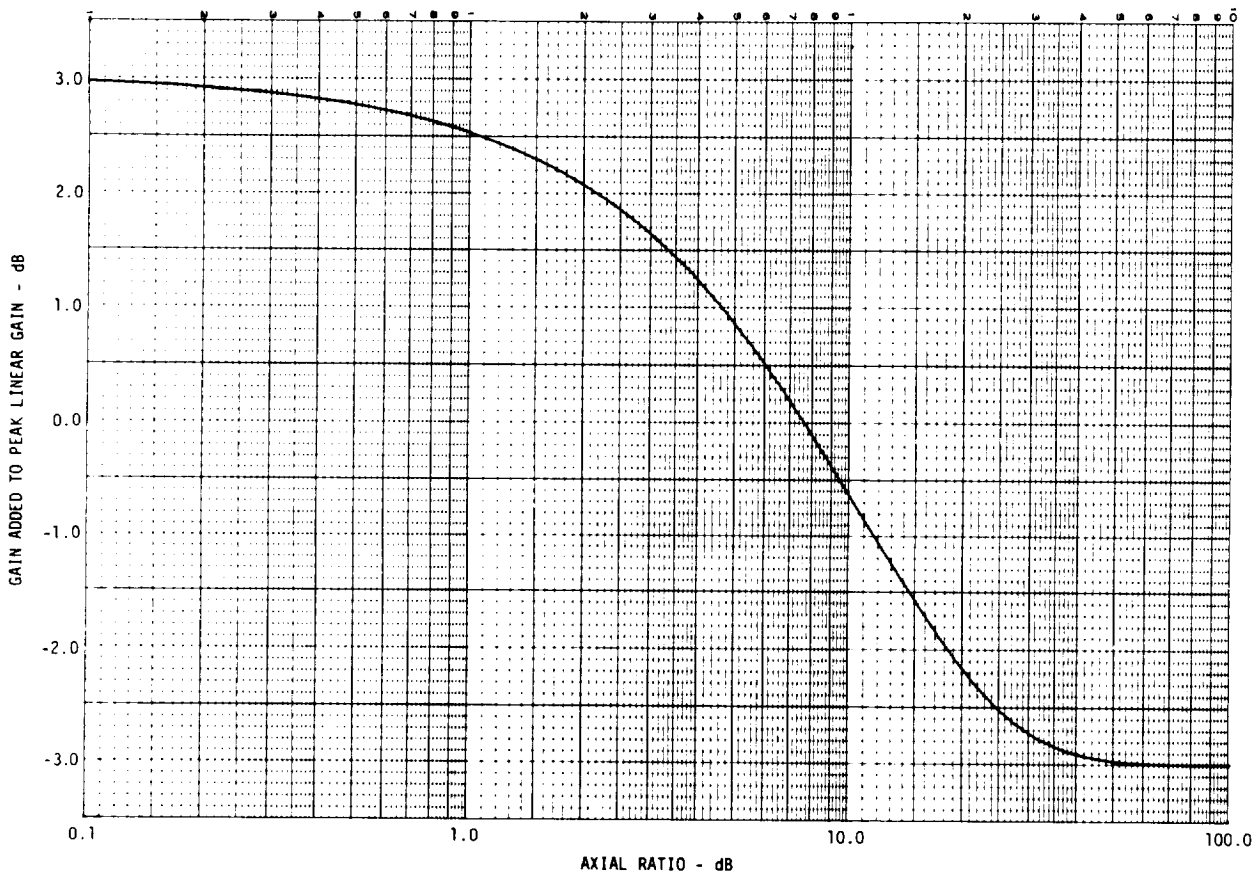


FIGURE 22 TEST SETUP FOR IMPEDANCE MEASUREMENTS

terns were measured at frequencies of 1.8, 2.1 and 2.3 GHz. The patterns were measured using rotating line or polarization in order to obtain axial ratio simultaneously with pattern shape. The peak linear gain can be converted to circular gain by adding a gain factor (figure 23) which is a function of axial ratio.  $\theta$ -plane patterns were taken for  $\phi$  angles of  $0^\circ$ ,  $45^\circ$ ,  $90^\circ$  and  $315^\circ$  ( $-45^\circ$ ). Figure 24 shows the coordinate system used for the antenna pattern. The pattern recording convention was such that the right hand side of the polar plots ( $\theta$  variable) corresponds to the  $\phi$  angle designated for the pattern plane. However, the left hand side of the rectangular plots corresponds to the right hand side of the polar plots, so that, visually, one is the mirror image of the other. A fixed ground plane and pattern tower rotation convention was maintained for each pattern to minimize pattern error due to gear backlash, etc. The signal level was reset to a reference level at each frequency by setting the peak gain of the standard gain horn radiation pattern to that level. The pattern range repeatability is estimated to be  $\pm 0.25$  dB.



**FIGURE 23 CONVERSION FROM PEAK LINEAR TO CIRCULAR GAIN**

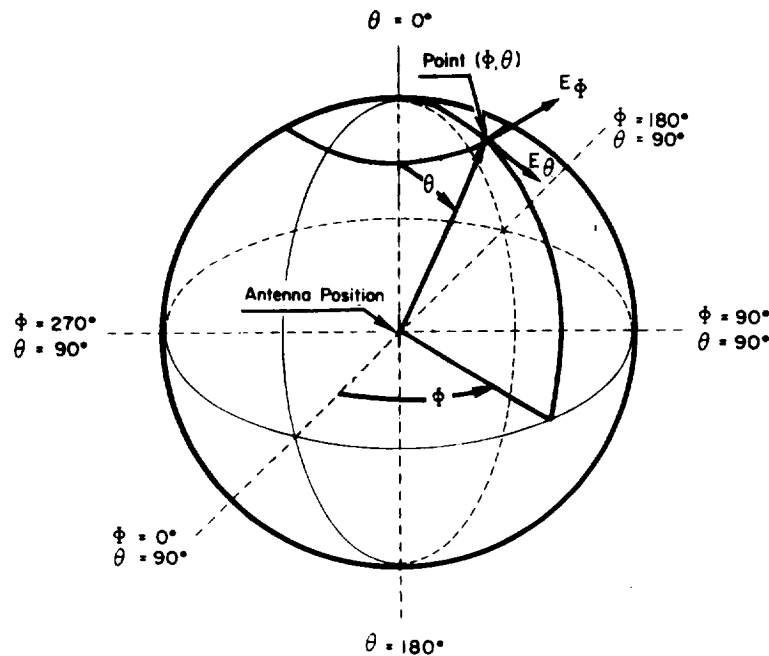


FIGURE 24 ANTENNA PATTERN COORDINATE SYSTEM

Since the VSWR of the antenna was very low, the impedance plots result in small spiraling circles around the center of the Smith Chart. To improve resolution at specific frequencies of interest, the reflection coefficient was also recorded with the magnitude increased by 10 dB (voltage ratio). The impedance was measured in two frequency ranges, 1.7 to 1.9 GHz and 2.0 to 2.4 GHz.

#### Test Results

The primary test results of interest are those from the electrical performance tests (radiation pattern and impedance measurements) performed after each simulation of the ground and flight (thermal/pressure) environments. The other test data from the environment simulations were used to verify that the respective test parameters were within preestablished limits necessary to meet test objectives.

Thermal environments verification. - Figure 25 shows the measured susceptor plate and edge tile temperature histories during ascent simulation for the first five tests. These temperature histories, also typical of the last five tests, show good repeatability. Figure 26 shows the measured pressure histories during the ascent simulation. The repeatability is generally good. Depressurization nominally began at about 40  $\pm$  10 sec after the test start, except for Tests 1, 3 and 9.



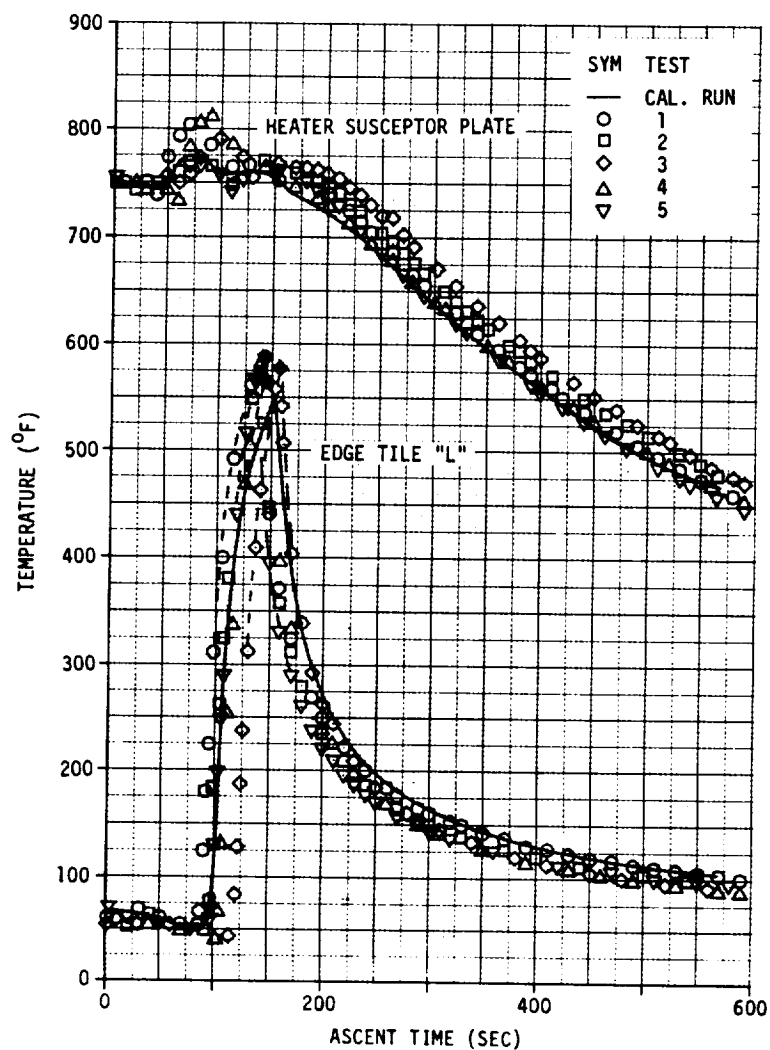


FIGURE 25 ASCENT HEATING REPEATABILITY - TESTS 1-5

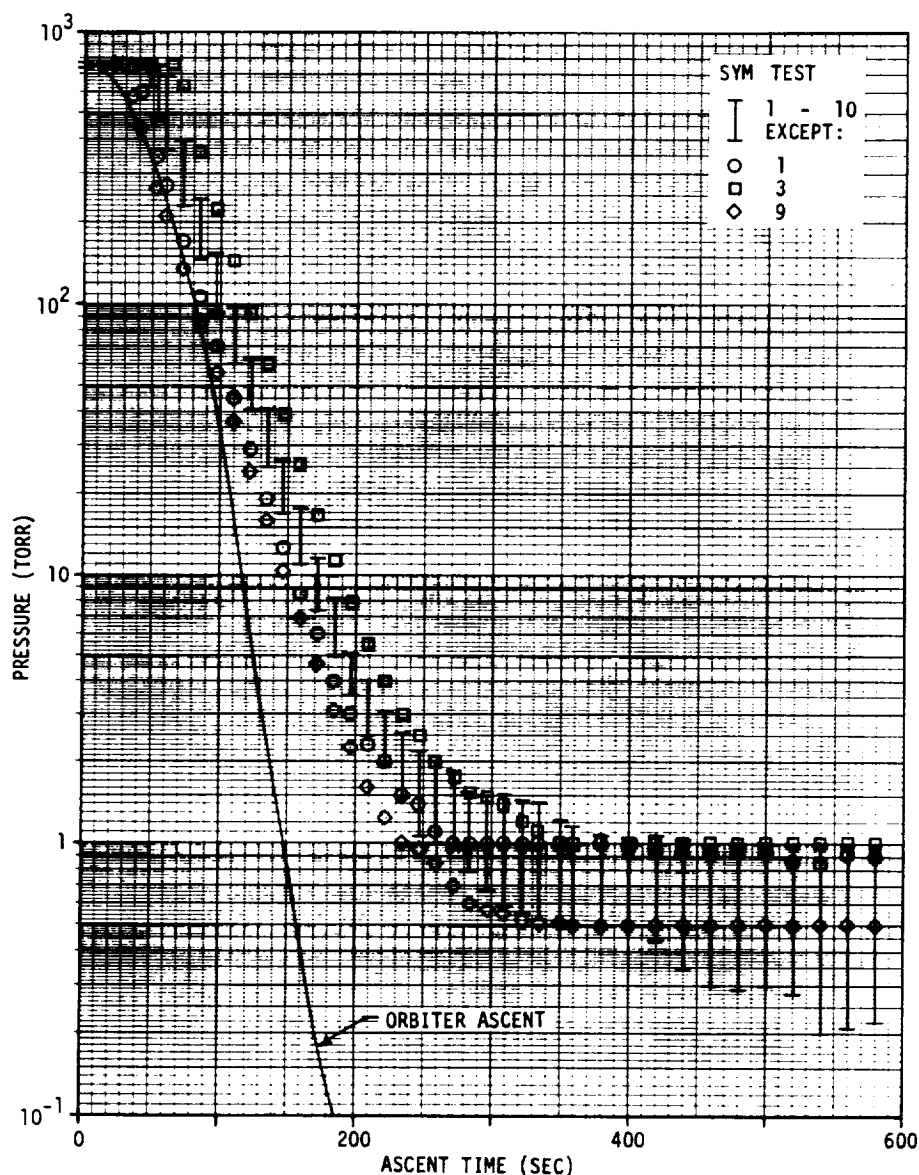


FIGURE 26 ASCENT PRESSURE SIMULATION - TESTS 1-10

The test fixture backside temperature histories during the hot orbit simulation tests are shown in figure 27. Except for thermcouple T/C 2, the temperature variations are very small. Figure 28 shows the pressure history for the first hot orbit test (Test 1). It is within 67 Pa (0.5 torr) of the pressures measured for the hot orbit tests that followed (Tests 2 through 5).

Figure 29 shows the temperature histories of the center and edge tiles during cold orbit calibration. The center tile is slightly colder than the edge tile.

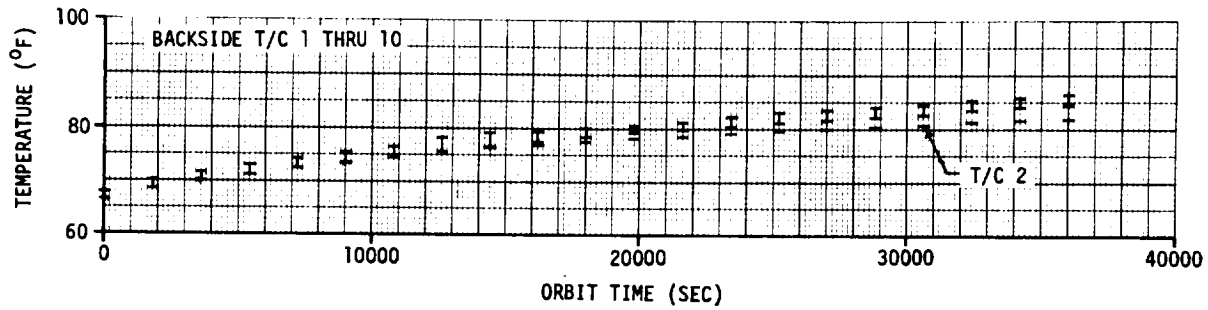


FIGURE 27 HOT ORBIT TEMPERATURE HISTORY TEST 1

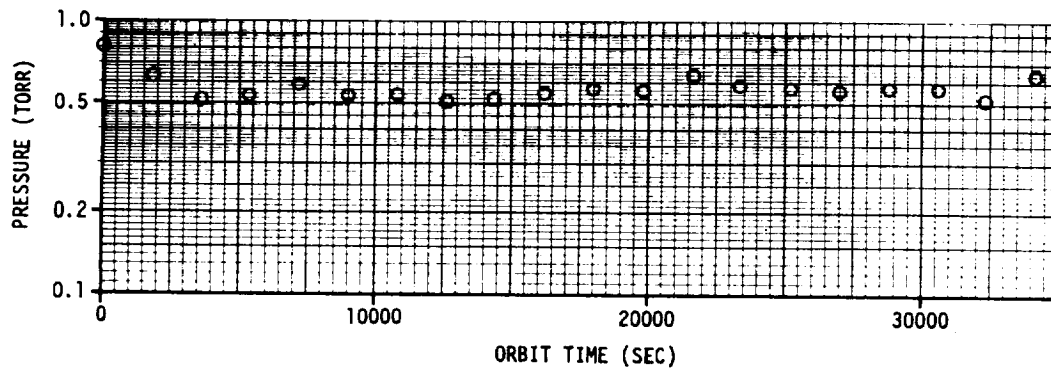


FIGURE 28 HOT ORBIT PRESSURE HISTORY TEST 1

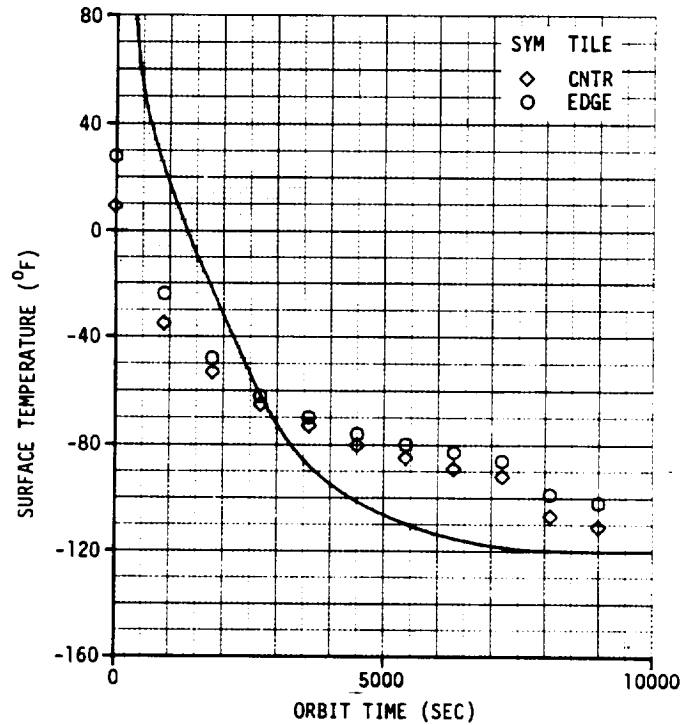


FIGURE 29 CALIBRATION FOR COLD ORBIT

Figure 30 shows the edge tile and test fixture backside temperature histories for the five cold orbit tests. The repeatability was within about 6 K (10°F). Figure 31 shows the cold orbit pressure histories. The scatter in the data is due in part to the limitation of the baratron pressure transducer (0 to 133 kPa (0 to 1000 torr)) used. The pressure is generally below 93.3 Pa (0.70 torr), the nominal low pressure limit of the test facility.

The radiant heater susceptor plate temperature histories for the first five entry simulations are shown in figure 32. These temperature histories are also typical of the last five tests. As can be seen, the repeatability is excellent. Figure 33 shows the measured pressure histories during the entry simulations. The repeatability is generally good.

The backside temperature histories for the test fixture during entry simulation are shown in figures 34 through 37. Figure 34 shows the output of all 10 thermocouples (figure 6) for entry from the hot orbit condition (Test 1). Thermocouple 2 did not function properly during this test. The temperature gradients are, in general, small (approx. 11 K (20°F)). Figure 35 shows the

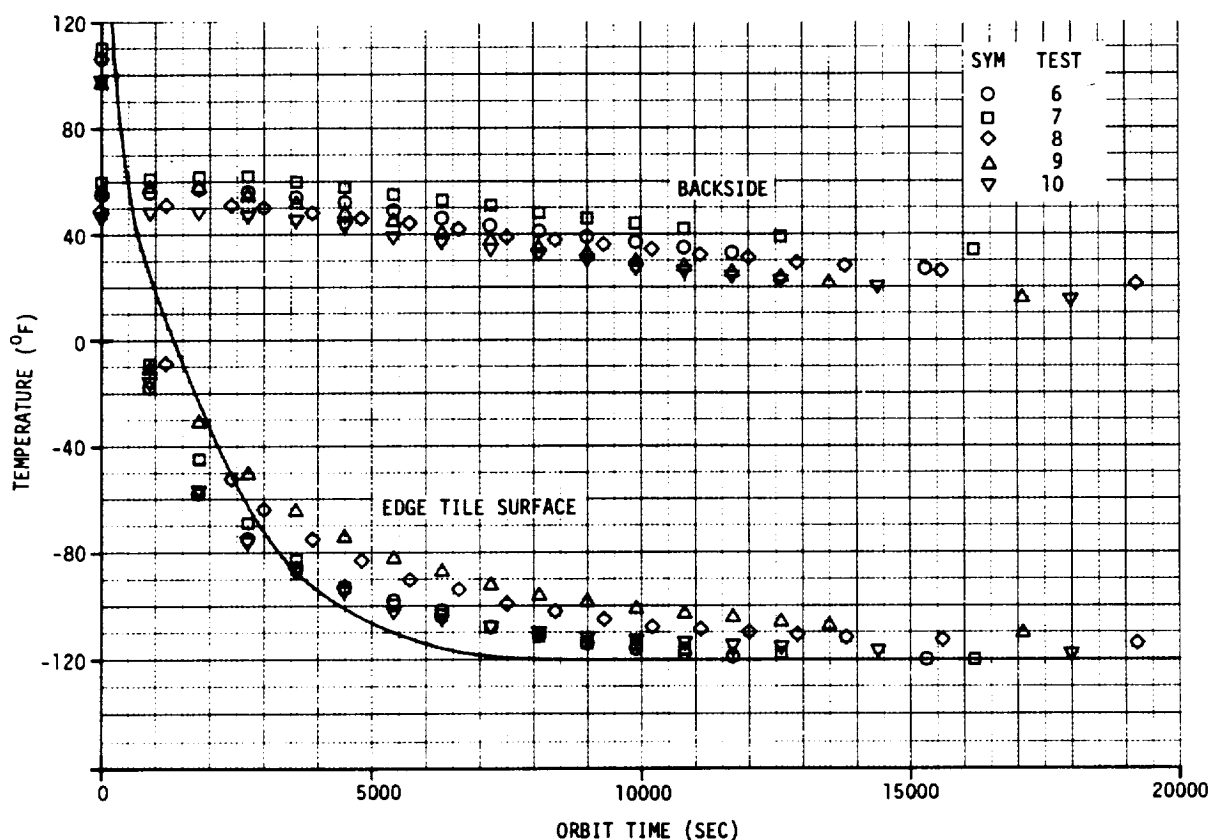


FIGURE 30 COLD ORBIT TEMPERATURE HISTORIES - TESTS 6-10

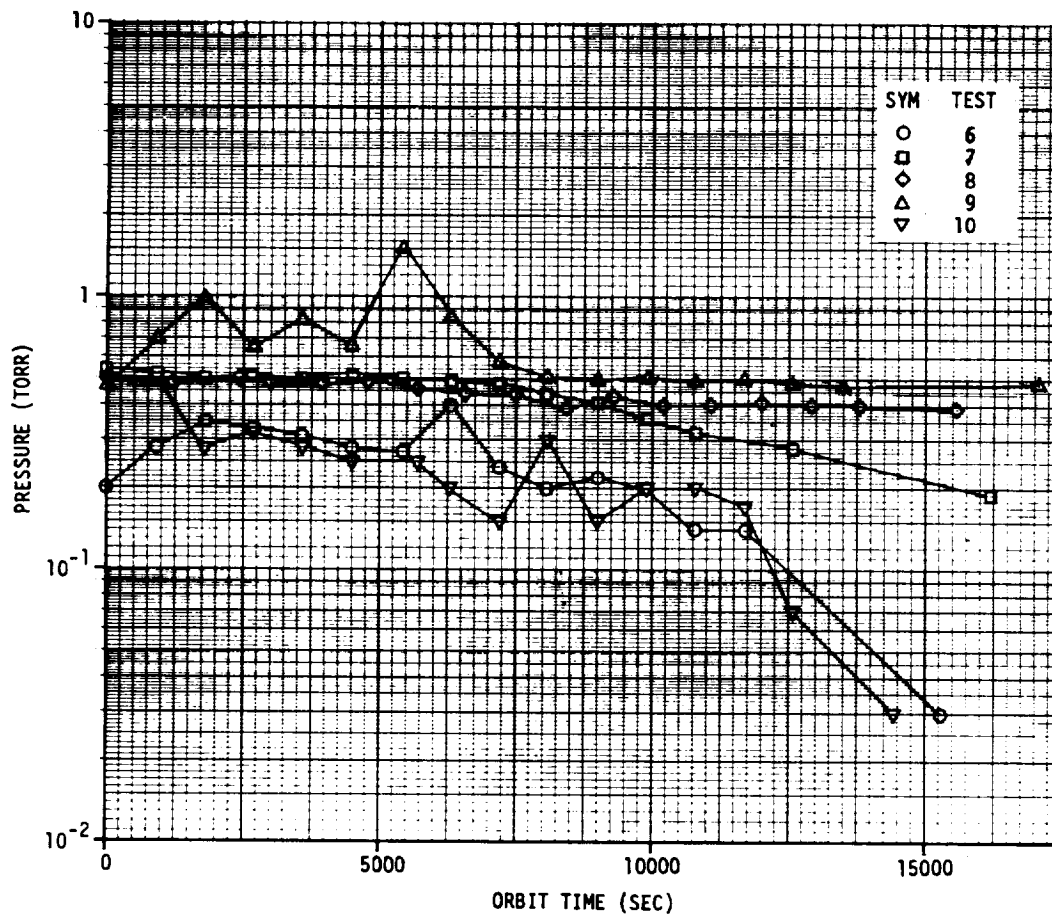


FIGURE 31 COLD ORBIT PRESSURE HISTORIES - TESTS 6-10

output of T/C 8 for all entry heating tests from the hot orbit condition. The variation in the peak temperature is within 8 K (15°F). Figure 36 shows the output of all 10 backside thermocouples for entry from the cold orbit condition (Test 6). The spread in temperature is about the same as for the hot orbit case (figure 34) but the peak temperature is lower by about the difference in the initial values. Figure 37 shows the output of T/C 8 for all the entry heating tests from the cold orbit conditions (Tests 6 through 10). The variation in the peak temperature is about the same as for the hot orbit case. In both the hot and cold orbit tests, the test fixture backside temperature rise from the initial condition was about 119 K (215°F). The spread in the outputs of T/C 8 is due to differences in the initial temperatures, variations in the local pressure and probably the repeatability of the input temperature pulse. In general, however, the temperature history repeatability was excellent.

Ground environments verification. - The verification of the ground environments was limited to the witness plates used to verify the dust and salt fog residue density, periodic observation of the humidity level, and general adherence to the procedures established by pretest experimentation. The particular dosage was subjective because there are no established environmental specifications which cover the contaminating effects investigated in this program. Table II shows the sequence and "dosage" used for each of the simulated ground environments during each test. There was no ground environment exposure prior to the first thermal test cycle. In two cases the humidity exposure time was extended from 58 ksec (16 hr) to 317 and 230 ksec (88 and 64 hr). During the last test cycle the dust and salt fog dosage was increased significantly.

Electrical performance. - Radiation patterns and impedance data were used for evaluating the electrical performance of the contaminated Shuttle TPS HRSI. The data obtained after each test cycle were compared with the pretest data and the changes determined.

Radiation patterns: The radiation patterns were evaluated in selected angular regions, at  $\theta = 60$  to  $70^\circ$ , both left and right of  $\theta = 0^\circ$ , and at  $\theta = 0^\circ \pm 5^\circ$  as shown in figure 38. The pattern regions at  $\theta = 60^\circ$  to  $70^\circ$  were selected for evaluation because the gain in that region is critical during Shuttle ascent and orbital insertion. The region at  $\theta = 0^\circ$  provides an intermediate point for evaluation. In these pattern regions, the worst case change in gain and/or axial ratio was used as the evaluation criteria.

Reference (baseline) radiation patterns (figures 39, 40 and 41) were measured before the MMAPA test fixture was exposed to the ground and thermal environments. The reference radiation patterns measured in rectangular coordinates are given in Appendix I. They were used for the analysis because of better resolution than the polar patterns. Typical radiation patterns after the test fixture was exposed to a number of ground and thermal environment test cycles (e.g., Test 4) are shown in figures 42, 43 and 44. The equivalent rectangular radiation pattern plots are shown in Appendix II. Comparison of these patterns (Test 4) with the reference patterns shows a 0.3 to 1.0 dB circular gain increase at 1.8 GHz (except at  $\phi = 315^\circ$ ), a +0.1 to -1.2 dB gain variation (primarily a decrease) at 2.1 GHz, and a 0.2 to 0.5 dB gain decrease at 2.3 GHz. These results are typical of the range of gain changes found in the radiation patterns.

A detailed analysis of the radiation patterns from each test was made and the results plotted to show the test by test variations relative to the reference data. The items considered were axial ratio, circular gain changes due to axial ratio changes, linear gain changes and total circular gain changes due to both linear gain and axial ratio changes.

Figures 45, 46 and 47 show the axial ratio variations of the left, right and center pattern regions for each of the test frequencies. The axial ratio changes are predominately on the plus side, which corresponds to a circular gain decrease. The maximum axial ratio increase or decrease was 1.4 dB.

The variations in circular gain caused by the changes in axial ratio (figures 45, 46 and 47) are shown in figures 48, 49 and 50. The maximum increase and decrease in circular gain for each frequency and pattern region is shown in table III. In the critical left and right pattern regions, the maximum gain loss ranges from 0.2 to 0.5 dB. In general, the gain decreases are more prevalent than the gain increases.

The changes in linear gain are shown in figures 51, 52 and 53. The respective values were corrected for the difference in the peak gain of the standard gain horn radiation pattern recorded at the beginning of each pattern set and that recorded with the reference patterns. Table IV shows the variation in the standard gain horn peak for all the tests. In most cases the variation is with  $\pm 0.2$  dB of the reference level.

The changes in circular gain with both linear gain and axial ratio changes combined are shown in figures 54, 55 and 56. At 1.8 GHz, the gain is increased for most tests, but at 2.1 GHz the opposite is true. However, at 2.3 GHz the gain changes are more evenly divided between increases and decreases. Data from two of the tests does not appear to be consistent with data from preceding or succeeding tests and, therefore, should be considered accordingly. The data in question is for Test 4 at 1.8 GHz and  $\phi = 315^\circ$  (figure 54) and Test 9 at 2.1 and 2.3 GHz for all  $\phi$  angles (figures 55 and 56).

In general, analysis of the radiation patterns for 1.8 and 2.3 GHz does not indicate any significant degradation in the electrical performance of the TPS which is attributable to contamination by the test environments. There is also no indication in the data at any of the test frequencies which reveals the difference between the hot and cold orbit simulations. At 2.1 GHz, however, the results of the radiation pattern analysis (figure 55) shows a gain decrease of about 1 dB, particularly for the  $\phi = 45^\circ$  and  $90^\circ$  plane patterns. Although the  $\phi = 45^\circ$  plane passes through the test fixture TPS surface area, where the coating created by the test environments seemed heaviest, it does not appear that this surface condition contributed to the gain decrease, since it was observed in the electrical test results after the first thermal test, and before the first ground environments test. Therefore, it is likely that the gain decrease was caused by the simulated entry heating, since this produces a temperature (867 K (1100°F)) high enough to burn the silicone resin (0.13 to 0.27% of the fiber weight) contained in the TPS tiles for waterproofing. Similar results were obtained in a previous test program (ref. 3) where entry heating was also simulated with a radiant heat source. In that case, the burning of the silicone resin (4

to 5% of the tile fiber weight) resulted in a carbonaceous coating which caused a transmission loss of 10 to 12 dB and considerable radiation pattern distortion. However, in the first part of that program (ref. 2), where entry heating was simulated in a plasma facility and where there was gap flow over the TPS surface, the change in electrical performance was negligible. This test result leads to the conclusion that the electrical performance degradation found in the current results may have been reduced if gas flow had been present over the TPS surface during the entry heating segment of the thermal test.

**Impedance:** The results of reference impedance measurements are shown in figures 57 and 58. The results of post environment test impedance measurements (e.g., Test 5) are shown in figures 59 and 60. Expanded scale (10 dB) plots (not shown) were also recorded in order to improve resolution of the data points for the frequencies selected for detailed evaluation. Comparison of figures 59 and 60 with the reference data shows minor changes which do not appear to be of significance. In order to determine if a test trend could be identified, the reflection coefficient magnitude and phase angle were taken from the impedance plots at 0.05 GHz increments from 1.70 to 1.90 GHz and 2.00 to 2.40 GHz. The VSWR magnitude and the associated mismatch loss were calculated from the reflection coefficient. Figures 61 and 62 show typical VSWR magnitude and angle, and mismatch loss variations over the frequency range. The maximum VSWR for any frequency or test was 1.47:1 (figure 63), which corresponds to a mismatch loss of 0.16 dB. This occurred at 2.25 GHz for Test 1 where the VSWR increased from 1.26:1 to 1.47:1, a mismatch loss increase of 0.1 dB. These changes in VSWR and mismatch loss are also the largest to be found in the data. With few exceptions the variation in VSWR is less than  $\pm 0.05$  about a particular average VSWR. The variation in phase angle is generally less than  $\pm 10^\circ$  and  $\pm 20^\circ$  in a few cases. The greatest VSWR angle variation (figure 62(d)) occurs where the VSWR is generally less than 1.1:1 and, therefore, would be of little significance.

Figures 64 and 65 show the data for all the tests plotted on an expanded scale Smith Chart. These plots show the combined variation of VSWR magnitude and phase angle at each of the test frequencies. The data points at each frequency, not identified by test number, are closely grouped except for a few isolated points.

In general, the impedance data does not show a change trend which would be expected to result in degraded antenna performance. In most cases the data scatter is small and both the VSWR magnitude and phase angle well behaved (i.e., their variations are small or insignificant).

Physical observations. - After each thermal test the test fixture surface was examined visually to evaluate the TPS surface appearance. The following observations were made:

1. Test 1 - Slight changes in the TPS surface appearance were noted. The gaps appeared to be coated with an oily substance, probably the silicone used for waterproofing. The outer edges of the TPS tiles had a smoky appearance.



2. Test 2 - The dust deposit appeared to be baked on and gave a crusty appearance with reddish colored spots distributed over the TPS surface.
3. Test 5 - The TPS surface appeared to have a more reddish coloring. However, photos taken to document this do not show this as clearly as desired. Figure 66 shows a photo of the test fixture after thermal Test 5. The coloring at the TPS surface edges different from the center. The TPS tile sides also show the smoky appearance mentioned above.
4. Test 6 - The reddish color on the TPS tiles surfaces appeared more intense. Figure 67 shows a photo of the test fixture surface. A discoloration can be seen over the surface in the form of speckles or dots. These dots were a more reddish in appearance than the adjacent surface.

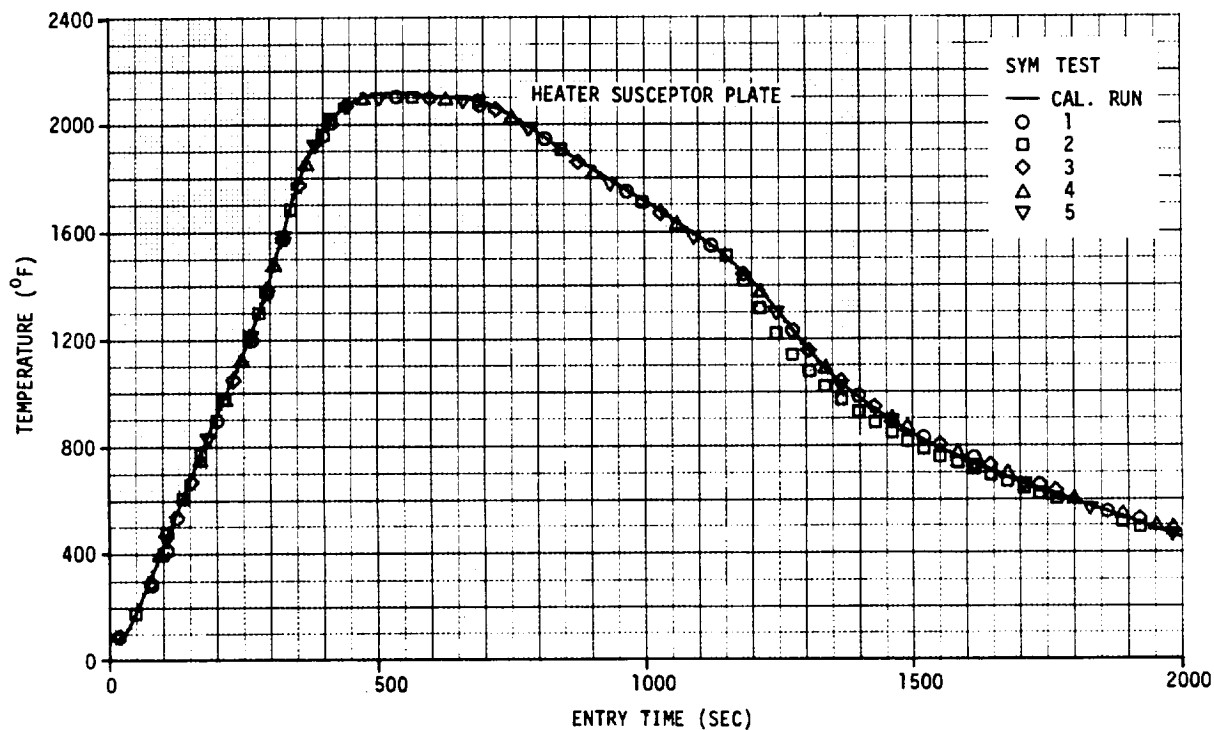


FIGURE 32 ENTRY HEATING REPEATABILITY - TESTS 1-5

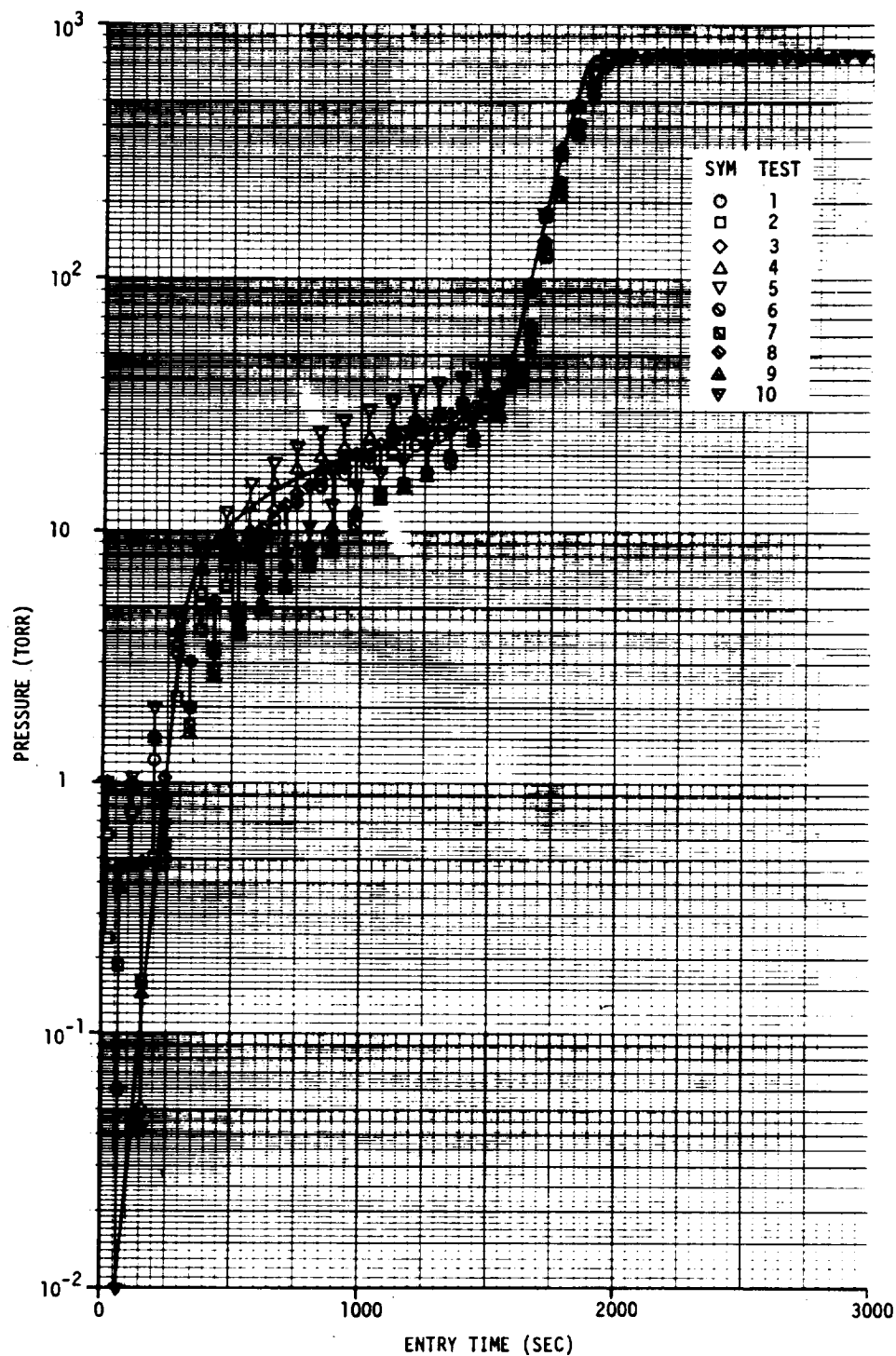


FIGURE 33 ENTRY PRESSURE HISTORIES - TESTS 1-10

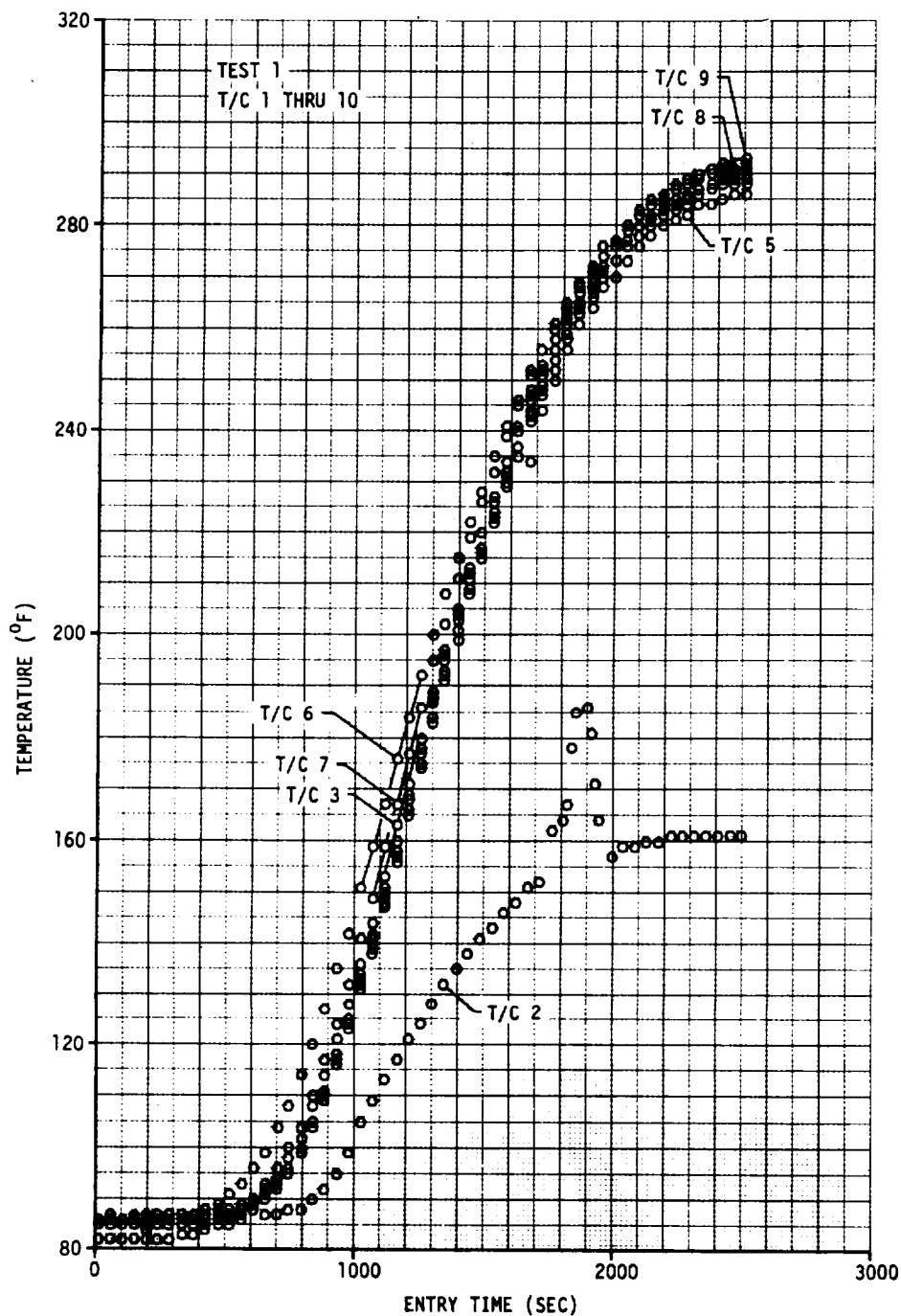


FIGURE 34 BACKSIDE TEMPERATURE HISTORIES DURING ENTRY  
FROM HOT ORBIT - TEST 1 (T/C 1-10)

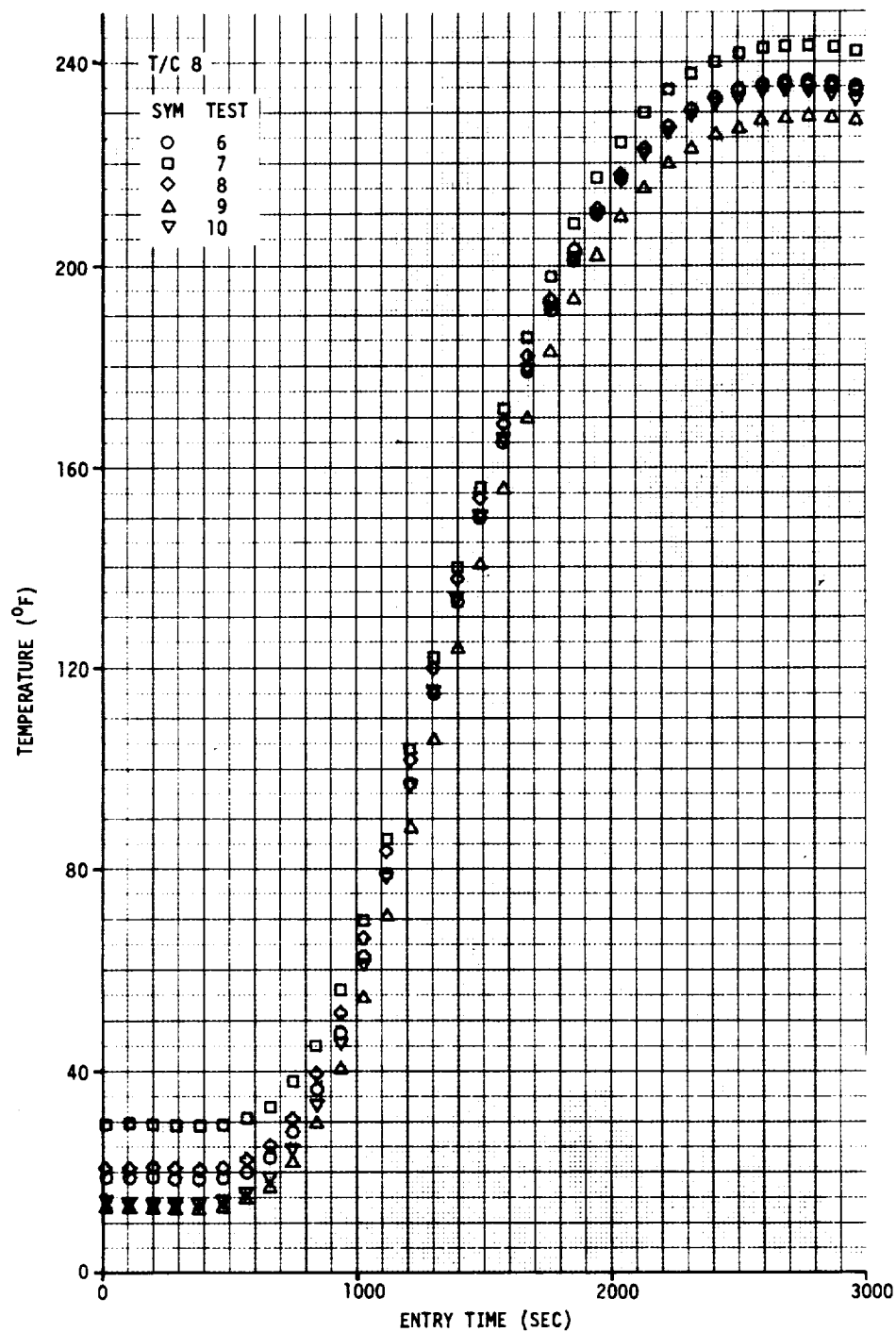


FIGURE 35 BACKSIDE TEMPERATURE HISTORIES DURING ENTRIES FROM HOT ORBIT - TESTS 1-5 (T/C 8 ONLY)

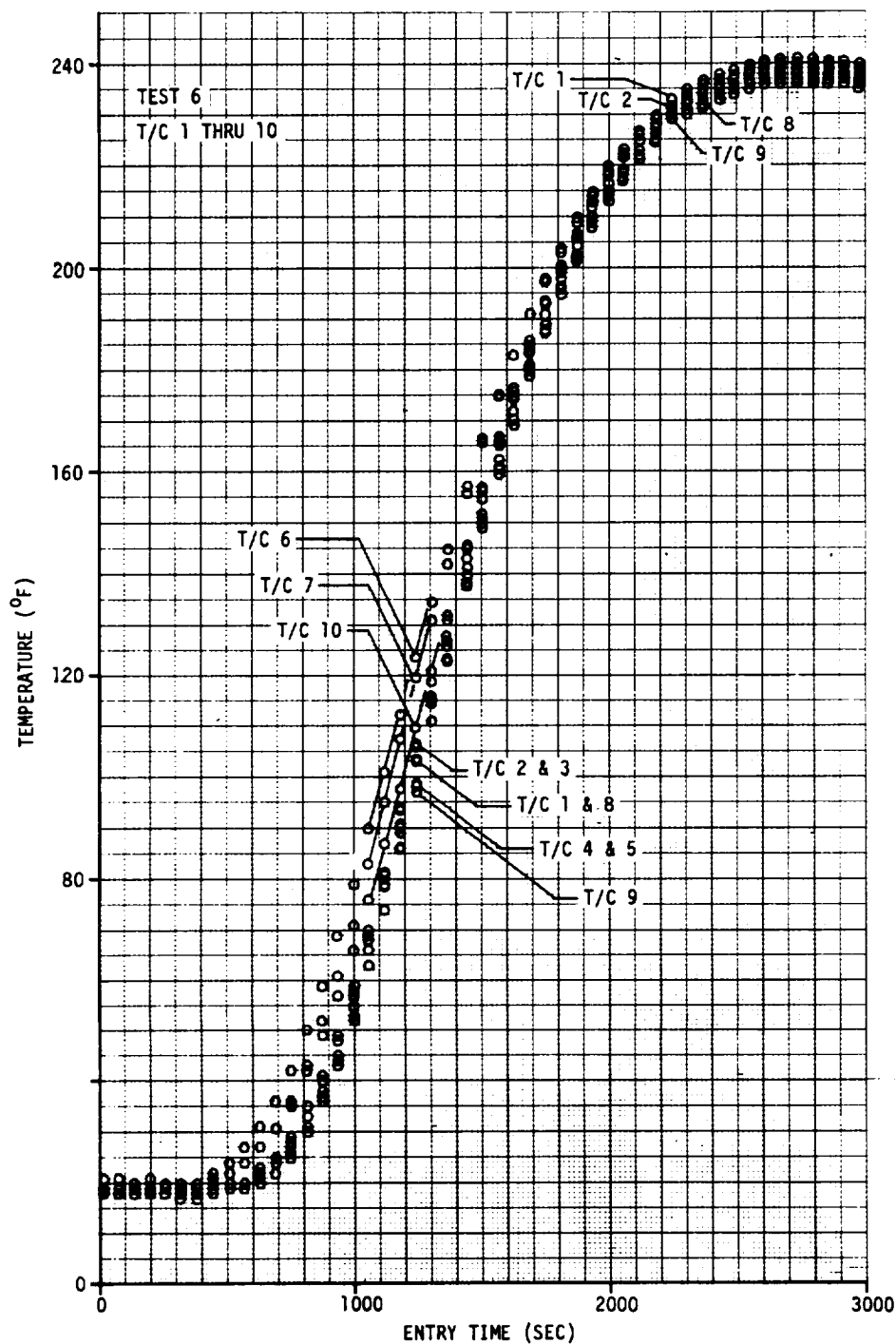


FIGURE 36 BACKSIDE TEMPERATURE HISTORIES DURING ENTRY  
FROM COLD ORBIT - TEST 6 (T/C 1-10)

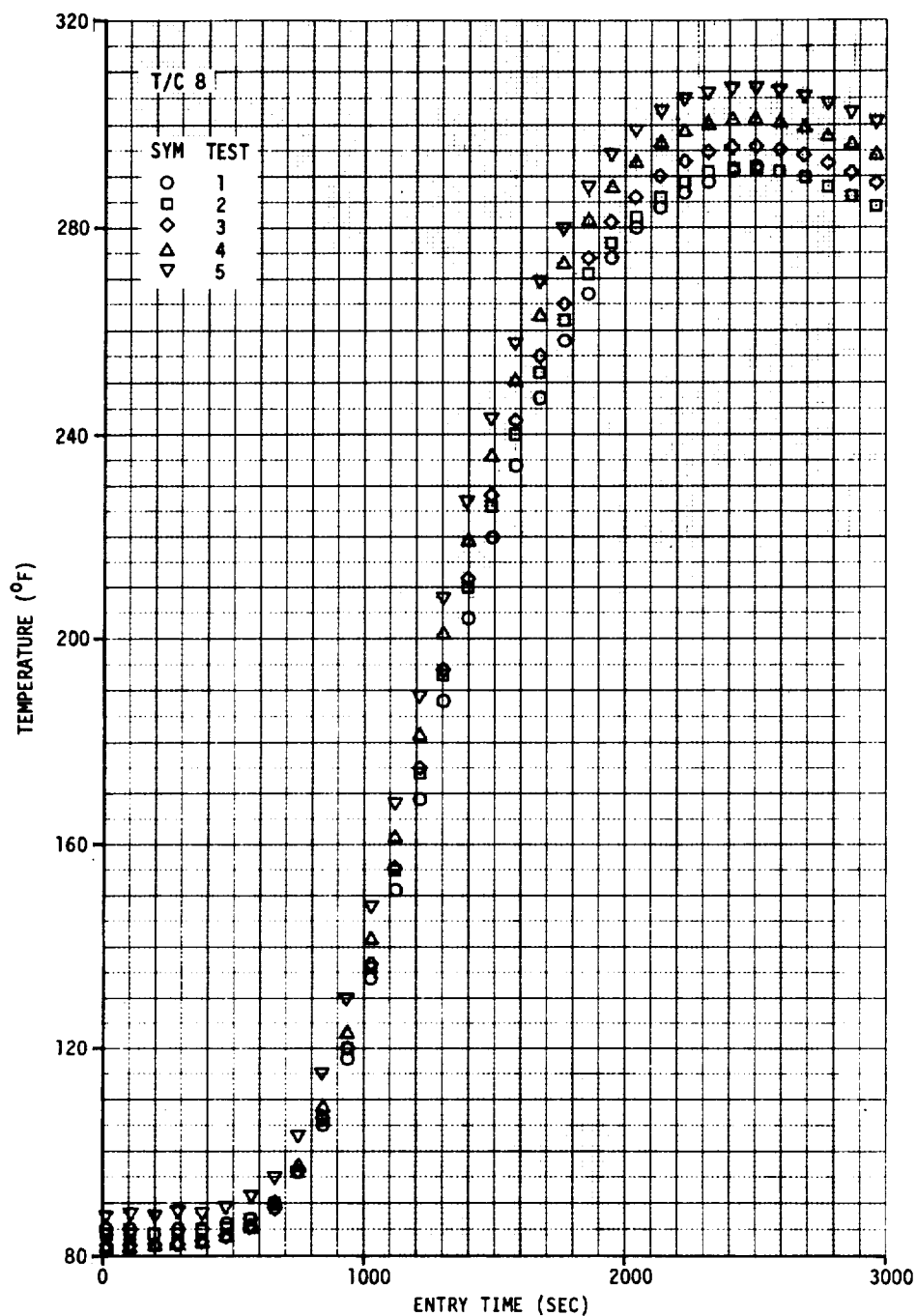


FIGURE 37 BACKSIDE TEMPERATURE HISTORIES DURING ENTRIES  
FROM COLD ORBIT - TESTS 6-10 (T/C 8 ONLY)

**TABLE II**  
**GROUND ENVIRONMENTS TEST SEQUENCES**

TEST NO.	ENVIRONMENT SEQUENCE						
	1	2	3	4	5	6	7
1							
2	H1	D1	S1	H2			
3	H1	D1	H2	S1	D1		
4	H2	S1	D1				
5	H1	D1	H2	S1	D1		
6	H1	D1	H2	S1	D1		
7	H1	D1	H3	S1	D1		
8	H1	D1	H4	S1	D1		
9	H1	D1	H1	S1	D1		
10	H2	S1	D1	S1	D1	S1	D2

NOTES: H1 = HUMIDITY (1 HR EXPOSURE)  
D1 = DUST (3.5 gm)  
S1 = SALT FOG (5 SEC SPRAY)  
H2 = HUMIDITY (16 HR EXPOSURE)  
H3 = HUMIDITY (88 HR EXPOSURE) - 12/23-12/27/76  
H4 = HUMIDITY (64 HR EXPOSURE) - 12/31/76-1/3/77  
D2 = DUST (10.5 gm)

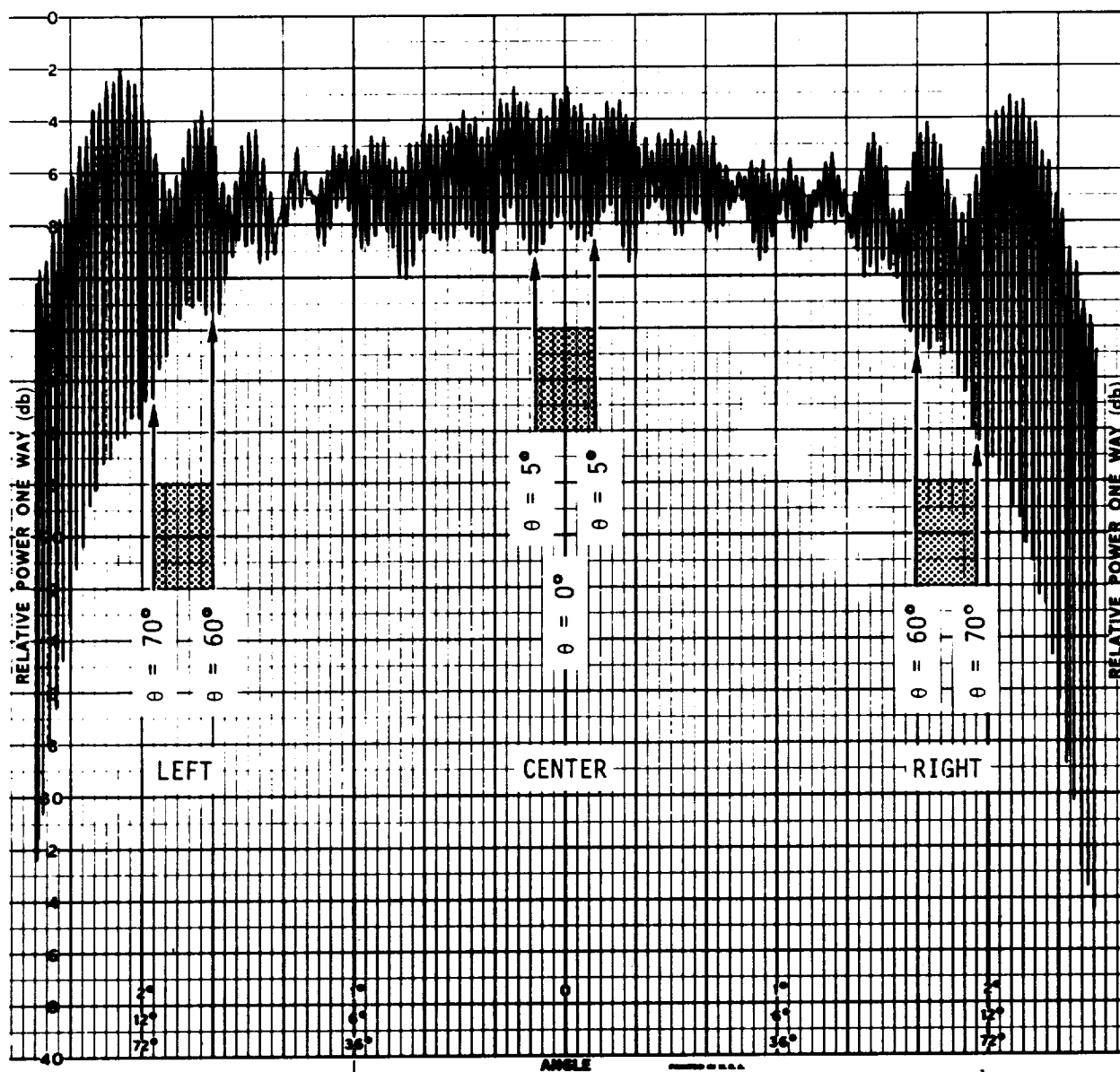


FIGURE 38 PATTERN REGIONS USED FOR ANTENNA PERFORMANCE ANALYSIS



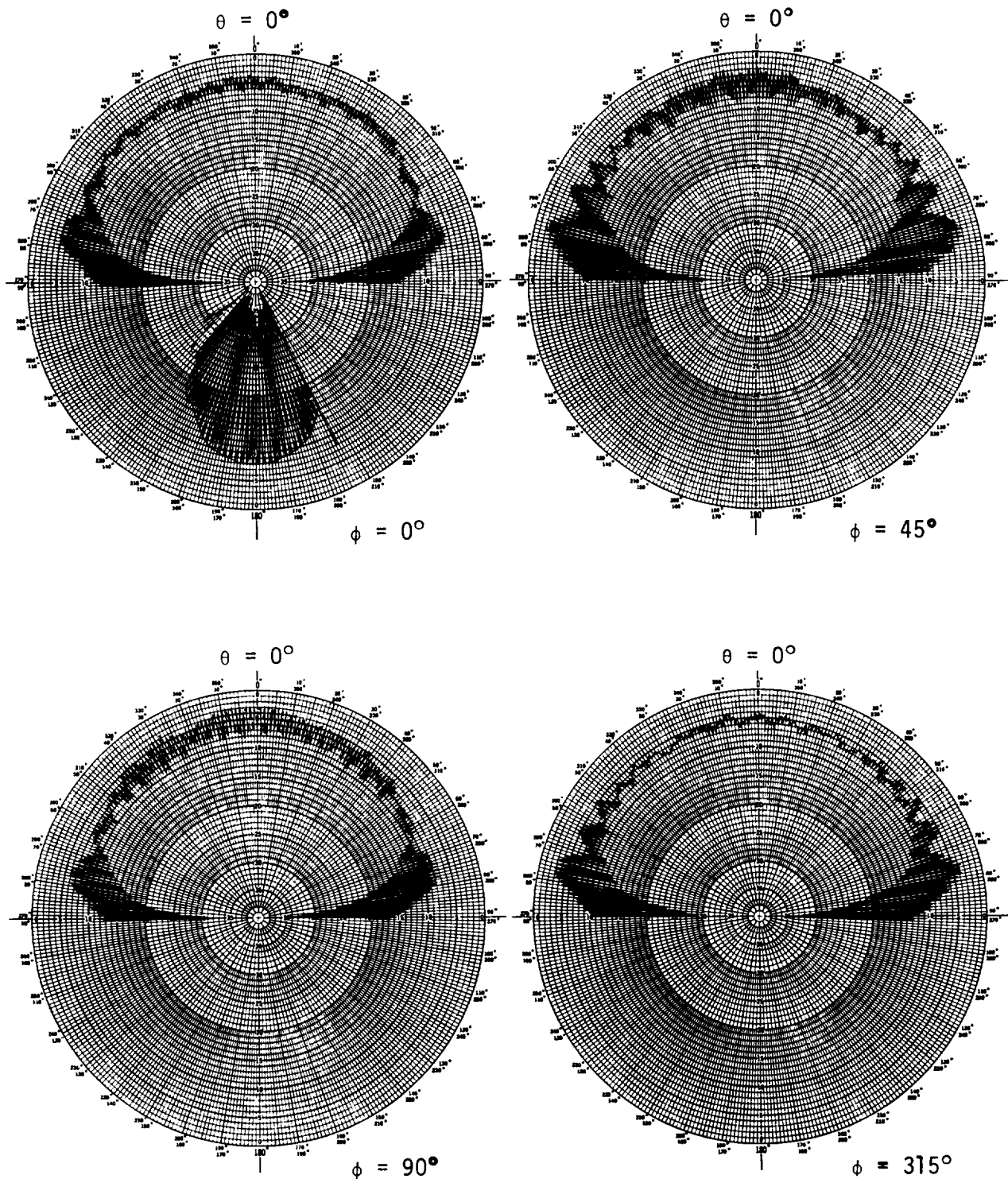


FIGURE 39 REFERENCE RADIATION PATTERNS (1.8 GHz)

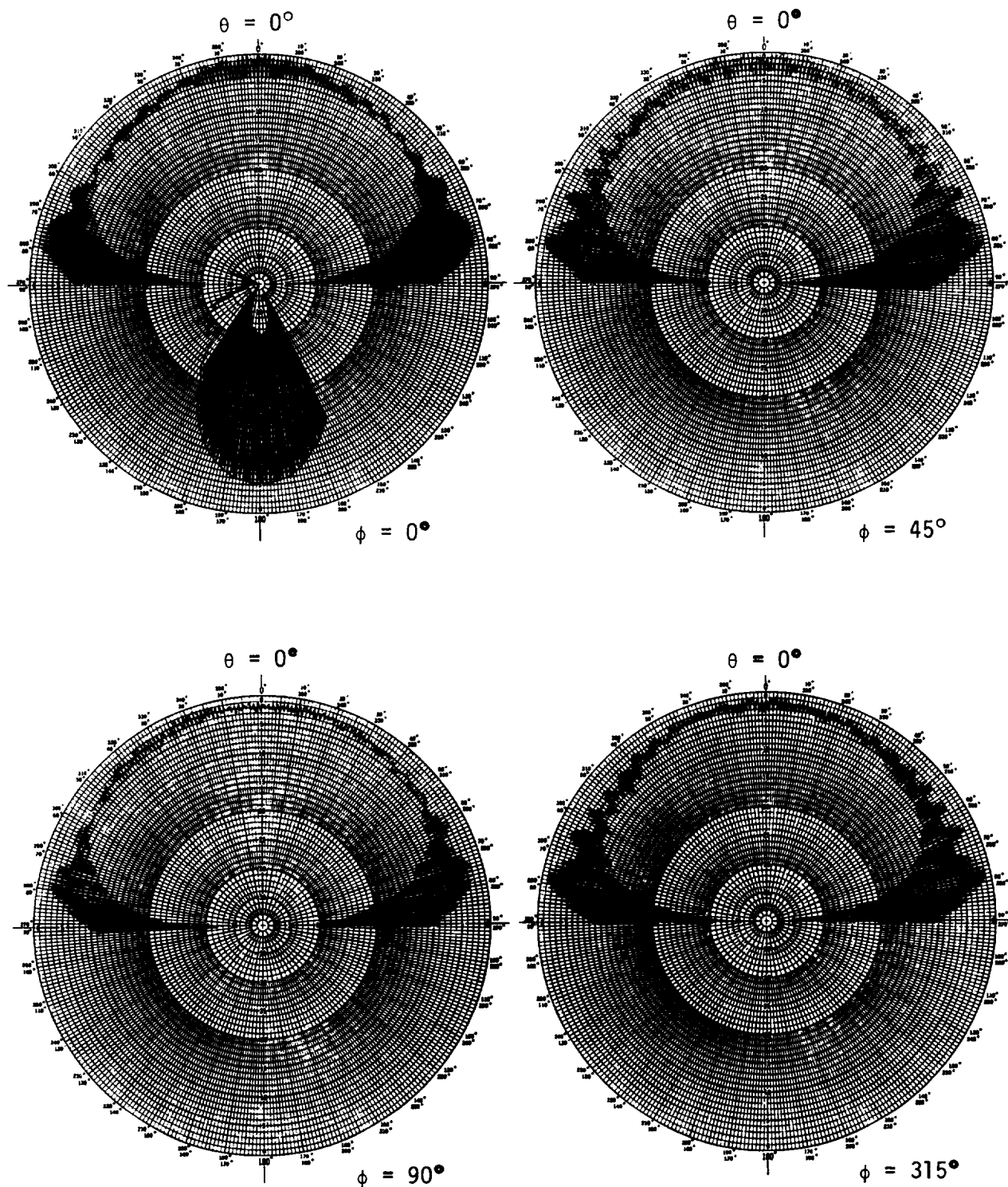


FIGURE 40 REFERENCE RADIATION PATTERNS (2.1 GHz)

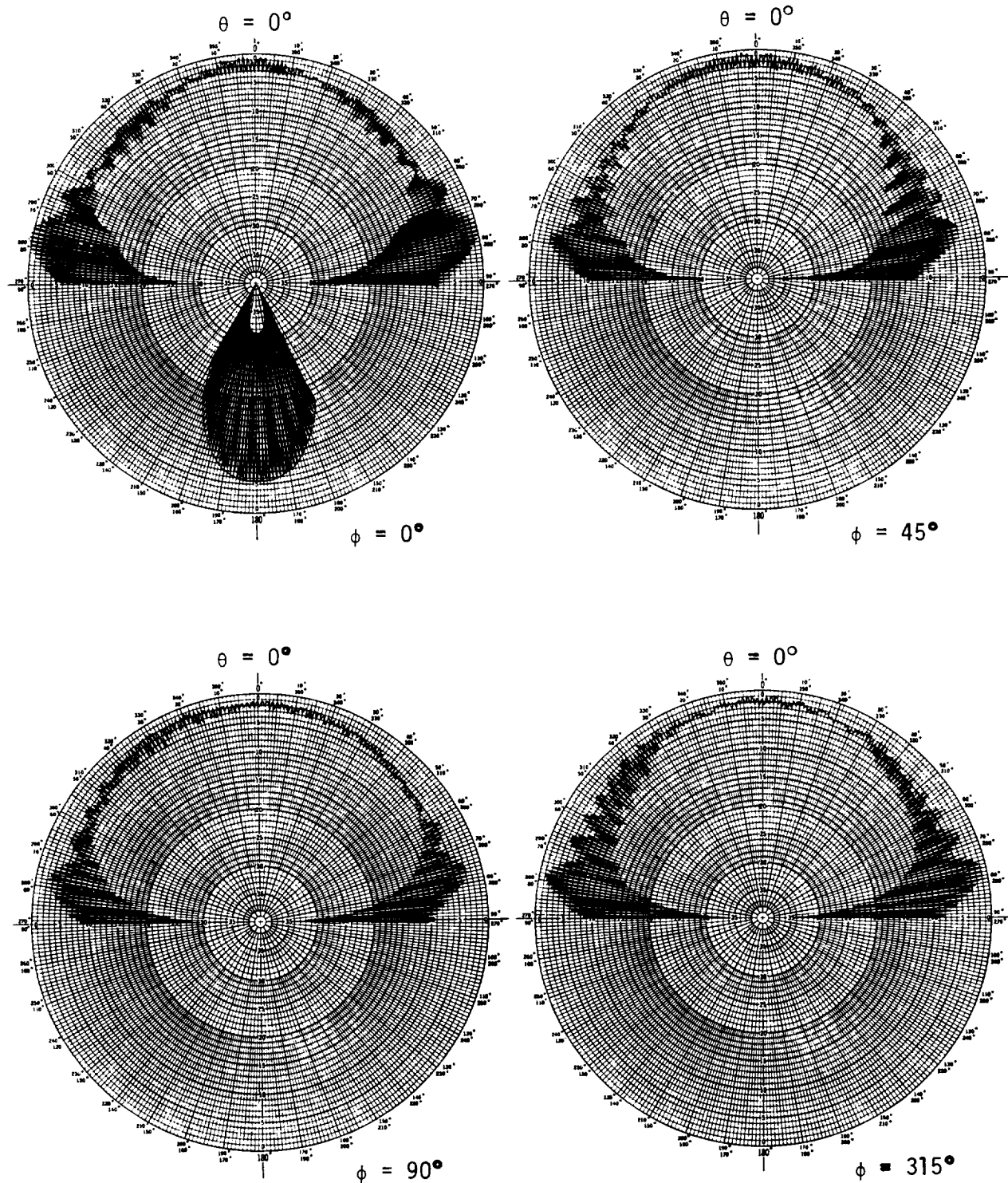


FIGURE 41 REFERENCE RADIATION PATTERNS (2.3 GHz)

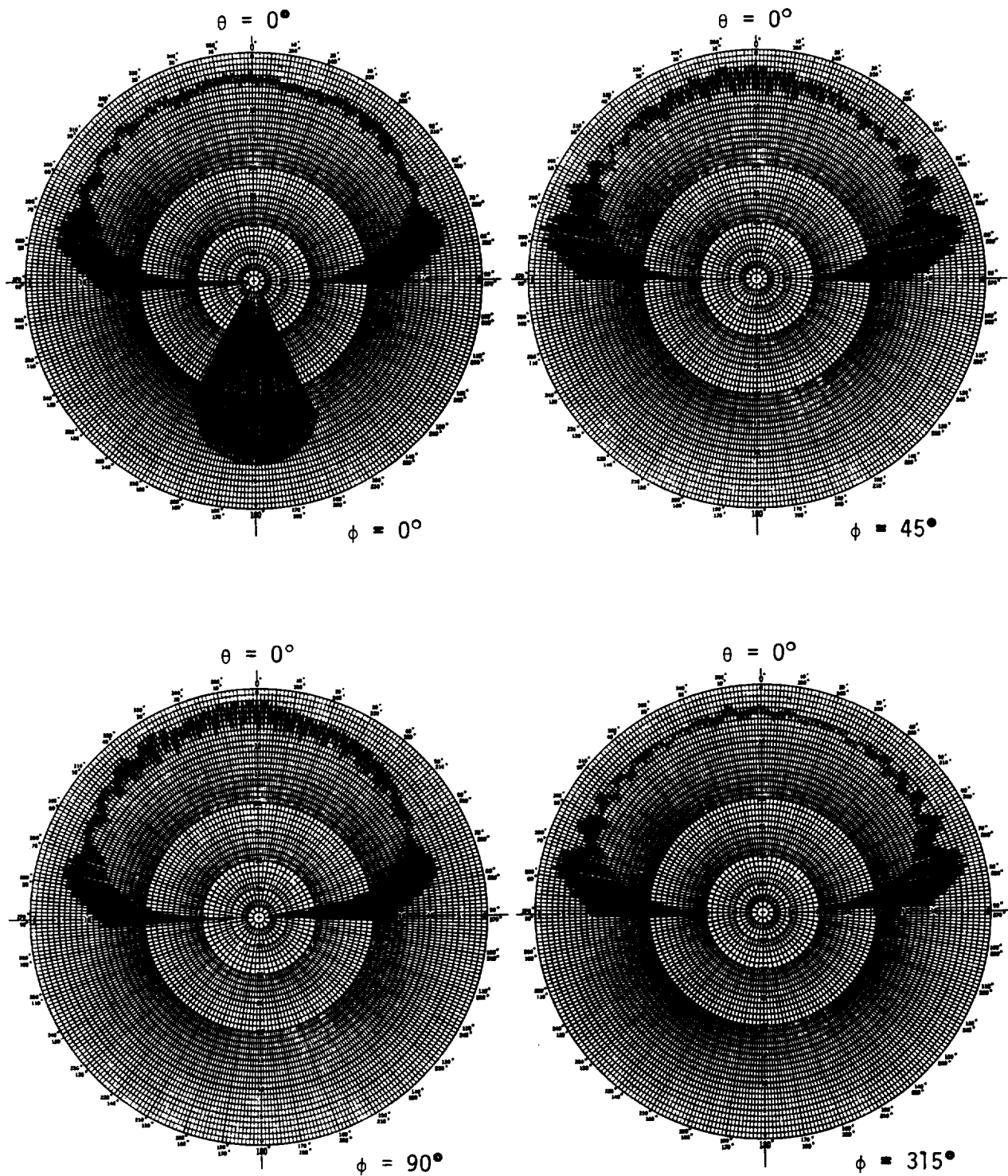


FIGURE 42 RADIATION PATTERNS - TEST 4 (1.8 GHz)

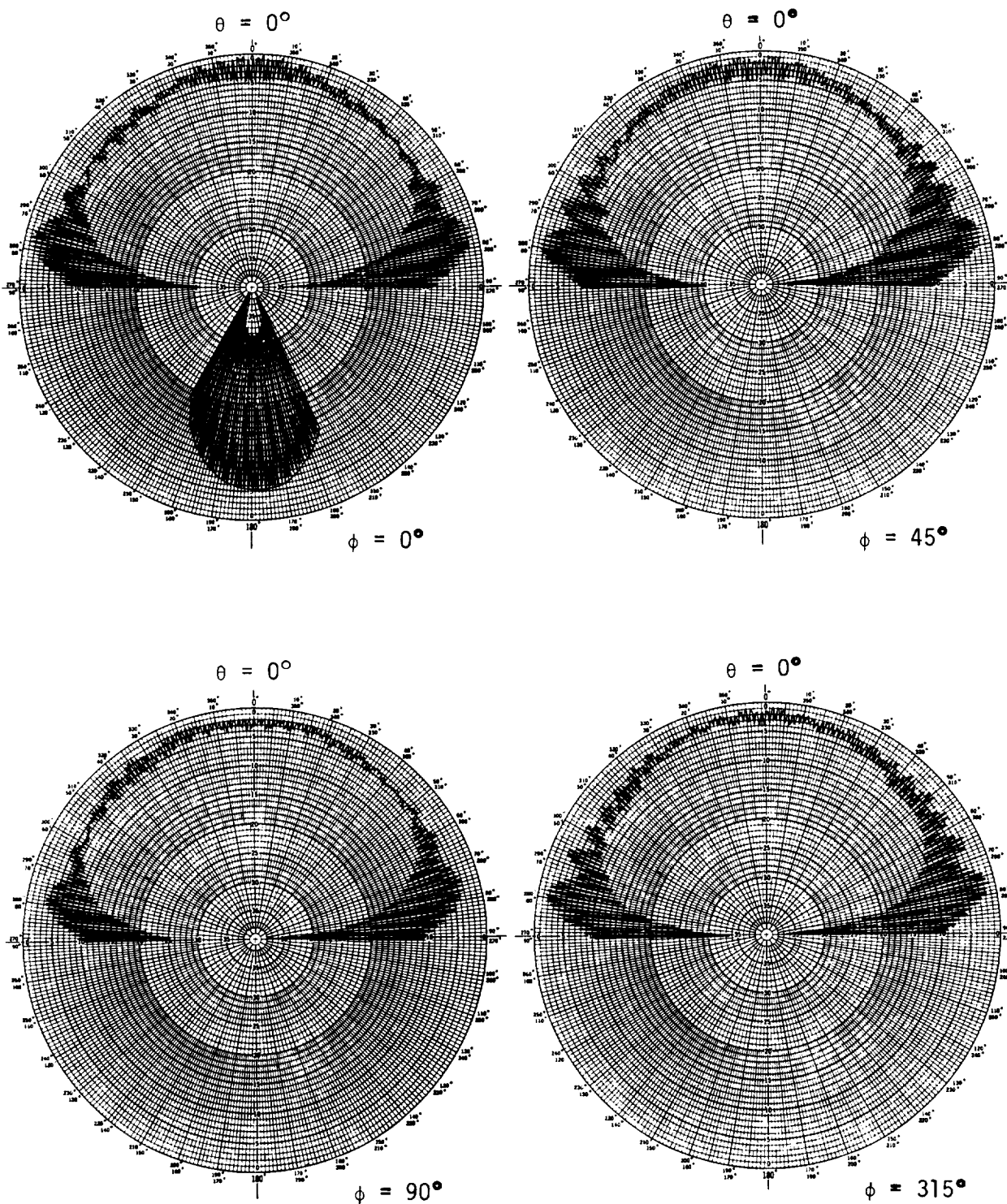


FIGURE 43 RADIATION PATTERNS - TEST 4 (2.1 GHz)



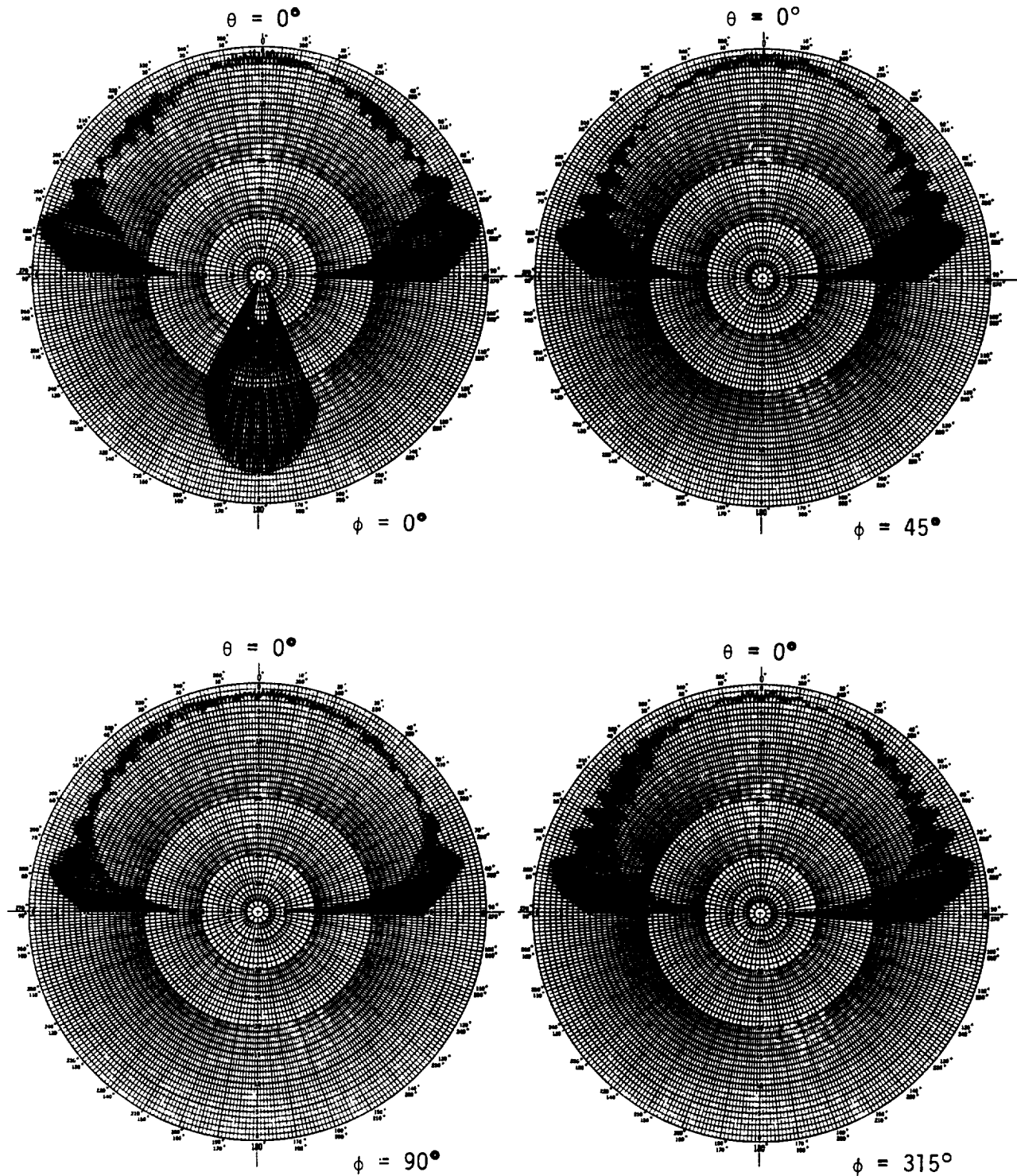


FIGURE 44 RADIATION PATTERNS - TEST 4 (2.3 GHz)

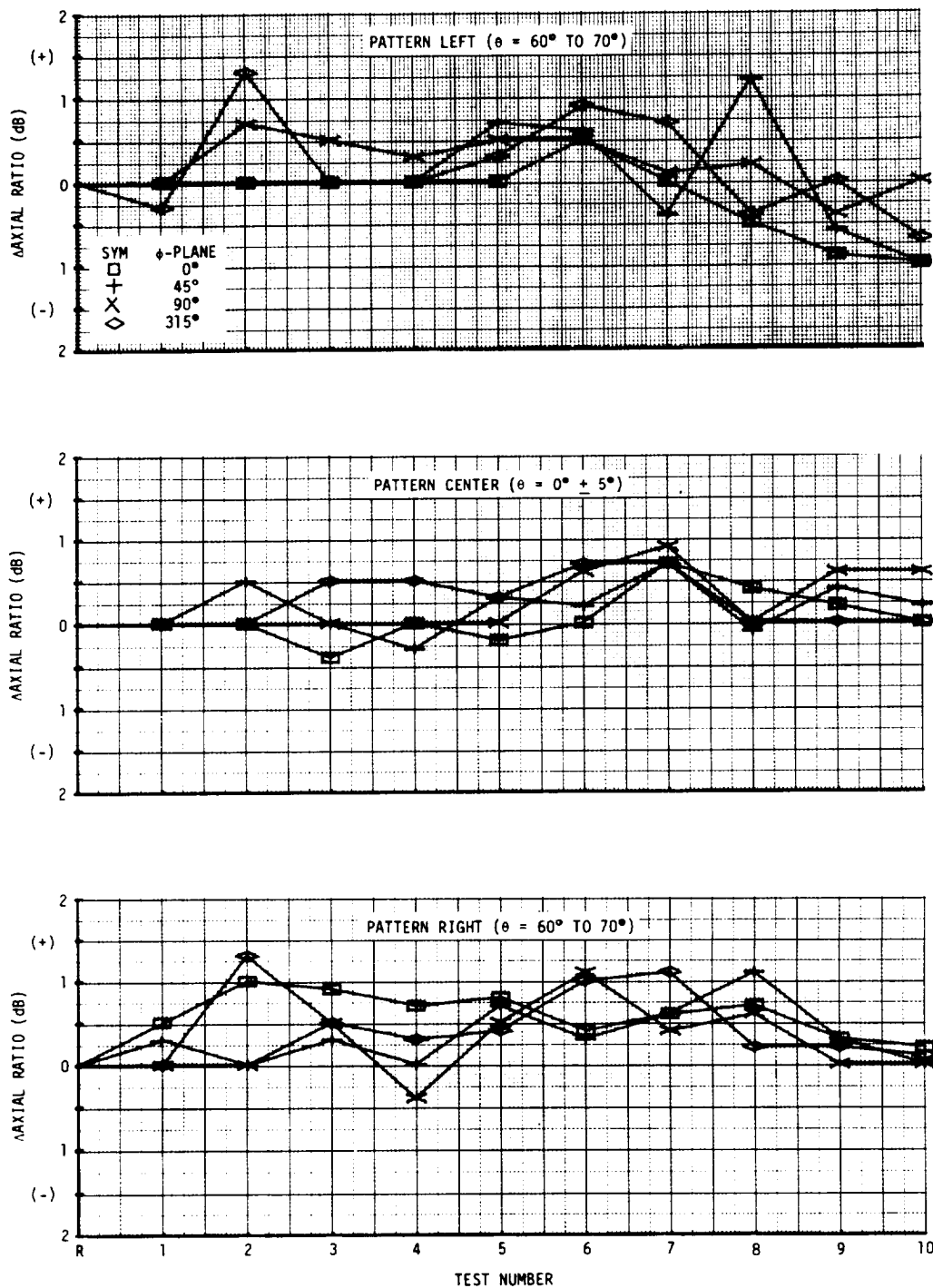


FIGURE 45 AXIAL RATIO CHANGES - 1.8 GHz

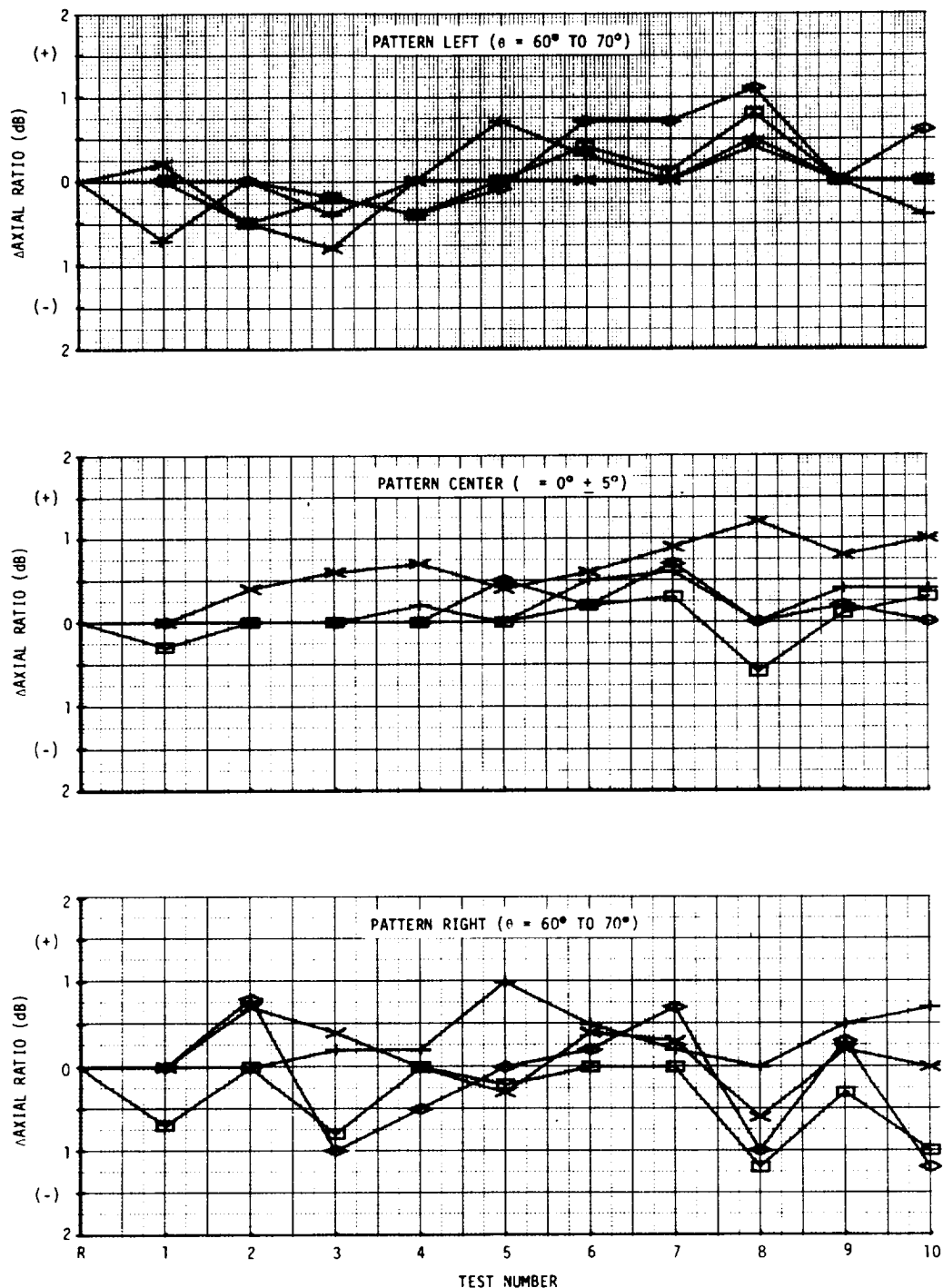


FIGURE 46 AXIAL RATIO CHANGES - 2.1 GHz



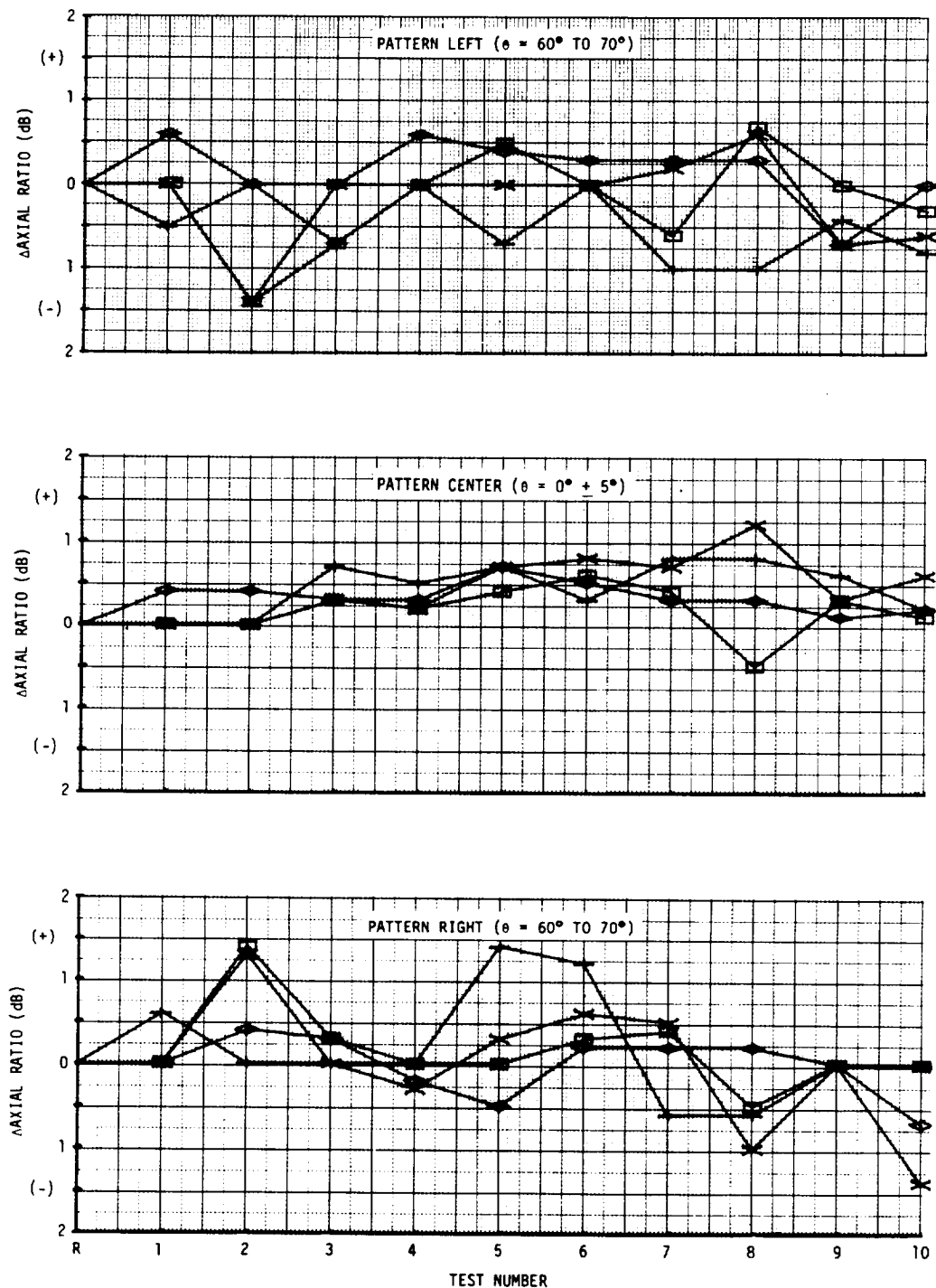


FIGURE 47 AXIAL RATIO CHANGES - 2.3 GHz

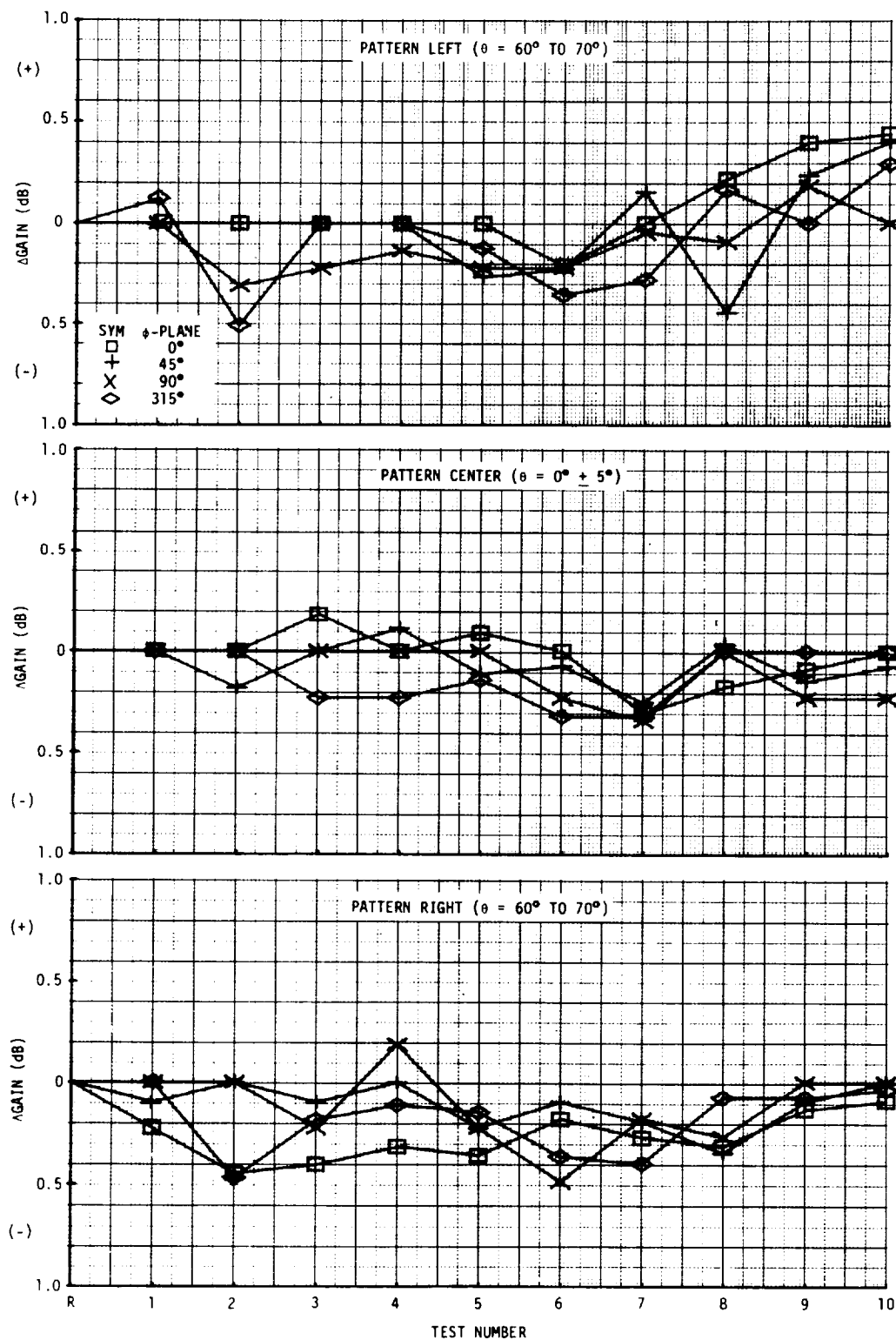


FIGURE 48 CIRCULAR GAIN VARIATIONS CAUSED BY AXIAL RATIO CHANGES - 1.8 GHz

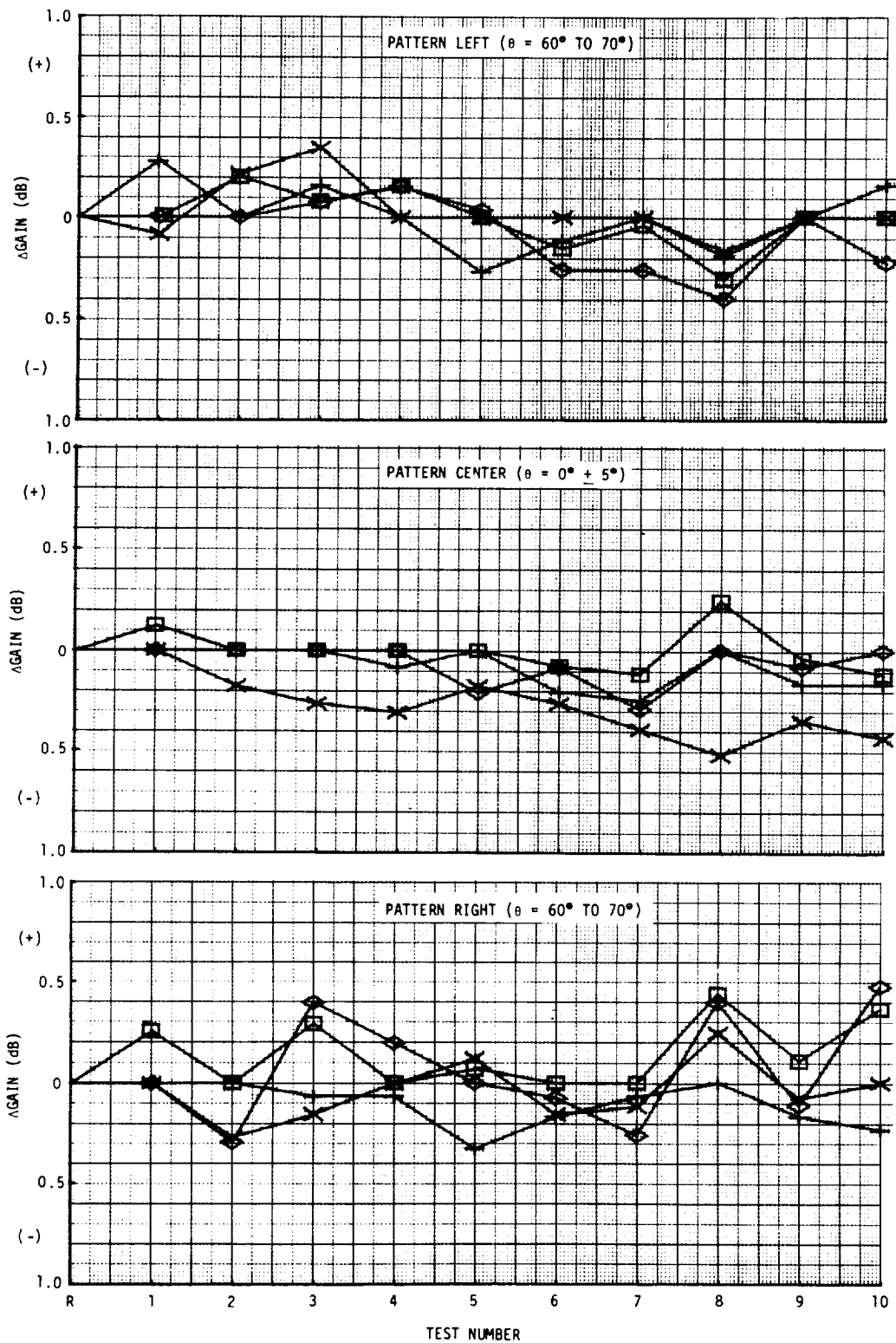


FIGURE 49 CIRCULAR GAIN VARIATIONS CAUSED BY AXIAL RATIO CHANGES - 2.1 GHz

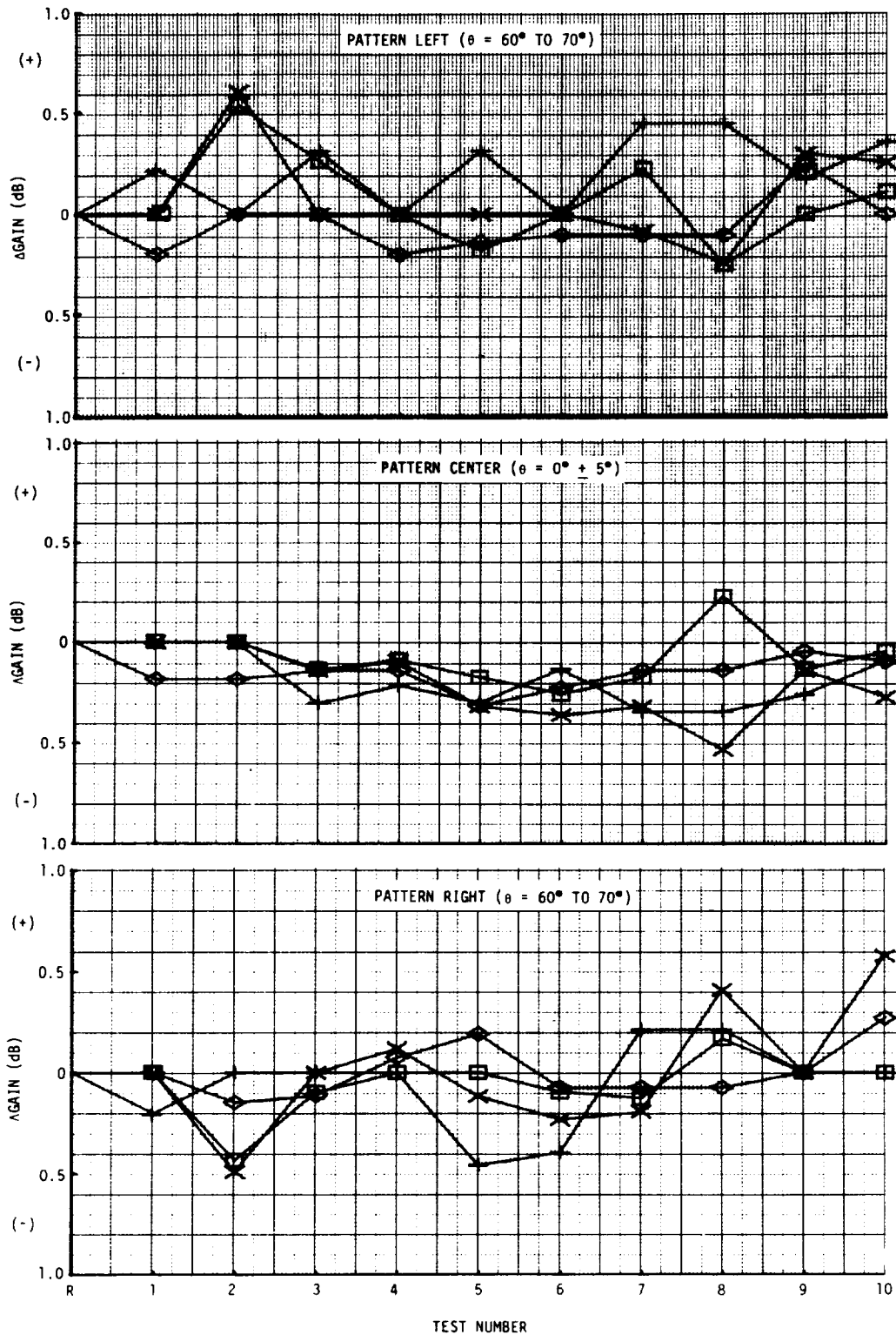


FIGURE 50 CIRCULAR GAIN VARIATIONS CAUSED BY AXIAL RATIO CHANGES - 2.3 GHz

**TABLE III**  
**MAXIMUM INCREASE AND DECREASE IN CHANGES**  
**CIRCULAR GAIN CAUSED BY AXIAL RATIO**

PATTERN REGION	FREQUENCY (GHz)					
	1.8		2.1		2.3	
	+dB	-dB	+dB	-dB	+dB	-dB
LEFT	0.4	0.5	0.3	0.4	0.6	0.2
RIGHT	0.2	0.3	0.4	0.4	0.6	0.5
CENTER	0.2	0.1	0.2	0.5	0.2	0.5

**DEVELOPMENT OF S-BAND ANTENNA INTERFACE DESIGN**  
**SHUTTLE ANTENNA RADOME TECHNOLOGY TEST PROGRAM**

**REPORT MDC E1478**  
**15 JUNE 1977**  
**VOLUME II**

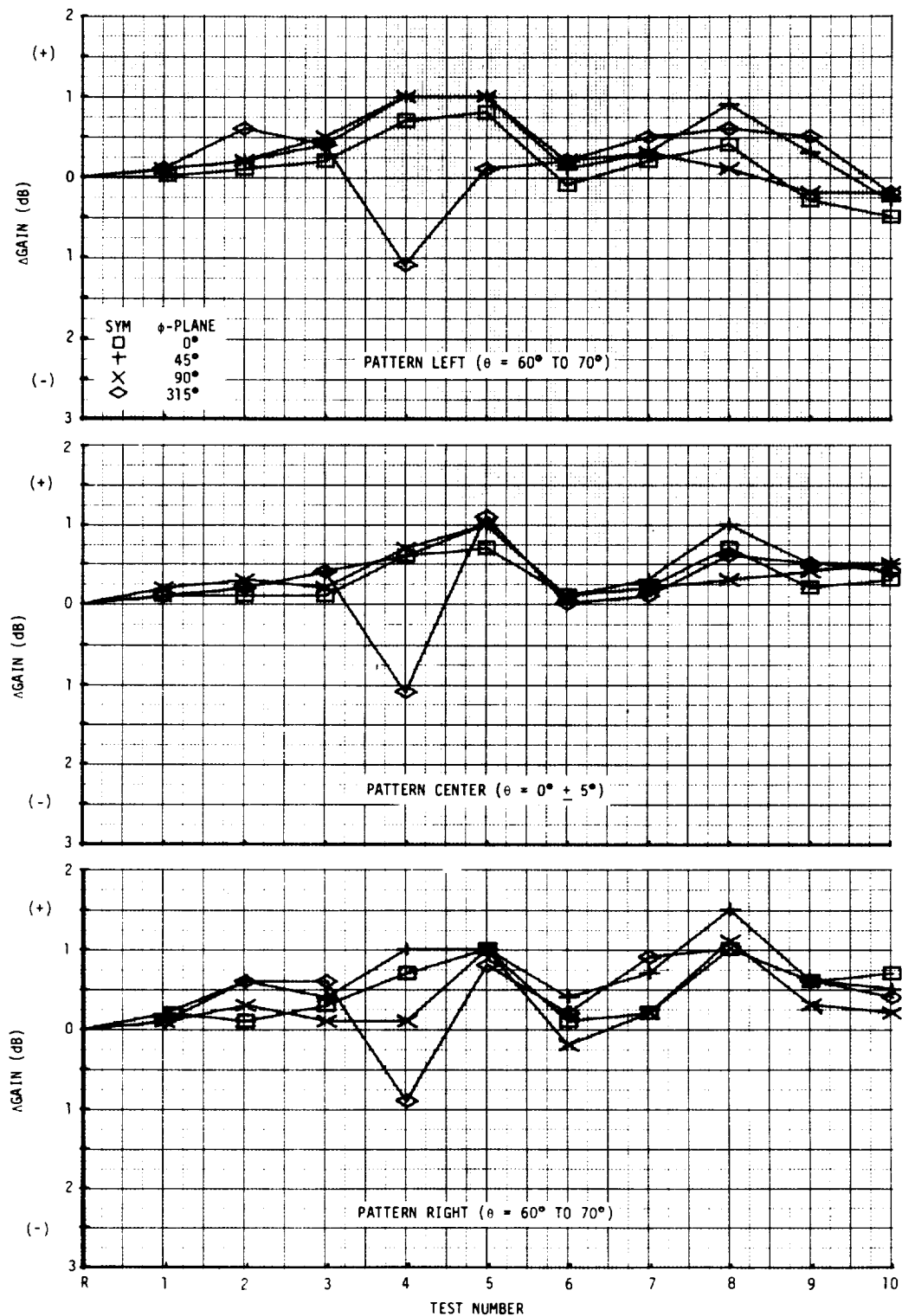


**FIGURE 51 LINEAR GAIN CHANGES - 1.8 GHz**

**DEVELOPMENT OF S-BAND ANTENNA INTERFACE DESIGN**  
**SHUTTLE ANTENNA RADOME TECHNOLOGY TEST PROGRAM**

**REPORT MDC E1478**  
**15 JUNE 1977**  
**VOLUME II**

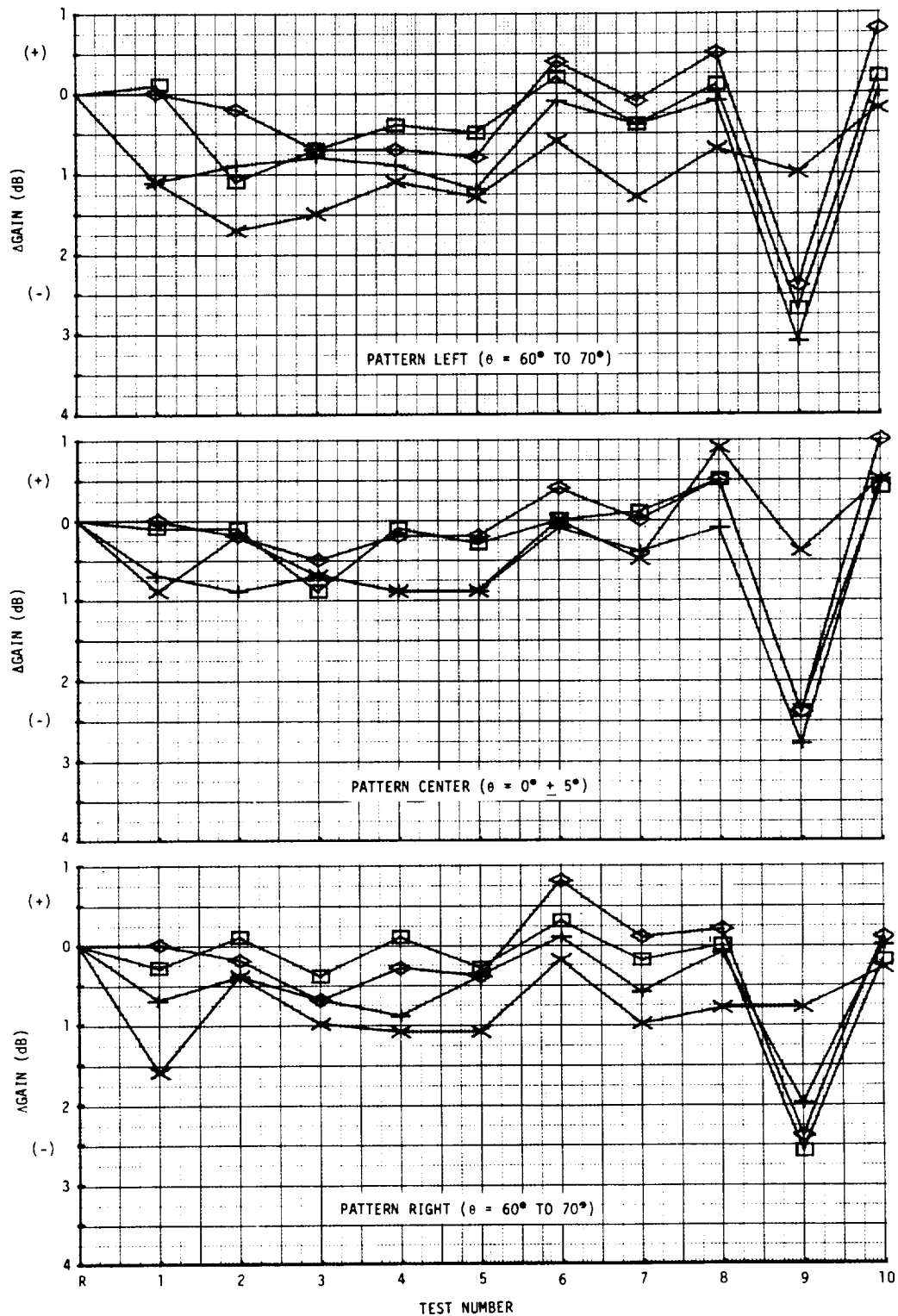


FIGURE 52 LINEAR GAIN VARIATIONS - 2.1 GHz

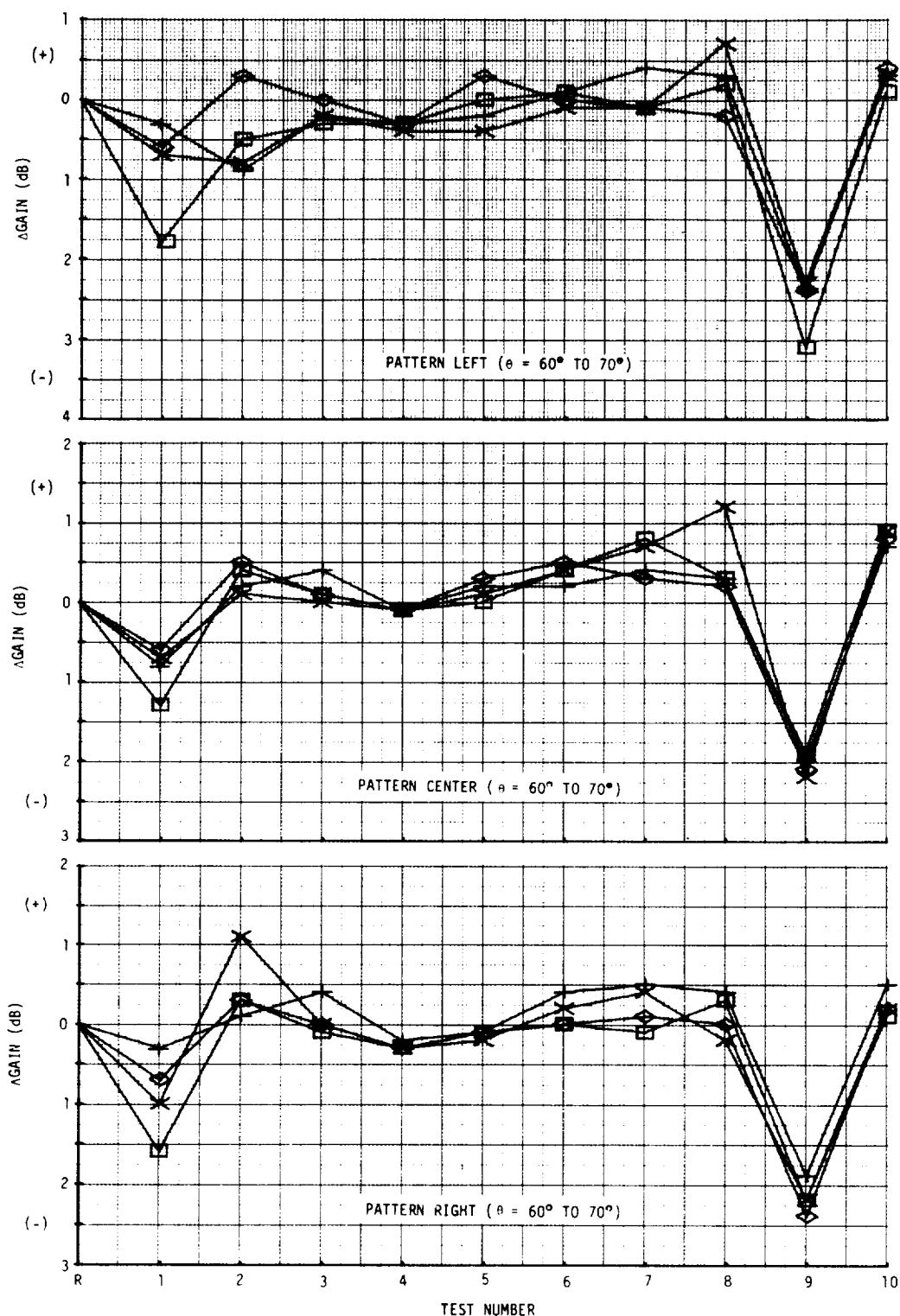


FIGURE 53 LINEAR GAIN CHANGES - 2.3 GHz



**TABLE IV**  
**STANDARD GAIN HORN PATTERN LEVEL (-dB)**

TEST NO.	FREQUENCY (GHz)		
	1.8	2.1	2.3
REF	7.8	5.2	5.3
1	7.9	5.3	5.2
2	7.6	5.1	5.3
3	7.8	4.5	5.3
4	7.7	5.1	5.4
5	7.8	5.1	5.4
6	7.8	5.2	5.5
7	7.8	5.1	5.2
8	7.8	5.1	5.1
9	7.6	4.8	5.2
10	8.0	5.2	5.2

NOTE: GAIN LEVELS ARE RECORDED  
LEVELS ON RECTANGULAR CHART  
PAPER WHICH HAS A MAXIMUM  
LEVEL OF 0 dB AND A MINIMUM  
LEVEL OF -40 dB.

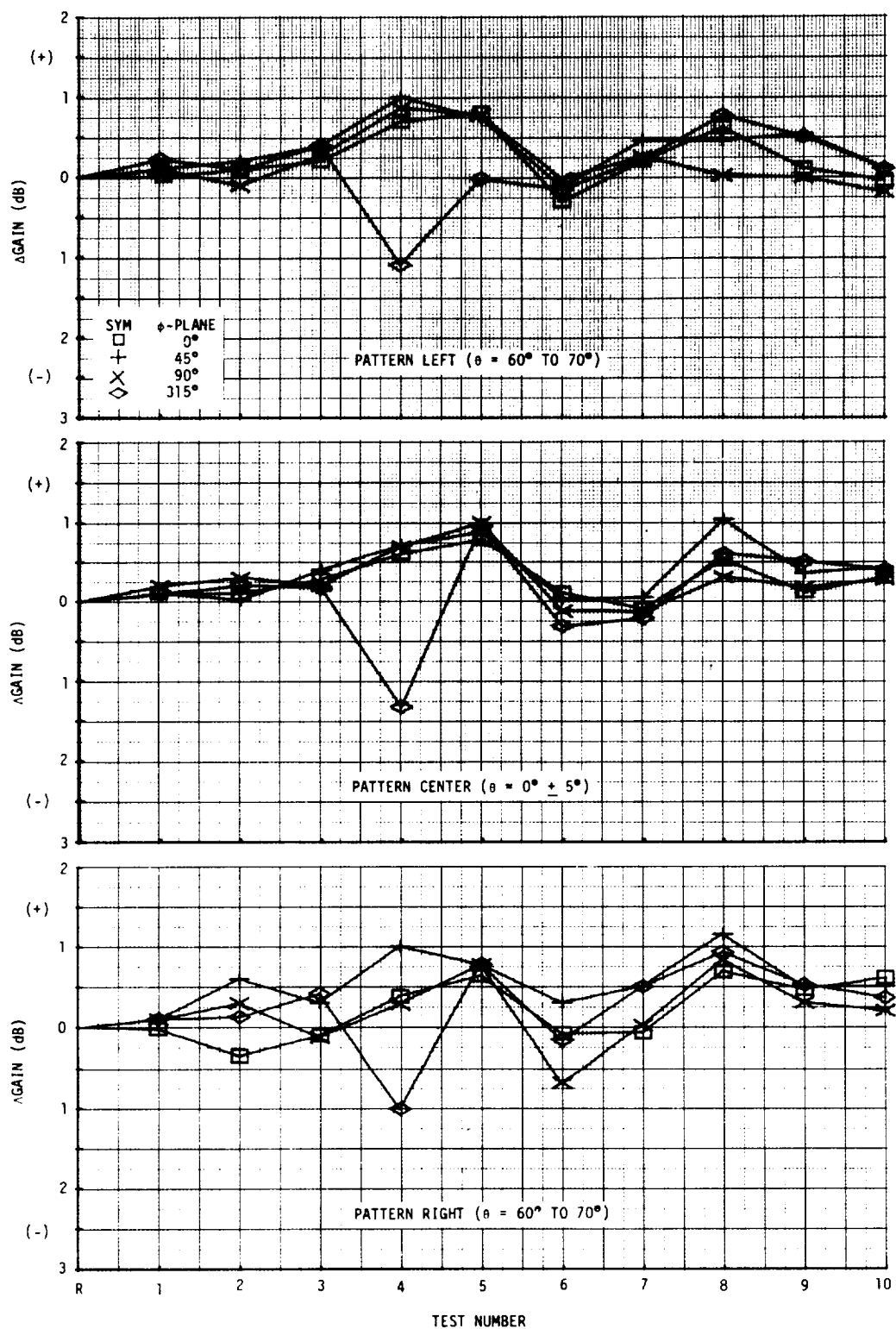


FIGURE 54 CIRCULAR GAIN VARIATIONS CAUSED BY AXIAL RATIO  
AND LINEAR GAIN CHANGES - 1.8 GHz

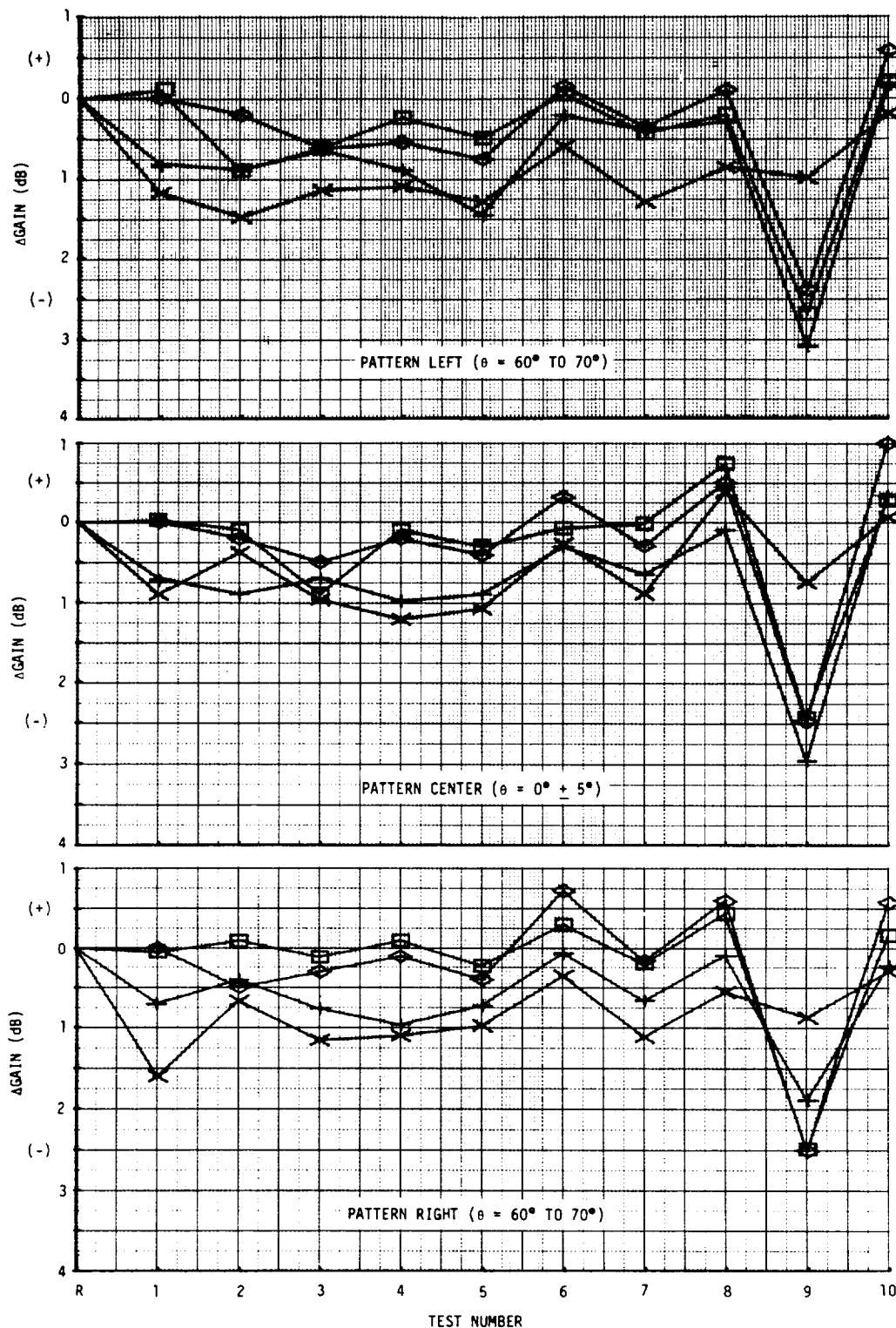


FIGURE 55 CIRCULAR GAIN VARIATIONS CAUSED BY AXIAL RATIO  
AND LINEAR GAIN CHANGES - 2.1 GHz

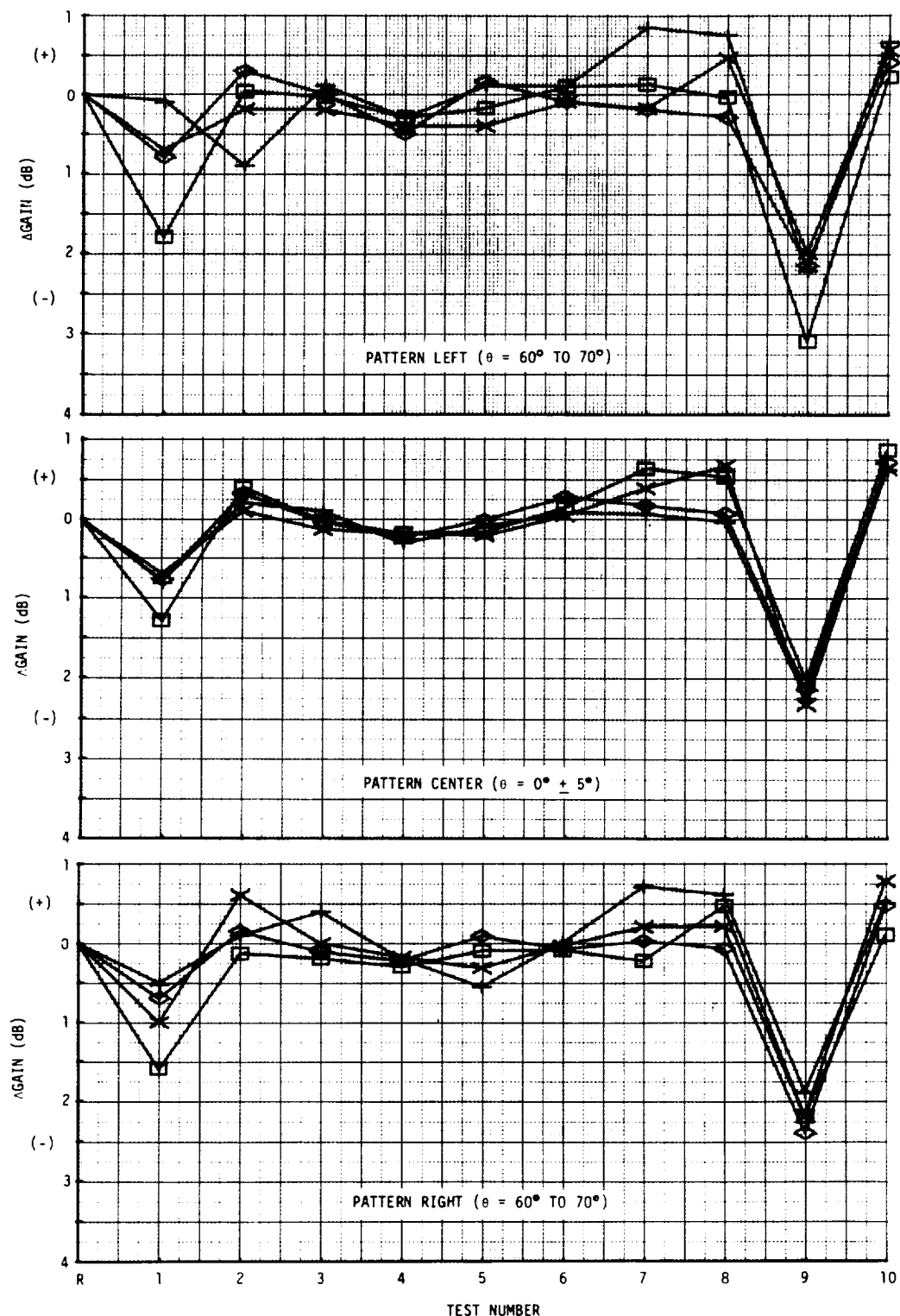


FIGURE 56 CIRCULAR GAIN VARIATIONS CAUSED BY AXIAL RATIO  
AND LINEAR GAIN CHANGES - 2.3 GHz

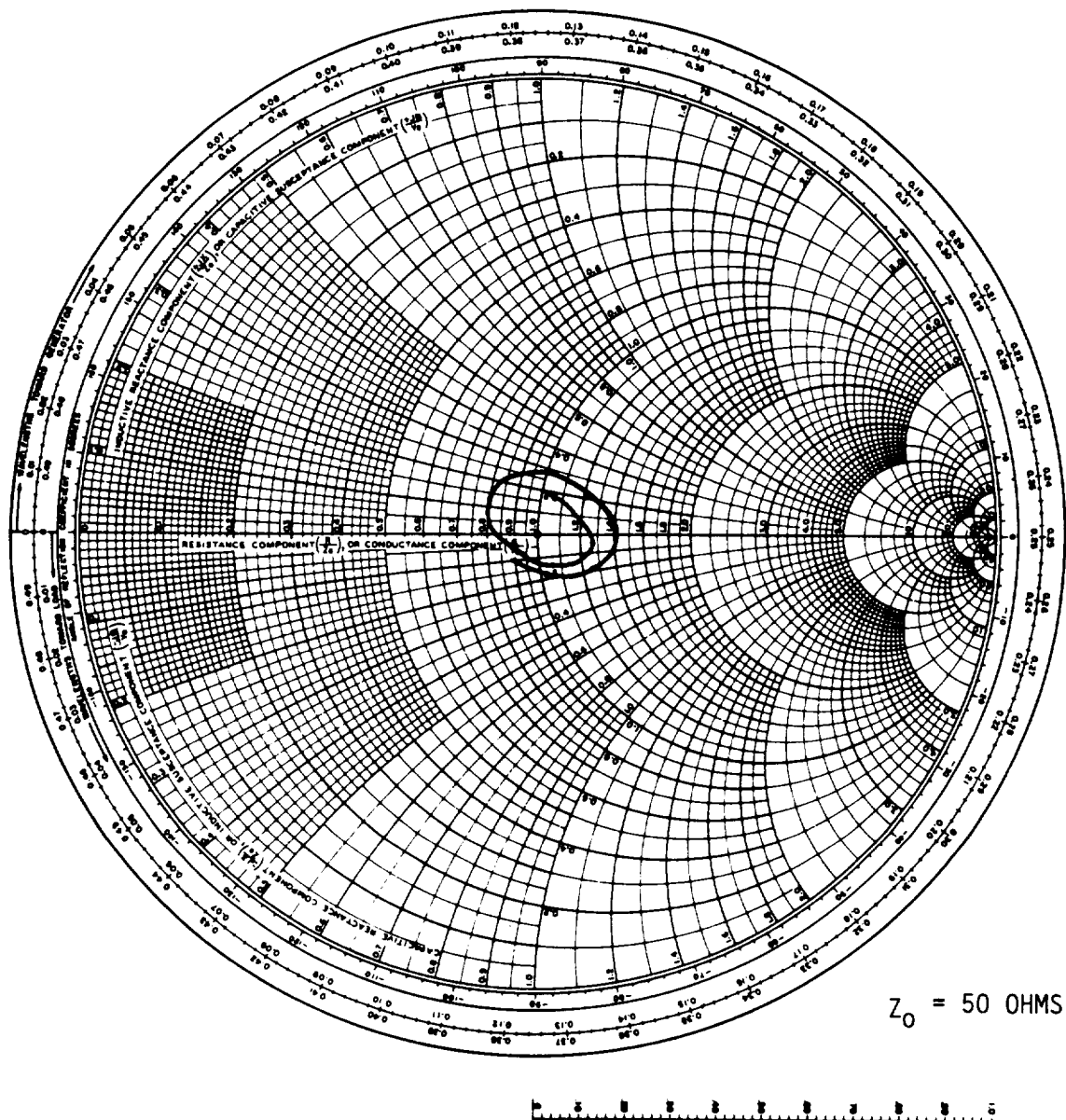


FIGURE 57 REFERENCE IMPEDANCE (1.7 - 1.9 GHz)



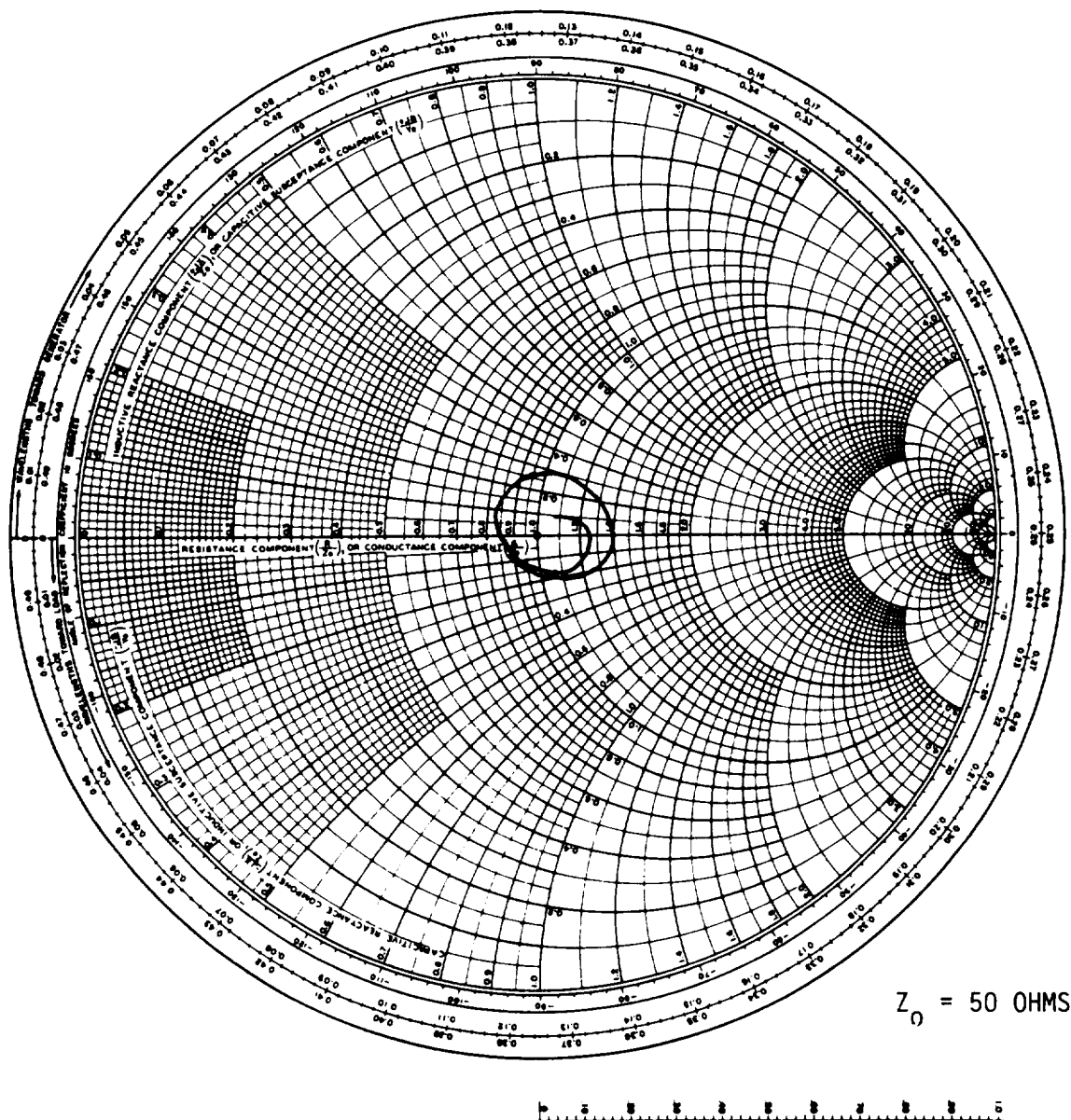
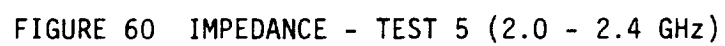
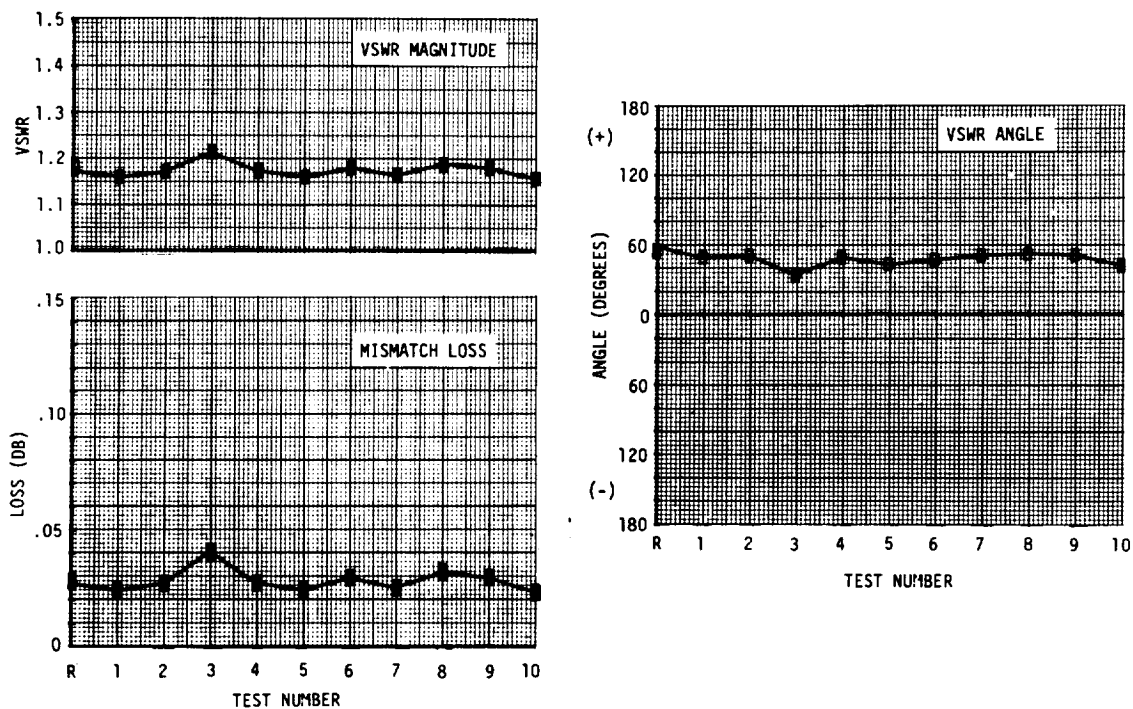


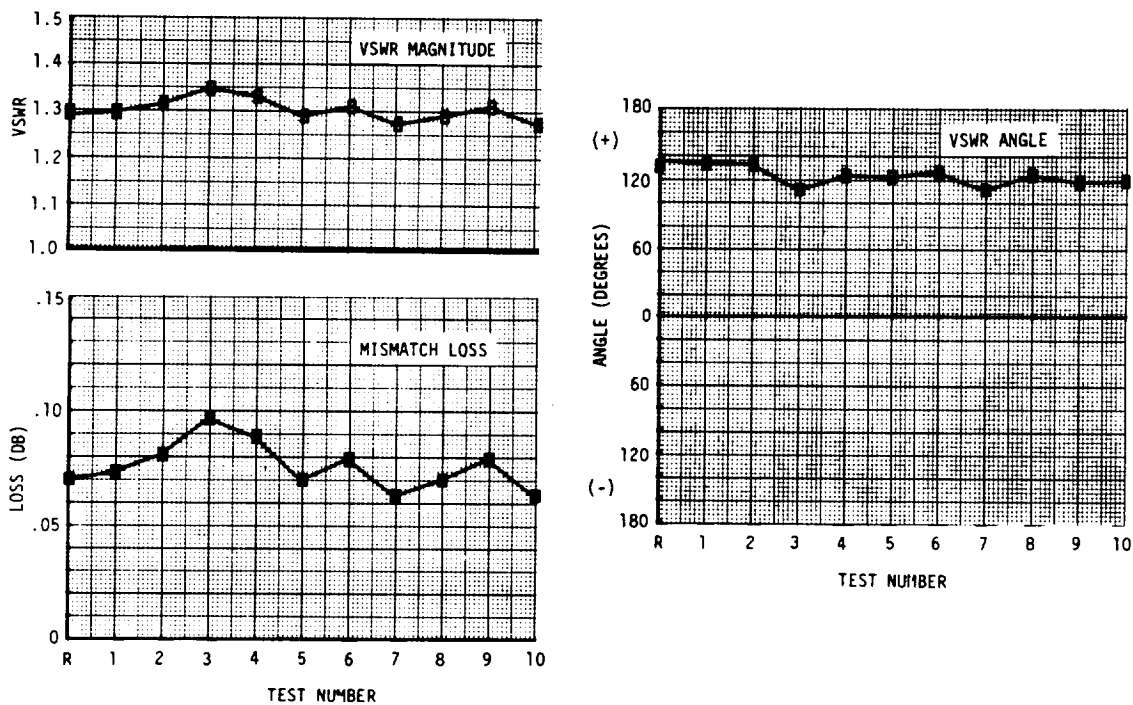
FIGURE 59 IMPEDANCE - TEST 5 (1.7 - 1.9 GHz)





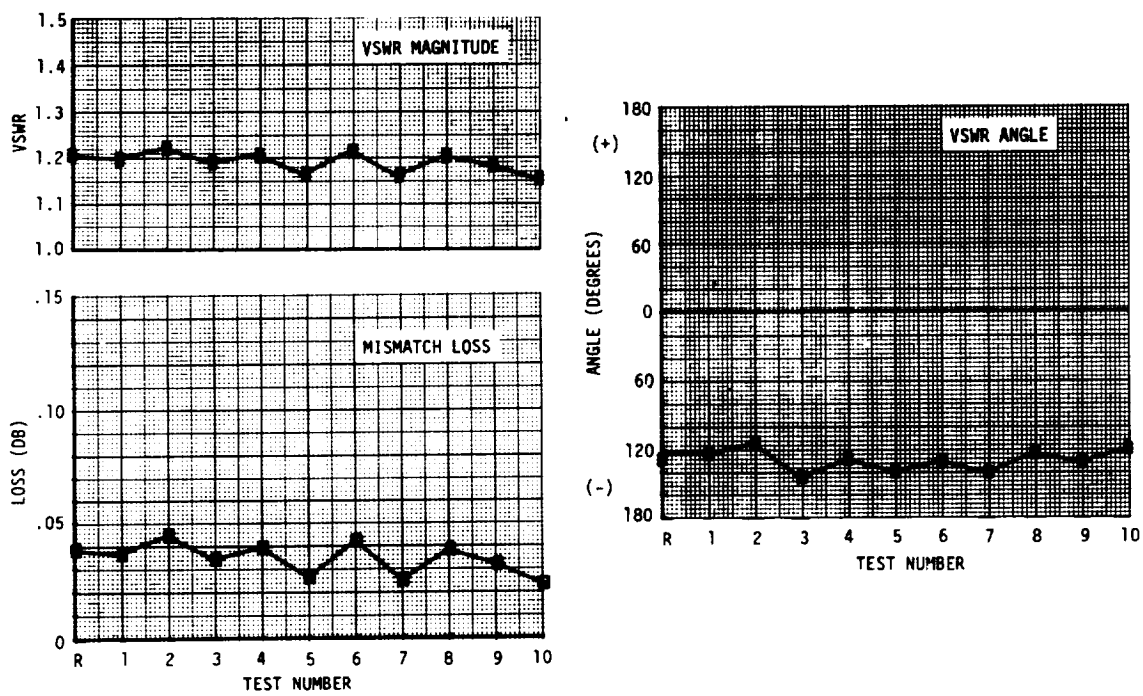


(a) 1.7 GHz



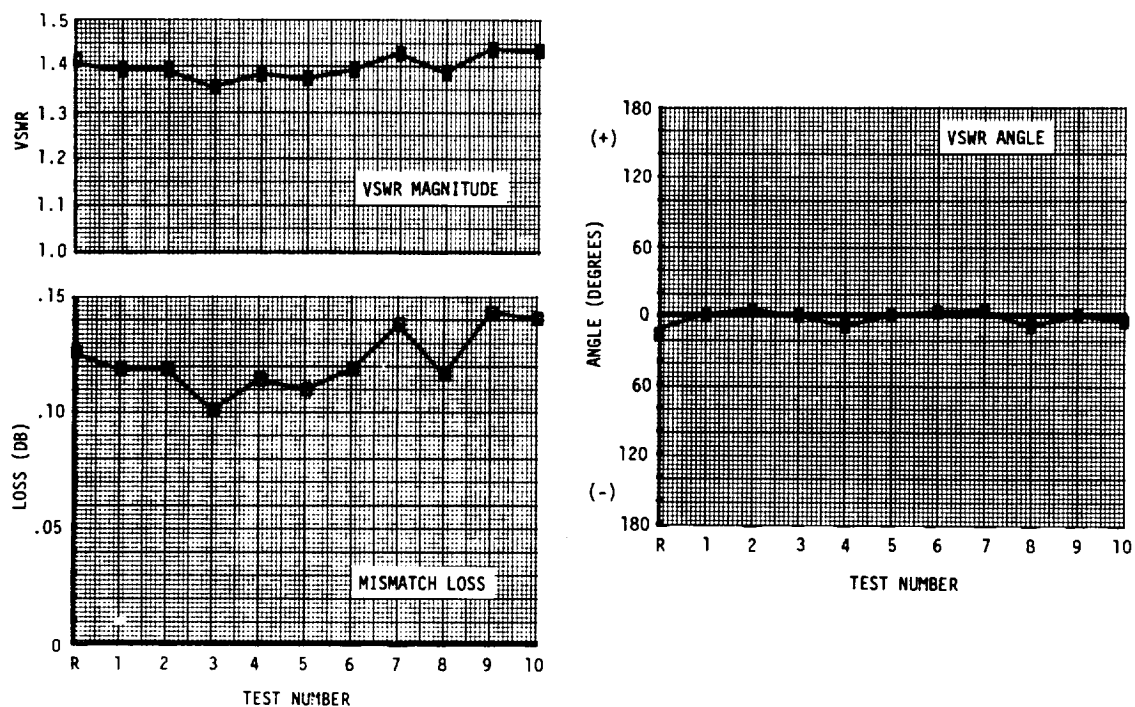
(b) 1.8 GHz

FIGURE 61 VSWR (MAGNITUDE AND ANGLE) AND MISMATCH LOSS - 1.7 TO 1.9 GHz

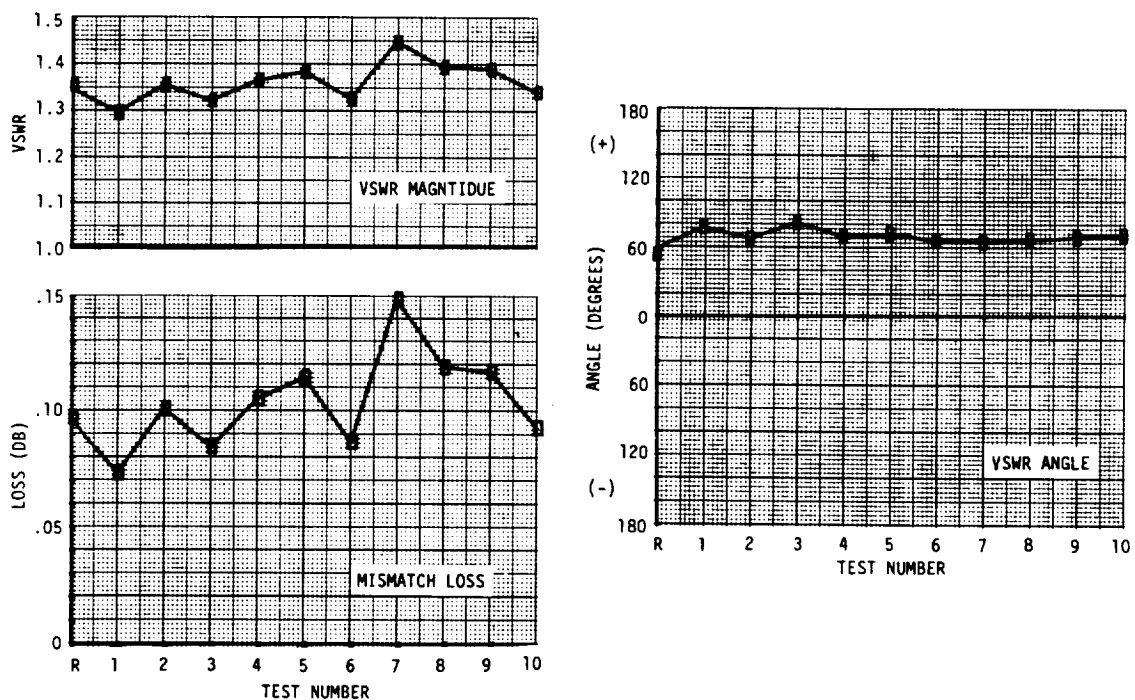


(c) 1.9 GHz

FIGURE 61 VSWR (MAGNITUDE AND ANGLE) AND MISMATCH LOSS - 1.7 TO 1.9 GHz (CONT)

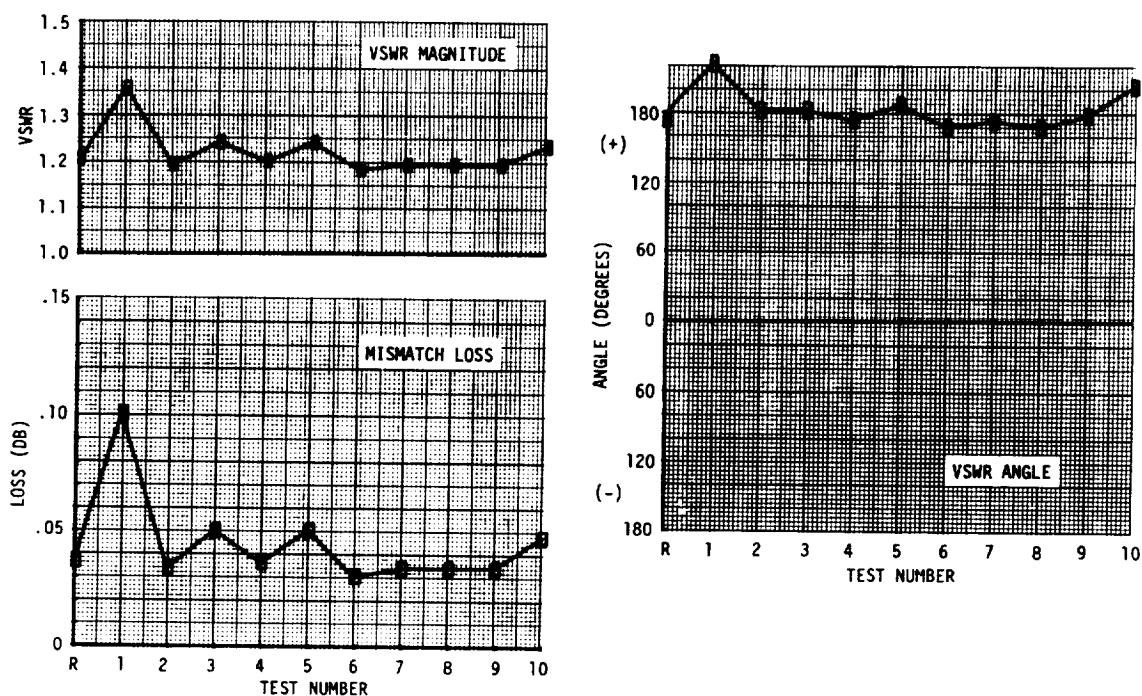


(a) 2.0 GHz

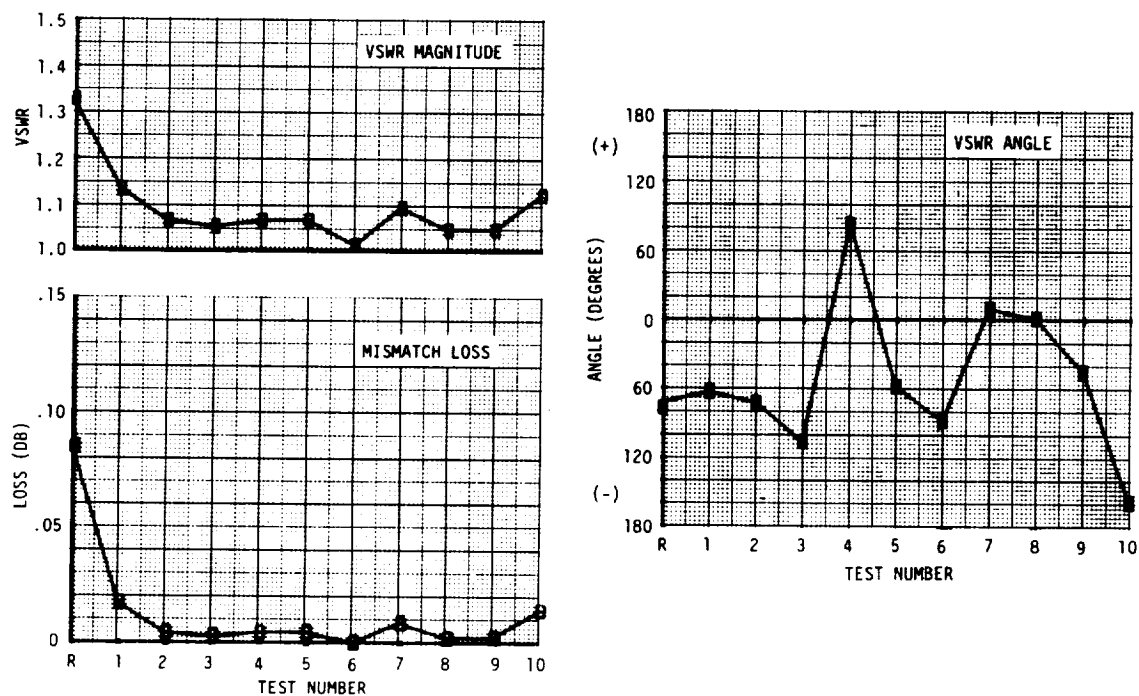


(b) 2.1 GHz

FIGURE 62 VSWR (MAGNITUDE AND ANGLE) AND MISMATCH LOSS - 2.0 TO 2.4 GHz

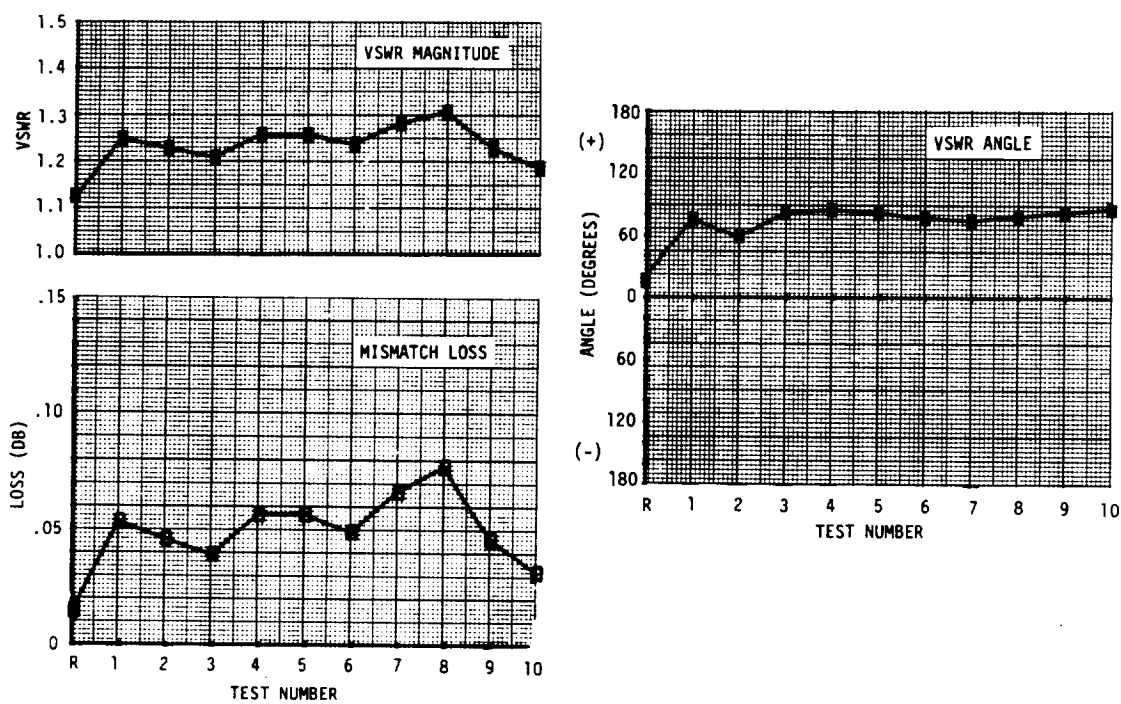


(c) 2.2 GHz



(d) 2.3 GHz

FIGURE 62 VSWR (MAGNITUDE AND ANGLE) AND MISMATCH LOSS - 2.0 TO 2.4 GHz (CONT)



(e) 2.4 GHz

FIGURE 62 VSWR (MAGNITUDE AND ANGLE) AND MISMATCH LOSS - 2.0 TO 2.4 GHz (CONT)

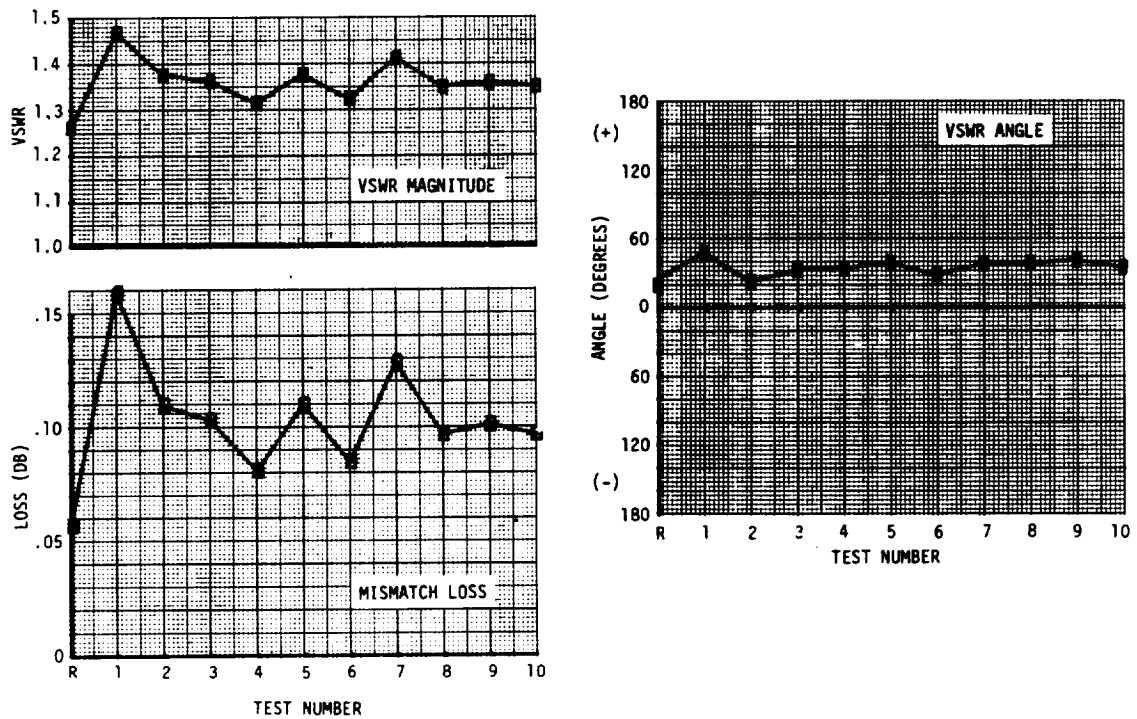


FIGURE 63 VSWR (MAGNITUDE AND ANGLE) AND MISMATCH LOSS - 2.2 GHz

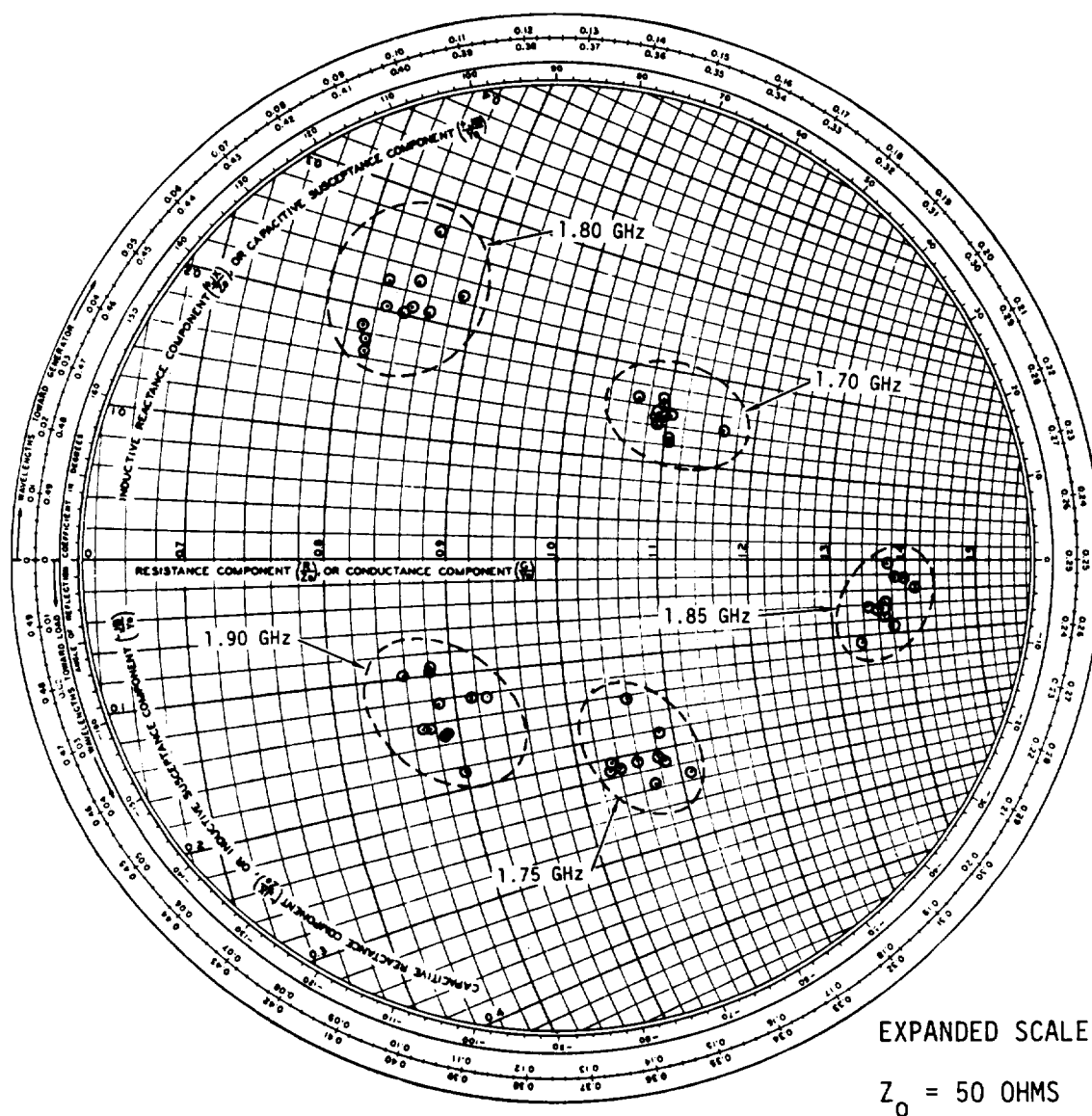
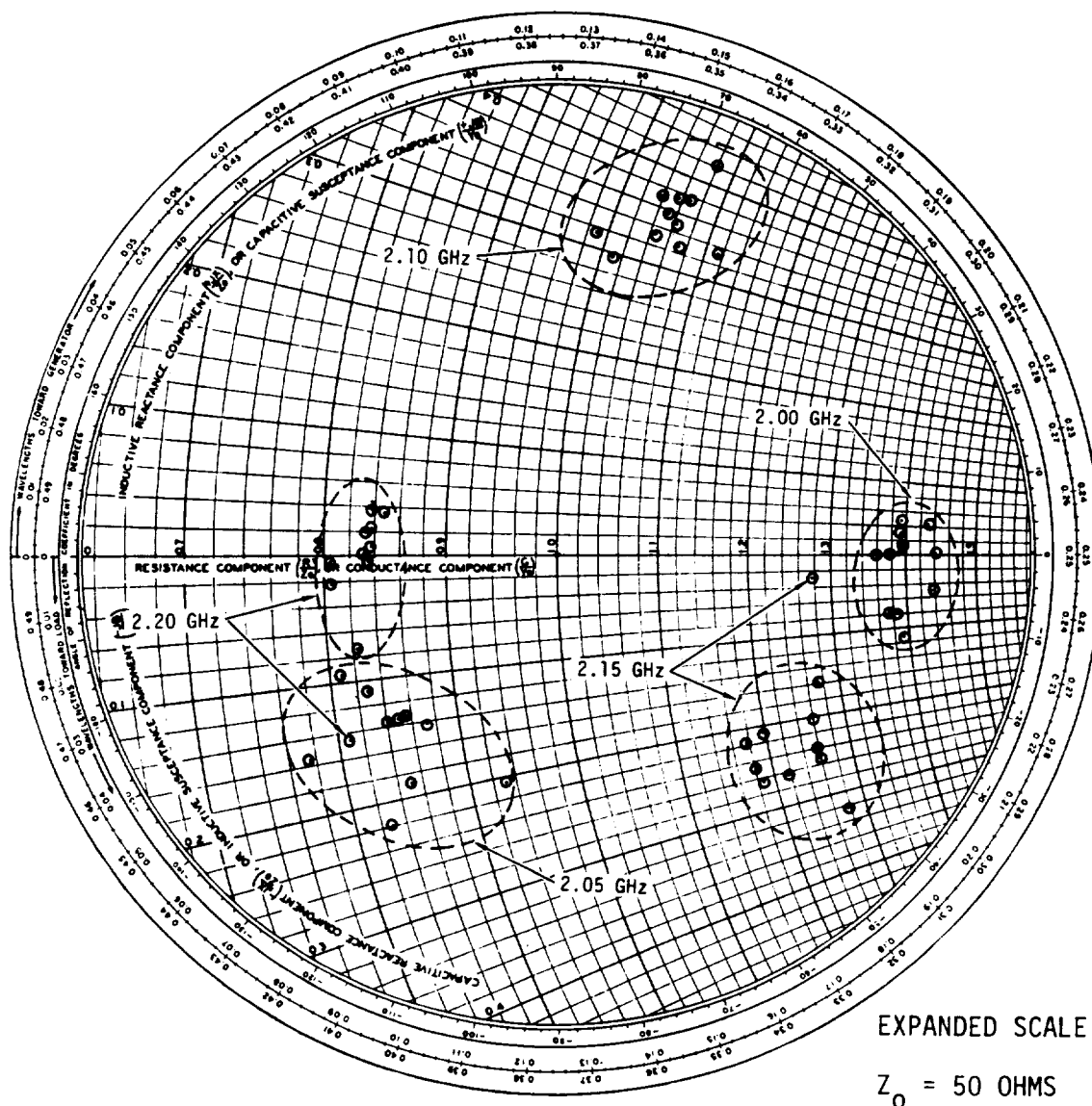


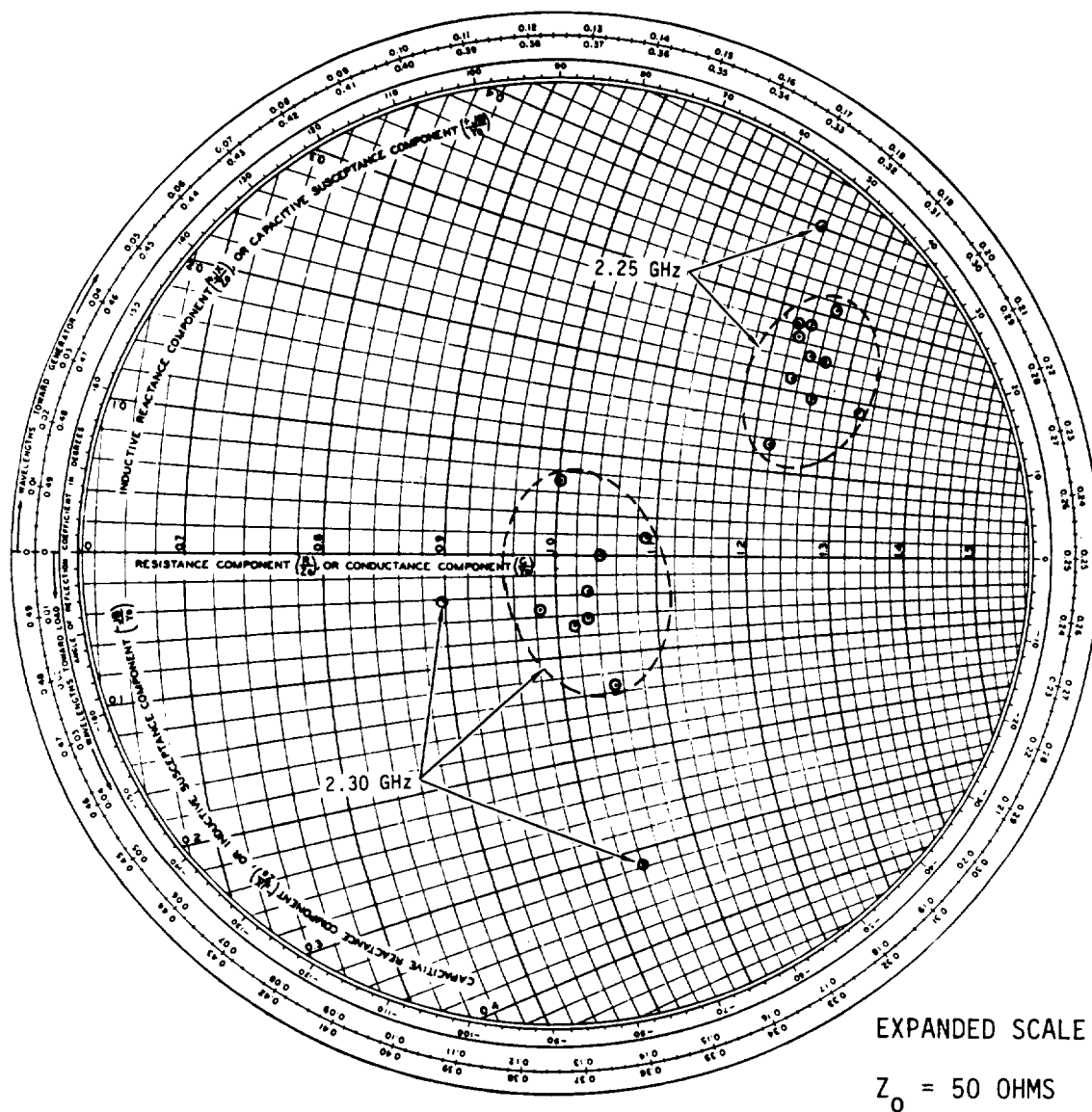
FIGURE 64 IMPEDANCE - TESTS 1-10 (1.7 - 1.9 GHz)



(a) 2.00 - 2.20 GHz

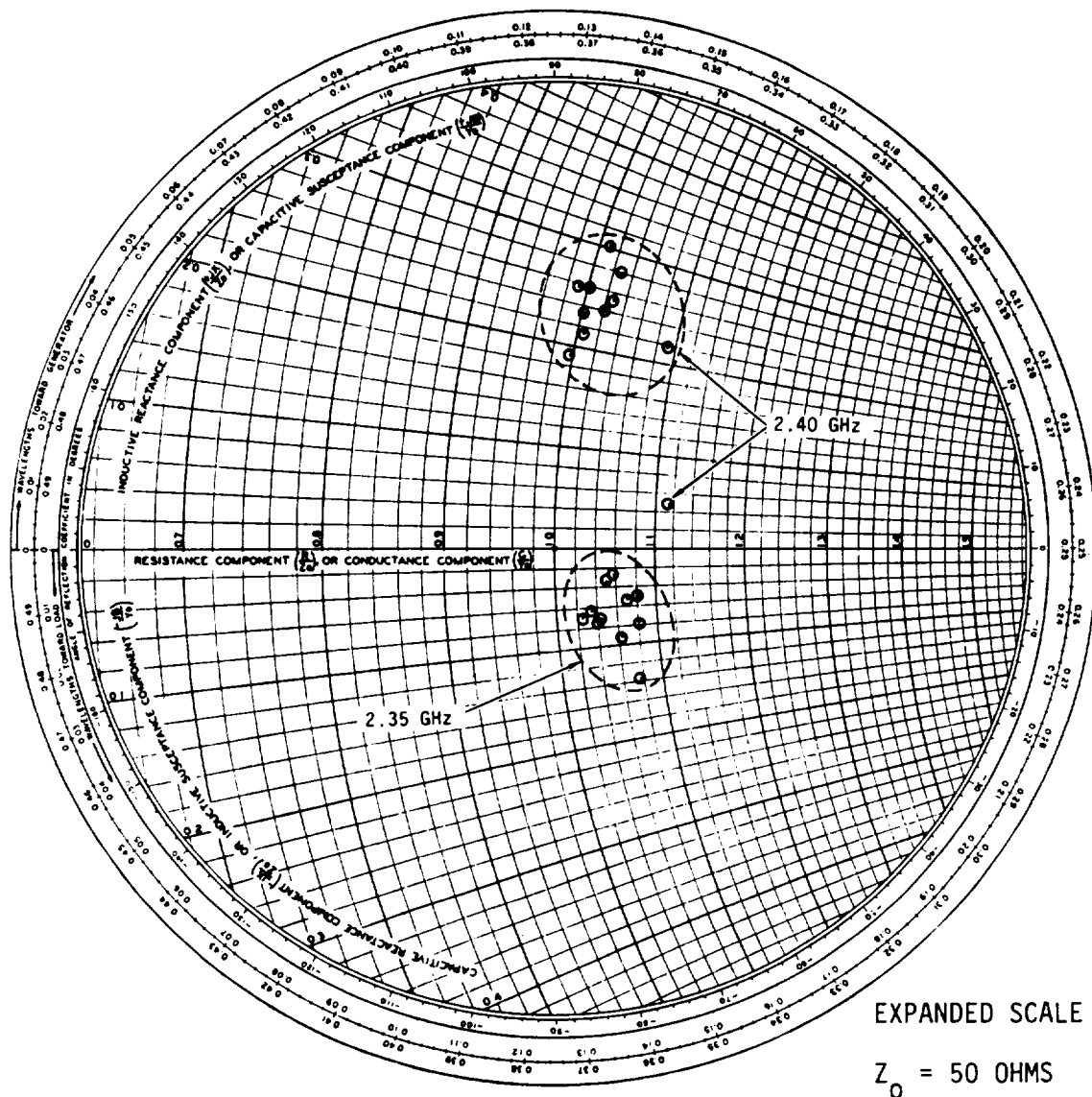
FIGURE 65 IMPEDANCE - TESTS 1-10 (2.0 - 2.4 GHz)





(b) 2.30 - 2.25 GHz

FIGURE 65 IMPEDANCE - TESTS 1-10 (2.0 - 2.4 GHz) (CONT)



(c) 2.35 - 2.40 GHz

FIGURE 65 IMPEDANCE - TESTS 1-10 (2.0 - 2.4 GHz) (CONT)

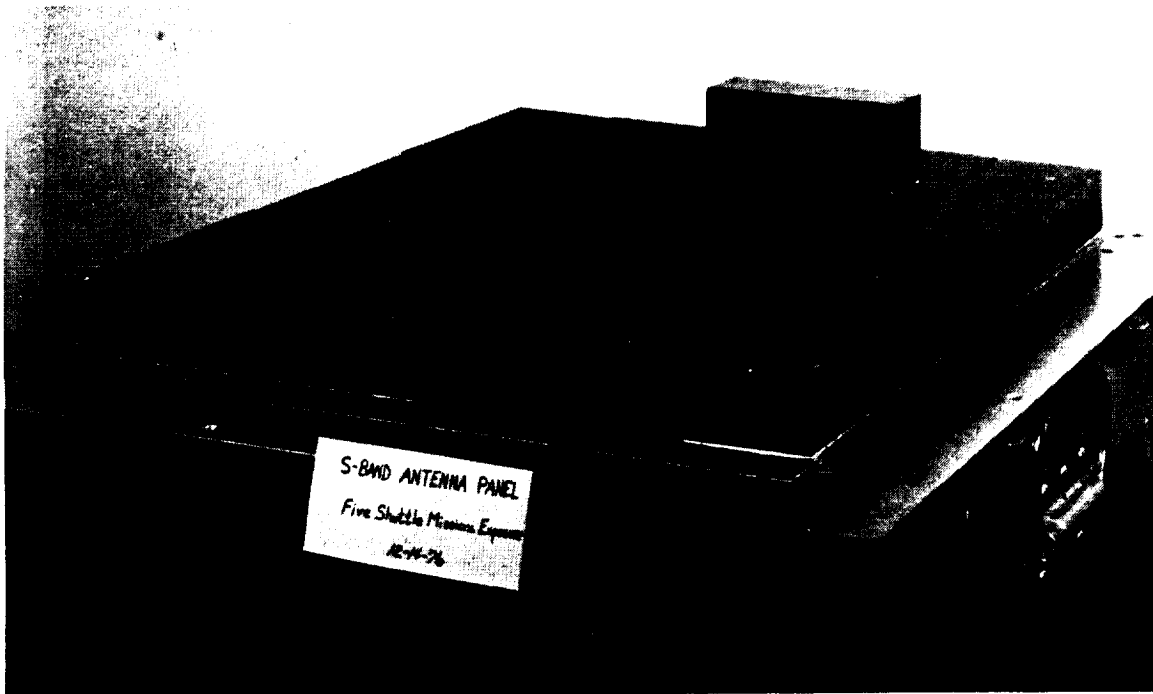


FIGURE 66 TEST FIXTURE AFTER TEST 5

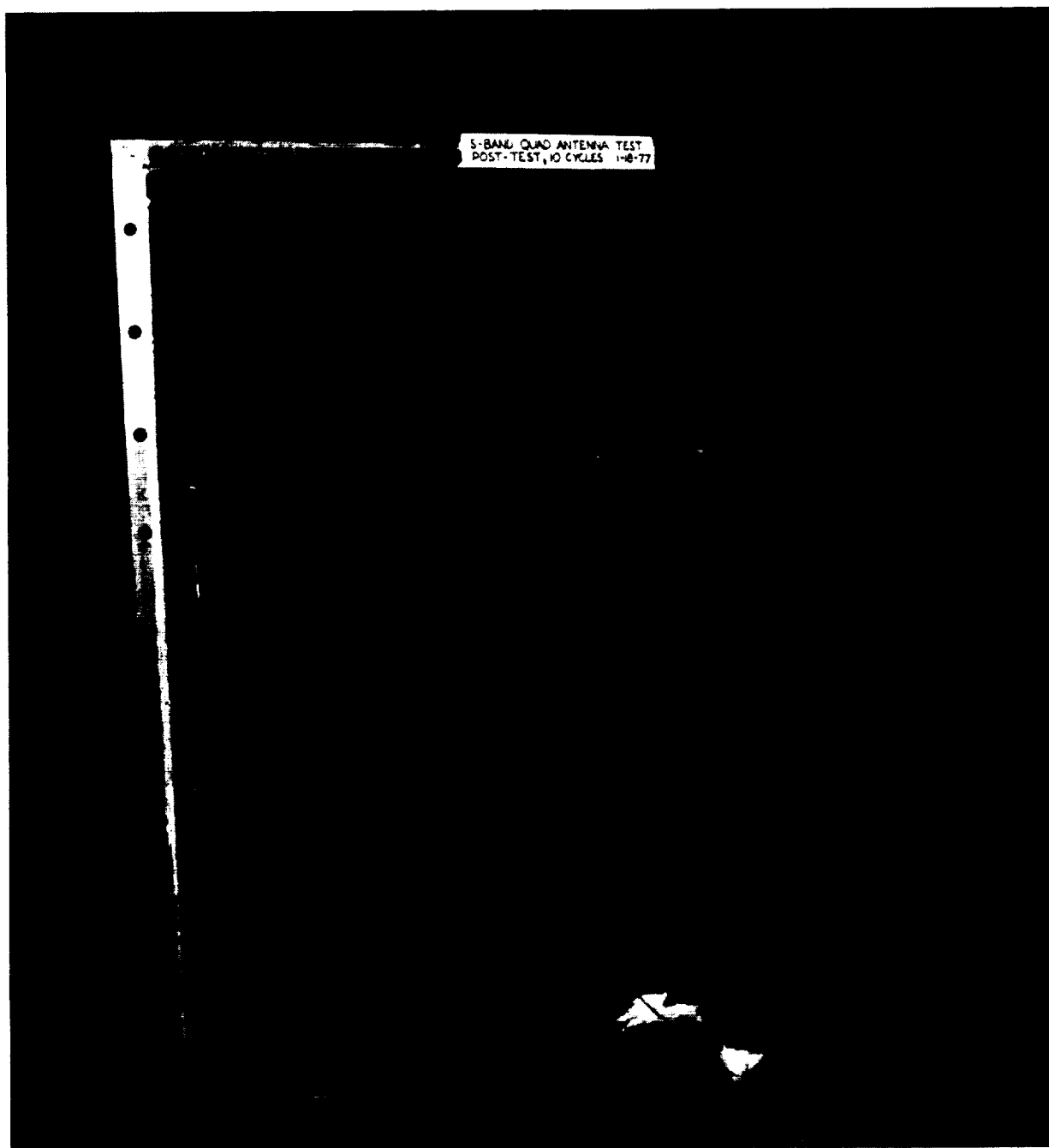


FIGURE 67 TEST FIXTURE AFTER TEST 6

## THERMAL VACUUM TESTING

The objective of this task (Task 2.3.1) was to validate the accuracy of the analytical thermal model developed in the first part of this contract (reference 1) for use in support of the Space Shuttle S-band Quad antenna design. The thermal model is a representation of the antenna and test fixture also designed and fabricated in the first part of this contract. Thus, node points in the analytical model are directly related to physical locations in the test fixture.

To accomplish this task, the latest Shuttle design data (e.g., heating rates and TPS thicknesses) were incorporated into the model to provide thermal vacuum test control parameters and response data for comparison with measured data. A test plan was prepared for two flight conditions, one simulating maximum heating in orbit (hot orbit), followed by entry heating and the other simulating a minimum heating (i.e., maximum cooling) orbit (cold orbit), also followed by entry heating. The data was analyzed by modifying the thermal model to account for actual test conditions and heat leaks at the test fixture boundaries.

This section describes the various environments simulated, the test facilities and configuration, and discusses the test results and the boundary modifications made to show the validity of the analytical thermal model.

### Test Fixture

The test fixture, originally designed and fabricated in the first part of this contract, used for the thermal vacuum testing, is described in Volume 1 of this report (reference 1). It was designed to account for all significant factors which would influence the thermal response of the antenna resulting from ascent, orbital and entry flight environments. These factors include various aspects of the Space Shuttle Orbiter construction in the vicinity of the antenna, the test facility and its capabilities, and the test setup and instrumentation requirements. A picture of the test fixture, wrapped with a Mylar multi-layer insulation blanket, is shown in figure 68. The insulation blanket is intended to minimize any side interface from the test facility by creating an adiabatic wall. Other photos and a detailed description of the test fixture may be found in reference 1.

Structure. - A sketch of the test fixture, which illustrates its design and construction details, is shown in figure 69. Basically, the fixture duplicates a nominal layer of SIP (Strain Isolator Pad) bonded to the structural skin, and the intervening substrate construction details to the interior cabin wall of the Space Shuttle Orbiter. A 0.254 mm (0.010 in.) sheet of stainless steel was bonded to the SIP to provide for controlling to outer bondline (HRSI (High Temperature Reusable Surface Insulation)/SIP) temperatures. The surface of the stainless steel sheet is sprayed with a high emissivity coating for improved thermal response from a radiant heat source or sink (i.e., Quartz-lamp heaters and/or vacuum chamber liquid nitrogen (LN<sub>2</sub>)-cooled shroud). The test fixture

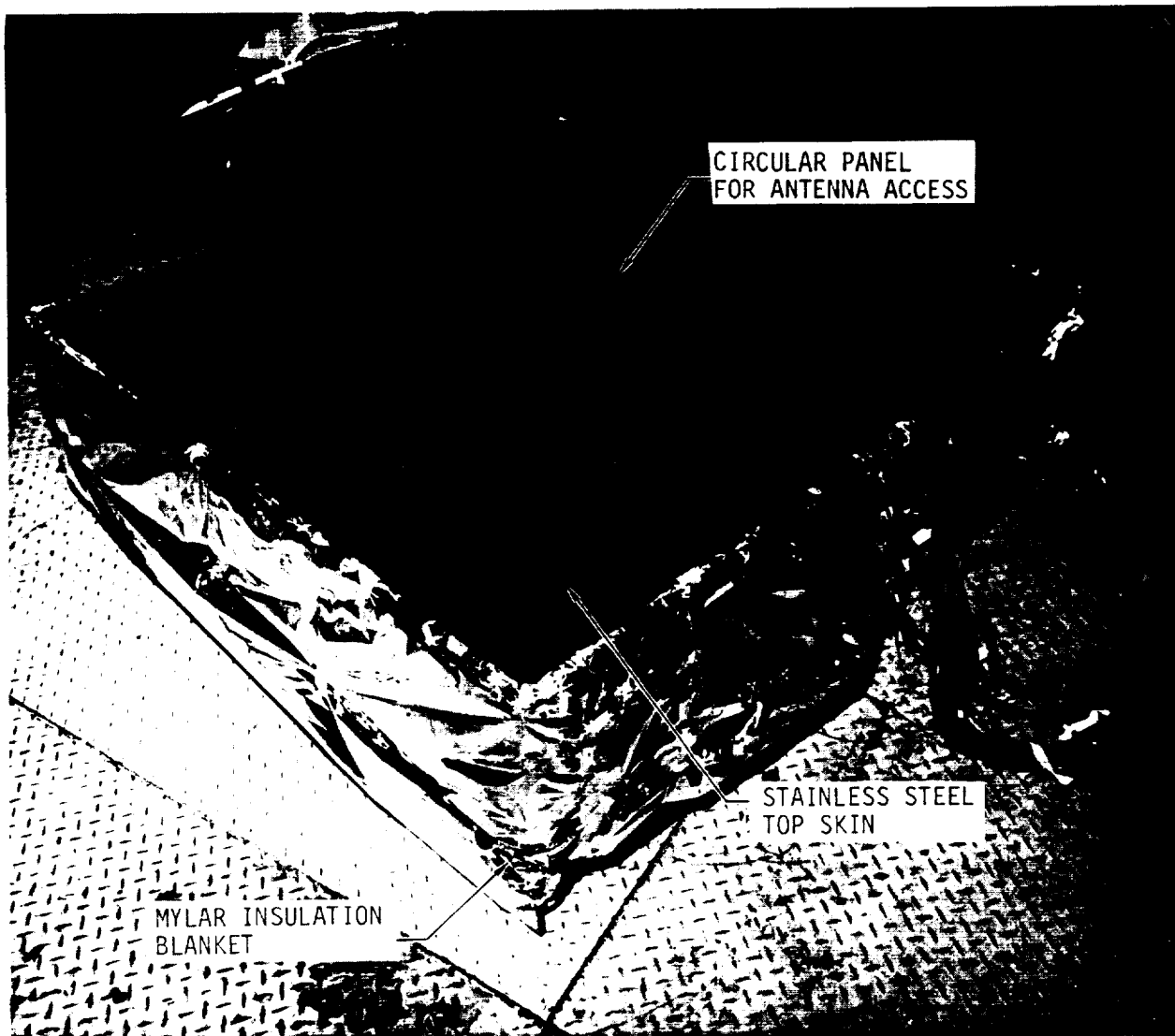


FIGURE 68 THERMAL TEST FIXTURE PRIOR TO INSTALLATION IN TEST CHAMBER

surface area, 1.23 x 1.23 m (4 x 4 ft), was determined from a trade-off of test facility size capabilities and requirements for an adiabatic boundary.

One slight deviation from the original design occurred in the internal insulation configuration. The 0.846 cm (0.333 in.) thick Multi-Layer Insulation (MLI) blanket under the TG-15000 insulation batt design was replaced by an equal thickness of the TG-15000 material. During test preparation the MLI material was not available. Substitution of the TG-15000 was considered the best choice from both the standpoint of analytical model modification and availability.

**DEVELOPMENT OF S-BAND ANTENNA INTERFACE DESIGN**  
**SHUTTLE ANTENNA RADOME TECHNOLOGY TEST PROGRAM**

**REPORT MDC E1478**  
**15 JUNE 1977**  
**VOLUME II**

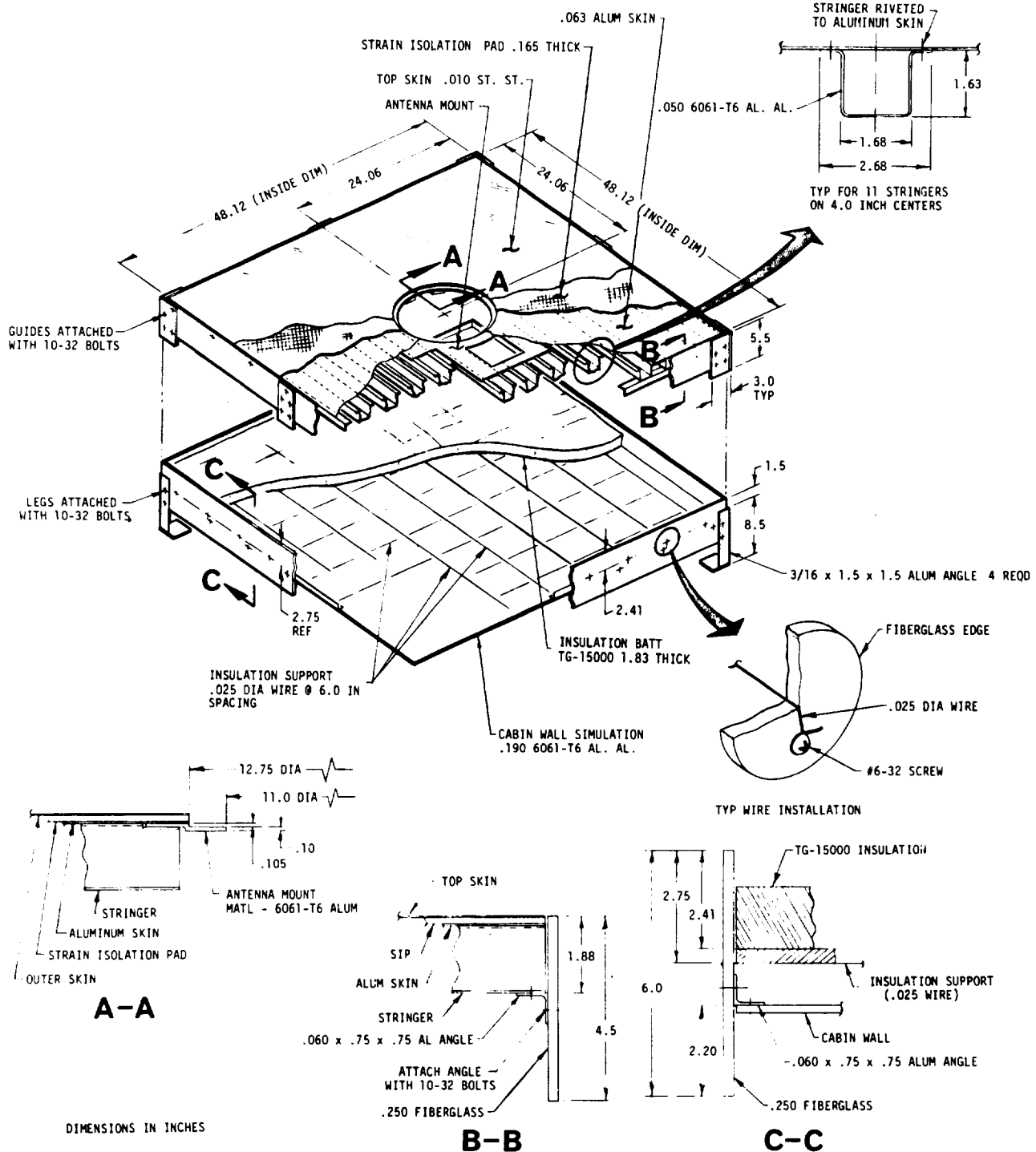


**FIGURE 69 THERMAL TEST FIXTURE - DESIGN DETAILS**

Antenna. - Photos of the S-Band antenna installed in the test fixture are shown in figures 70 through 72. This installation was provided for by a removable circular panel of stainless steel and SIP (figure 70) which was bonded to the antenna after installation. After bonding, the gap around the panel edges was covered with a metallic tape to minimize any radiant heating into the gap and painted black to match the emissivity of the stainless steel top skin (figure 68).

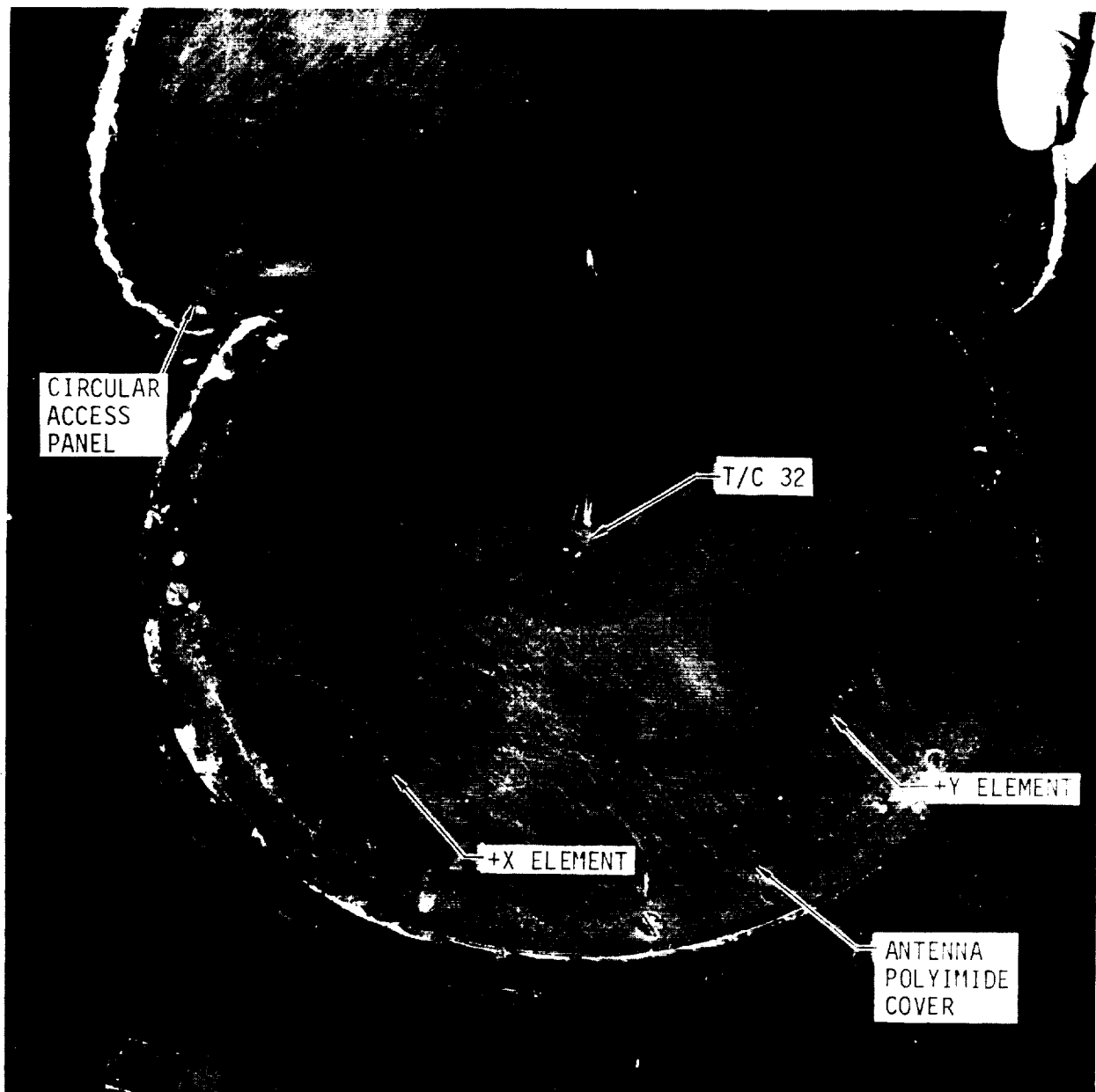


FIGURE 70 ANTENNA INSTALLATION IN TEST FIXTURE - TOP VIEW



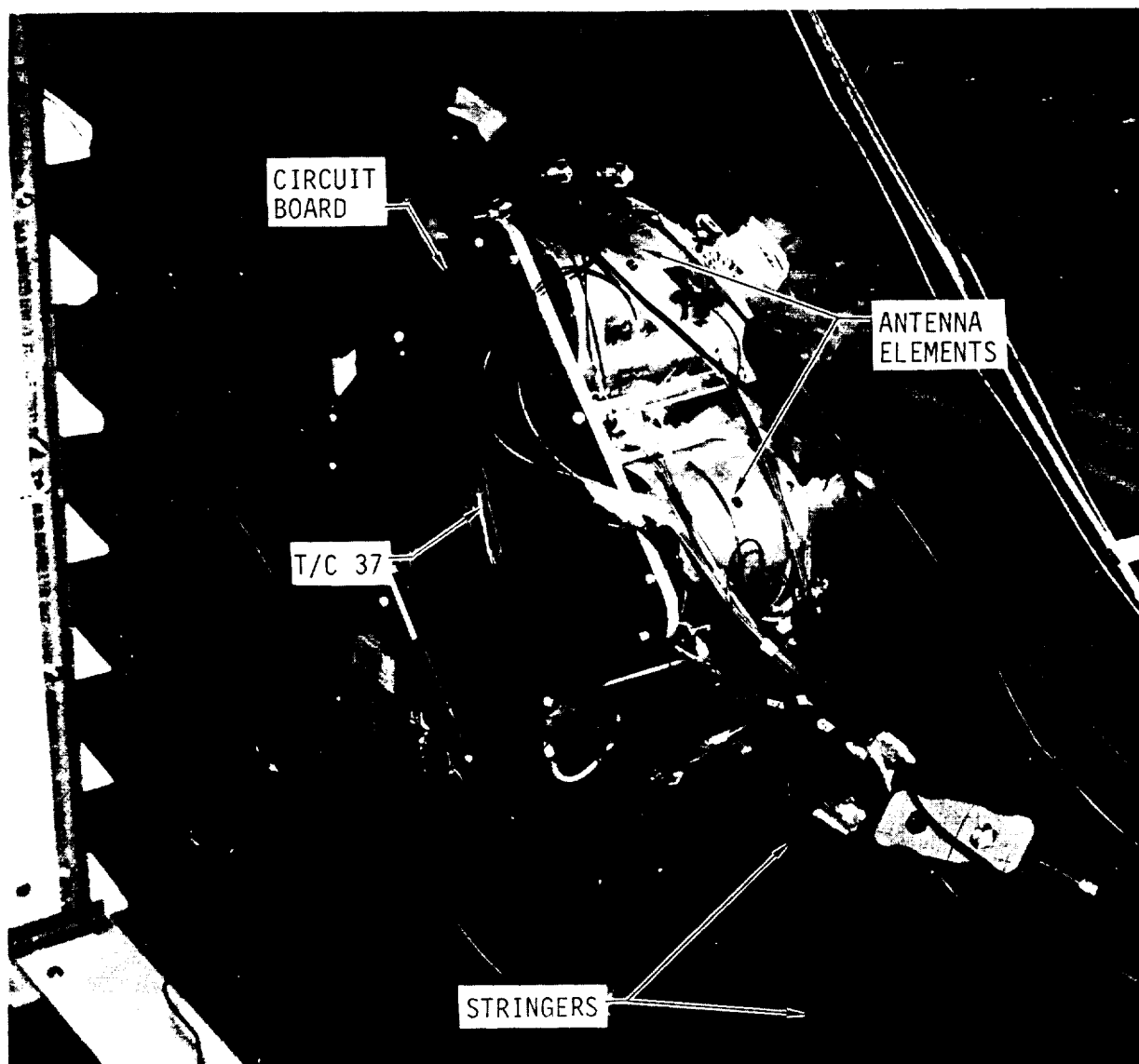
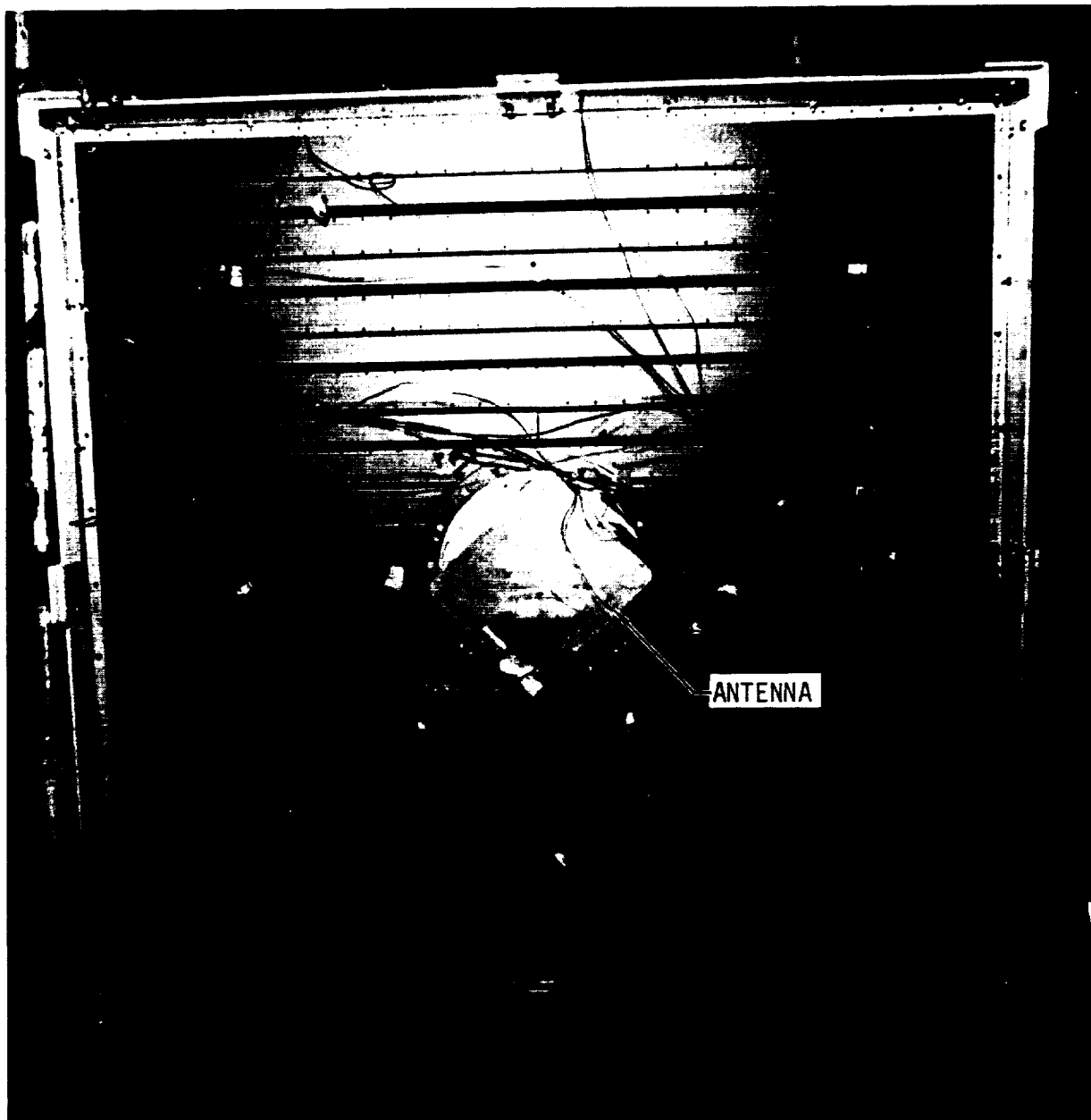


FIGURE 71 ANTENNA INSTALLATION IN TEST FIXTURE - BOTTOM VIEW



**FIGURE 72 TEST FIXTURE WITH ANTENNA - BOTTOM VIEW**

The antenna as received did not include a dust cover. The dust cover provides a barrier to heat transfer between the backside of the antenna components and the surrounding structure and is included in the analytical thermal model. At first, elimination of the dust cover from the analytical thermal model was considered. However, this was found to be a not-so-simple and uncertain task because of the computer program complexity. Therefore, it was decided to improvise a dust cover from aluminum foil (heavy gage) and tape, coat it with black emittance paint, and install it as shown in figure 73.



FIGURE 73 ANTENNA WITH DUST COVER INSTALLED

Instrumentation. - The test fixture and the antenna were instrumented with 49 28-gage Type K (Chromel-Alumel) thermocouples: 33 on the test fixture and 16 on the antenna. Descriptions of all the thermocouples, their locations and corresponding nodes in the analytical thermal model are listed in table V.

**DEVELOPMENT OF S-BAND ANTENNA INTERFACE DESIGN**  
**SHUTTLE ANTENNA RADOME TECHNOLOGY TEST PROGRAM**

**REPORT MDC E1478**  
**15 JUNE 1977**  
**VOLUME II**

**TABLE V**  
**THERMAL TEST FIXTURE INSTRUMENTATION LOCATIONS**

NUMBER	COMPONENT	LOCATION	THERMAL MODEL NODE NO.
1	S.S. skin (14)	X=0, Y=16 Top Side	216
2	↓	X=16, Y=-16	214
3	↓	X=-16, Y=0	222
4	↓	X=-16, Y=16	214
5	↓	X=0, Y=8	220
6	↓	X=16, Y=0	222
7	↓	X=8, Y=0	223
8	↓	X=8, Y=8	219
9	S.S. skin	Center, Top Side	224
10	Structural skin (13)	X=8, Y=8 Top Side	156
11	↓	X=8, X=-8	156
12	↓	X=-8, Y=-8	156
13	↓	X=-8, Y=8	156
14	↓	X=0, Y=16	153
15	↓	X=16, Y=0	159
16	↓	X=0, Y=-16	153
17	Structural skin	X=-16, Y=0 Top Side	159
18	S.S. skin	X=16, Y=16 Top Side	214
19	↓	X=-16, Y=-16	214
20	S.S. skin	X=0, Y=-16 Top Side	216
21	Structural skin	X=-16, Y=16 Top Side	146
22	↓	X=16, Y=16	151
23	↓	X=16, Y=-16	151
24	↓	X=-16, Y=-16	151
25	Structural skin	X=-16, Y=16 Top Side	151
26	TG-15000 (2)	X=0, Y=0 Top Side	265
27	TG-15000	X=12, Y=12 Top Side	265
28	Cabin Wall (4)	X=12, Y=12 Top Side	276
29	↓	X=12, Y=-12	276
30	↓	X=-12, Y=-12	276
31	Cabin wall	X=-12, Y=12 Top Side	276
32	Antenna aperture cover (1)	Center Outside	69
33	Antenna flange (2)	r=5.0, $\theta=22.5$ , Inside	76
34	Antenna flange	r=5.0, $\theta=202.5$ Inside	76
35	Antenna flange (2)	r=5.0, $\theta=67.5$ Inside	71
36	Antenna flange	r=5.0, $\theta=247.5$ Inside	71
37	Circuit Board (1)	Center Bottom	225/230
38	Center element wall (2)	z=-2.0, $\theta=45$	63
39	Center element wall	z=-2.0, $\theta=225$	63
40	+X element wall (2)	z=-2.0, $\theta=45$	60
41	+X element wall	z=-2.0, $\theta=225$	59
42	+Y element wall (2)	z=-2.0, $\theta=45$	61
43	+Y element wall	z=-2.0, $\theta=225$	62
44	-X element wall (2)	z=-2.0, $\theta=45$	59
45	-X element wall	z=-2.0, $\theta=225$	60
46	-Y element wall (2)	z=-2.0, $\theta=45$	62
47	-Y element wall	z=-2.0, $\theta=225$	61
48	S.S. skin	X=16, Y=8 Top Side	218
49	S.S. skin	X=8, Y=16 Top Side	215
50	Pressure		

The locations of thermocouples on the test fixture structure and insulation are illustrated in figure 74. The 14 thermocouples located on the stainless steel top sheet were used for regulating heat input (i.e., controlled to the outer bondline temperatures) and/or verifying symmetrical heating of similar areas. The four thermocouples (T/C 28 through 31) on the bottom plate were used for controlling to a "cabin wall" temperature. The remaining 15 thermocouples on the test fixture skin/stringer panel and TG-15000 top side, and the 16 thermocouples on the antenna were used to measure thermal responses. Sketches of antenna thermocouple locations and their relative nodes in the analytical model are shown in figures 75 through 77. The antenna cover thermocouple installation is shown in figure 70.

Some of the thermocouple locations described above differ from those originally defined in the design of the test fixture (reference 1). Five thermocouples were relocated to the stainless steel surface to provide: (1) better control and check on symmetry of heat input, and (2) more thorough description of temperatures for verification of the analytical thermal model. Also, no thermocouples were located on the improvised dust cover as originally specified.

Wherever feasible, particularly on the stainless steel top skin and antenna, the thermocouple junction was formed by utilizing the surface itself. That is, the thermocouple wires were separated by about 1.6 mm (1/16 in.) and individually attached to the surface by tack-welding (stainless steel) or taping (antenna). This attachment method essentially eliminates erroneous response due to the separation of a junction from the surface.

Thermocouples on the structural skin/stringer panel, which measure the TPS inner bondline temperature, were installed during fabrication of the test fixture. The thermocouple leads were passed through holes in the stringers and skin and bonded to the outer surface (figure 78).

The leads of TG-15000 insulation thermocouples were simply twisted to form a junction and stuck into the upper surface of the batt (figure 79). One thermocouple was located in the center of the test fixture (immediately under the antenna dust cover) and the other in the center of the positive X-Y quadrant (figure 74).

The thermocouple installation on the bottom panel used for maintaining a "cabin wall" boundary temperature is shown in figure 80.

#### Thermal Environments

The Thermal Vacuum testing sequence consisted of only orbital and entry simulation. Pretest analyses indicated that no significant temperature changes occur during ascent at or inward of the outer bondline, (i.e., HRSI/SIP interface) and, therefore, that simulation of the ascent environment was unnecessary.

THERMOCOUPLE LOCATION

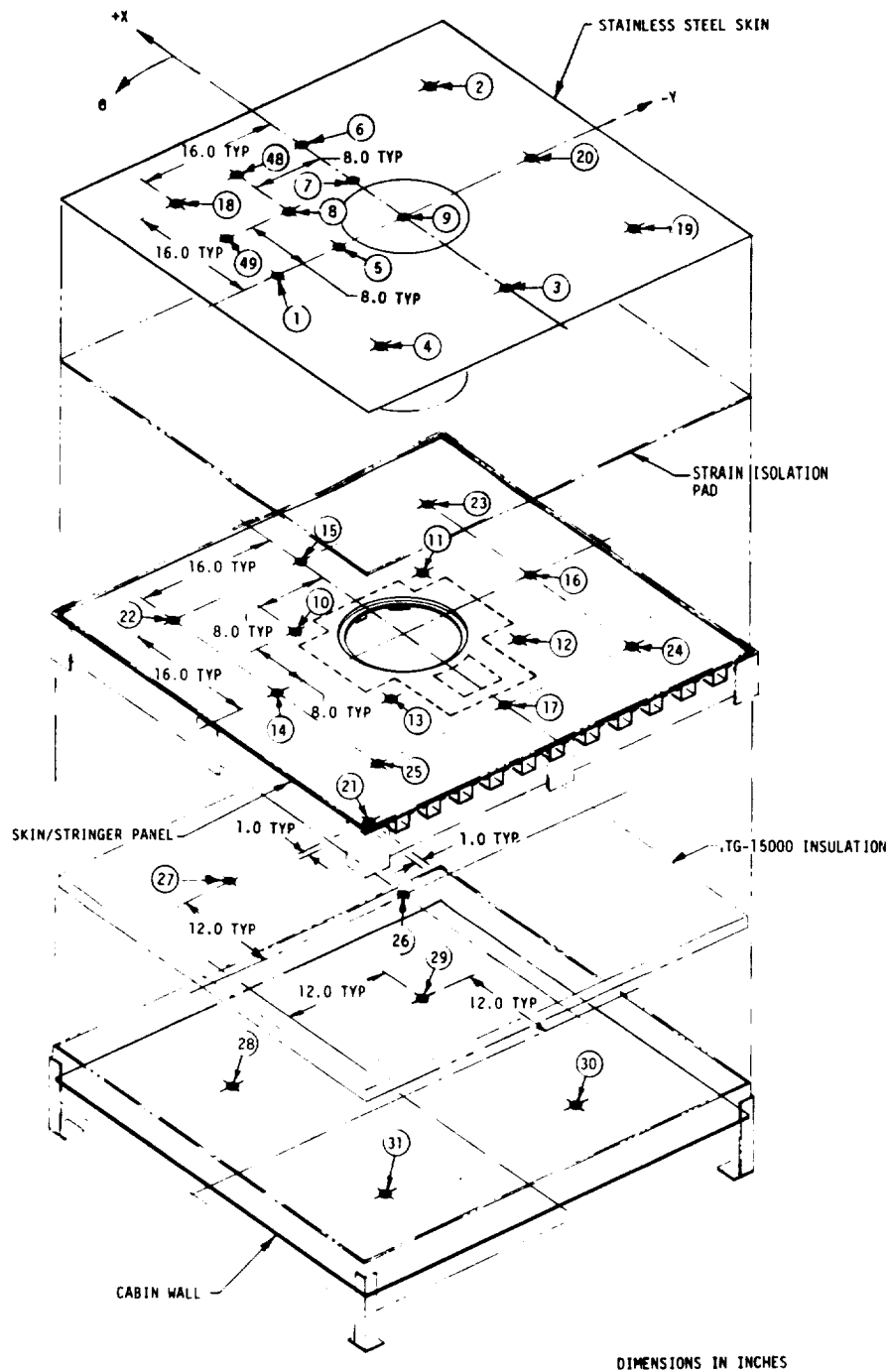


FIGURE 74 TEST FIXTURE THERMOCOUPLE LOCATIONS

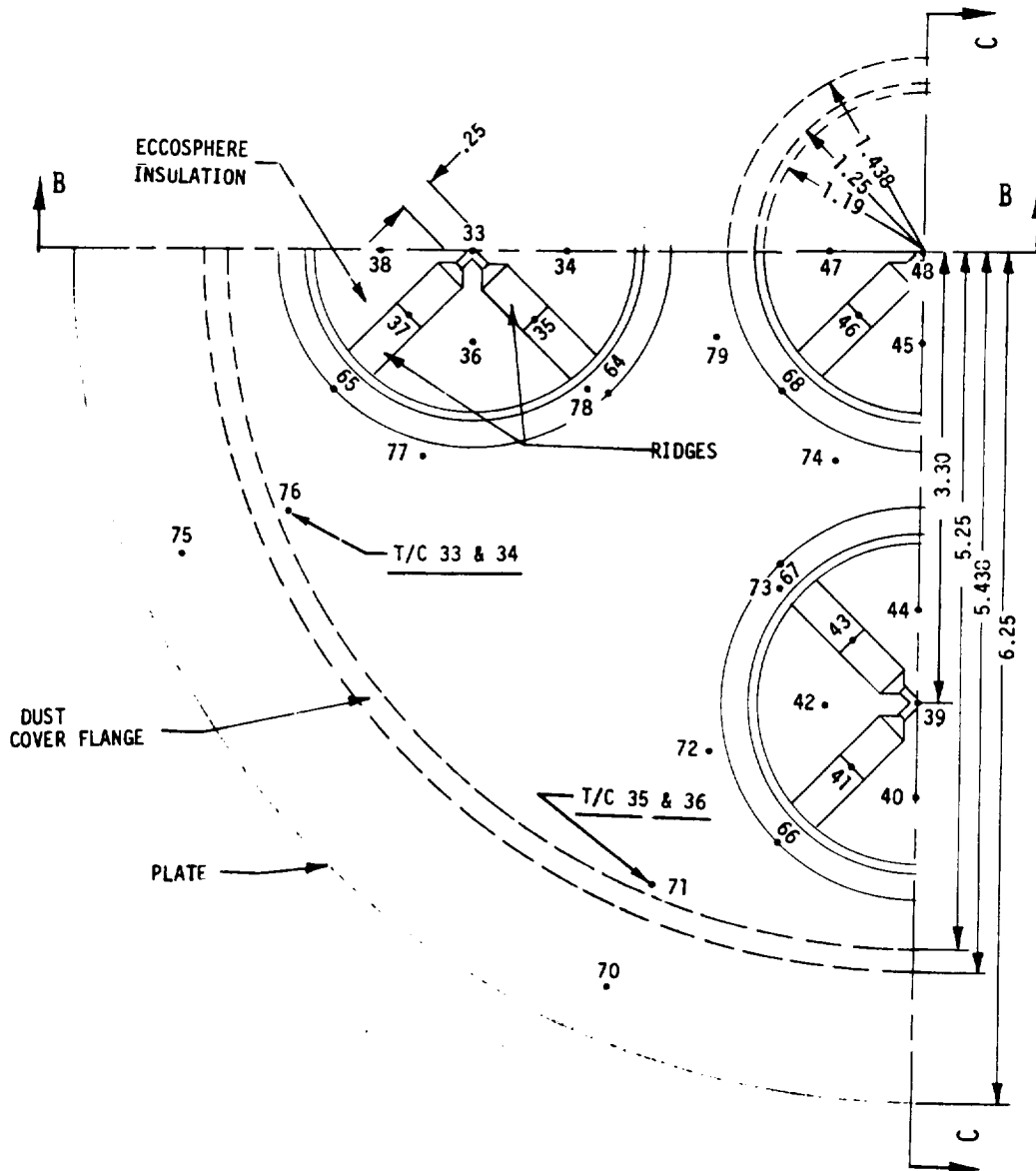


FIGURE 75 ANTENNA THERMOCOUPLE LOCATIONS AND NODAL ARRAY - TOP VIEW

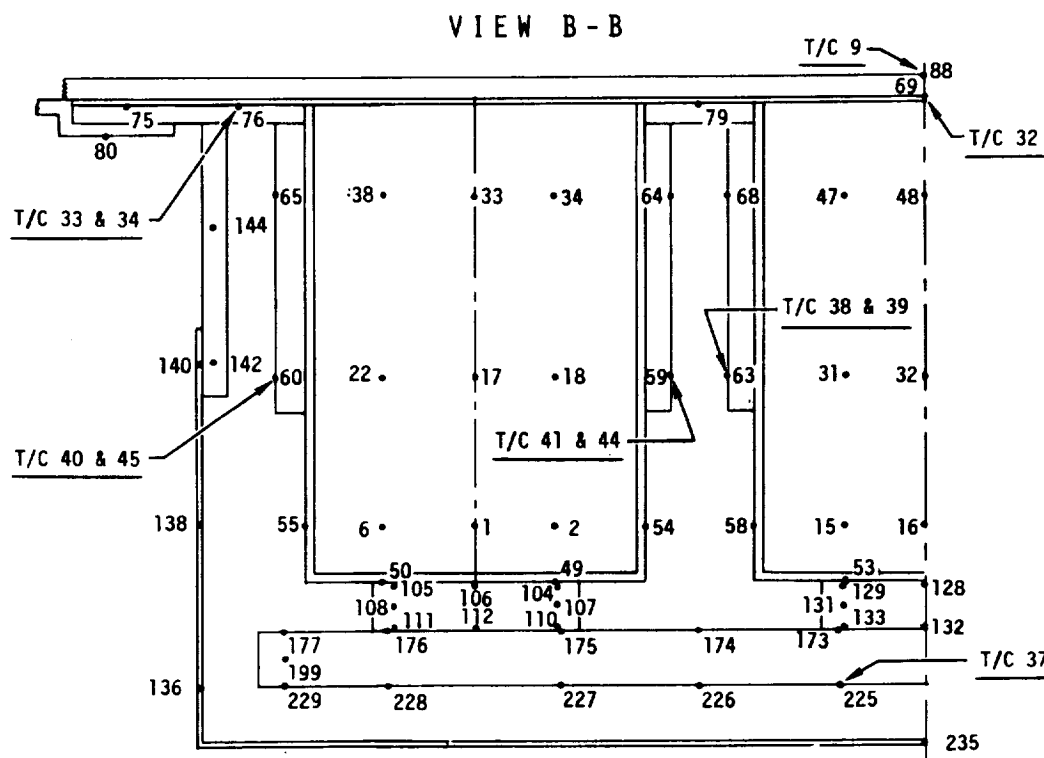


FIGURE 76 ANTENNA THERMOCOUPLE LOCATIONS AND NODAL ARRAY - SIDE VIEW B-B

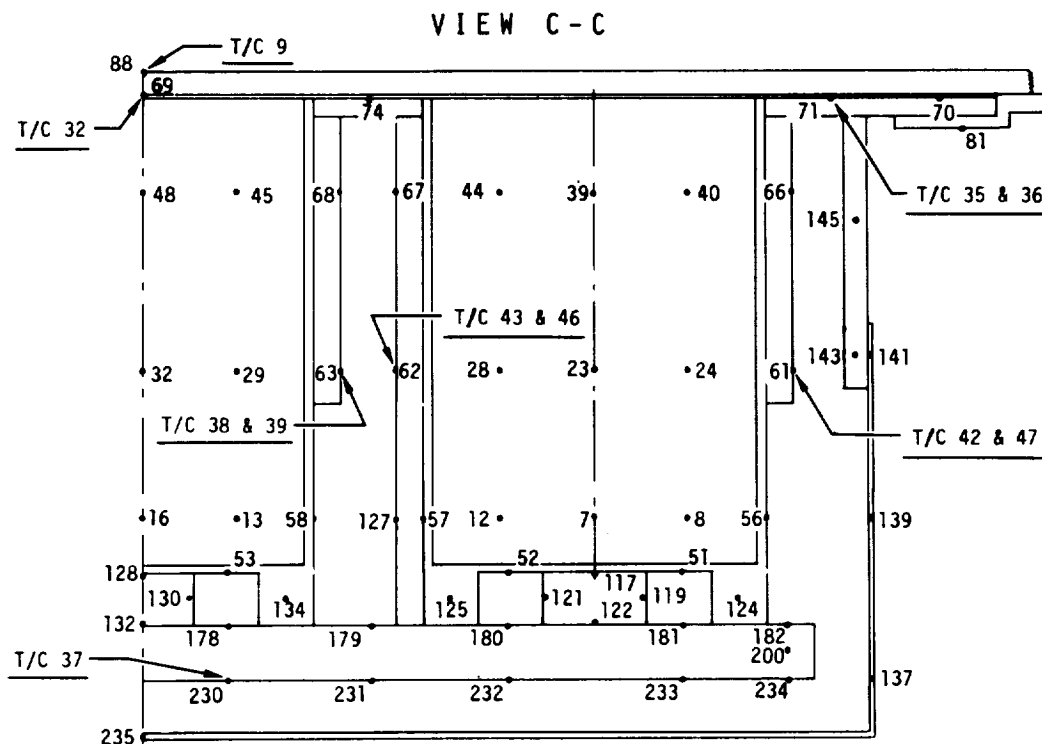


FIGURE 77 ANTENNA THERMOCOUPLE LOCATIONS AND NODAL ARRAY - SIDE VIEW C-C



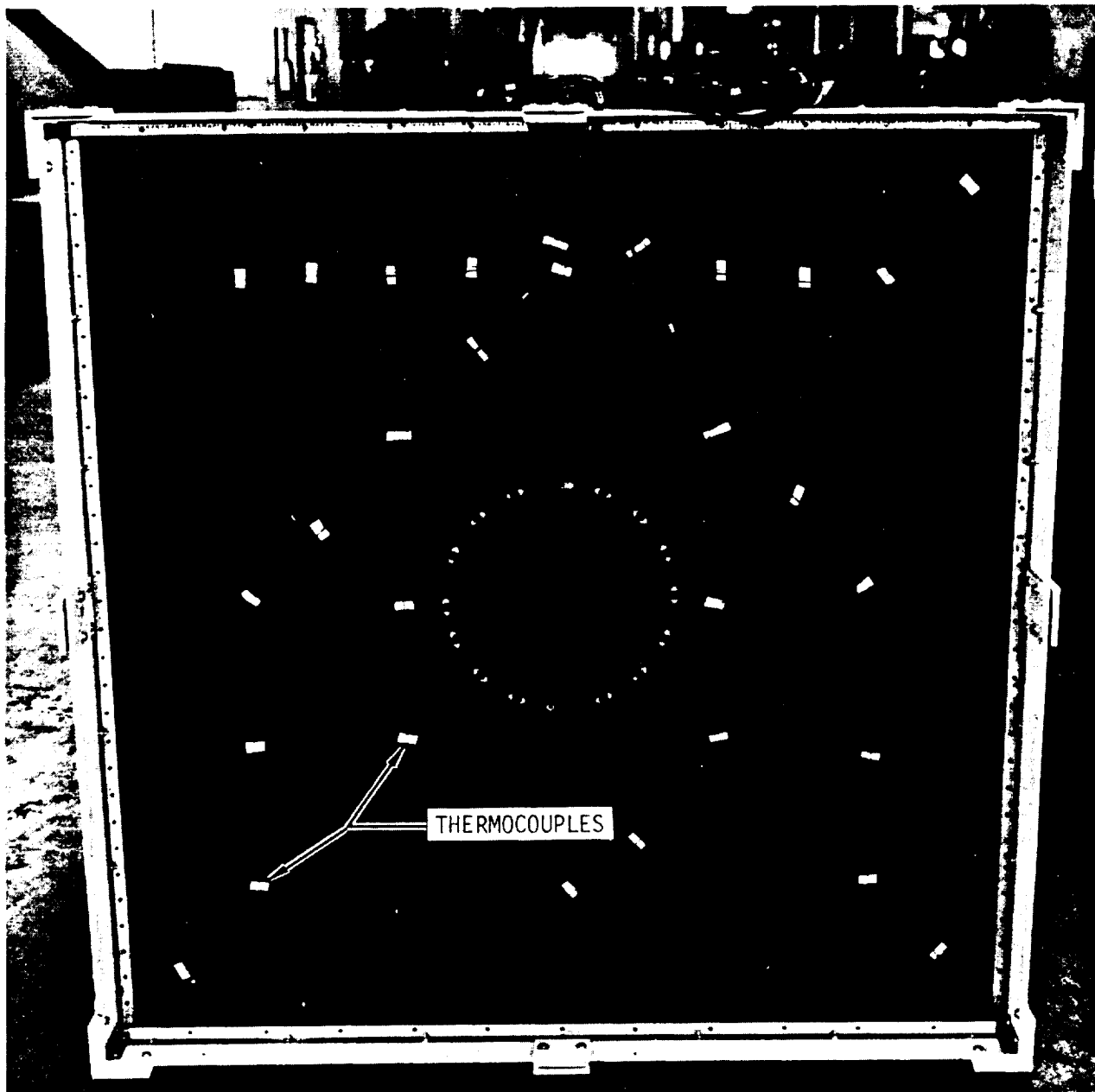


FIGURE 78 SKIN-STRINGER PANEL THERMOCOUPLE INSTALLATION

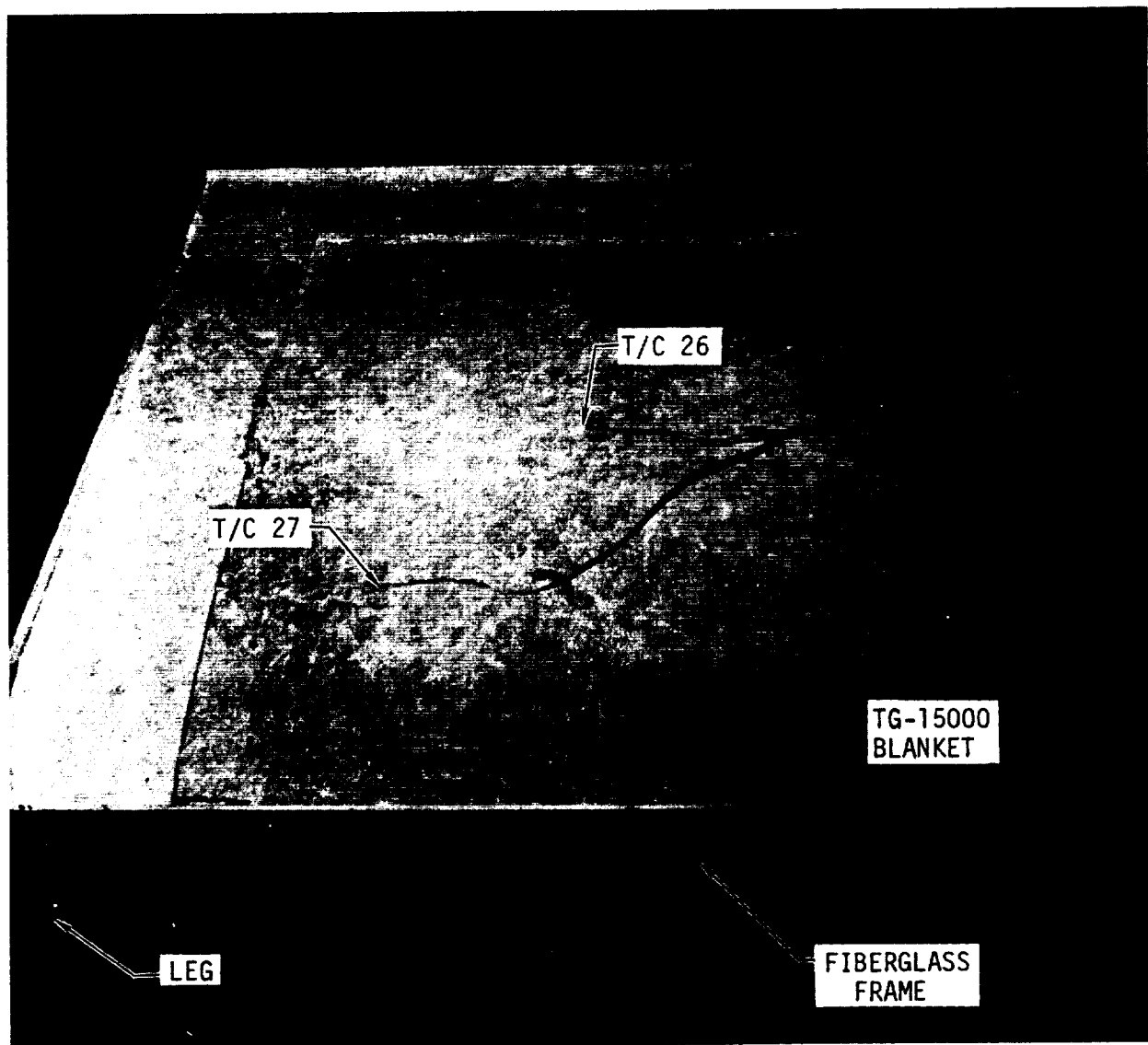


FIGURE 79 TG-15000 INSULATION THERMOCOUPLE INSTALLATION

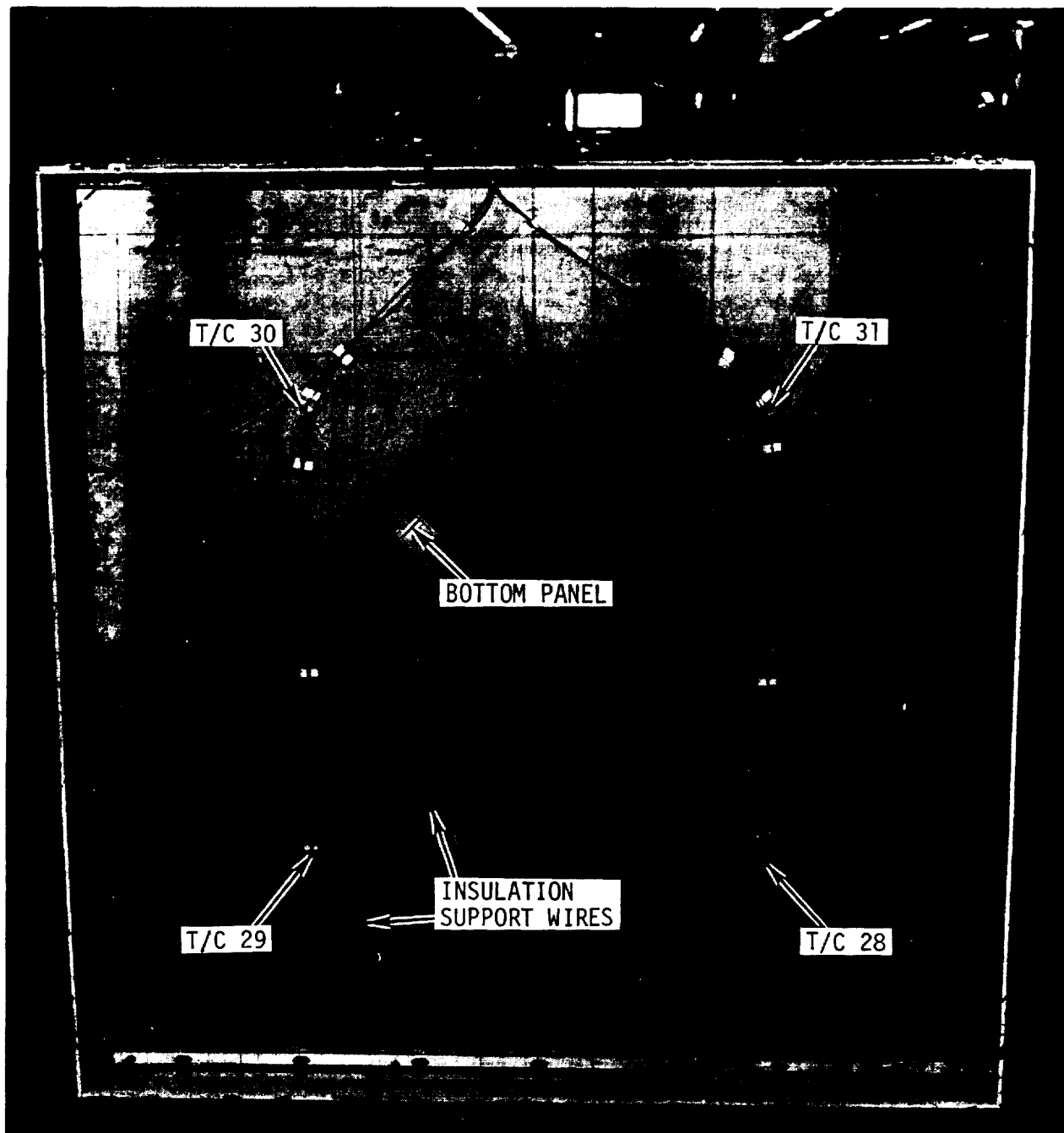


FIGURE 80 CABIN WALL PANEL THERMOCOUPLE INSTALLATION

Two environments were simulated: one for a hot orbit condition with subsequent entry, and the second for a cold orbit and entry. The hot orbit represents a condition of continuous solar illumination of the TPS over the antenna, and the cold orbit the contrary. The two extreme orbital conditions were considered since they provide a set of limiting environments for checking the analytical thermal model.

Temperature. - Analyses of the orbital conditions considered for these tests revealed that duplication of orbital temperature histories would necessitate test times of excessive duration. Thus, orbital temperature simulation (figure 81) consisted of achieving the computed outer-bondline equilibrium temperature within a reasonable time which would not thermally shock the test fixture and antenna. This temperature was then maintained sufficiently long to stabilize substructural and antenna temperatures and provide a roughly steady state condition prior to initiating entry. The simulation of the two orbital conditions primarily provided different initial temperatures and as shown subsequently, slightly different temperature profiles for check-out of the analytical thermal model.

The thermal model (figure 82) developed in the first part of this contract (reference 1) was modified to update the HRSI thickness to 4.57 cm (1.8 in.) and

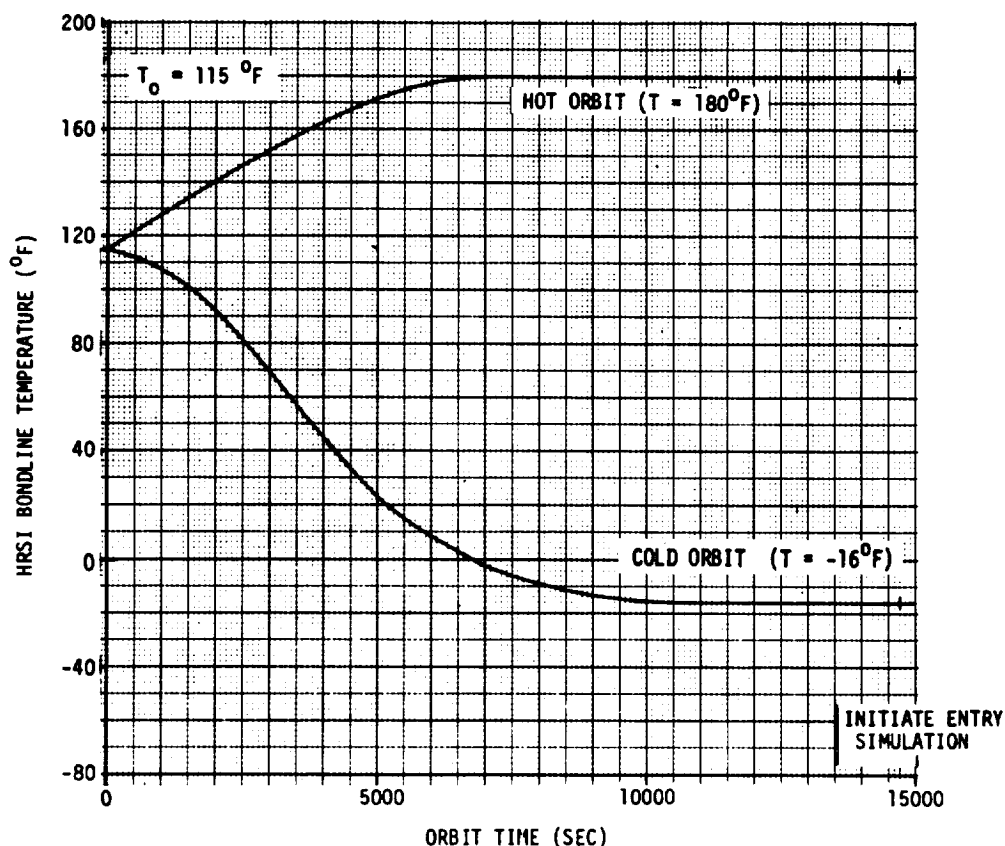


FIGURE 81 HRSI BONDLINE TEMPERATURES FOR ORBITAL REPRESENTATION

the outer bondline (HRSI/SIP) thermal response was then determined for the antenna region using a current entry heating history (figure 83) supplied by NASA-JSC. This heat flux history is for entry from the hot orbit condition. The TPS surface temperature history in figure 83 is that computed at node location 314 (figure 82), i.e., for the HRSI surface at an outboard location of  $X = Y = 40.6$  cm (16 in.). The curve, identified by the symbol for total heat flux, is the amount which is actually transferred into the model allowing for surface reradiation.

The resulting thermal responses at the outer bondline for entry from the two orbital conditions are illustrated in figure 84. As indicated, a maximum temperature gradient (difference) of over 28 K (50°F) may occur over the bondline (or the test fixture stainless steel top skin).

Pressure. - The minimum attainable vacuum chamber pressure of about 1.33 mPa ( $10^{-5}$  torr) was considered adequate for representing orbital conditions. The pressure history, supplied by NASA, at the lower S-band Quad antenna location during the Space Shuttle Orbiter entry is indicated by the solid curve in figure 85. Duplication of this environmental parameter is necessary to account for the pressure-dependent heat transfer through such materials as the SIP and TG-15000. However, since this dependence is on pressure order of magnitude, a history defined by the dashed curve was considered an adequate representation for test purposes, besides being easier to maintain.

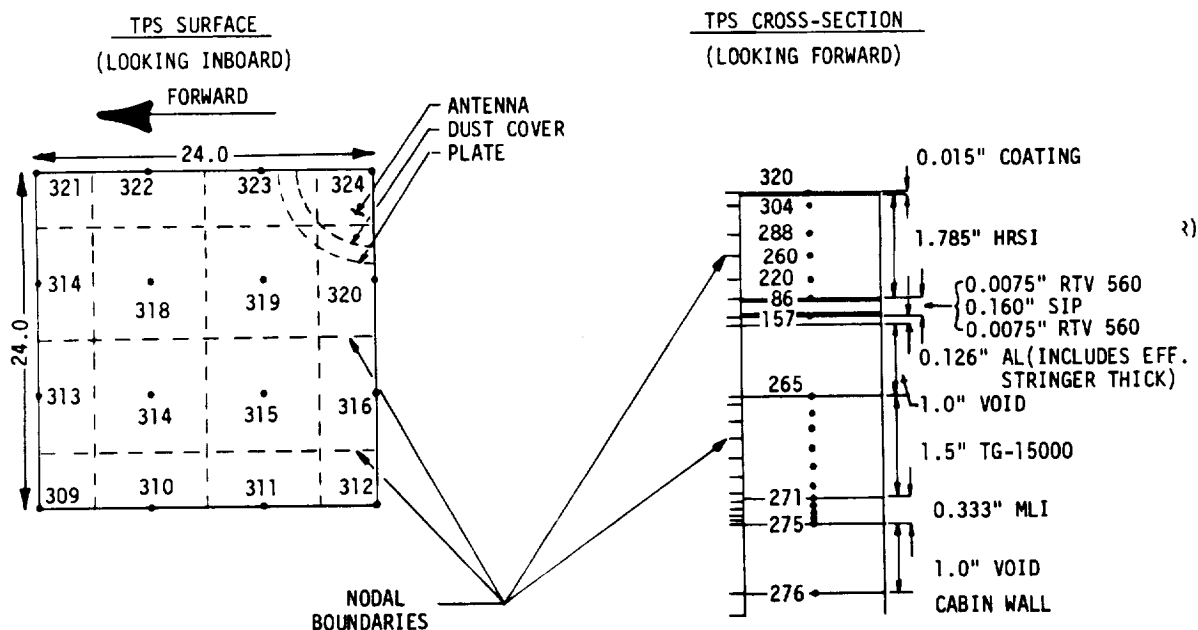


FIGURE 82 THERMAL MODEL NODAL DISTRIBUTION - TPS/STRUCTURE/INSULATION

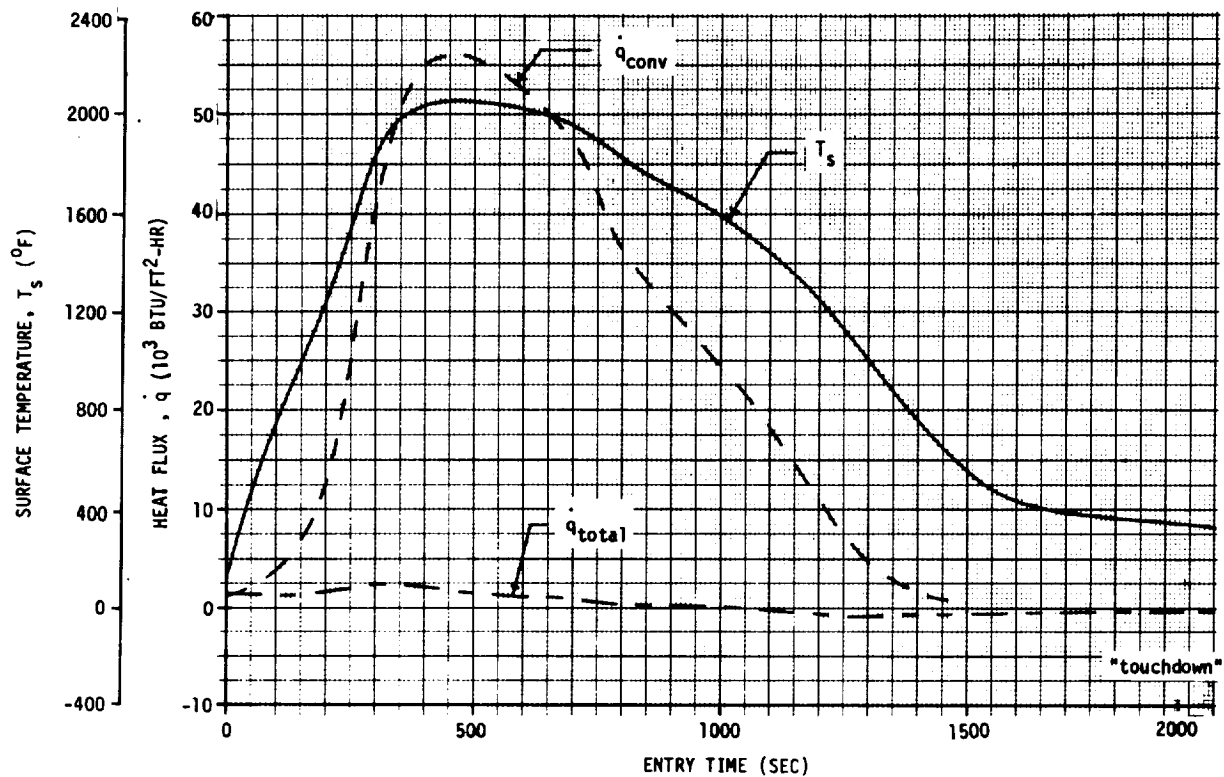


FIGURE 83 ENTRY TPS SURFACE HEATING ENVIRONMENT - HOT ORBIT

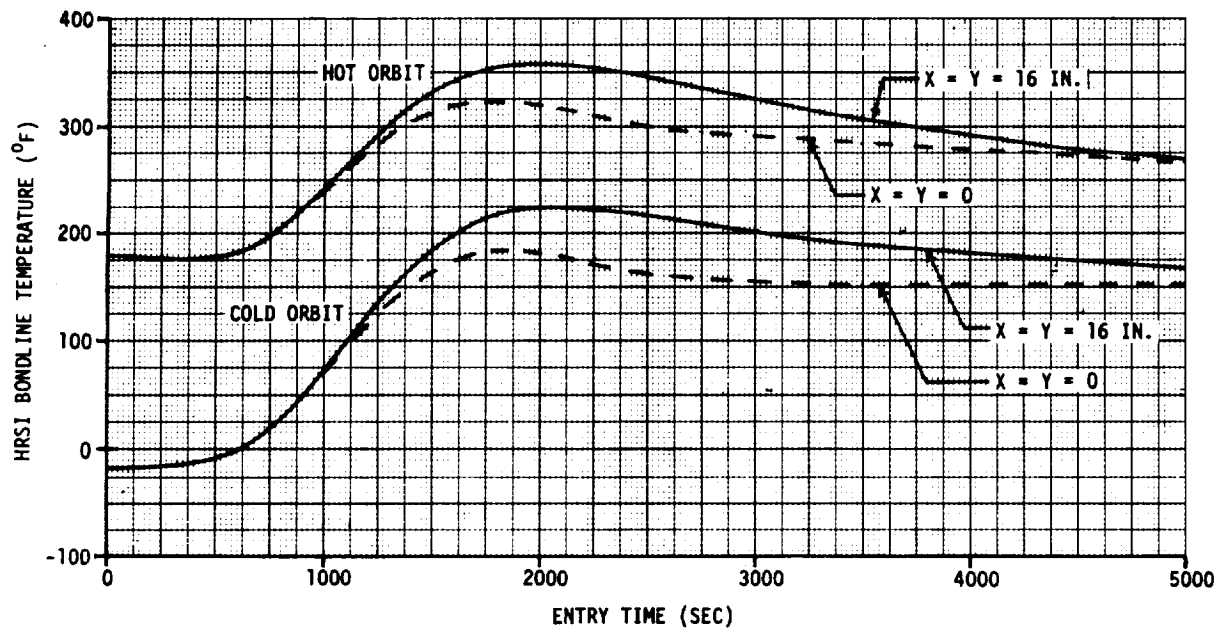


FIGURE 84 ENTRY HRSI BONDLINE THERMAL RESPONSE - HOT AND COLD ORBITS

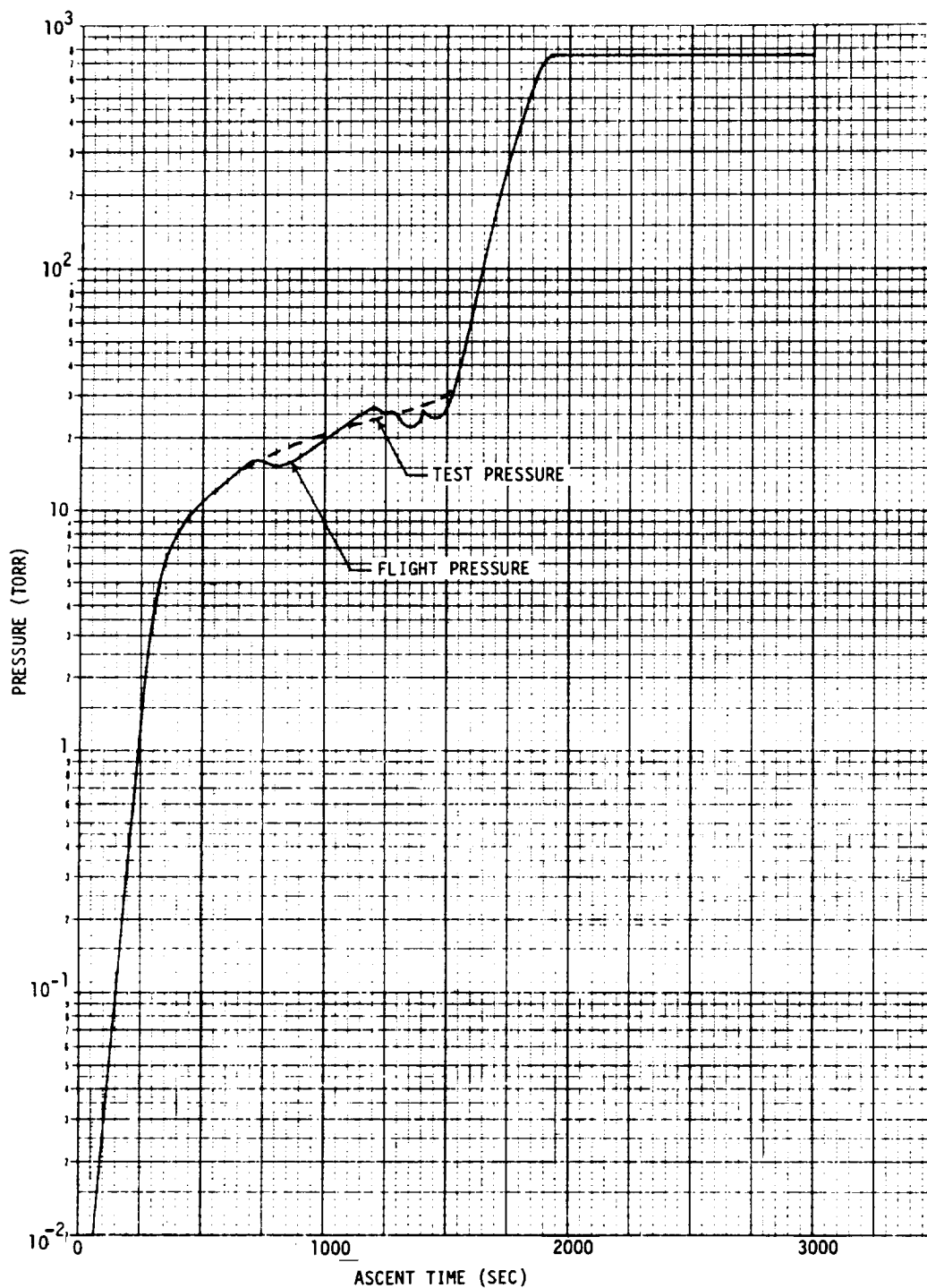


FIGURE 85 ENTRY PRESSURE ENVIRONMENT

### Test Facility

The Thermal Vacuum tests were conducted in Space Chamber E located in Building 33 of the NASA-JSC Thermal Vacuum Laboratory. Quartz-lamps and the vacuum chamber liquid-nitrogen-cooled shroud were used to provide the required heating/cooling environments. A data acquisition system was utilized to store data for post test processing and simultaneously display thermocouple temperatures for thermal environment control.

Temperature simulation equipment. - A sketch illustrating the test setup is shown in figure 86. Photos of the various items depicted in the sketch and/or used for environmental simulation are shown in figures 87 through 91. An aluminum plate was provided inside the chamber (figures 87 and 88) to support the test fixture under the radiant heat source. For thermal isolation, Teflon pads, approximately 0.64 cm (0.25 in.) thick, were placed under the test fixture legs.

Besides acting as a platform for the test fixture, the support plate was also used as a radiation source/sink to maintain the cabin wall boundary temperature at the bottom panel of the test fixture. Strip heaters were fastened to its lower surface (figure 89) for temperature control, and both of its surfaces were coated with a high emissivity paint to promote radiative heat transfer with the bottom panel (cabin wall) of the test fixture and the liquid nitrogen-cooled shroud. Narrow blankets of Mylar (figure 89) were located under the support plate to reduce the radiation view factor to the shroud and keep its cooling effect from overpowering the heating capabilities of the strip heaters.

A grid of Mylar curtains (figures 86 and 89) was used to provide individually controlled areas of heating over the test fixture surface. Each grid area was roughly 40.5 cm (16 in.) square and encompassed the heat input from a bank of three parallel Quartz lamps. Space between the lamps permitted radiation to the chamber shroud for cooling purposes or balancing the heat input from the lamps, as required.

The lamp filaments were also 46.6 cm (16 in.) long, but the lamp casing and mounts required a total length of about 51 cm (20 in.). This caused the network of lamps to protrude beyond the curtains (figure 89). However, a radiometer survey indicated no serious influence on the heating distributions in the affected grids. This survey also revealed an insignificant increase of heat transfer along the grid edges, particularly in the corners.

Heat output of the lamps was regulated using the rheostat-type controllers shown in figure 90. Similar controllers, also shown in figure 90, were used for the strip heaters attached to the bottom plate of the test fixture support. The data system console displayed temperature data required for varying the individual controllers.



A 18 ○	B 6 ○	C 2 ○
D 1 ○	E 9 ○	D' (20) ○
A' (4) ○	B' (17) ○	C' (19) ○

TEMPERATURE CONTROL REGIONS

NOTES

- LETTERS IDENTIFY AREAS HEATED BY LAMPS ON SAME CONTROLLER (CIRCUIT)
  - LAMP BANKS IN CIRCUITS AA' AND BB' WIRED IN PARALLEL
  - LAMP BANKS IN CIRCUITS CC' AND DD' WIRED IN SERIES
- NUMBERS IDENTIFY SURFACE T/C
  - NOT IN PARENTHESIS USED FOR CONTROL
  - IN PARENTHESIS USED FOR CHECK OF SYMMETRICAL HEATING

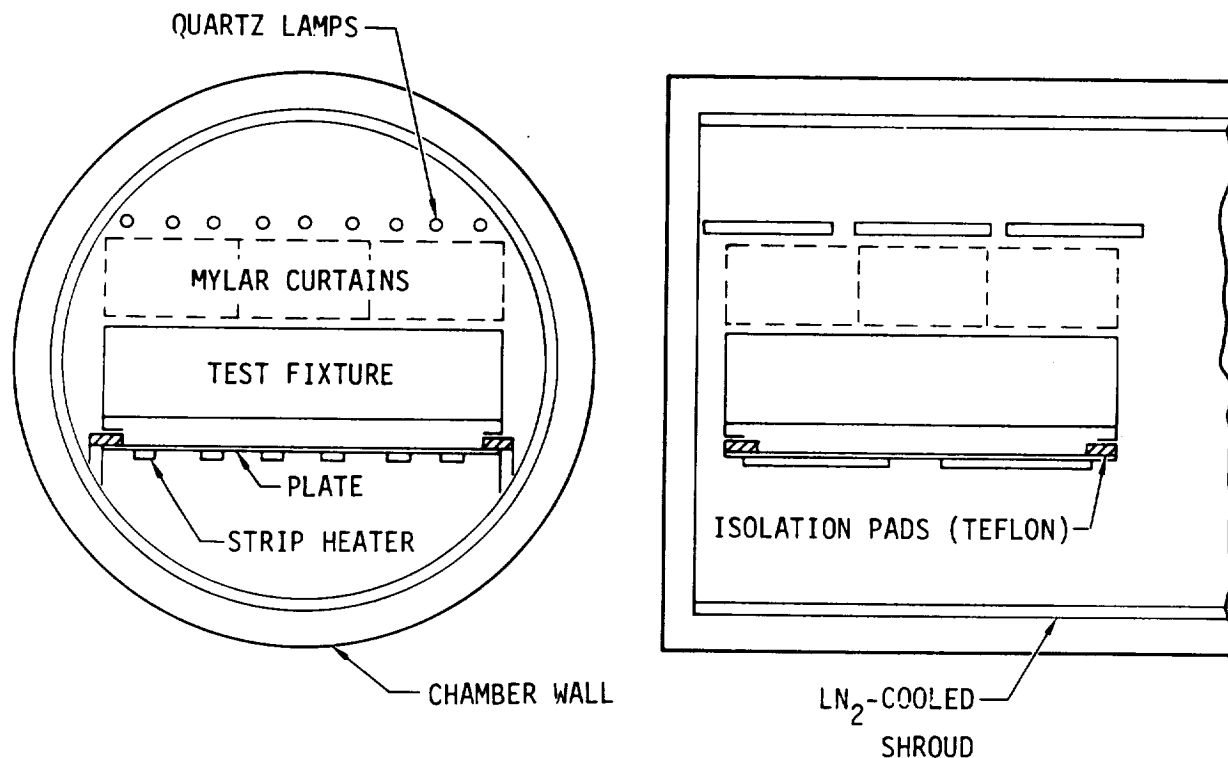
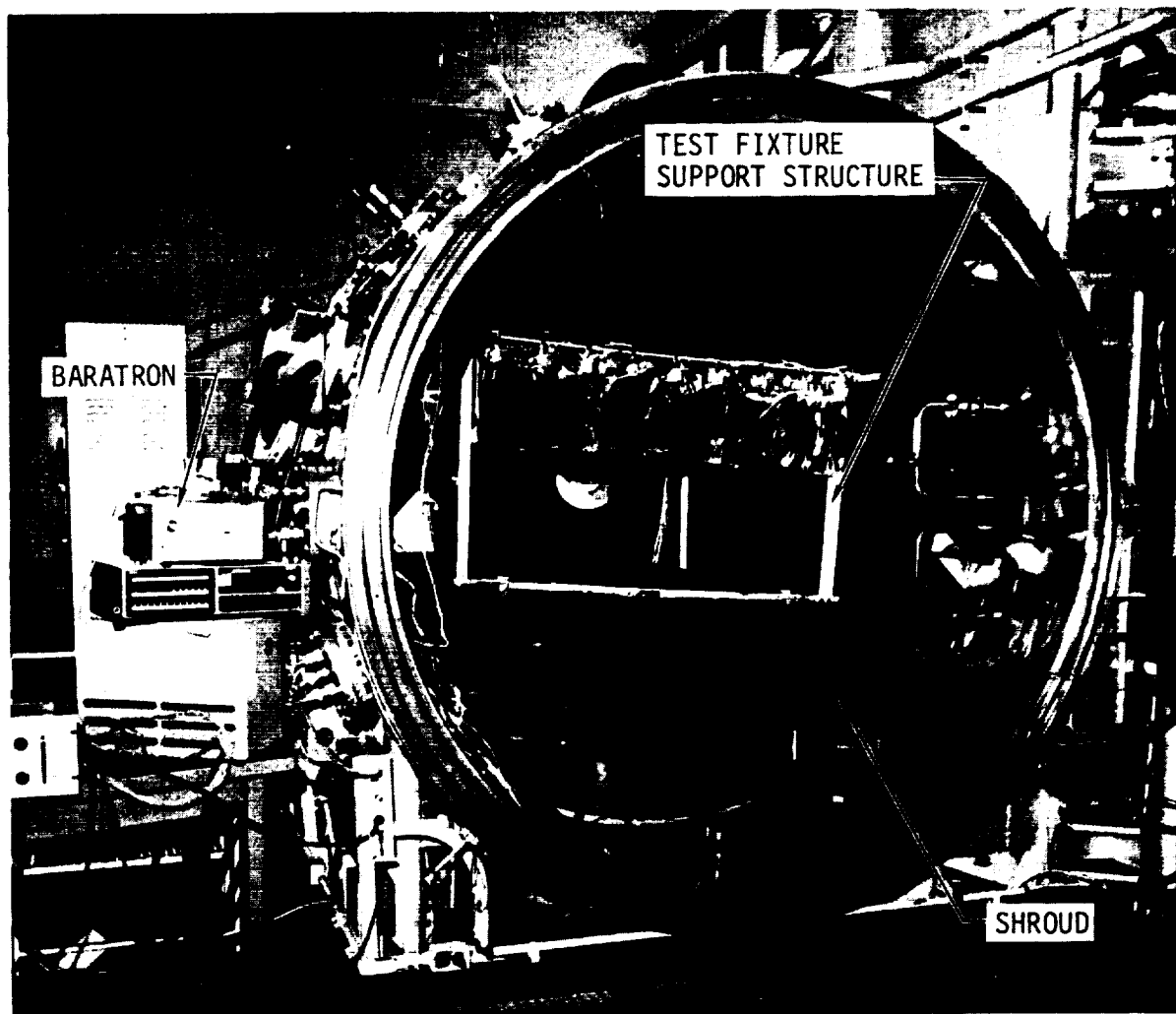


FIGURE 86 THERMAL VACUUM TEST SETUP



**FIGURE 87 NASA-JSC SPACE CHAMBER E WITH TEST FIXTURE SUPPORT STRUCTURE**

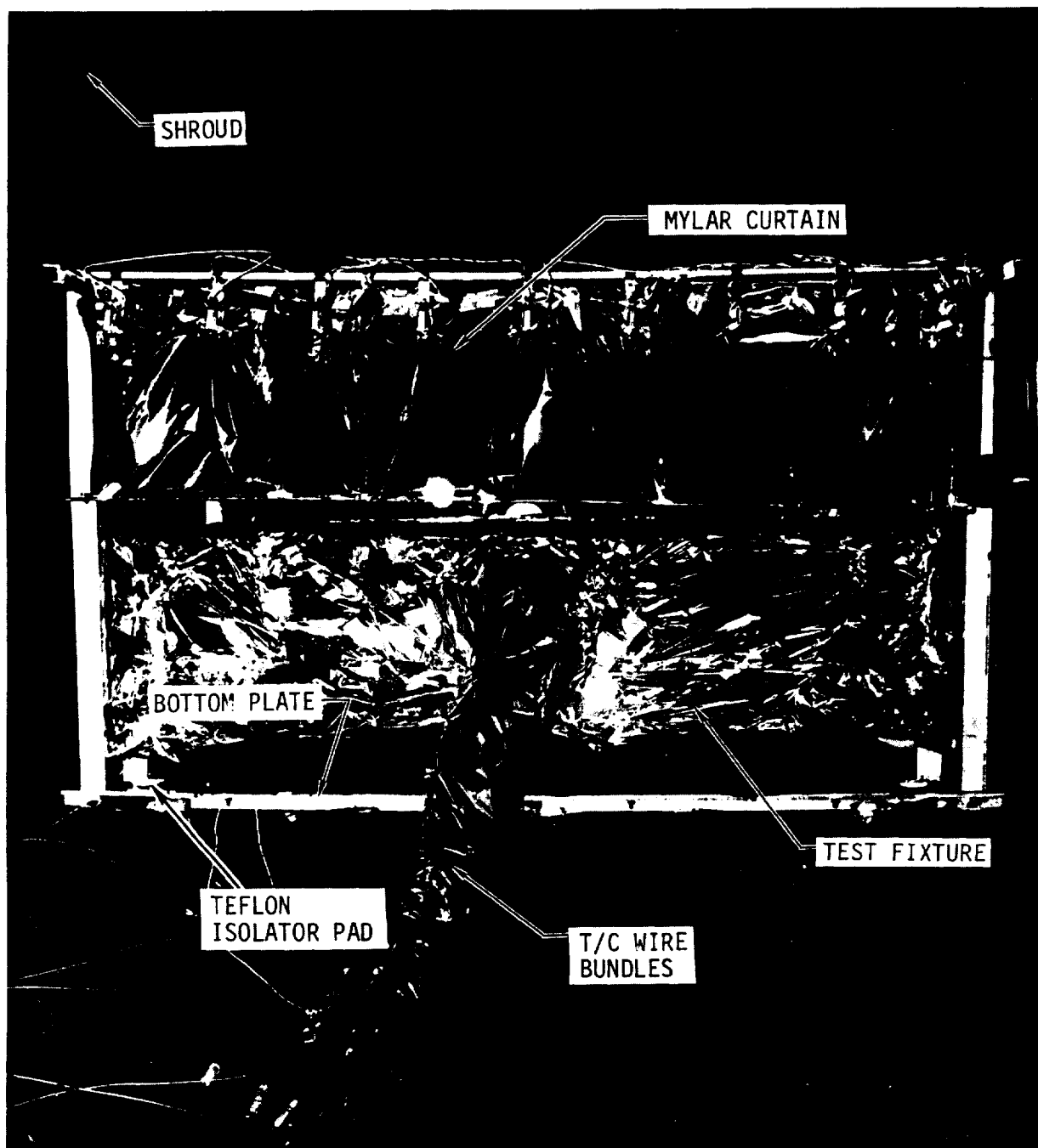


FIGURE 88 THERMAL VACUUM TEST INSTALLATION

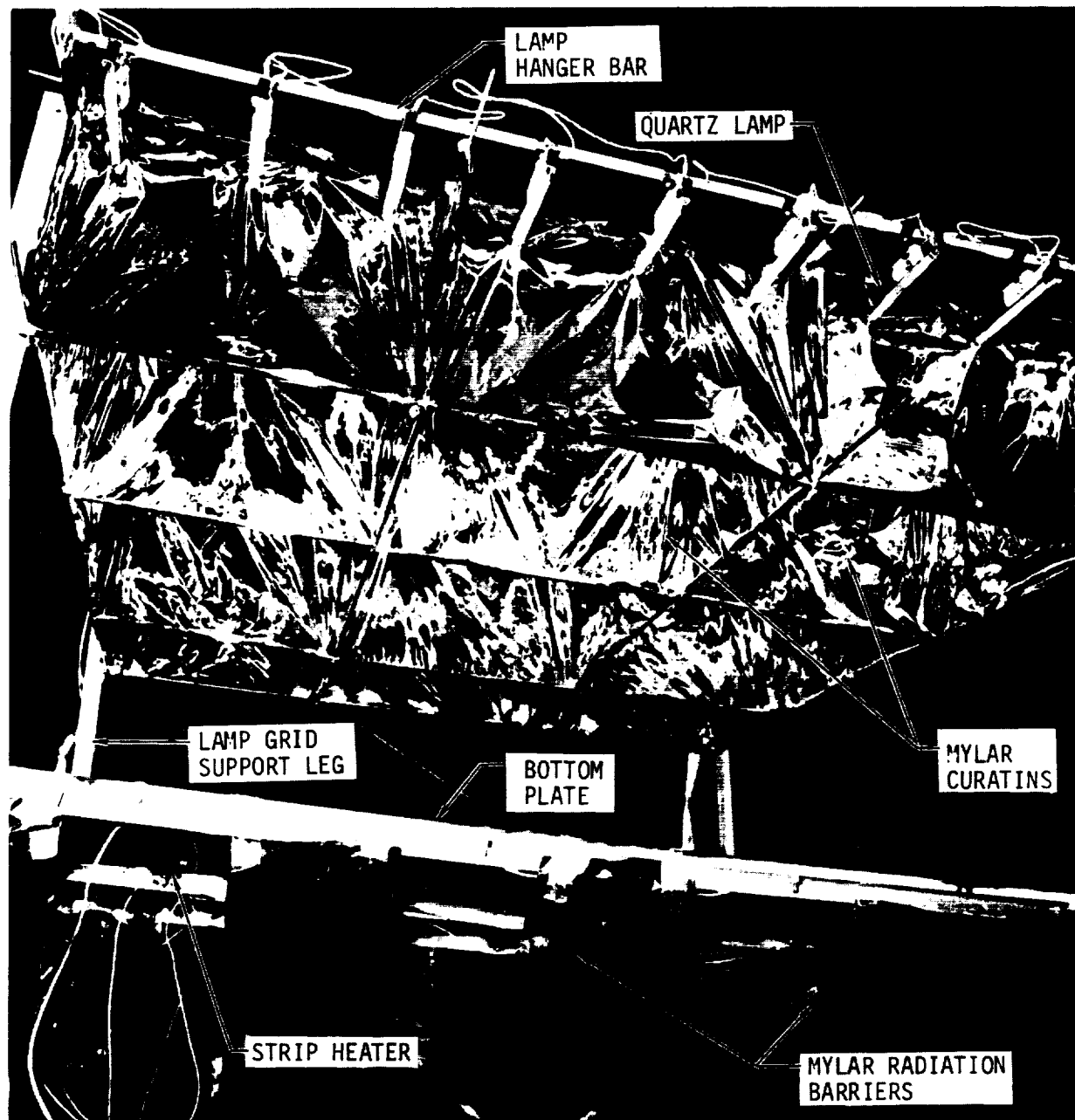


FIGURE 89 THERMAL ENVIRONMENT CONTROL CONFIGURATION

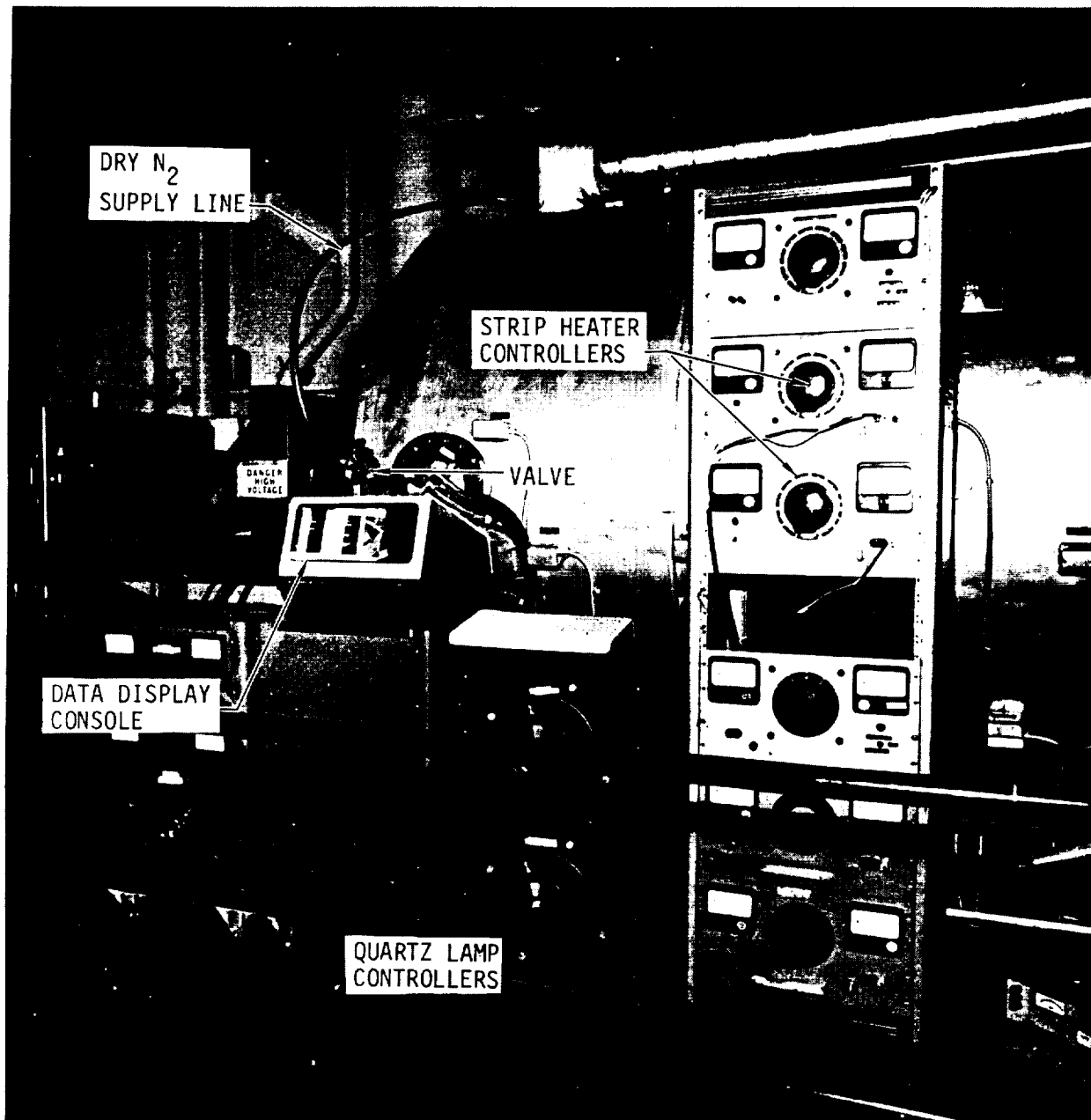
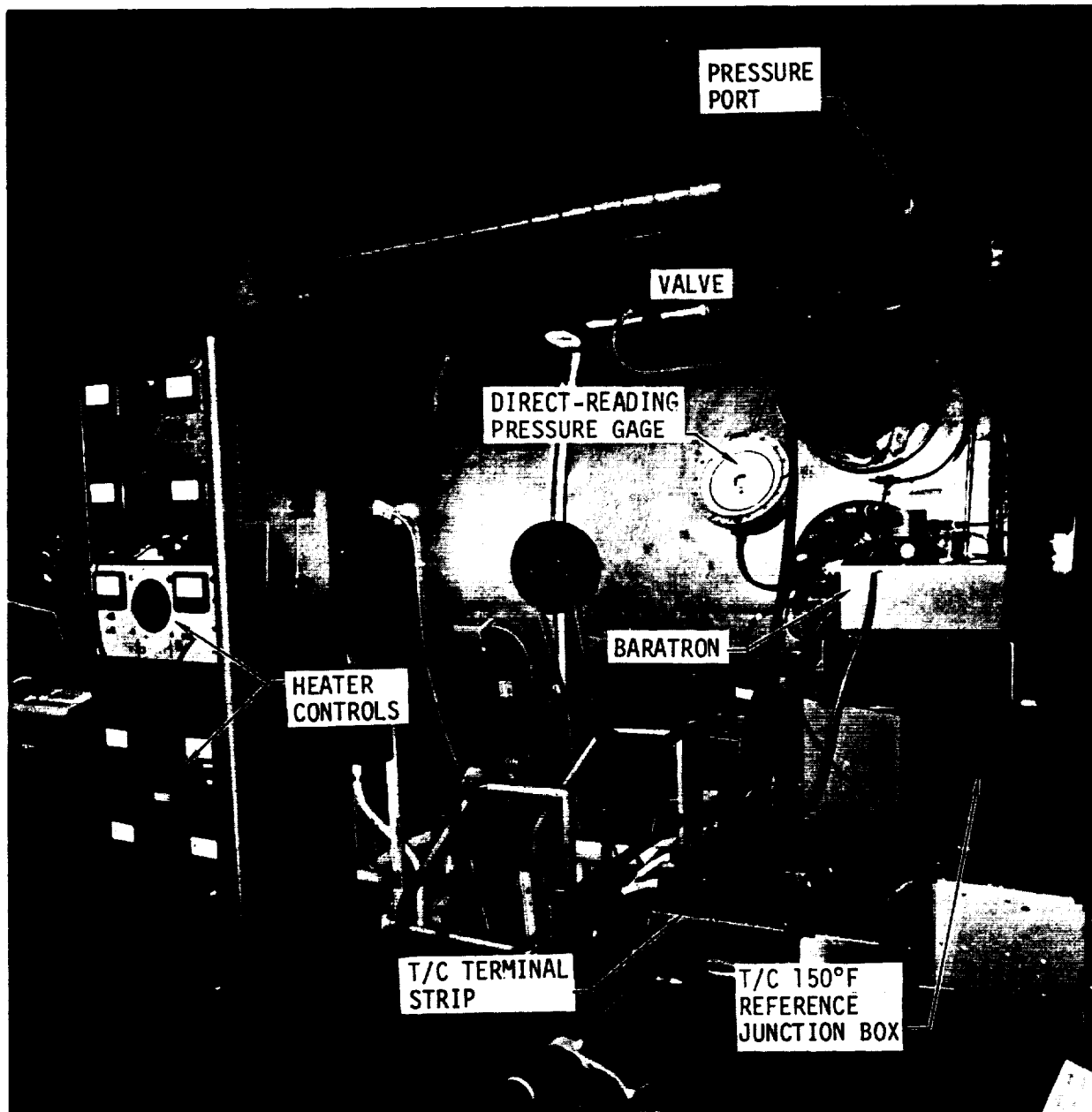


FIGURE 90 HEATER CONTROL UNITS



**FIGURE 91 ENVIRONMENT CONTROL AND DATA ACQUISITION SYSTEMS**

Adequate control for the nine grid openings was provided using only five controllers. Because of the symmetry of both test fixture construction and bondline temperature distributions, two lamp banks over areas having the same temperature were wired to the same controller. Lamp banks on the same controller are identified in figure 86 by the use of the same letter, and prime, in the grid schematic. As noted in this figure, the lamp banks in circuit AA' and BB' were wired in parallel, and those in CC' and DD' in series. As will be discussed later, the type of circuit for connecting the two lamp banks appears to have influenced heating symmetry. The lamp bank in the center grid (circuit E) was individually controlled.

Pressure simulation equipment. - For the thermal vacuum tests, active pressure control was required during entry simulation only. Control was achieved by manually-operated valves and reading a Wallace and Tiernan, 0 to 133 kPa (0 to 1000 torr absolute) gage. Chamber pressure was recorded on the data system from a baratron pressure transducer with a 0 to 13 kPa (0 to 100 torr) head. The chamber was repressurized with dry nitrogen gas and shop air (figures 90 and 91). The dry nitrogen was used to minimize or eliminate possible condensation on the test fixture and chamber shroud.

Data acquisition system. - A Hewlett-Packard data system was used to record the output from the 49 thermocouples located on the test fixture and antenna and from the baratron pressure transducer. The thermocouple outputs were converted to temperatures (in °F) by the data system and along with the baratron output, stored on magnetic tape for post test processing (tabulation and plotting). Simultaneously, 40 selected data channels (both control and response thermocouples temperature data) were displayed on a console located by the heater controls.

#### Test Procedure

The Thermal Vacuum tests consisted of simulating the thermal environments (temperature and pressure) experienced by the TPS substrate and antenna by regulating the boundary temperature and ambient pressure conditions of the test fixture. Calculated temperature histories considered representative of the two extreme orbital environments and subsequent entry were used for these conditions. The TPS substrate and the antenna thermal responses were measured and recorded for comparison with the predicted values.

The general flow of test operations is illustrated in figure 92. The chamber pressure was controlled to represent the orbital condition and the time-dependent variation during entry. Heat input to the test fixture was provided by individual banks of Quartz lamps radiating through a grid of Mylar curtains to the top surface of the test fixture, and strip heaters controlling the temperature of the support plate for radiation to the test fixture bottom surface (i.e., cabin wall boundary).

Thermal control. - All temperature control was accomplished by manual regulation of rheostat-type heaters to control the heat transfer at the top and bottom surfaces of the test fixture.

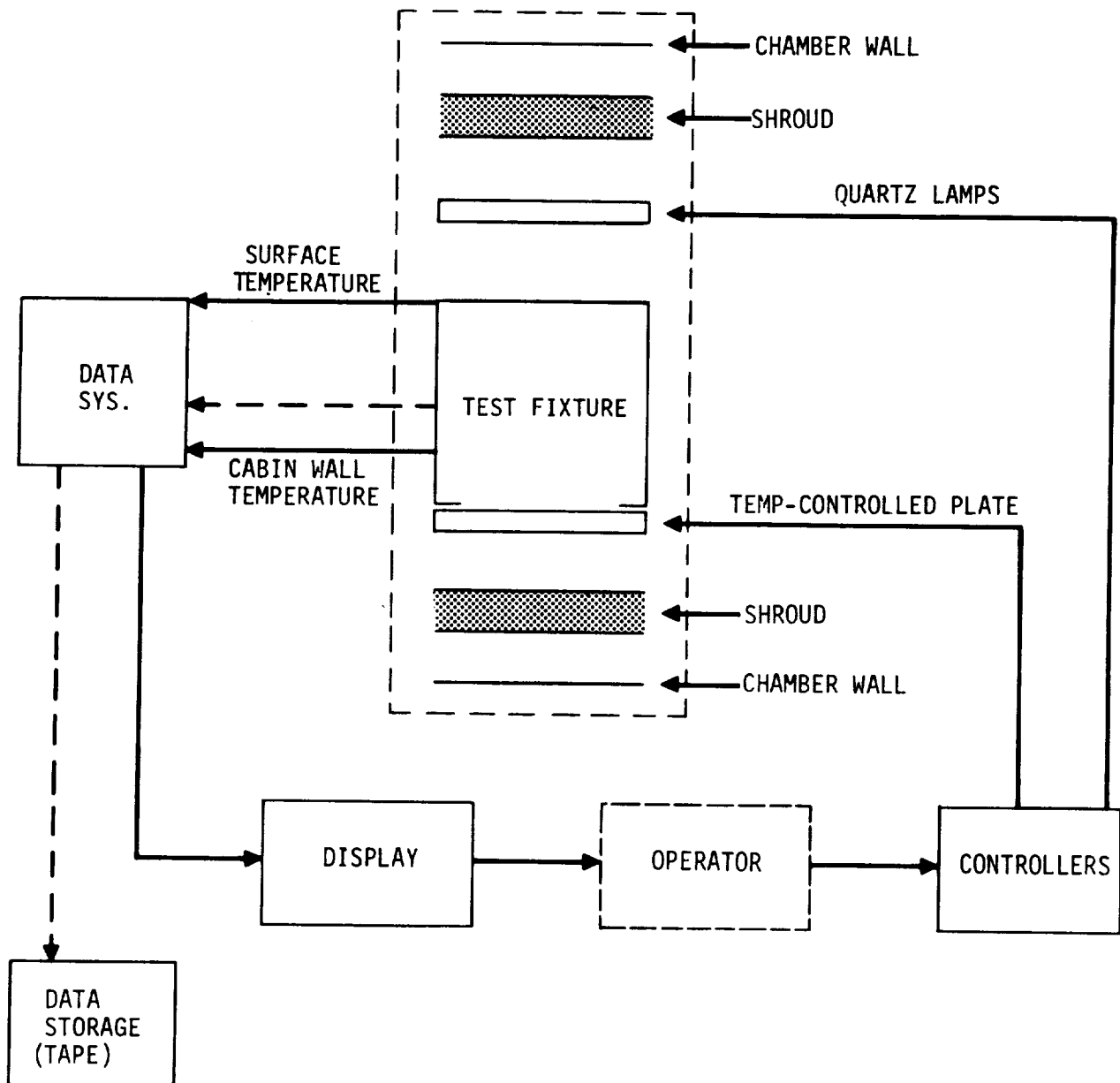


FIGURE 92 ENVIRONMENTAL CONTROL SCHEMATIC



Temperatures over the test fixture top surface (i.e., stainless steel top skin) were obtained by adjusting the output of a control unit until the measurement of the respective "control" thermocouple (T/C 1, 2, 6, 9 or 18), matched the desired value. These thermocouples (figures 74 and 86) along with four others (T/C 3, 4, 19 and 20) were located in the center of a skin area under each lamp/curtain grid. The heating of two symmetric areas was controlled to only one surface temperature to minimize the number of control units. The four non-control thermocouples (referred to as "companions" (e.g., T/C 20 is a companion of T/C 1)) were used for the purpose of checking the temperature symmetry of uncontrolled areas.

The remaining top skin thermocouples (T/C 5, 7, 8, 48 and 49) played a relatively minor role in thermal control. Along with four of the control thermocouples (T/C 1, 6, 9 and 18) they formed a three-by-three matrix of measurement points to match the nine innermost computation (node) points of the outer TPS bondline in the analytical model.

The four thermocouples (T/C 28 through 31) on the bottom panel of the test fixture were used with two controllers for the strip heaters on the bottom plate to maintain the panel at a constant "cabin wall" temperature of about 307 K (92°F) for an entire test.

Except for T/C 48 and 49, temperatures measured by all of the above thermocouples were displayed on a data system console located near the heater control units. During the test, the displayed temperatures were monitored for any ambiguities, especially significant deviations between control and companion thermocouples. The data display was also used to monitor substructural and antenna temperatures. These temperatures were used to ascertain stabilized conditions and adequate test duration.

Pressure control. - The pressure was controlled by manually operated valves. Specific control procedures for orbit and entry simulation are discussed in the following sections.

Pretest. - Prior to testing, the top half of the test fixture (figure 74) was removed and all interior and bottom panel thermocouples checked for response, location and identification. The top half was then replaced and the fixture sides wrapped with an insulation blanket. This blanket, consisting of about 8 to 10 folds of Mylar foil, was on the average about 2.54 cm (1.0 in.) thick. The blanket was lapped over the fiberglass edge structure of the test fixture, leaving only the stainless steel top skin directly exposed. The thermocouples on the top skin were then checked for response, location and identification.

After the thermocouple checks, the test fixture was placed on the bottom plate of the support structure inside the chamber (figure 88). Alignment of the test fixture with the Quartz-lamp/Mylar-curtain grid was checked to ensure balance of the top surface areas under lamp banks on the same controller.

The chamber was then closed and pumped down, and the fixture was preconditioned to achieve stabilized temperatures of about 319 K (115°F) over the top surface and 307 K (92°F) on the bottom panel. These temperatures were maintained until a steady-state condition was approximated throughout the test fixture before initiating the test.

Orbit temperature. - From the stabilized initial condition mentioned above, temperatures of the top test fixture surface were controlled to one of the temperature histories shown in figure 81. The hot orbit test was performed first.

The outer bondline orbital-equilibrium temperature was maintained until the various substrate and antenna temperatures as observed on the data system console reached an approximately stabilized condition. When the stable condition was achieved, entry simulation was initiated. During the entire orbital simulation, chamber minimum pressure was maintained. It was monitored periodically using an ion pressure gage.

Entry temperature. - The temperatures of the top surface were controlled to the appropriate temperature histories shown in figures 93 and 94 for entry after either the hot or cold orbit simulation, respectively. These figures also show variations over the test fixture surface computed using the analytical thermal model and discussed in the Thermal Environment section (figure 84). The solid curves identify both the control and companion thermocouple temperature histories. The dashed curves indicate the computed response temperatures at other surface thermocouple locations.

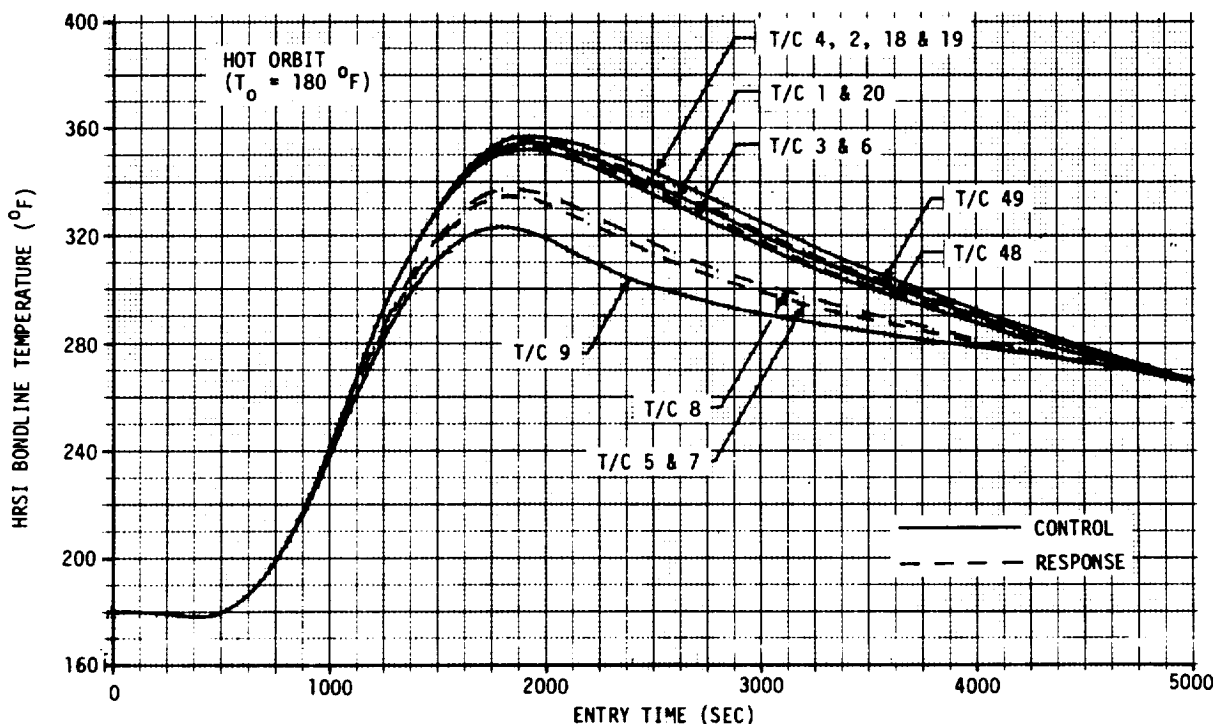


FIGURE 93 CALCULATED HRSI BONDLINE TEMPERATURE HISTORIES - ENTRY FROM HOT ORBIT

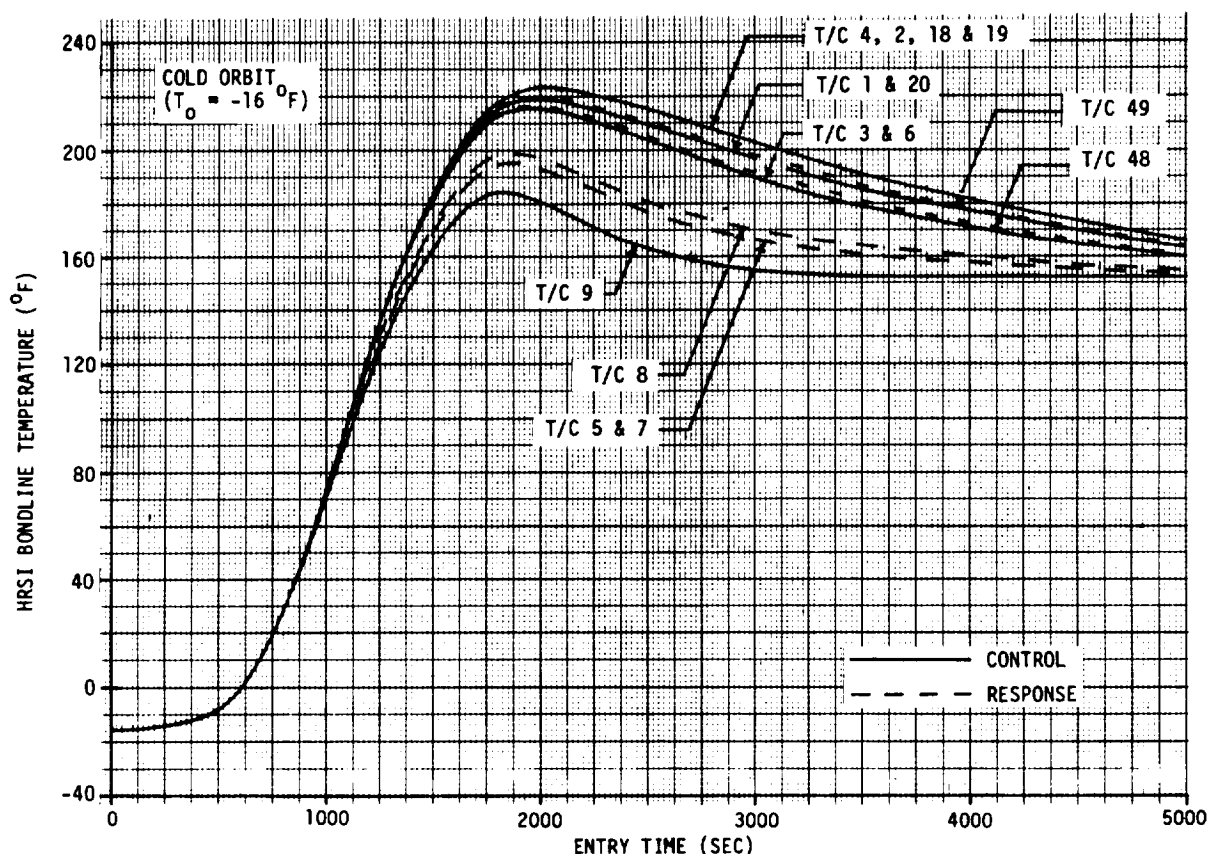


FIGURE 94 CALCULATED HRSI BONDLINE TEMPERATURE HISTORIES - ENTRY FROM COLD ORBIT

Substrate temperatures displayed on the data system console were also monitored to determine if they had peaked out in the time period predicted by pre-test analysis. The test was then terminated.

Entry pressure. - The entry pressure environment was simulated by repressurizing the chamber to that defined by the dashed curve in figure 85. Chamber pressure was manually controlled to the reading on the Wallace and Tiernan gage. Readings from this gage were recorded at 120 second intervals to supplement the measurements of the baratron pressure transducer recorded on the data system.

During the initial entry phase (0 to 1500 sec), the chamber was repressurized with dry nitrogen to minimize condensation (the shroud still contained liquid nitrogen). After this time, the nitrogen was augmented with "shop" air in a best attempt, within facility capabilities and availability of nitrogen, to achieve the rapid rise to ambient pressure. The same general testing sequence and procedure was followed for both the hot and cold orbit test conditions.

Posttest. - After both tests were completed, the test fixture was removed from the chamber and examined for causes of any discrepancies noted during monitoring of the displayed data.

### Test Results

The results of the thermal vacuum tests consist of temperature data from forty-nine thermocouples located on the test fixture and antenna and pressure data for the vacuum chamber. These data were used to verify that the environments simulated were representative of orbital and entry flight conditions and to determine the associated substructural and antenna thermal responses. The measured thermal responses are compared with analytical results for the same environments to verify the accuracy of the thermal model.

Temperature simulation. - Temperature measurements obtained from the "control" thermocouples for the simulation of hot orbit and subsequent entry are shown in figures 95 and 96 and those for the cold orbit and entry in figures 97 and 98. In general, the deviations from the desired temperature histories are small and not of major significance. During the entry simulation, the time dependent distribution was achieved well within acceptable limits. Therefore, representation of the outer bondline temperature distribution appears to be satisfactory.

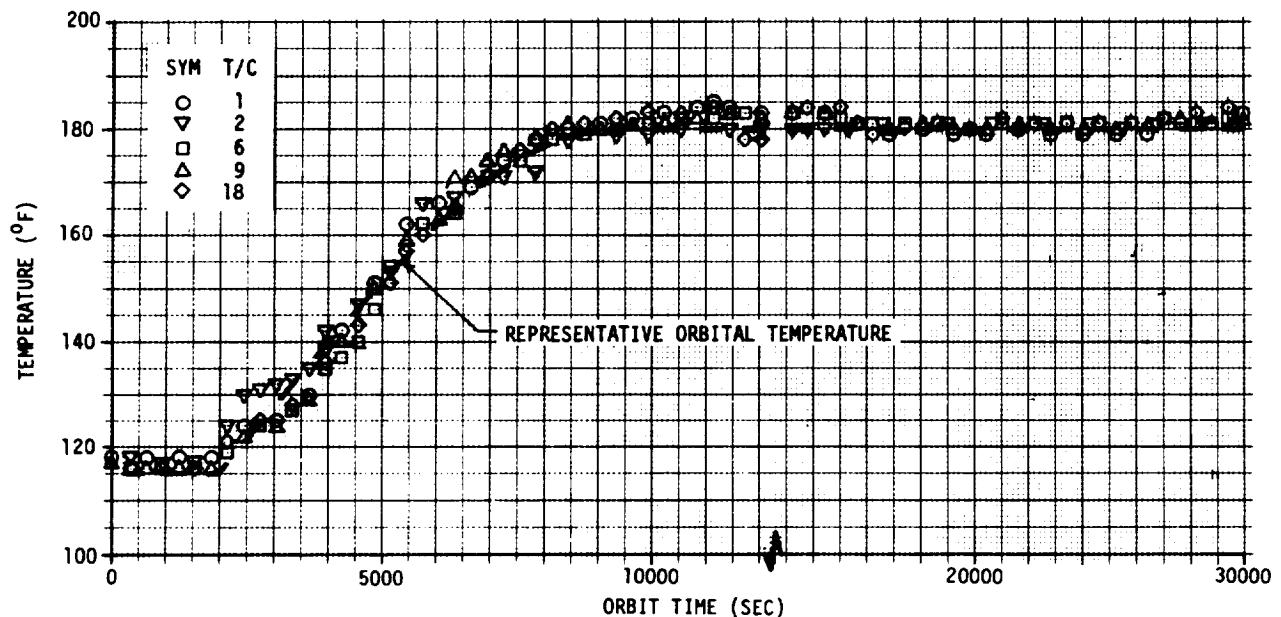


FIGURE 95 SIMULATION OF HOT ORBIT

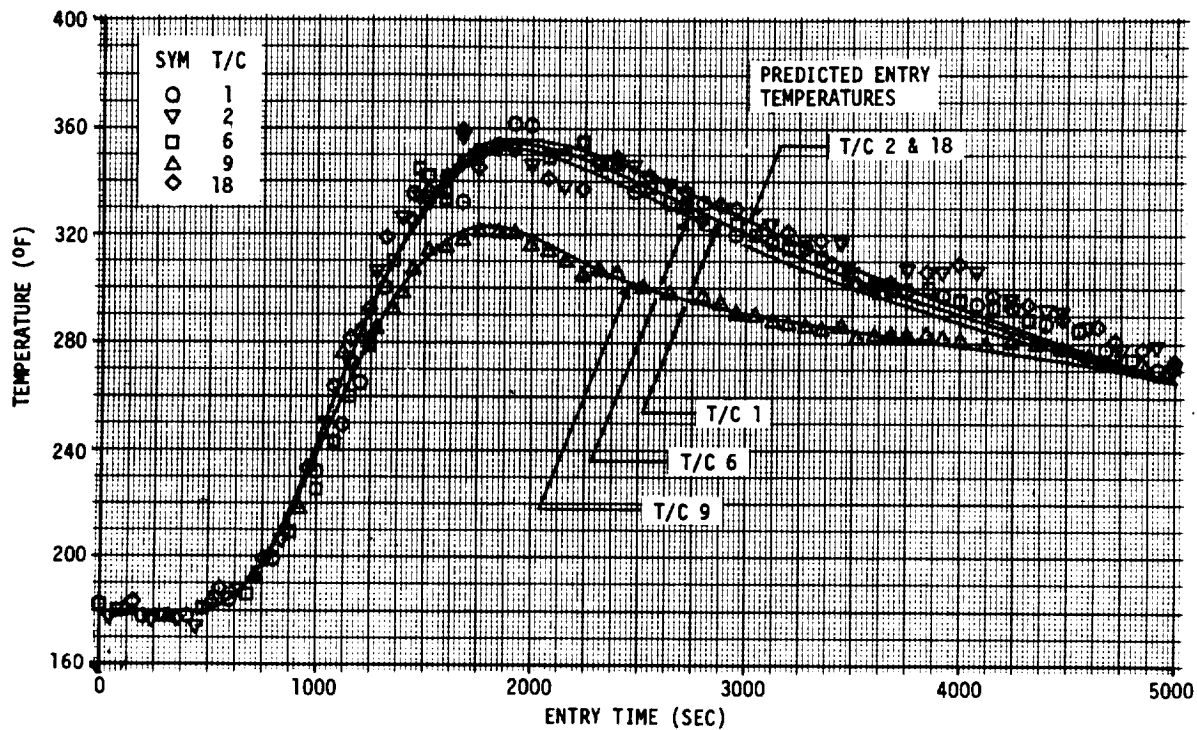
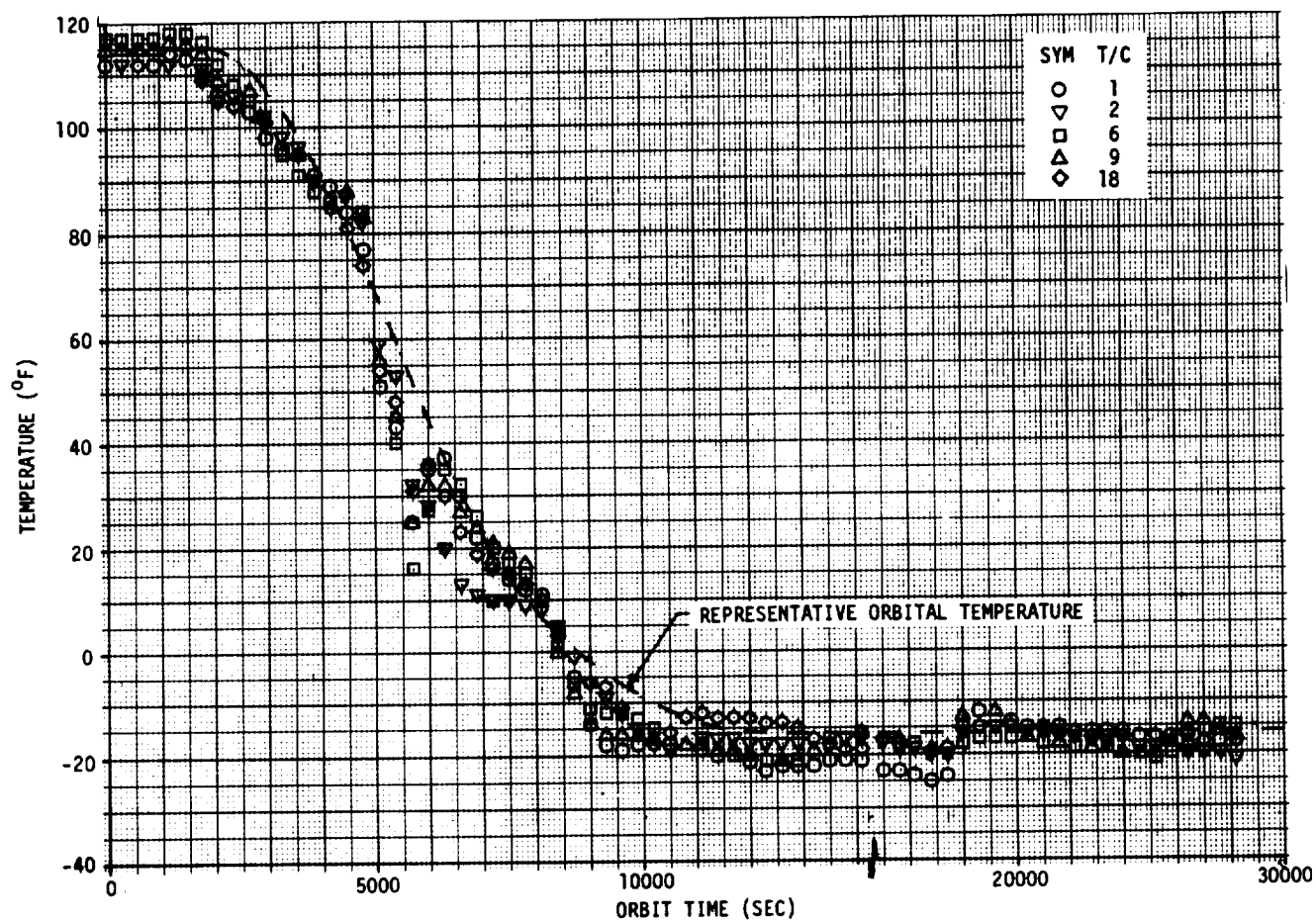


FIGURE 96 TEST SIMULATION OF ENTRY - HOT ORBIT

The degree to which heating symmetry was achieved (i.e., equally heating areas under lamps on the same controller) is illustrated in figure 99. Temperatures of four "control/companion" thermocouple sets (i.e., thermocouples for the top skin areas heated by lamps on the same controller) are shown and compared for the relatively quiescent environment of hot orbit simulation. Temperatures measured by the two symmetrical thermocouple sets (T/C 6 and 3, and T/C 18 and 4) differ by about 8 to 11 K (15 to 20°F) which is large in comparison with the differences of the other two sets. These differences are attributed to a random deviation in lamp resistances and efficiencies, and/or the type of circuit by which the two lamp banks were wired to the controller. For the areas in question, the lamp banks were wired in parallel; surface temperatures deviated less under lamp banks wired in series.

**DEVELOPMENT OF S-BAND ANTENNA INTERFACE DESIGN**  
**SHUTTLE ANTENNA RADOME TECHNOLOGY TEST PROGRAM**

**REPORT MDC E1478**  
**15 JUNE 1977**  
**VOLUME II**



**FIGURE 97 TEST SIMULATION OF COLD ORBIT**

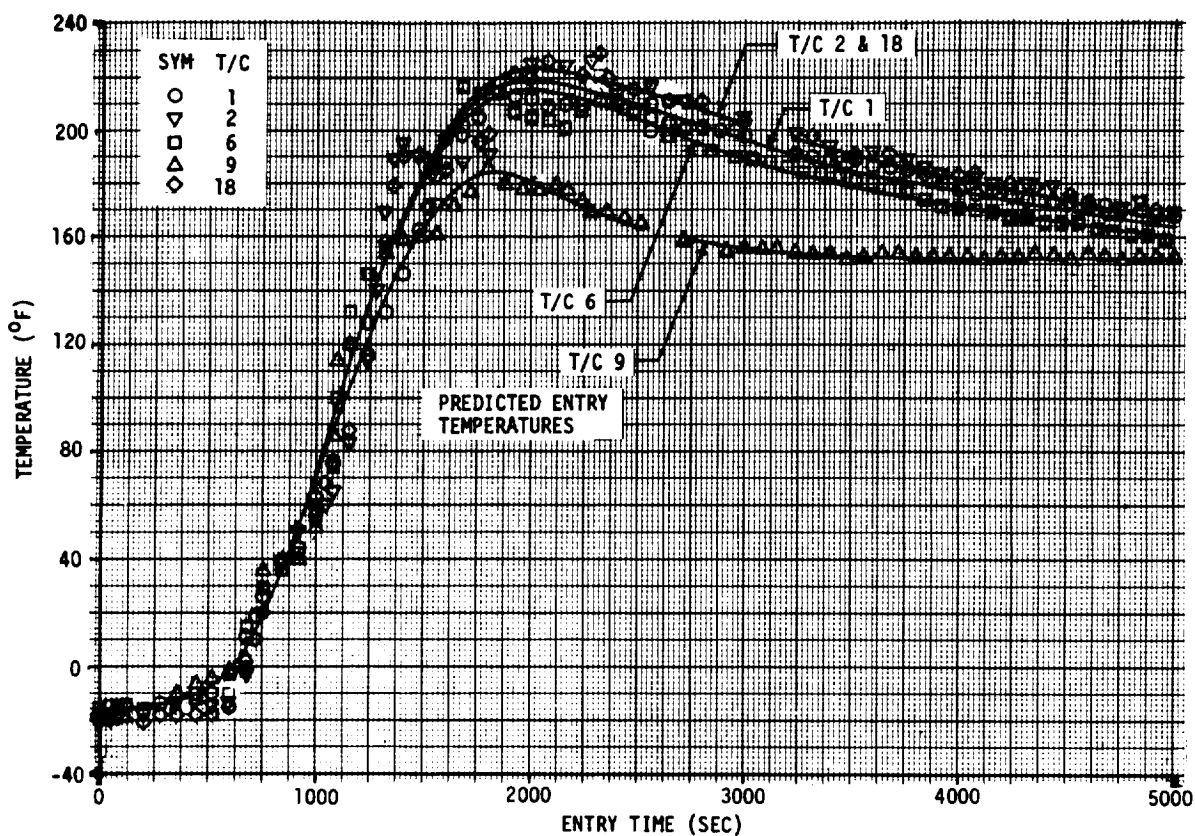


FIGURE 98 TEST SIMULATION OF ENTRY - COLD ORBIT

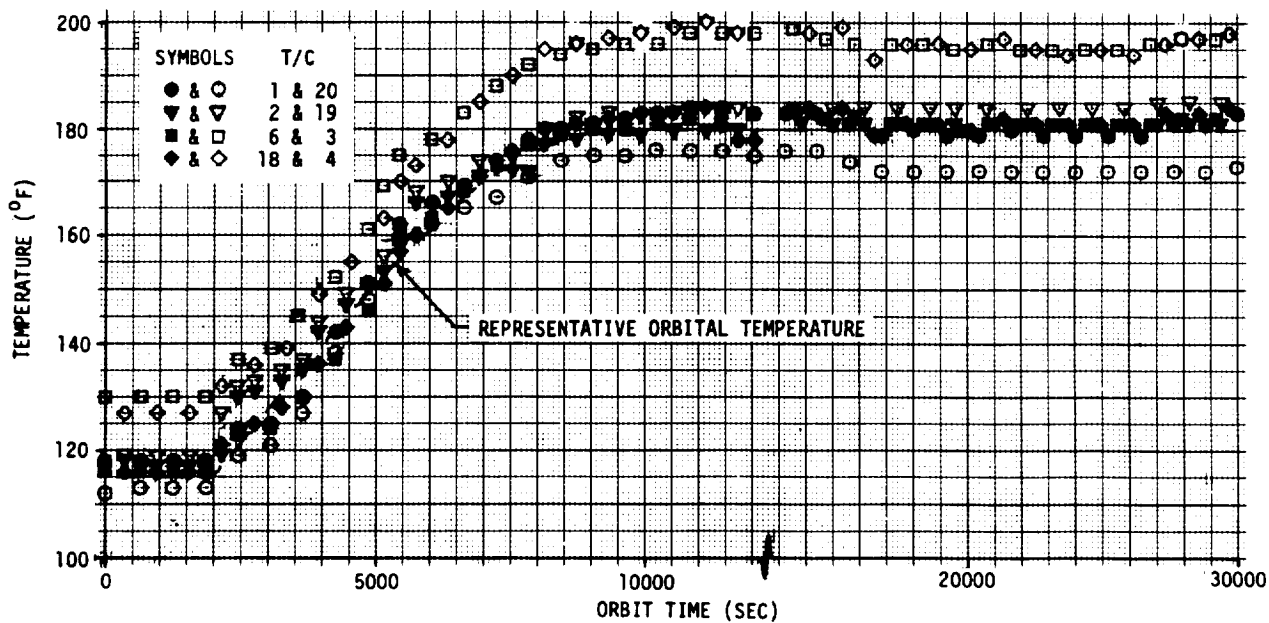


FIGURE 99 SYMMETRY OF ORBITAL HEATING - HOT ORBIT

This surface heating asymmetry during orbit simulation, however, appears to have had little influence on substrate temperature distributions. Temperatures of the structural skin measured by the corresponding sets T/C 15 and 17, and T/C 22 and 25, (figure 100) which are located immediately under the above-mentioned surface thermocouples (figure 74, i.e., T/C 15 is under T/C 6, etc.), differ by less than 3 K (5°F). The lack of symmetry was slightly more severe during the simulation of entry as evidenced by temperature histories from the same two sets of surface thermocouples (figure 101). These temperatures recorded for the entry from hot orbit differ by as much as 30 K (55°F). Correspondingly, temperature differences between the substrate thermocouples also increased as shown in figure 102 but still remained less than 6 K (10°F). Similar asymmetric heating results were found for the cold orbit and entry simulation. In that case the structural temperature asymmetry also appears to have been of minor significance. It is also possible that the differences of structural skin temperatures would have been affected by heat transfer to the test fixture frame structure discussed later.

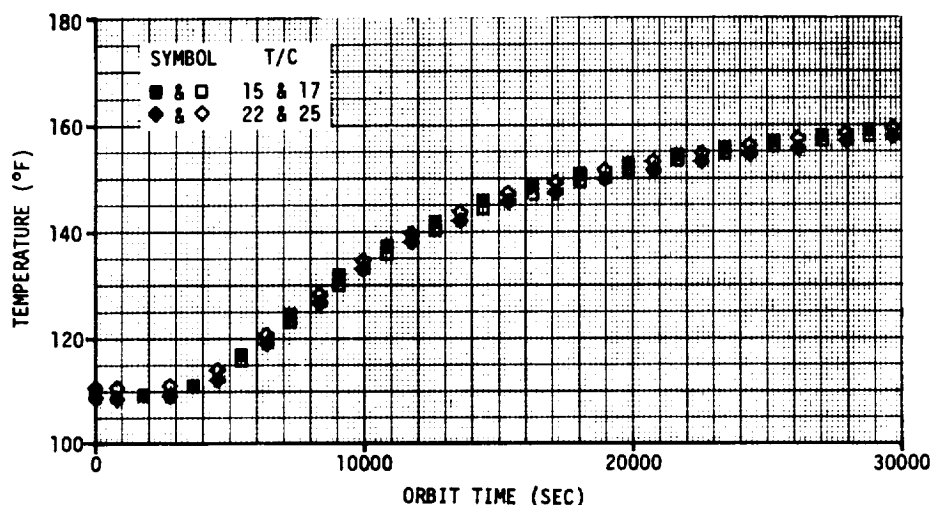


FIGURE 100 SYMMETRICAL STRUCTURAL THERMAL RESPONSES - HOT ORBIT



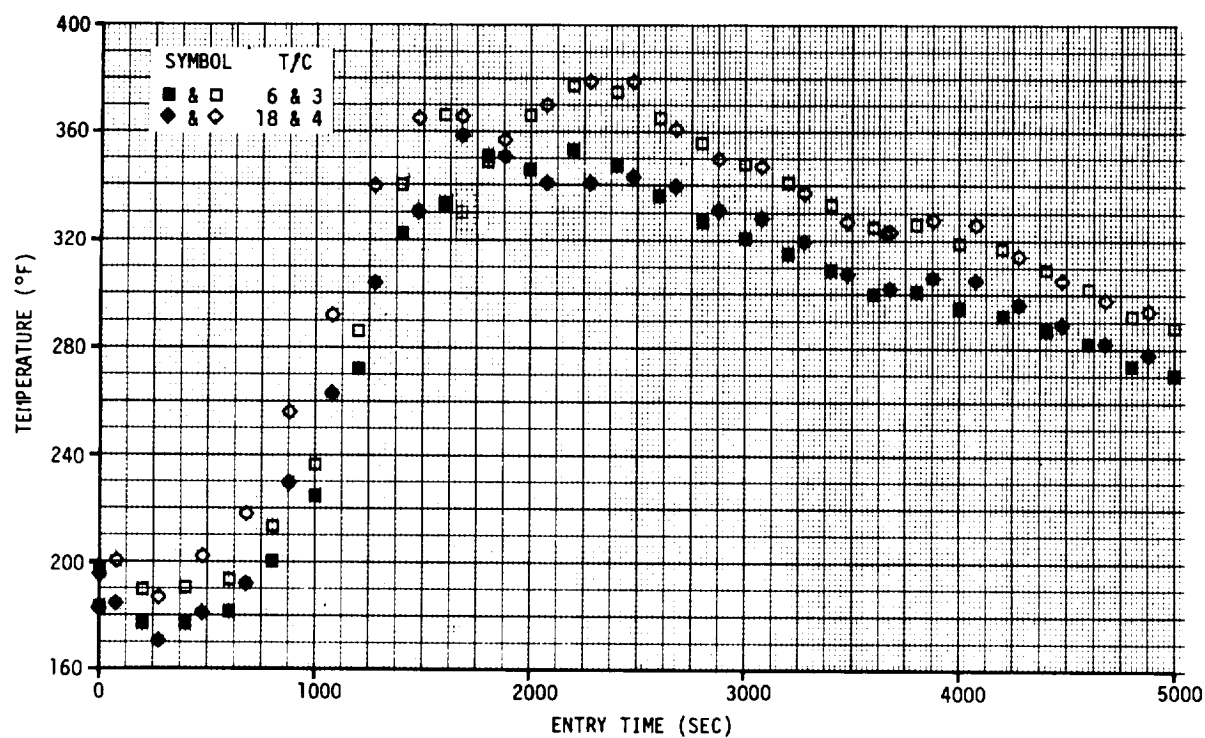
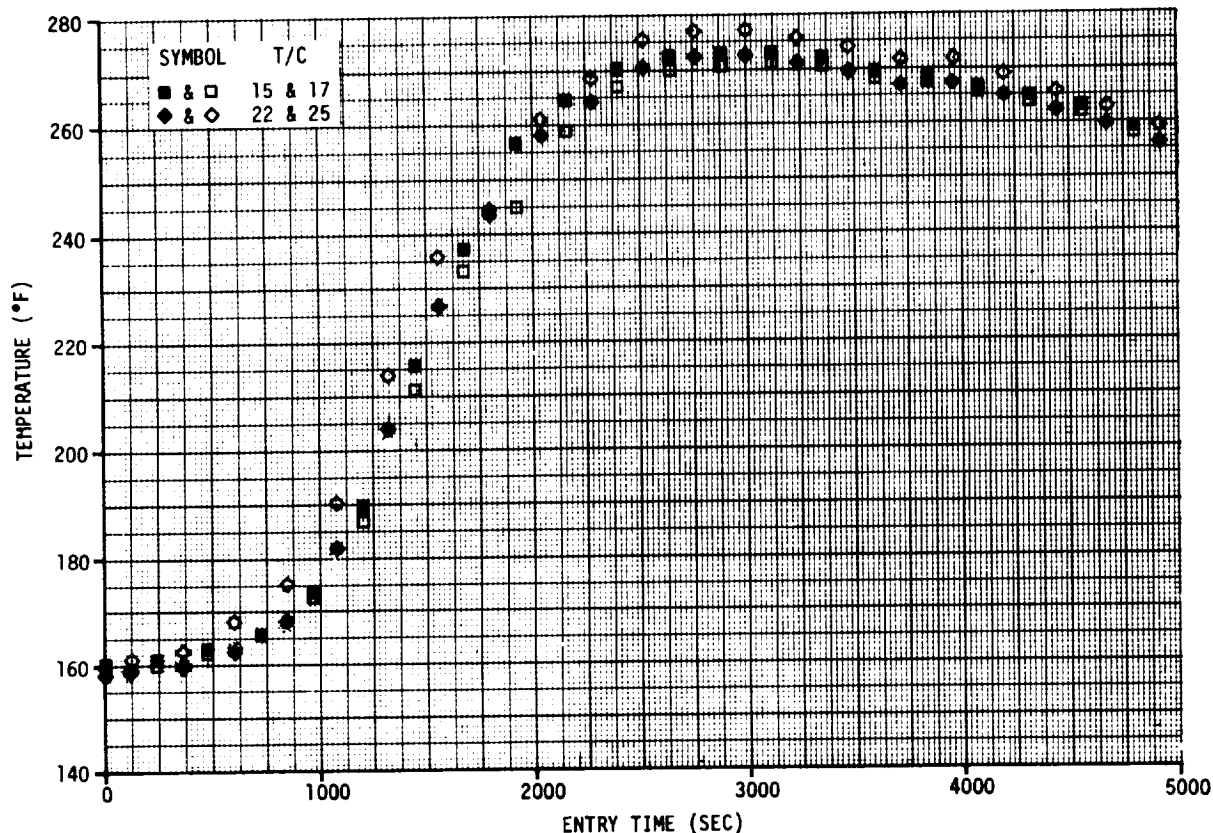


FIGURE 101 SYMMETRY OF ENTRY HEATING - HOT ORBIT



**FIGURE 102 SYMMETRICAL STRUCTURAL THERMAL RESPONSES - ENTRY (HOT ORBIT)**

The uniformity of top surface temperatures for the hot orbit condition is illustrated in figure 103 which presents the data from all the surface thermocouples. As shown, all the data fall within the limits set by the differences between "control" and "companion" thermocouple measurements (figure 99). The scatter not attributed to asymmetric heating is well within the thermocouple tolerance.

Temperatures recorded for the four surface thermocouples, T/C 5, 7, 8 and 9, located within the bounds of the center grid are indicative of the non-uniformity of heat transfer within the grid because of the curtain arrangement. For the hot orbit conditions presented in figure 103, and more graphically during the following entry simulation (figure 104), the temperatures of the peripheral thermocouples T/C 5, 7 and 8 are consistently higher than that at the center, T/C 9. These higher temperatures are attributed to reduced view factors, due to proximity of the curtains, for radiative losses to the cold vacuum chamber shroud. This effect is most noticeable in the entry temperature histories (figure 104) when, after peak temperatures are achieved and radiative cooling prevails, temperatures at the periphery and center diverge. T/C 5 went bad during the entry simulation, and therefore, is not included in figure 104.

**DEVELOPMENT OF S-BAND ANTENNA INTERFACE DESIGN**  
**SHUTTLE ANTENNA RADOME TECHNOLOGY TEST PROGRAM**

**REPORT MDC E1478**  
**15 JUNE 1977**  
**VOLUME II**

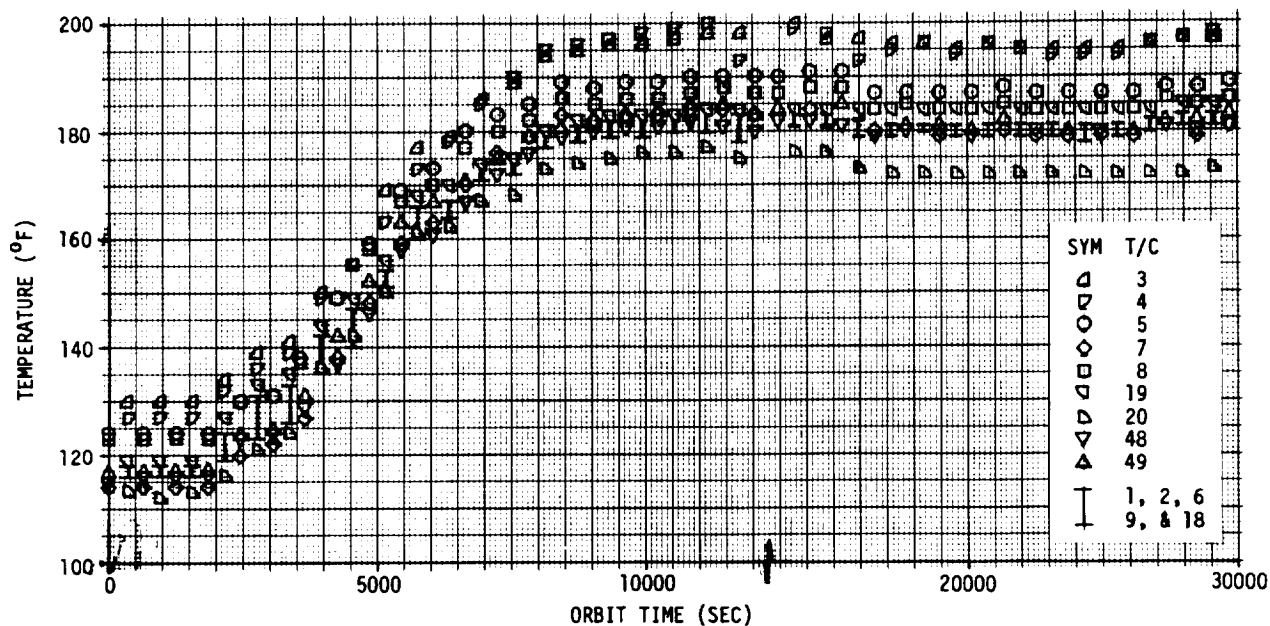


FIGURE 103 SURFACE TEMPERATURE DISTRIBUTION - HOT ORBIT

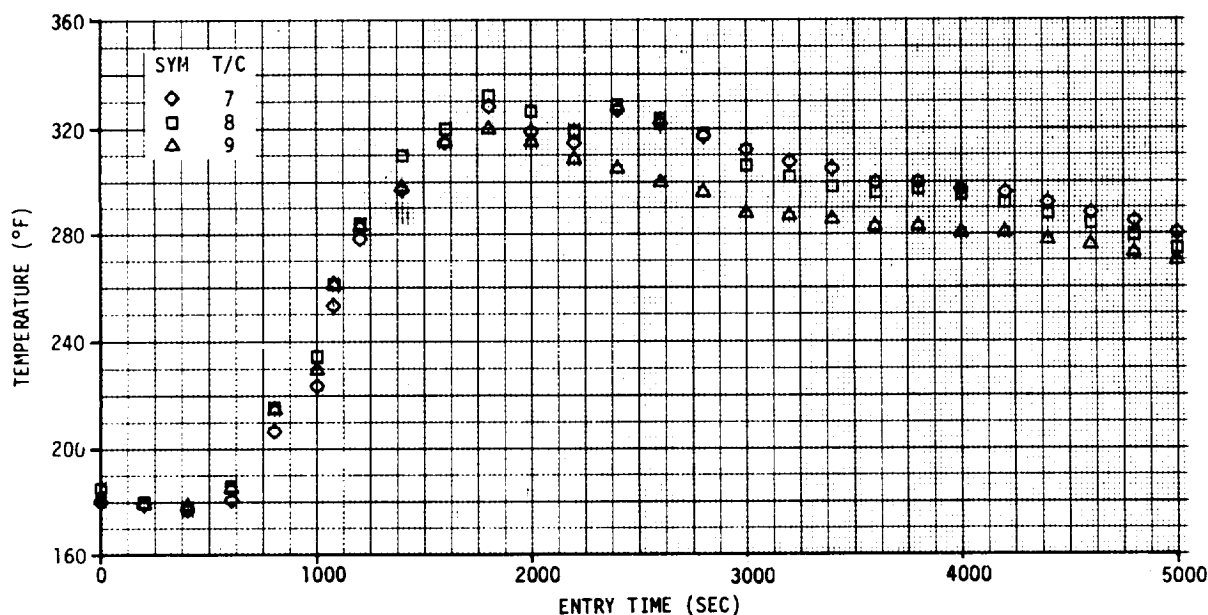


FIGURE 104 GRID HEATING UNIFORMITY - ENTRY FROM HOT ORBIT

**DEVELOPMENT OF S-BAND ANTENNA INTERFACE DESIGN**  
**SHUTTLE ANTENNA RADOME TECHNOLOGY TEST PROGRAM**

**REPORT MDC E1478**  
**15 JUNE 1977**  
**VOLUME II**

Temperatures measured on the test-fixture bottom panel, which simulated the cabin wall boundary, during the two simulated orbital and entry conditions are shown in figures 105 through 108. For comparison, these figures include a dashed line representing the constant 307 K (92°F) value for a nominal cabin wall. Maintaining the nominal cabin wall temperature was difficult because of the thermal inertia of the three structures involved, i.e., the calrod heaters, test fixture support plane and cabin wall panel. Some slight excursions from the design nominal are noted, but overall the desired boundary condition was achieved.

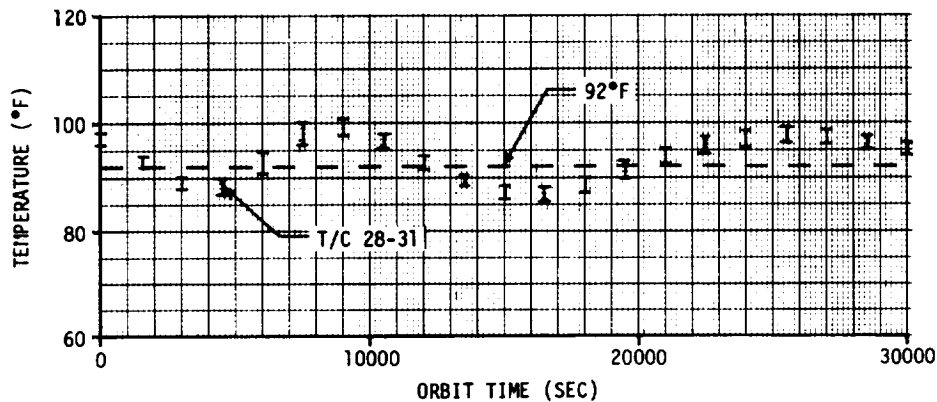


FIGURE 105 CABIN WALL TEMPERATURE - HOT ORBIT

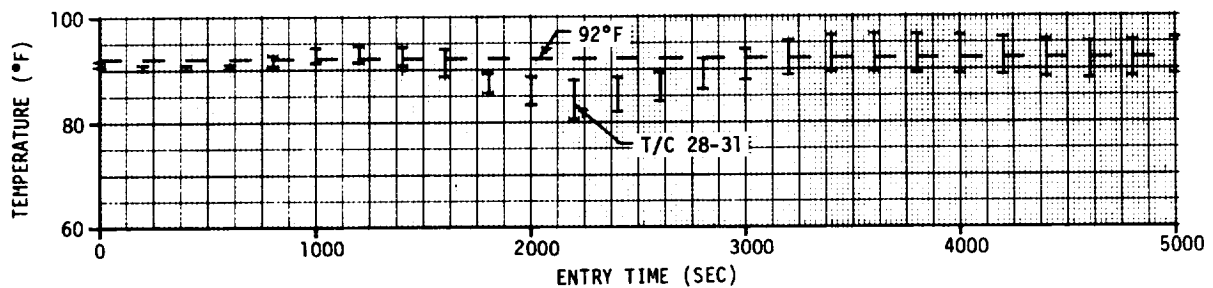


FIGURE 106 CABIN WALL TEMPERATURE - ENTRY FROM HOT ORBIT

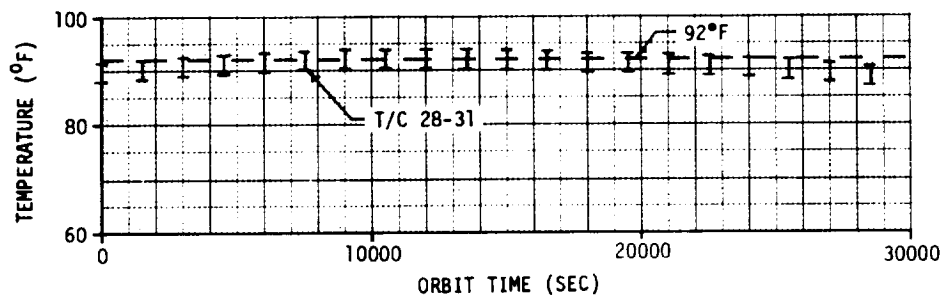


FIGURE 107 CABIN WALL TEMPERATURE - COLD ORBIT

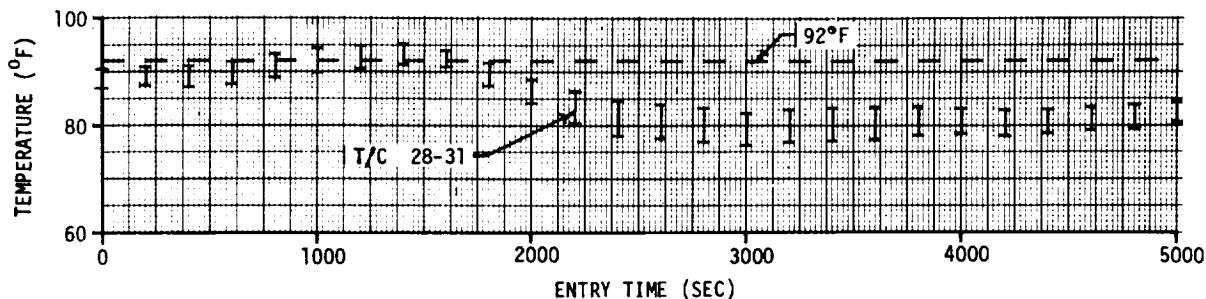


FIGURE 108 CABIN WALL TEMPERATURE - ENTRY FROM COLD ORBIT

Pressure simulation. - During orbital simulation, the chamber was maintained at its minimum pressure. Pressure measurements obtained periodically during both hot and cold orbital simulations varied from about 4 to 7 mPa ( $3 \times 10^{-5}$  to  $5 \times 10^{-5}$  torr).

Pressure measurements obtained from the direct reading gage and the baratron during both entry simulations are shown in figures 109 and 110. Readings from the gage used for pressure control were manually recorded at 120 sec intervals. Baratron measurements were recorded on the data acquisition system at 10 sec intervals, but for data reduction and analyses purposes were tabulated every 40 sec. Included in these two figures, for comparison, is the pressure curve representative of the Space Shuttle Orbiter entry history.

For both entry conditions, the measurements from the two instruments corroborate each other and show good agreement with the flight history for pressures less than 27 kPa (200 torr) in the interval 0 to 1700 sec. At the higher pressures, the required mass flow for the desired repressurization rate could not be supplied by chamber back-fill equipment as configured. However, in this range the influence of pressure on the pressure dependent thermal conductivity of insulation (e.g., SIP and TG-15000) within the test fixture is essentially negligible. Therefore, the inability to duplicate the last 200 to 300 sec of the flight pressure history should have little, if any, impact on substrate thermal responses.

Thermal response. - The thermal response of the various test fixture items was evaluated by considering five groups of similarly located thermocouples. The respective groups are representative and include most of the thermocouples on the test fixture and antenna. Those omitted are either within the limits of the data presented or are not required to show validation of the analytical thermal model. With the exception noted, the range of temperatures measured from all the thermocouples within a group is shown rather than the output of the individual thermocouple. This approach was taken because in most cases the data points are tightly grouped.

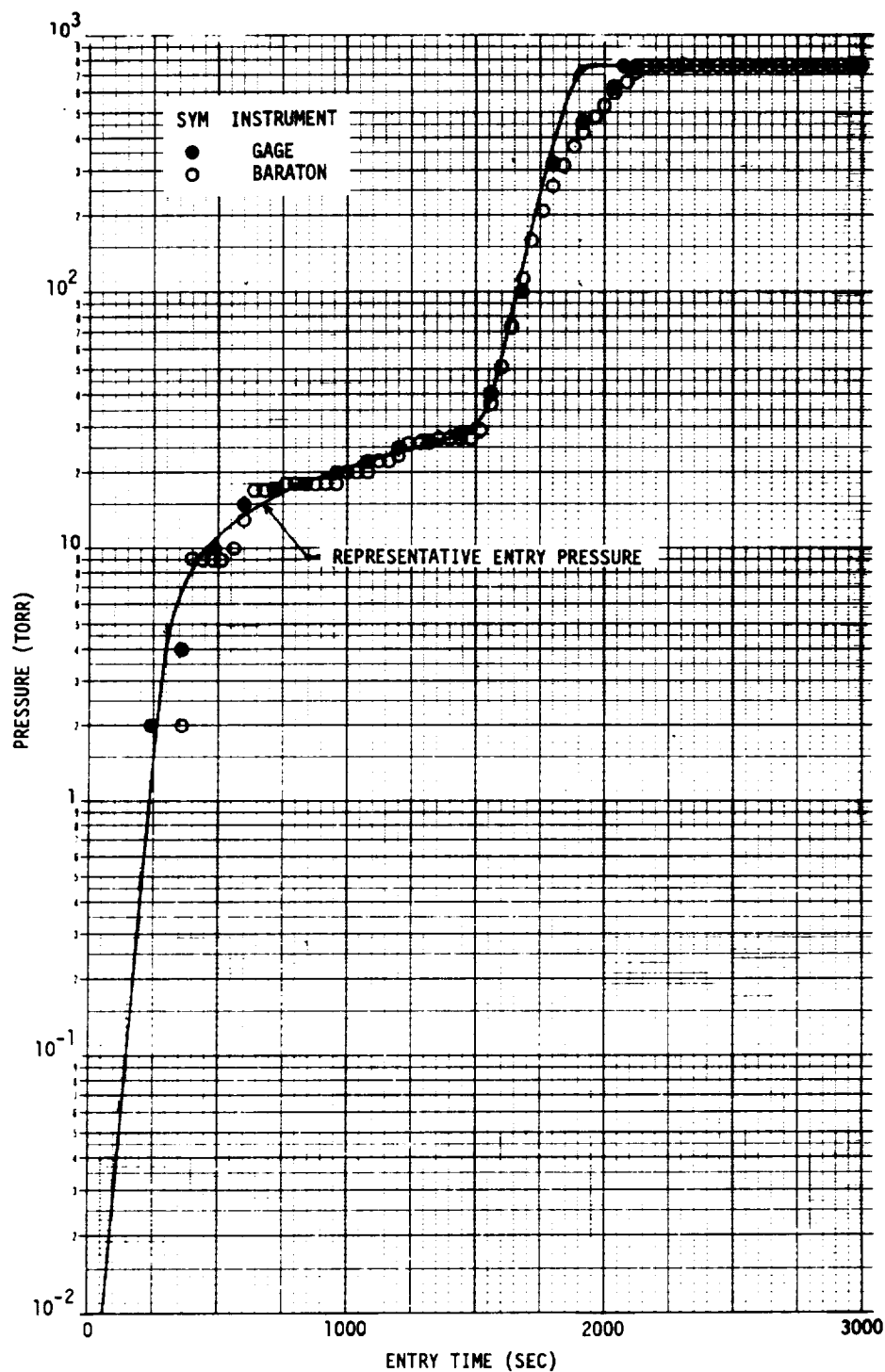


FIGURE 109 ENTRY PRESSURE HISTORY - HOT ORBIT

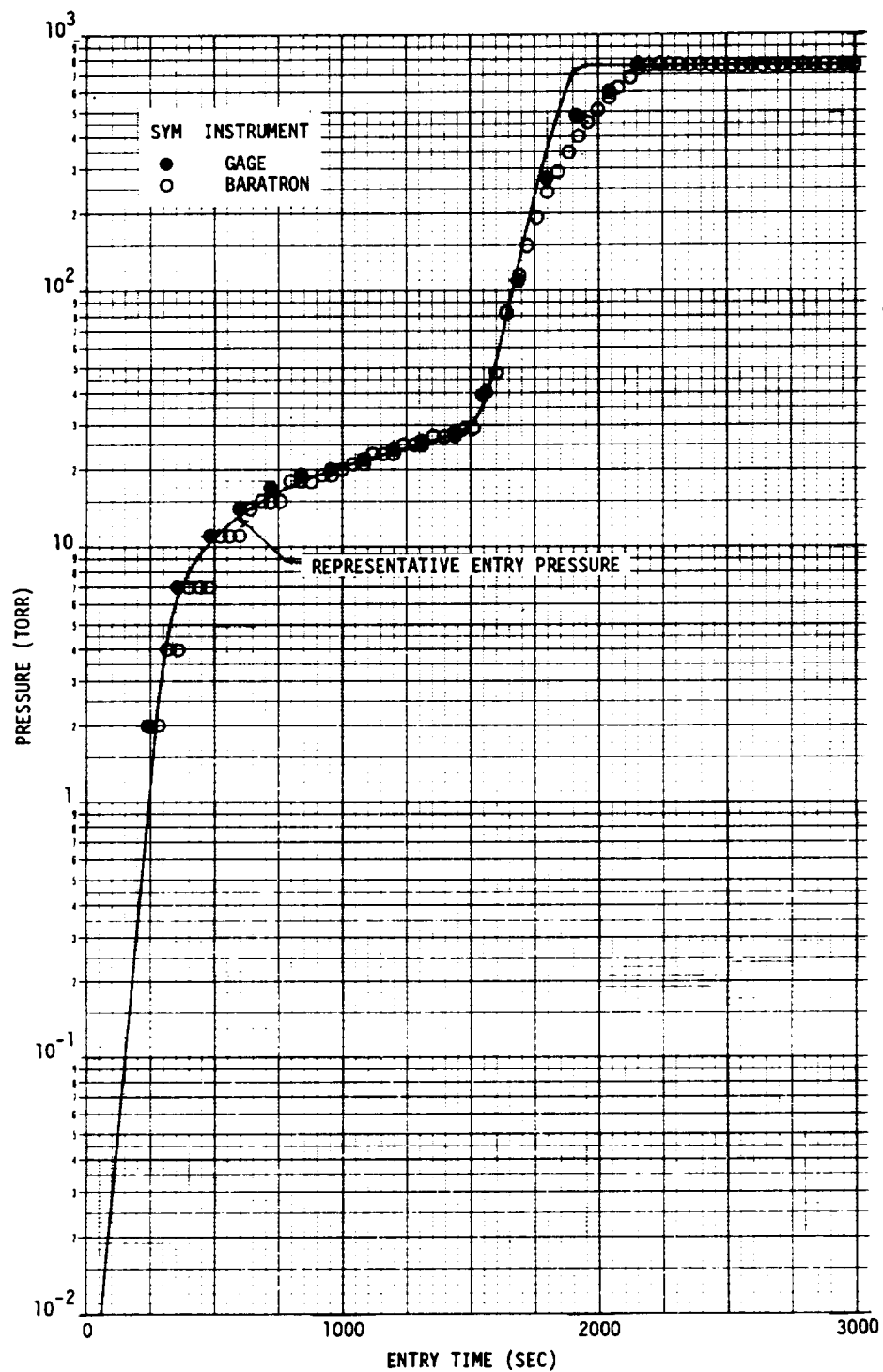


FIGURE 110 ENTRY PRESSURE HISTORY - COLD ORBIT

Figures 111 through 114 show the measured substrate thermal responses starting with the outboard and inboard structural skin locations, and then the antenna flange and elements from the first entry test. For the structural and flange responses, the data bands show the range of temperature measurements from the four symmetrically located (same radius) thermocouples (figure 74). An exception is in figure 112, in which the temperature history from T/C 10 is individually identified because, except for the very end of the test, it is consistently lower in magnitude than the other three. For element responses, the data band includes measurements from all ten thermocouples (T/C 38 through 47) on the five elements. The narrowness of the band of element temperatures tends to corroborate analytical estimates of temperature differences of less than one degree.

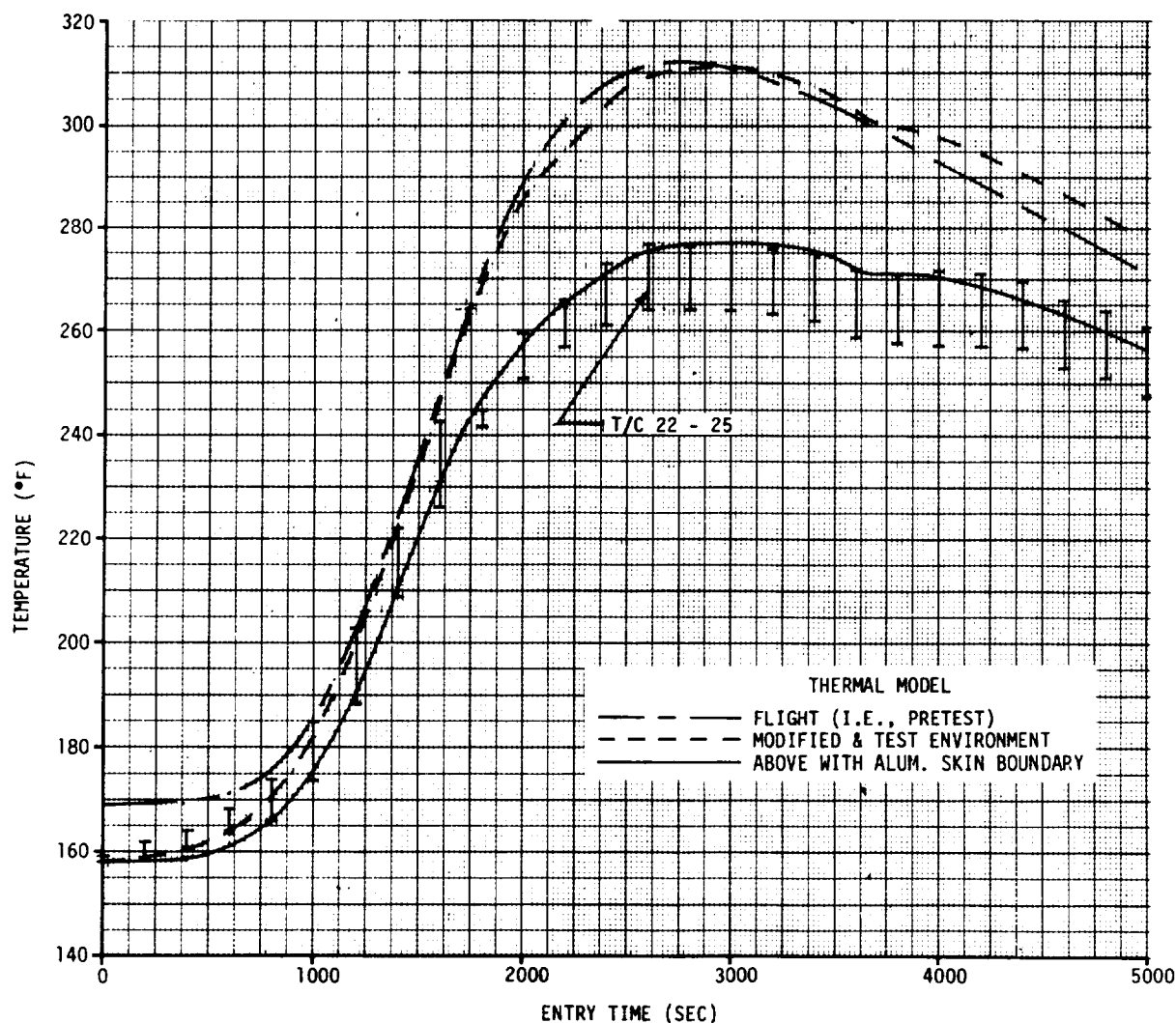


FIGURE 111 OUTBOARD STRUCTURAL SKIN TEMPERATURES - ENTRY FROM HOT ORBIT



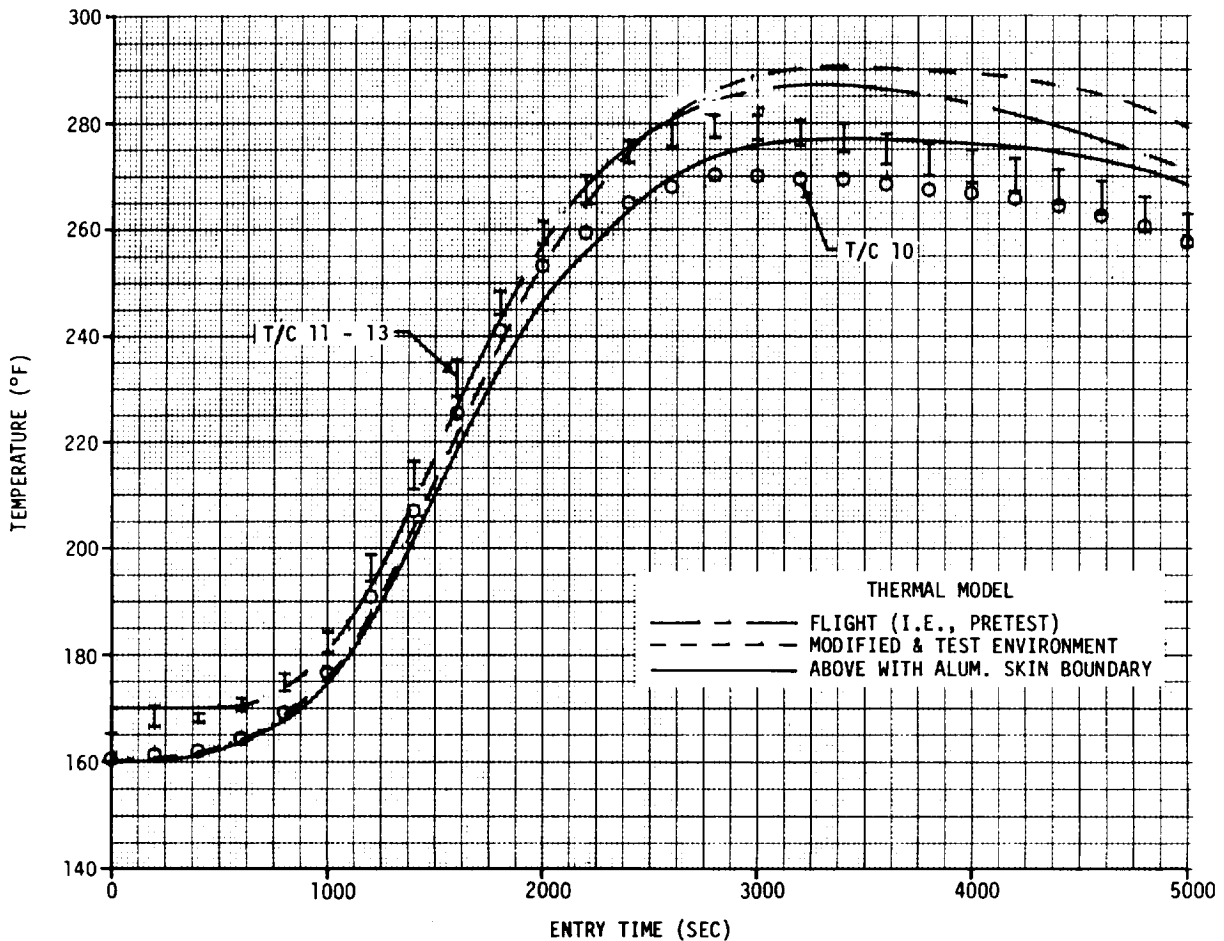


FIGURE 112 INBOARD STRUCTURAL SKIN TEMPERATURES - ENTRY FROM HOT ORBIT

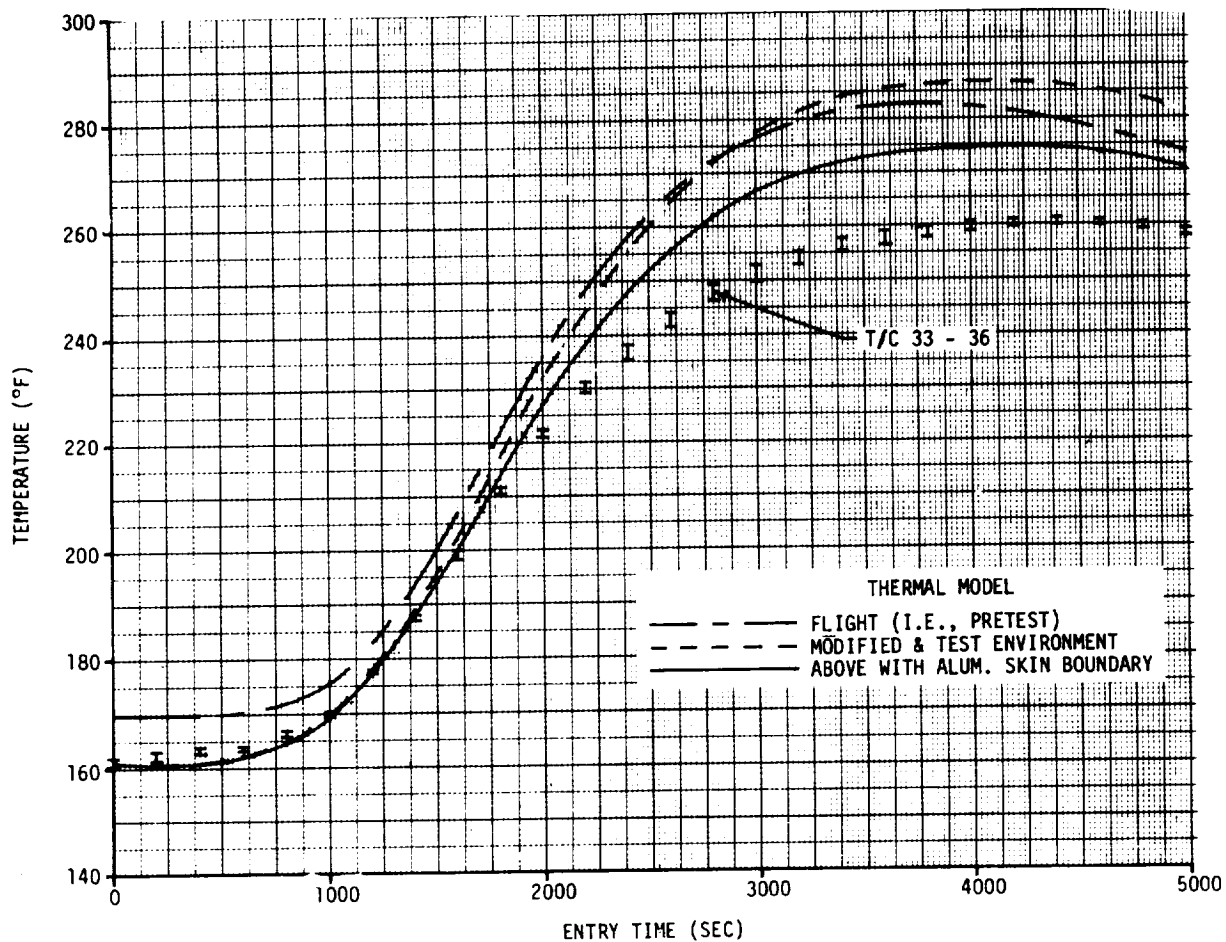


FIGURE 113 ANTENNA FLANGE TEMPERATURES - ENTRY FROM HOT ORBIT

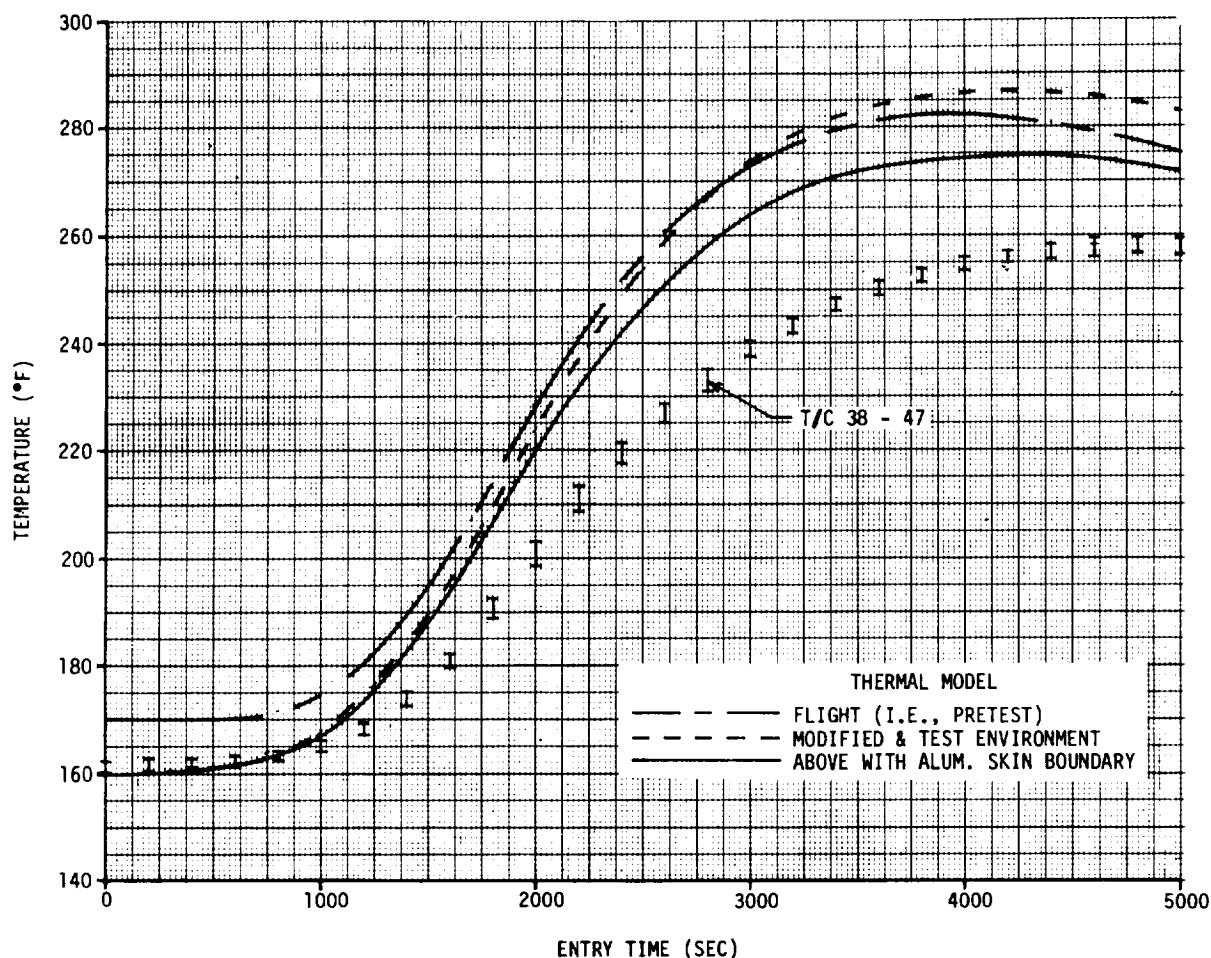


FIGURE 114 ANTENNA ELEMENT TEMPERATURES - ENTRY FROM HOT ORBIT

The computed responses from three different analytical thermal model configurations are also included in figures 111 through 114. The first of these is the pretest, or flight, calculations obtained along with computation of HRSI bondline (or top skin) temperatures. This response is represented by the alternately broken curve. At first, the large differences between these calculations and the measured temperatures, shown for the outboard skin location and antenna elements, were attributed to minor discrepancies between the thermal model and test article. This was supported by the reasonable agreement at the inboard skin location data (figure 112).

To account for these deviations, the model was slightly altered. Nodes representing the HRSI tiles and coating were removed and replaced by a layer representing the 0.254 mm (0.010 in.) thick stainless steel top skin. The layer of MLI material was replaced with an equal thickness of TG-15000. In this configuration, the measured surface temperatures in the positive X-Y quadrant, the bottom panel temperature and the chamber pressure were used as inputs to the thermal model. That is, the time-dependent temperatures of the nodal computation points were forced to follow the measurements from the thermocouple at the corresponding location. Initial temperatures were either obtained directly or inferred from measurements. It was noted at this time that other dissimilarities between model and test article still existed, such as the improvised dust cover and antenna configuration (e.g., element wall thickness and element support ring). However, inclusion of these differences into the model would have required extensive modifications which were considered beyond the scope of this contract. Subsequent usage of the term "modified thermal model" indicates reference to the model revisions described above.

Resulting calculations using the modified thermal model are indicated by the dashed curves in these figures. As shown, these changes had little effect on the resulting temperatures. However, they tend to validate the adequacy of the simulated environment to produce valid substrate thermal responses.

After further study, it was then noted that analytical temperatures at the outboard structural skin locations were higher than at the inboard location. However, measured temperatures at these two locations are practically identical as shown in figure 115. This figure shows data from the two (inboard and outboard) structural thermocouples (T/C 13 and 25) along with that from T/C 21 in the same -X, +Y quadrant. However, T/C 21 is 2.54 cm (1.0 in.) from the 0.635 cm (0.25 in.) thick fiberglass test fixture frame (figures 69 and 74). From analytical calculations and practical engineering considerations, thermocouples located further from the heat sink effect of the antenna should record higher temperatures. That is, the temperature of T/C 21 should be higher than T/C 25 which should be higher than T/C 13. However, as shown in figure 115, the temperatures of T/C 13 and T/C 25 are essentially the same, and that of T/C 21, which should be the highest temperature, is actually the lowest. This behavior was taken as an indication of a significant heat leak from the skin/stringer structure through its supporting aluminum angles (figure 69) to the test fixture fiberglass side structure.

To account for this effect, calculations were again performed using the temperature history of T/C 21 for all of the structural skin nodes along the outboard boundary of the thermal model. The resulting temperature histories are indicated by the solid curves in figures 111 through 114. As expected, since its nodal point is adjacent to boundary nodes, the largest effect is seen in the temperature computed for the outboard skin location (T/C 22 through 25) figure 111. Also, as the distance inward increases, the significance of simulating the edge losses diminishes, but does improve the correlations with measured temperatures.

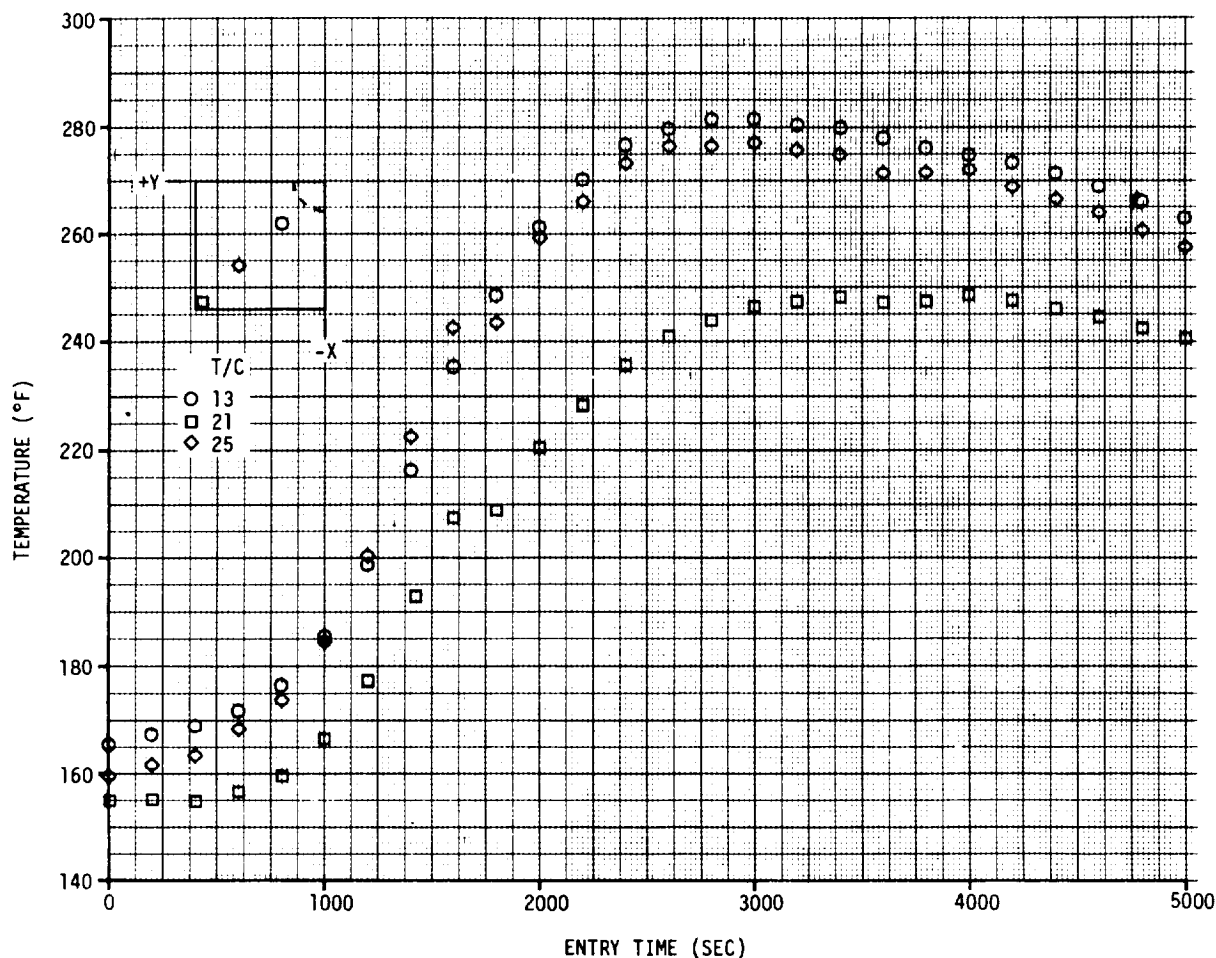


FIGURE 115 STRUCTURAL SKIN TEMPERATURE DISTRIBUTION - ENTRY FROM COLD ORBIT

Temperatures measured by the two thermocouples (T/C 26 and 27) at the top surface of the TG-15000 insulation during the simulation of entry from hot orbit are shown in figure 116. Included in the figure are the three calculated temperature histories. It can be seen that the modified thermal model with the use of data from T/C 21 brings the measured and calculated data in much better agreement. The large differences in temperatures recorded by these two thermocouples are attributed primarily to the radiation view factors associated with their locations. Radiative heat transfer for T/C 27 to the backside of the skin/stringer panel, which is hotter than the antenna, is relatively unobstructed; whereas that for T/C 26 is significantly reduced due to the presence of the antenna dust cover. Even without the dust cover, lower temperatures for T/C 26 would be expected since most of its heat transfer would occur with the relatively cooler antenna. It is also possible that these temperatures could be influenced by heat transfer from the backside of the structural skin by a mixed mode of free/forced convection which could be significant with chamber repressurization, and is not accounted for in the analytical model. Heat transfer by this mode would also be higher at the outboard locations due to the larger gap between the structure and insulation, enhancing the development of convective currents.

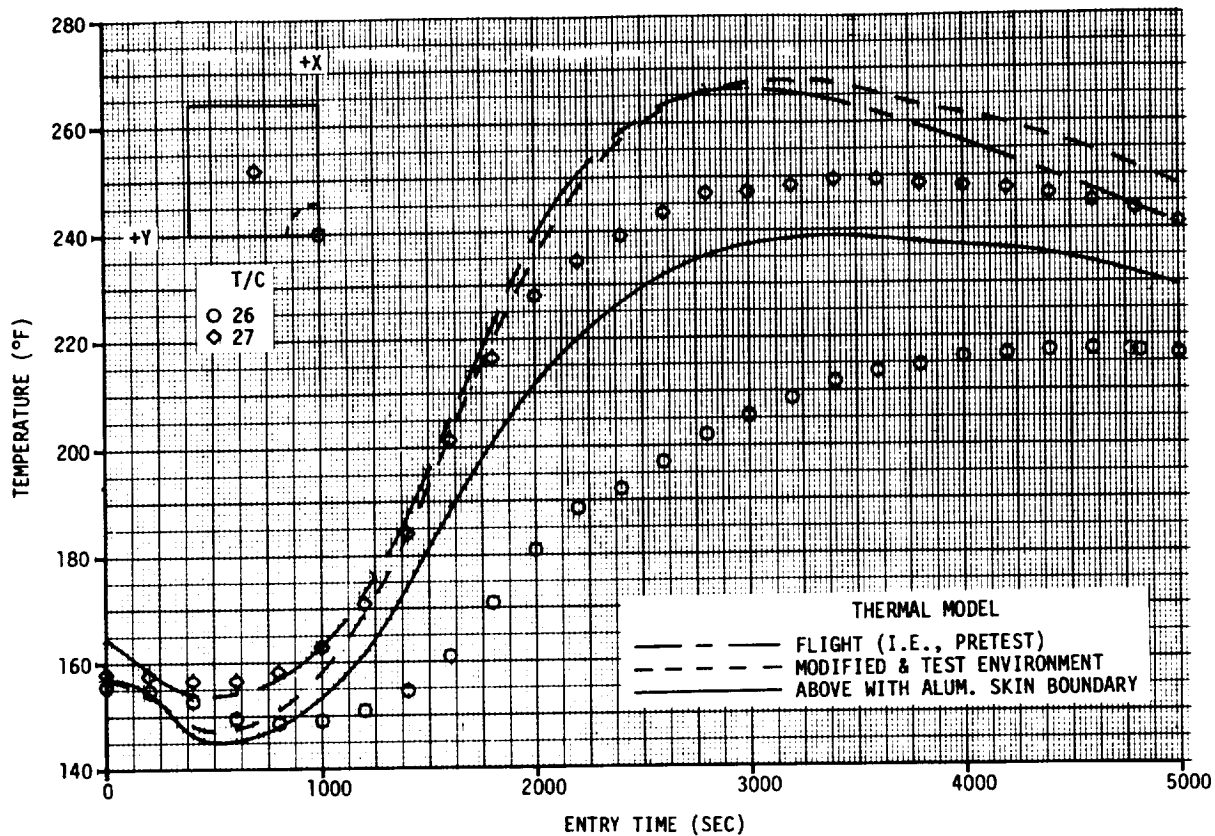


FIGURE 116 INSULATION TEMPERATURES - ENTRY FROM HOT ORBIT

Measurements of the SIP and antenna polyimide cover bondline temperature (T/C 32) were excluded from this and subsequent analyses because the data appeared to be erroneous. Posttest inspection, prompted by irregularities noted during test monitoring, revealed improper thermocouple installation and bonding of the removable circular panel over the antenna (see figure 70). A transparent tape failed to hold the thermocouple junction in contact with the antenna cover surface and consequently the output was considered invalid. The bonding layer of RTV also appeared exceptionally thick and included numerous voids. These irregularities in the RTV could have influenced the response of antenna measurements (figures 113 and 114).

Similar comparisons of measured and calculated temperature responses for the less dynamic environment of hot orbit simulation are presented in figures 117 through 121. In the same order as before, these figures include the responses for the outboard and inboard skin locations (figures 117 and 118), the antenna flange and elements (figures 119 and 120) and the top surface of the insulation blanket (figure 121). The analytical responses included in these figures are from the modified thermal model utilizing measured surface temperatures and pressure as input, with and without the use of T/C 21 data as a structural skin boundary. The magnitude of the deviations from the modified thermal model predictions are much smaller than those obtained in the entry case. The agreement is best for the structural skin. The measured temperature rise of the antenna flange and elements lags the predicted temperature as in the entry case.

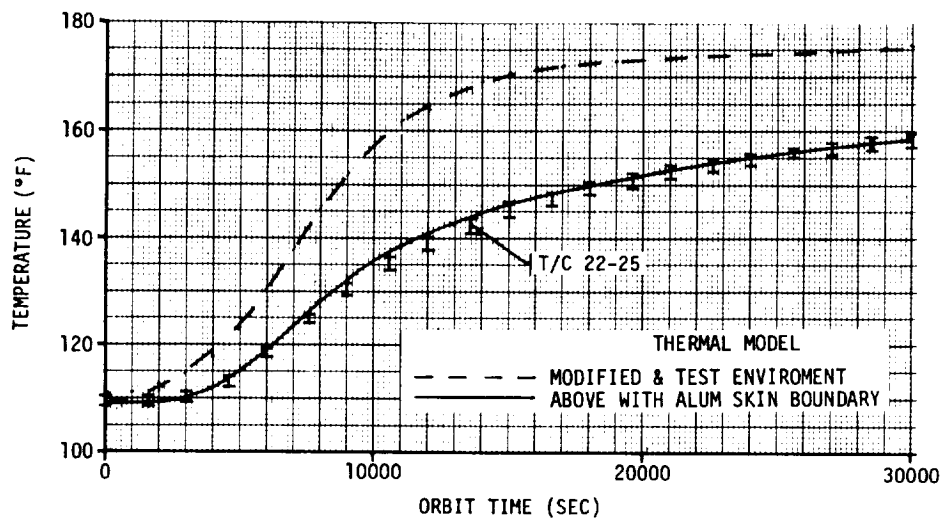


FIGURE 117 OUTBOARD STRUCTURAL SKIN TEMPERATURES - HOT ORBIT

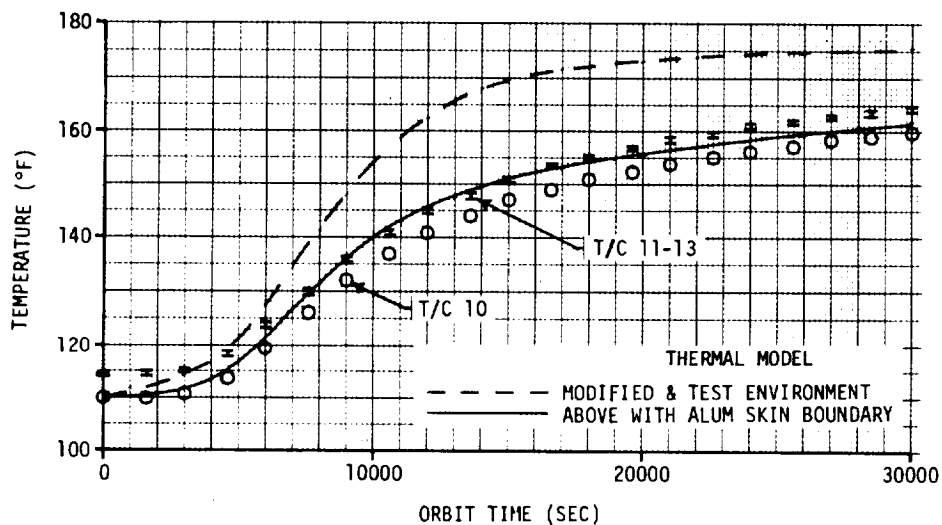


FIGURE 118 INBOARD STRUCTURAL SKIN TEMPERATURES - HOT ORBIT

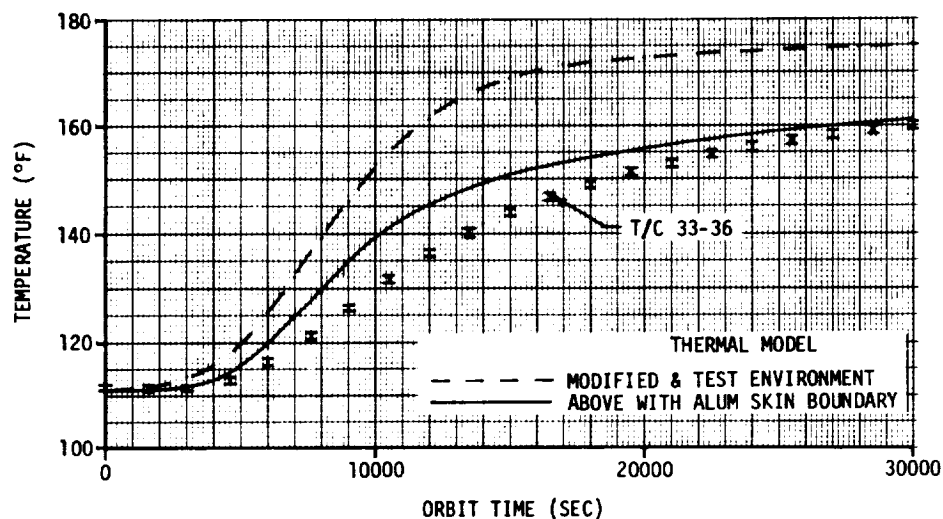


FIGURE 119 ANTENNA FLANGE TEMPERATURES - HOT ORBIT

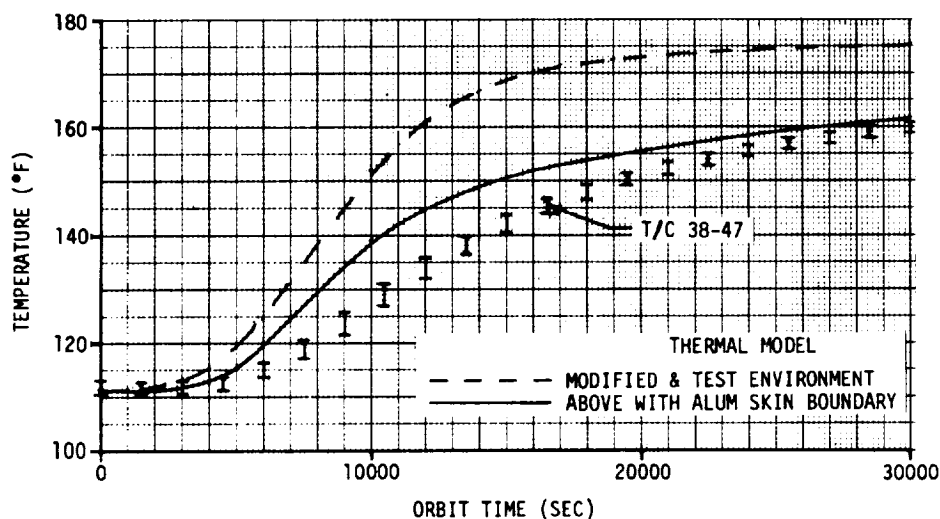
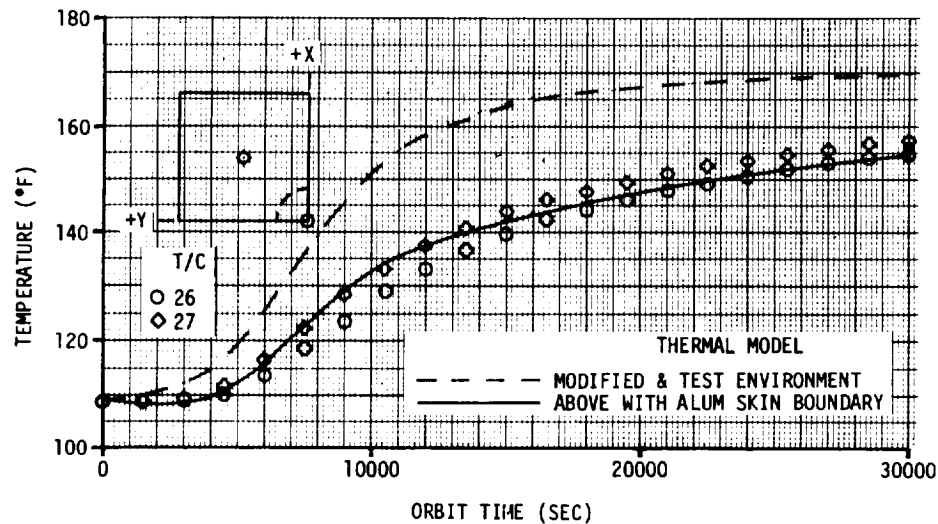


FIGURE 120 ANTENNA ELEMENT TEMPERATURES - HOT ORBIT





**FIGURE 121 INSULATION TEMPERATURES - HOT ORBIT**

Temperatures measured at the same locations on the structure, antenna and insulation during the simulation of the cold orbit condition and the subsequent entry are shown in figures 122 through 126 and 127 through 131, respectively. Included in these figures are the calculated temperatures from the modified thermal model with use of T/C 21 data to account for heat transfer to the test fixture fiberglass sides. The agreement shown between measured and calculated responses for the relative environment and location further supports the preceding validation of the thermal model.

Discussion. - From the preceding data comparisons it is seen that calculated temperatures show better agreement with test measurements when the thermal model accounts for the heat leak to the test fixture side structure. The respective comparisons of measured and calculated results show that as the test conditions affecting the test fixture response are incorporated into the analytical thermal model the agreement between results is improved. In most cases the predictions are well within experimental tolerances. Where the predicted and measured deviate the prediction is usually on the conservative side. No matter how rigorous the design of the test fixture and the simulation of flight environments, it is difficult to duplicate the flight configuration. Therefore, for validation purposes, the analytical thermal model should incorporate the flexibility to accommodate any inconsistencies between flight and test.

One shortcoming of the analytical model illustrated in figure 116 is that it does not account for such transverse gradients in the insulation material. From the backside of the skin/stringer panel and bottom of the antenna dust cover (figures 75 through 77) the model is one-dimensional to the cabin wall (figure 82, nodes 265 through 276). Hence, the analytical temperature calculated for this surface is essentially an averaged or integrated value for the radiative heat transfer. Thus, the calculated temperature history from the modified model

**DEVELOPMENT OF S-BAND ANTENNA INTERFACE DESIGN**  
**SHUTTLE ANTENNA RADOME TECHNOLOGY TEST PROGRAM**

**REPORT MDC E1478**  
**15 JUNE 1977**  
**VOLUME II**

using the data from T/C 21 is corroborated by falling between the two measured temperatures and the close agreement with T/C 27 data based on an averaged area for heat transfer for each thermocouple.

The influence of the free convection mode of heat transfer may also be considered for predicting the structural and antenna components. The temperature histories for entry from a hot orbit (figures 111 and 112), for example, indicate relatively sharp changes in slope when atmospheric pressures are reached during repressurization. A free convection condition would account, to some extent, for the structural and antenna temperatures being lower than predicted because cooling would be accelerated. The significance of free convection during entry is supported by the better agreement of the orbital temperatures (predicted and measured) which result from radiative heat transfer only.

Of the five locations examined, the agreement between calculated and measured temperature histories is good or acceptable, except for the antenna elements where the slope of the measured temperature rise is noticeably less than that calculated and the magnitude is 8 to 14 K (15 to 25°F) less. This discrepancy is probably due to the differences between the analytical model and the test antenna. The test antenna elements had thicker walls and did not contain eccosphere insulation. Of these, the thicker elements walls are the most likely source for the differences noted. The thicker walls create a larger thermal mass which results in both a slower temperature rise and a lower maximum temperature. It is also possible that the thicker, than normal, layer of RTV with the numerous voids over the antenna could contribute to a lower overall antenna temperature.

The small amount of scatter in the antenna element temperature histories and the small differences between the antenna flange and element temperature histories tend to correlate and confirm the analytical trends. Calculated temperatures for the antenna elements vary by less than one degree overall. Calculated temperatures for the flange initially lead those for the elements by 6 K (10°F), but then converge and peak out together. Because of small differences between separate element temperatures it appears that representation of the antenna in the thermal model could have been less sophisticated.

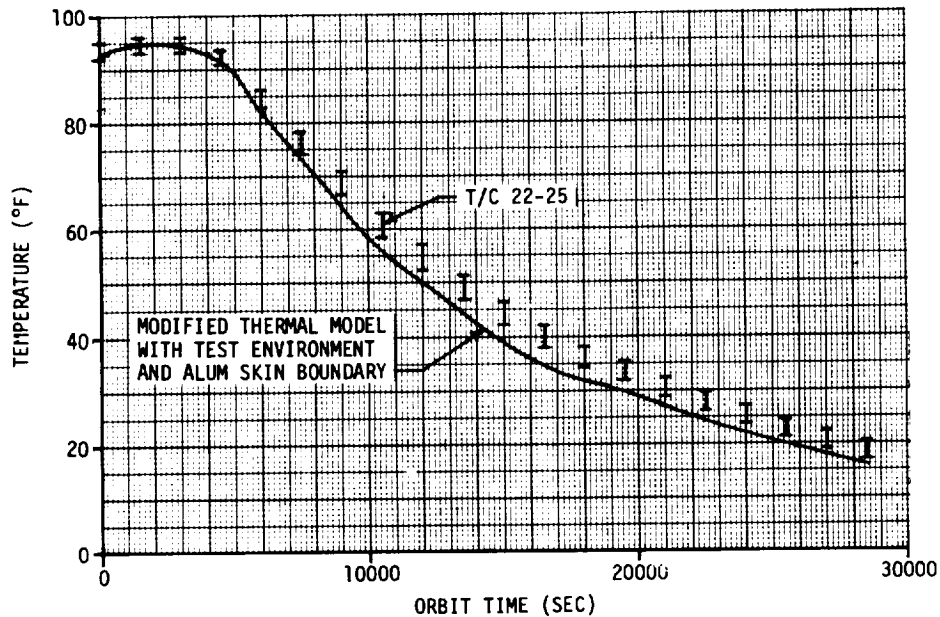


FIGURE 122 OUTBOARD STRUCTURAL SKIN TEMPERATURES - COLD ORBIT

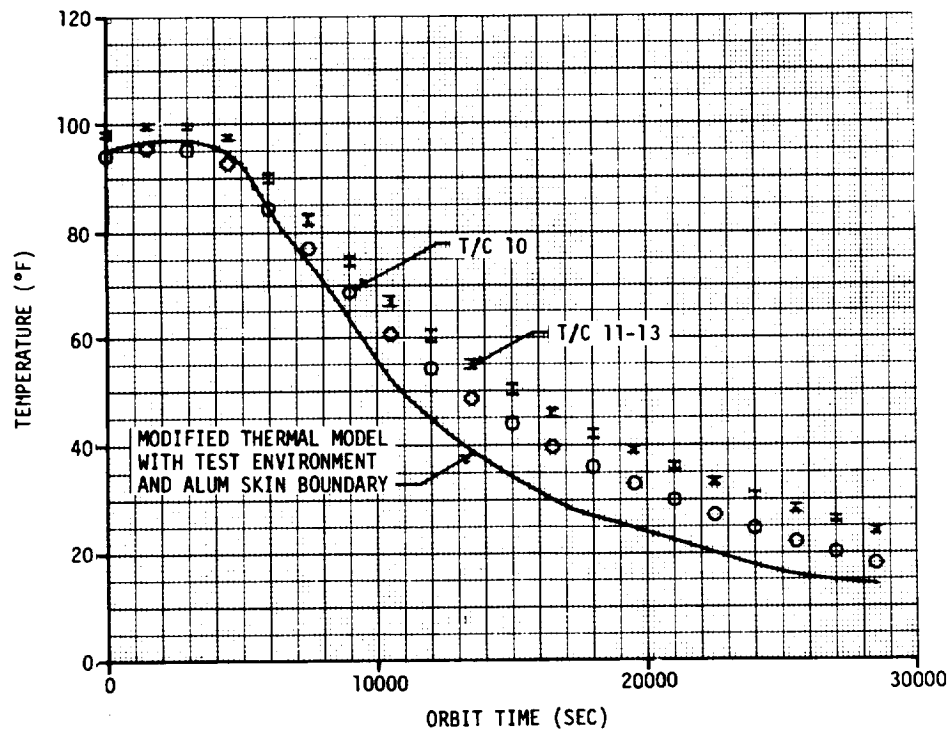


FIGURE 123 INBOARD STRUCTURAL SKIN TEMPERATURES - COLD ORBIT

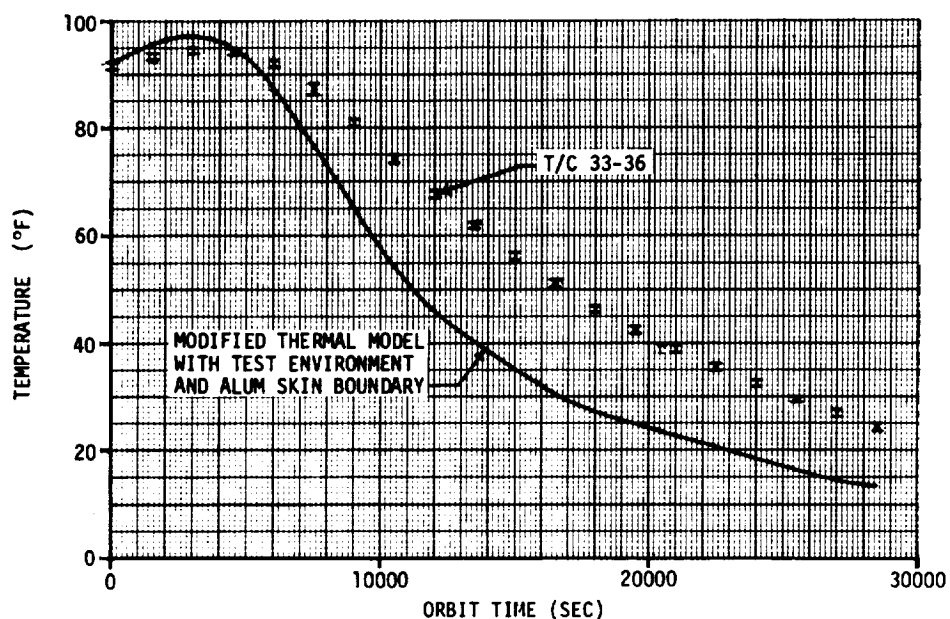


FIGURE 124 ANTENNA FLANGE TEMPERATURES - COLD ORBIT

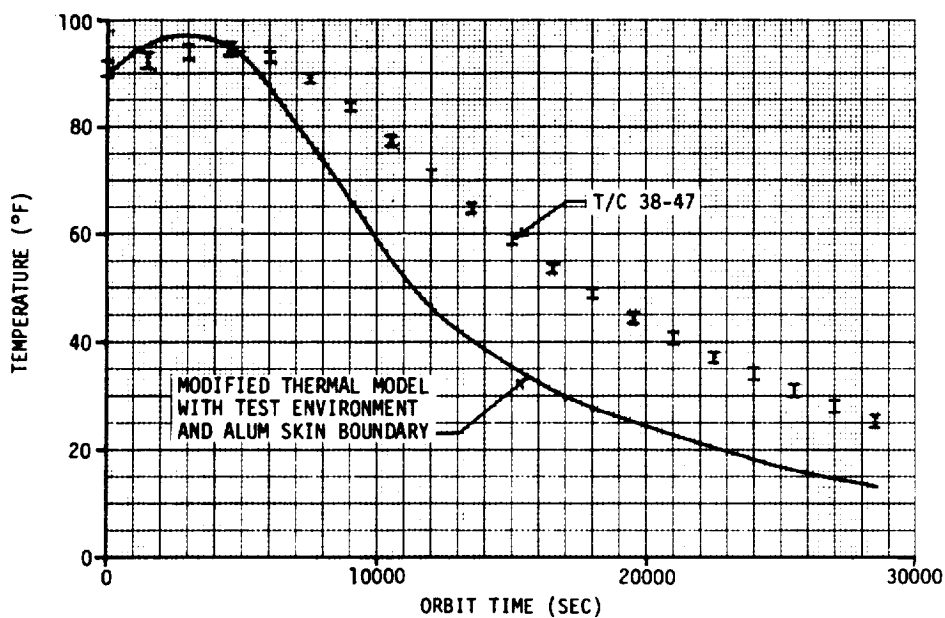


FIGURE 125 ANTENNA ELEMENT TEMPERATURES - COLD ORBIT

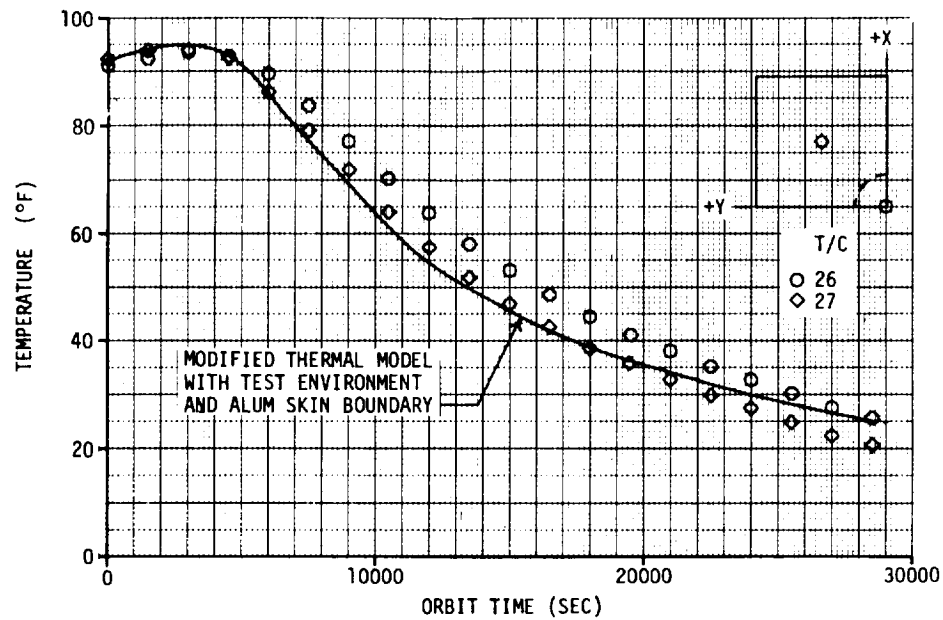


FIGURE 126 INSULATION TEMPERATURES - COLD ORBIT

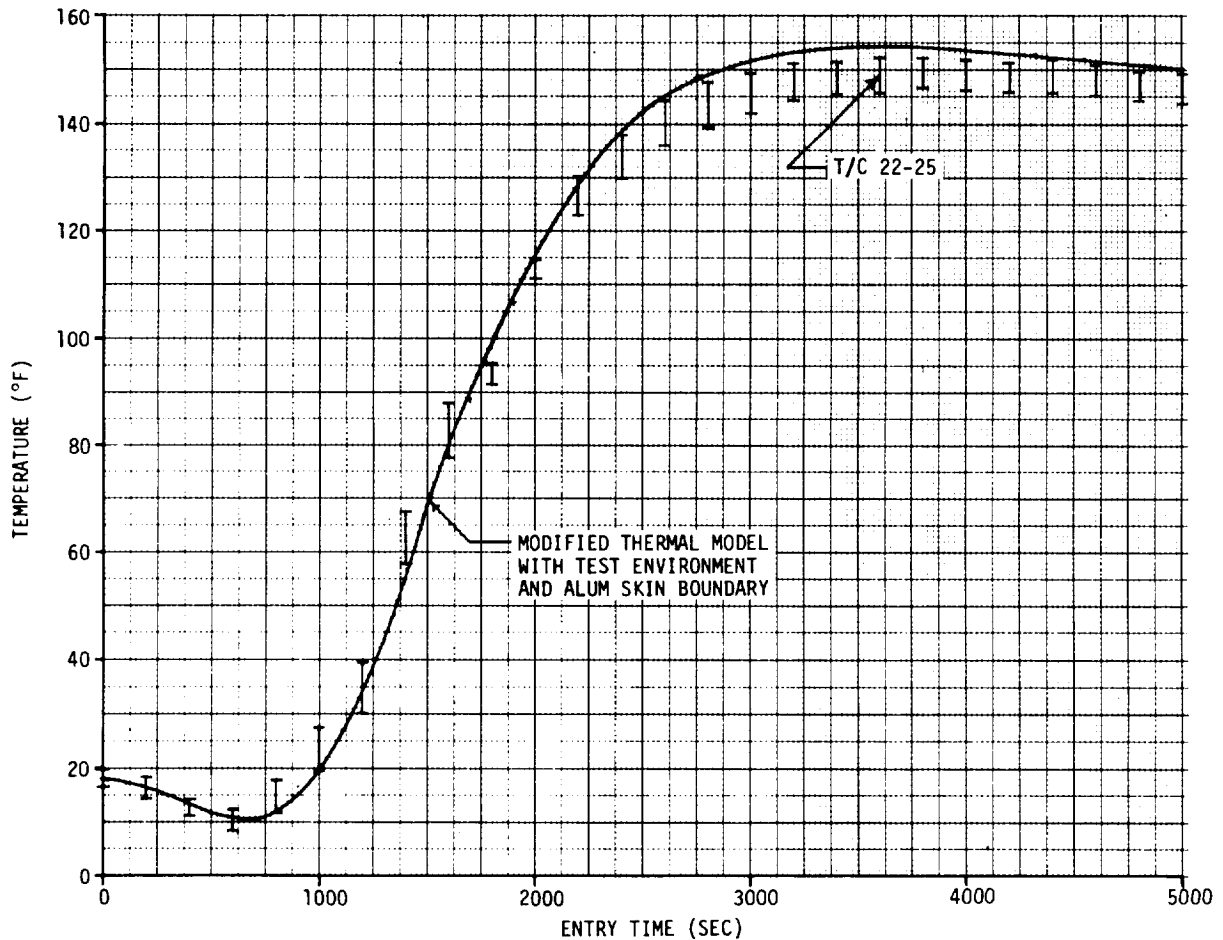


FIGURE 127 OUTBOARD STRUCTURAL SKIN TEMPERATURES - ENTRY FROM COLD ORBIT

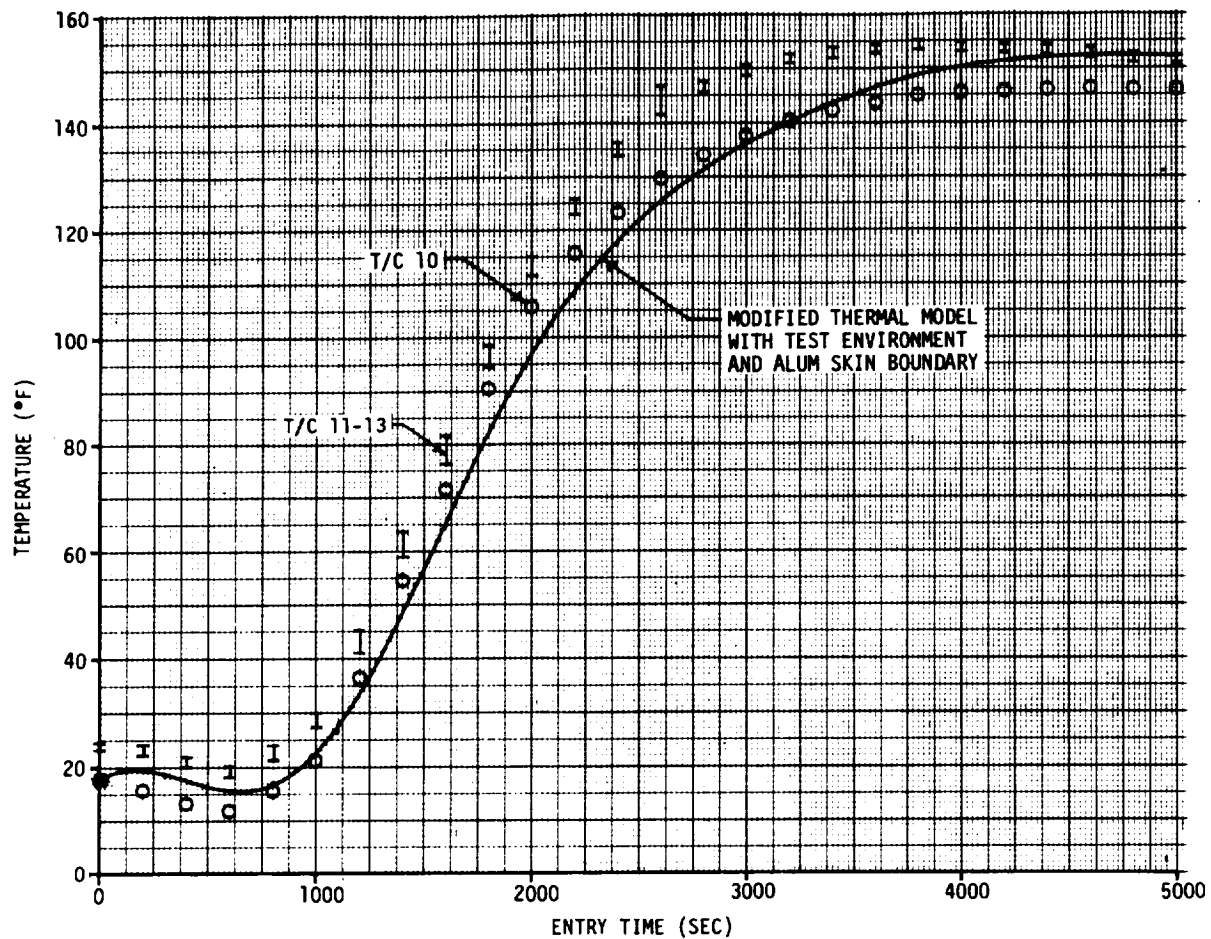


FIGURE 128 INBOARD STRUCTURAL SKIN TEMPERATURES - ENTRY FROM COLD ORBIT

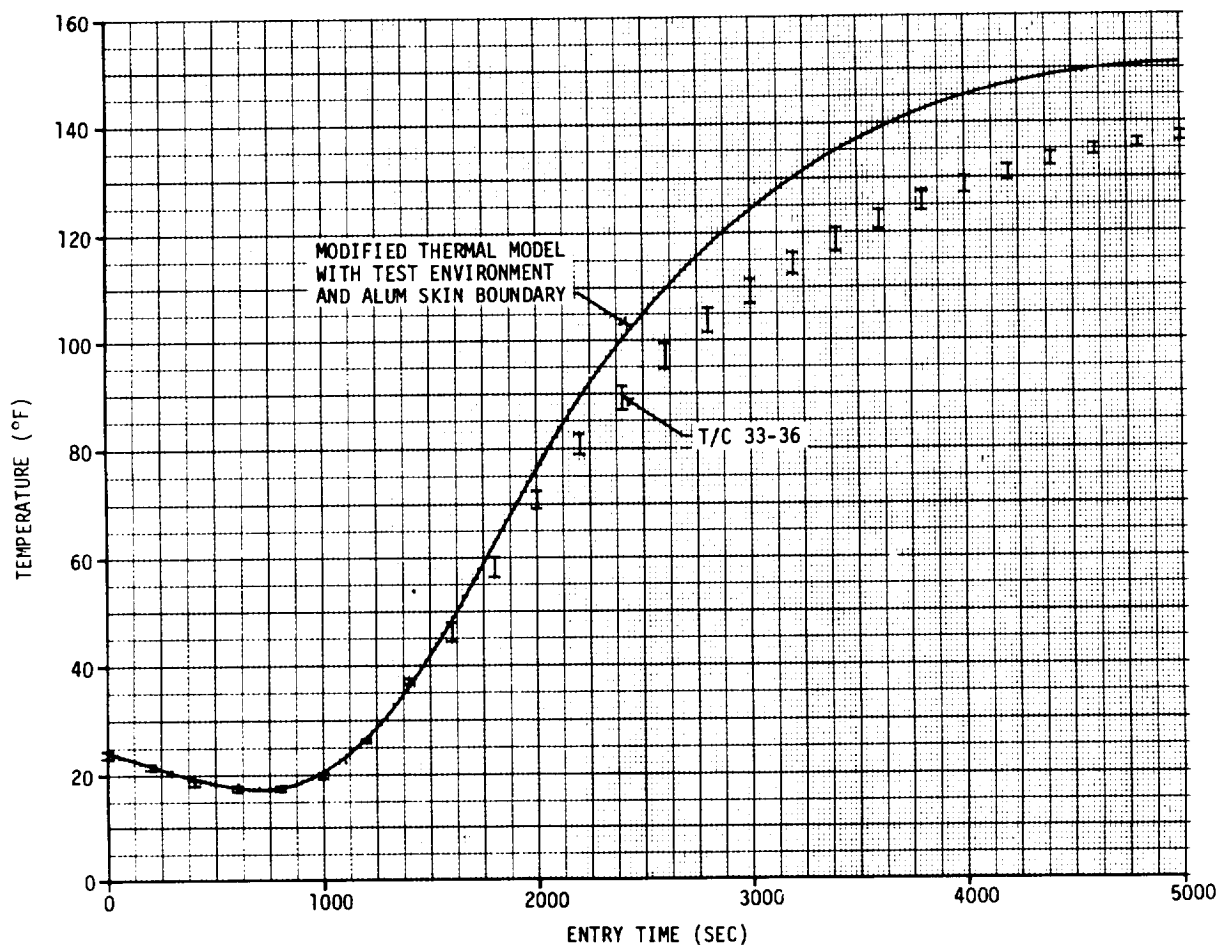


FIGURE 129 ANTENNA FLANGE TEMPERATURES - ENTRY FROM COLD ORBIT

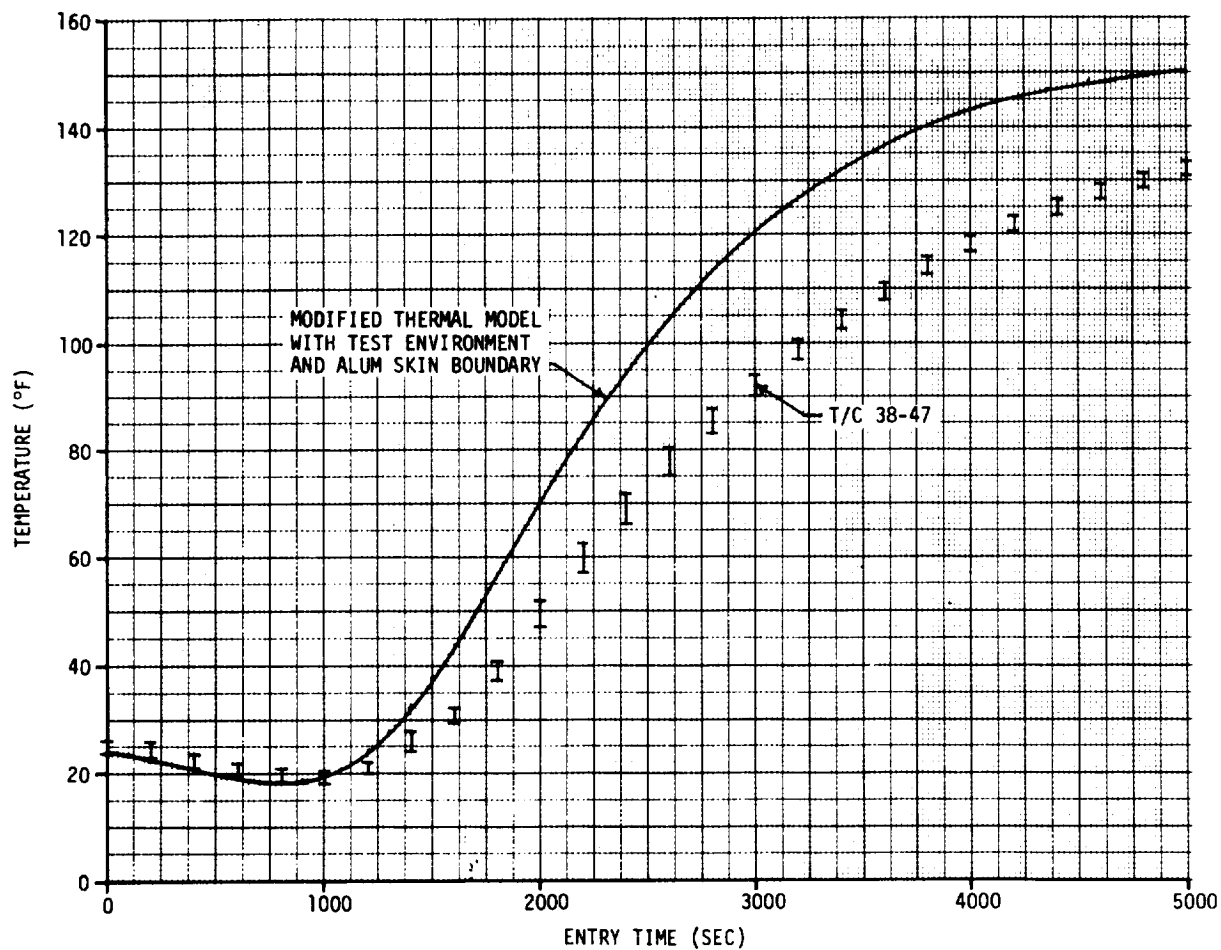


FIGURE 130 ANTENNA ELEMENT TEMPERATURES - ENTRY FROM COLD ORBIT



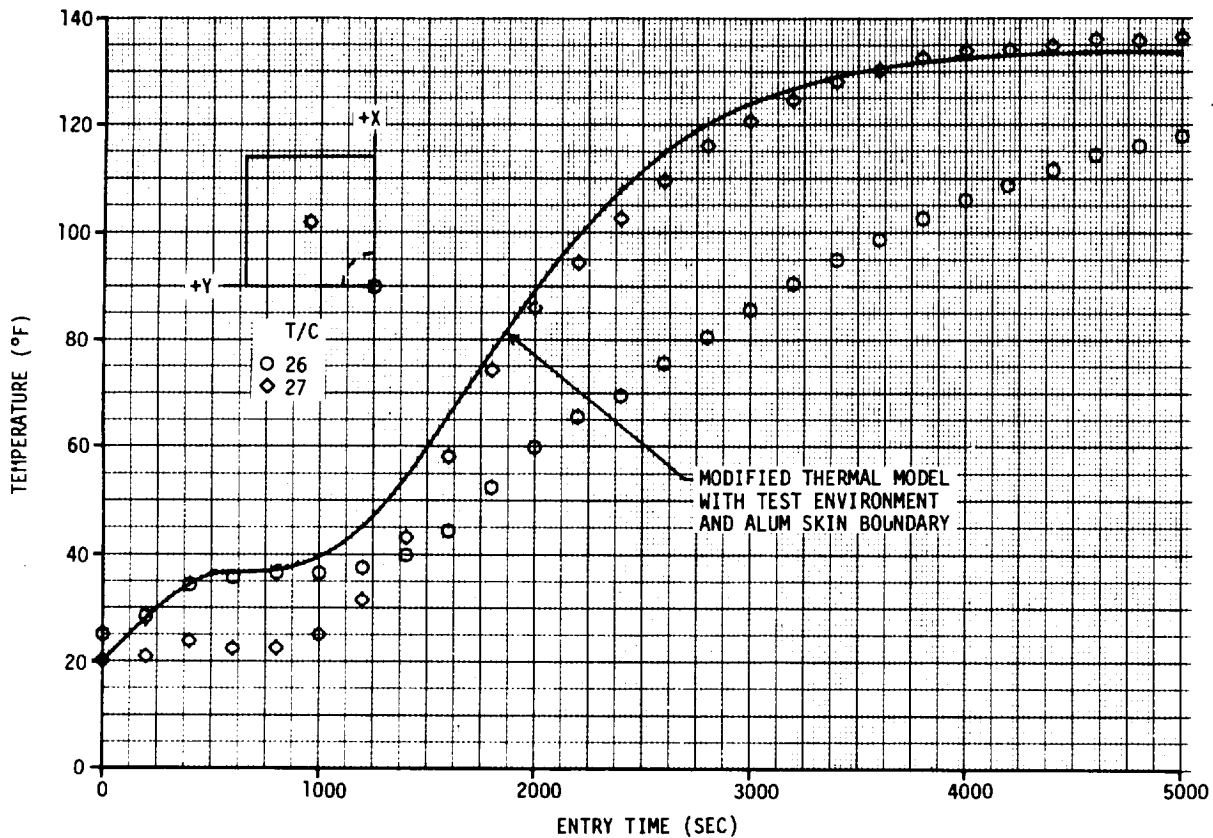


FIGURE 131 INSULATION TEMPERATURES - ENTRY FROM COLD ORBIT



**REFERENCES**

1. Kuhlman, E. A., "Development of S-band Antenna Interface Design," NAS 9-14722, McDonnell Douglas Astronautics Company-East, Volume I, Final Report, MDC E0896, April 1976.
2. Kuhlman, E. A., "High Temperature Antenna Development for Space Shuttle," NAS 9-13304, McDonnell Douglas Astronautics Company-East, Volume I, Final Report, MDC E0896, July 1973.
3. Kuhlman, E. A., "High Temperature Antenna Development for Space Shuttle," NAS 9-13004, McDonnell Douglas Astronautics Company-East, Volume II, Final Report, MDC E0896, April 1974.

**DEVELOPMENT OF S-BAND ANTENNA INTERFACE DESIGN  
SHUTTLE ANTENNA RADOME TECHNOLOGY TEST PROGRAM**

**REPORT MDC E1478  
15 JUNE 1977  
VOLUME II**

THIS PAGE INTENTIONALLY LEFT BLANK

**APPENDIX A**

**REFERENCE RADIATION PATTERNS IN RECTANGULAR COORDINATES**

The radiation patterns in rectangular coordinates given in this appendix correspond to the radiation patterns in polar coordinates given in figures 39, 40 and 41 of the text. These patterns were used as the reference or baseline data for analyzing the patterns after each thermal test.

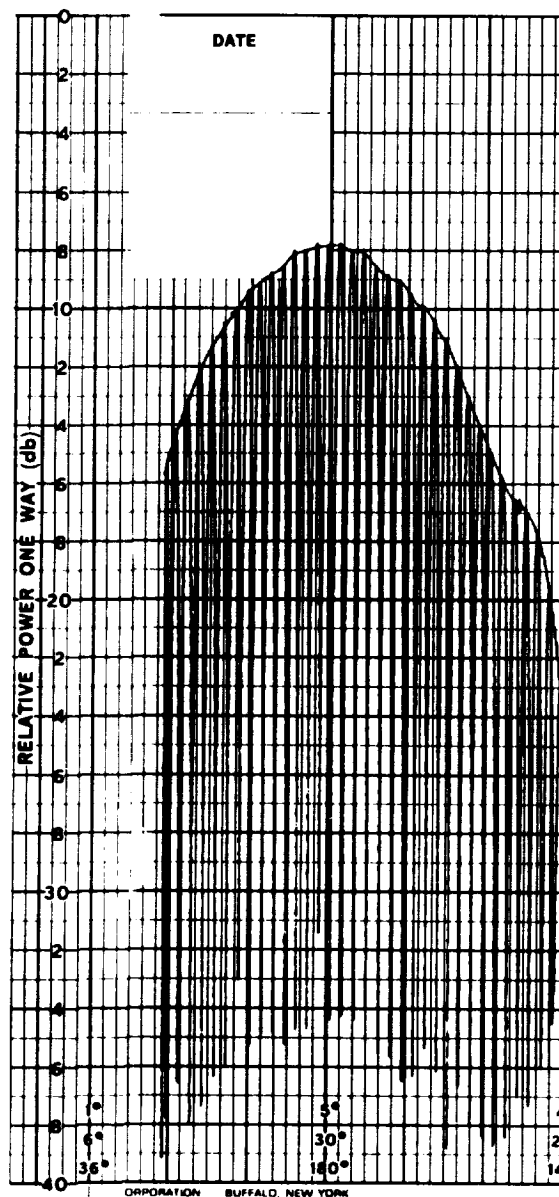
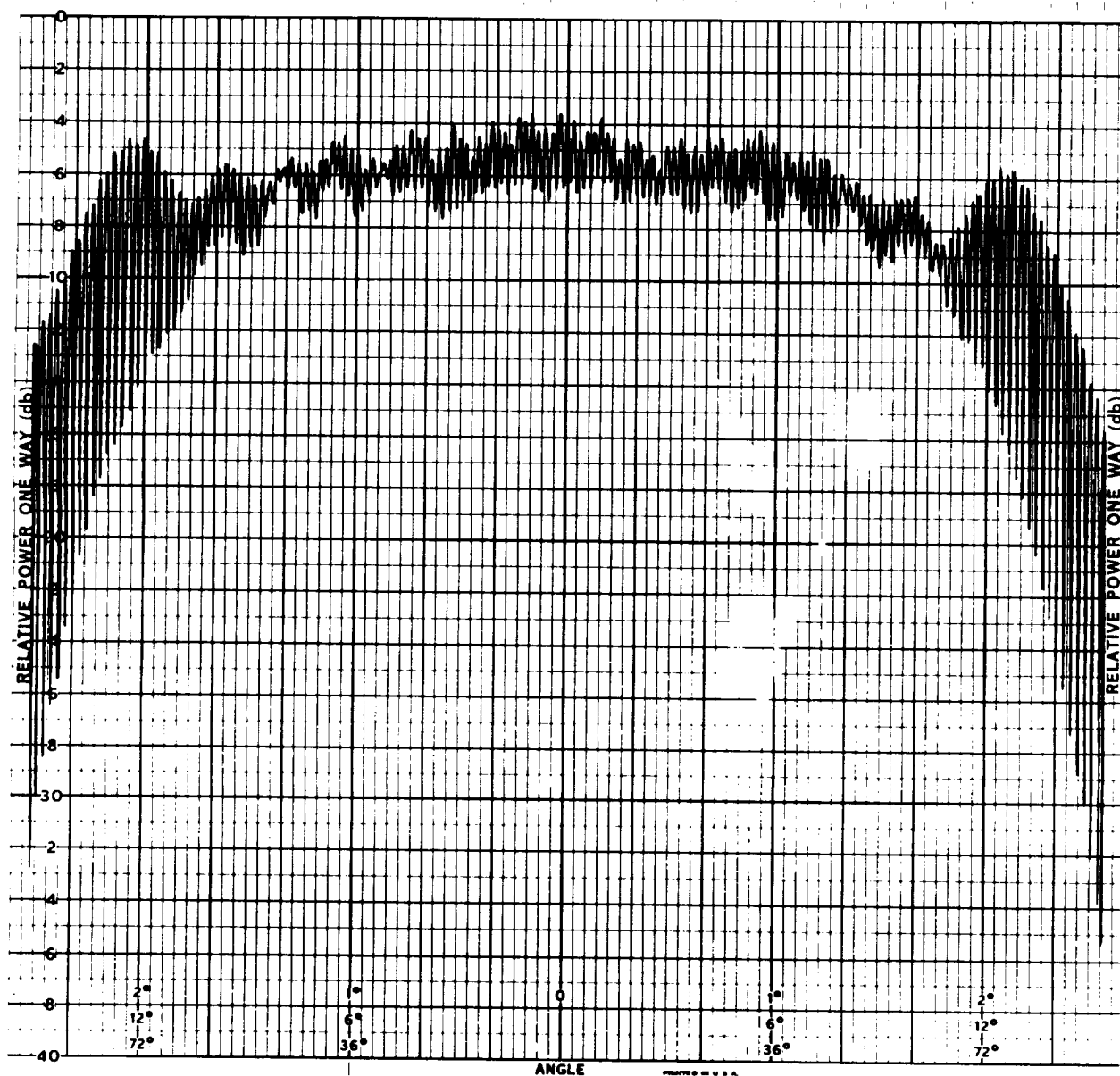
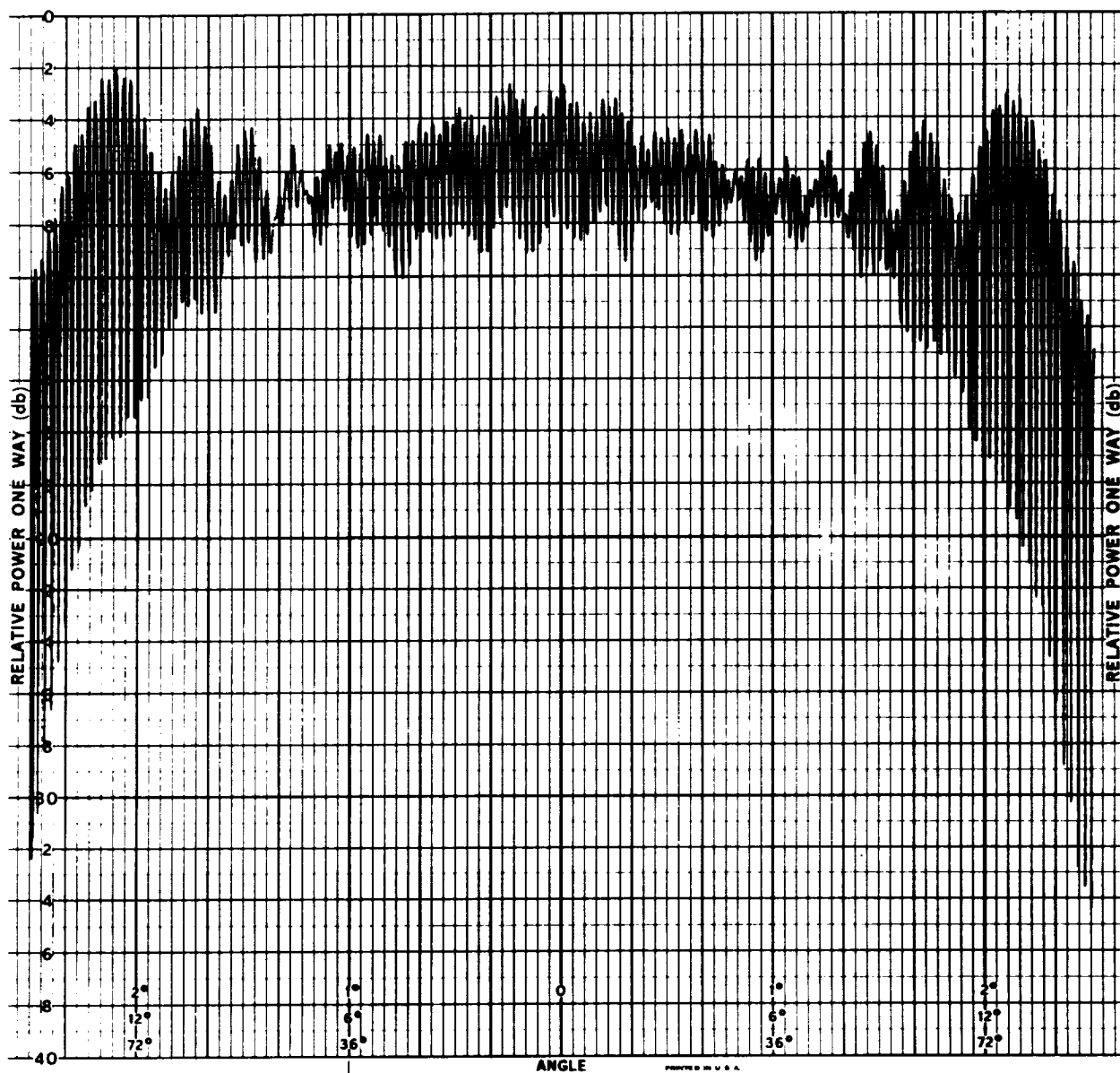


FIGURE 132 STANDARD GAIN HORN REFERENCE LEVEL - 1.8 GHz



(a)  $\phi = 0^\circ$

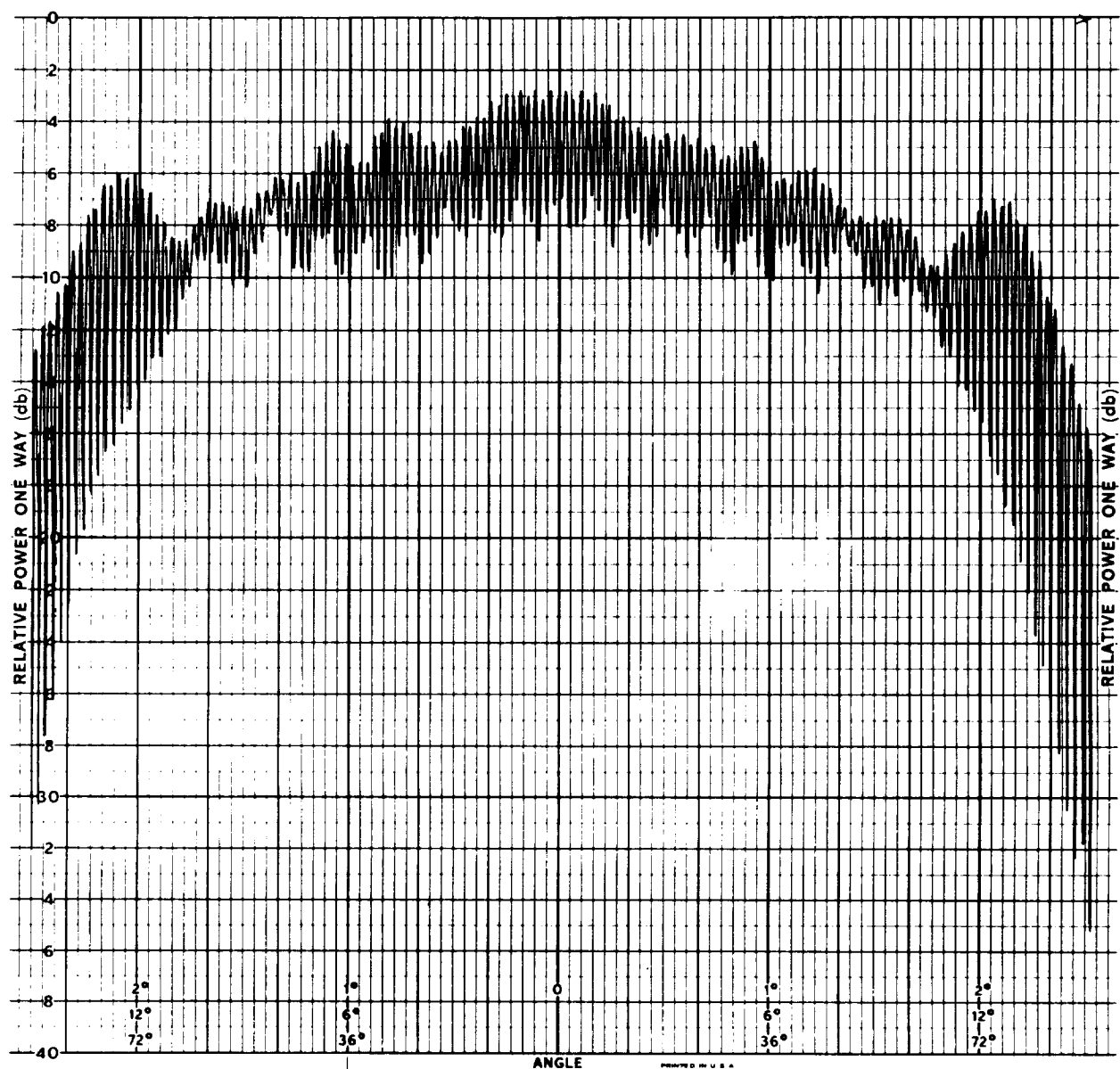
FIGURE 133 REFERENCE RADIATION PATTERNS - 1.8 GHz



(b)  $\phi = 45^\circ$

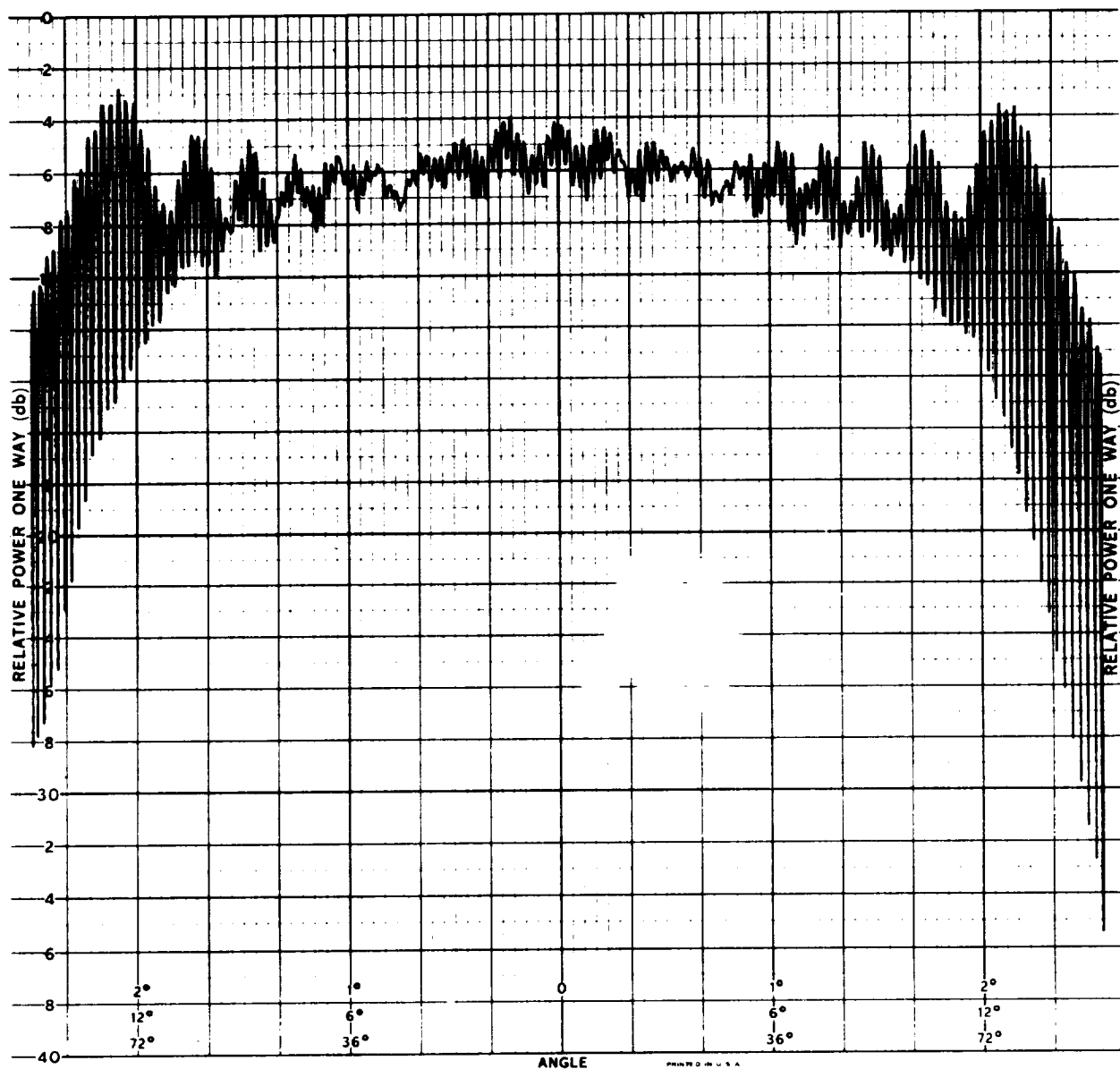
FIGURE 133 REFERENCE RADIATION PATTERNS - 1.8 GHz (CONT)





(c)  $\phi = 90^\circ$

FIGURE 133 REFERENCE RADIATION PATTERNS - 1.8 GHz (CONT)



(d)  $\phi = 315^\circ$

FIGURE 133 REFERENCE RADIATION PATTERNS - 1.8 GHz (CONT)

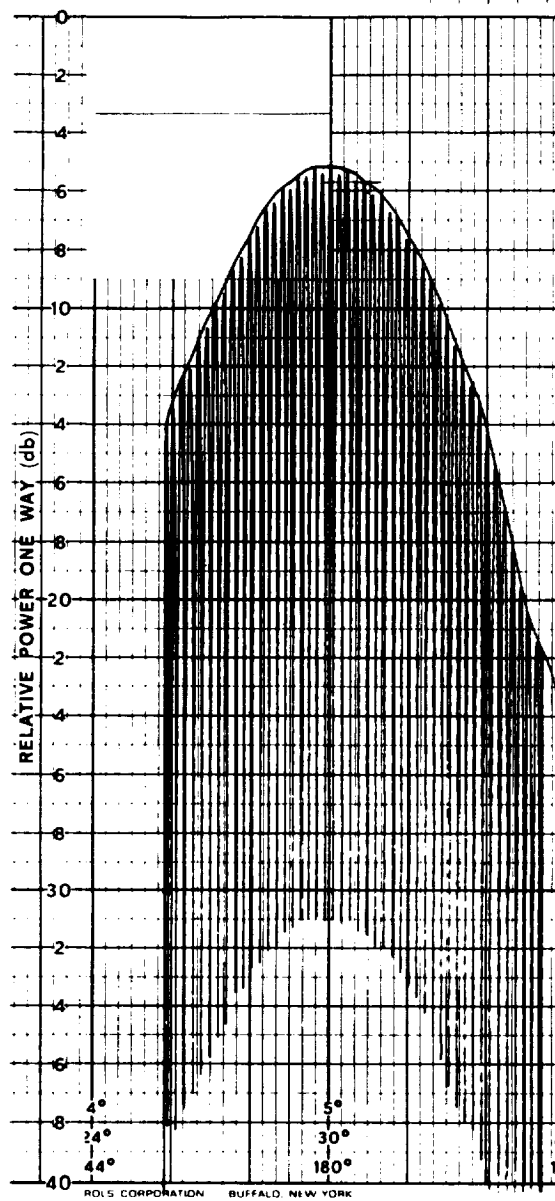
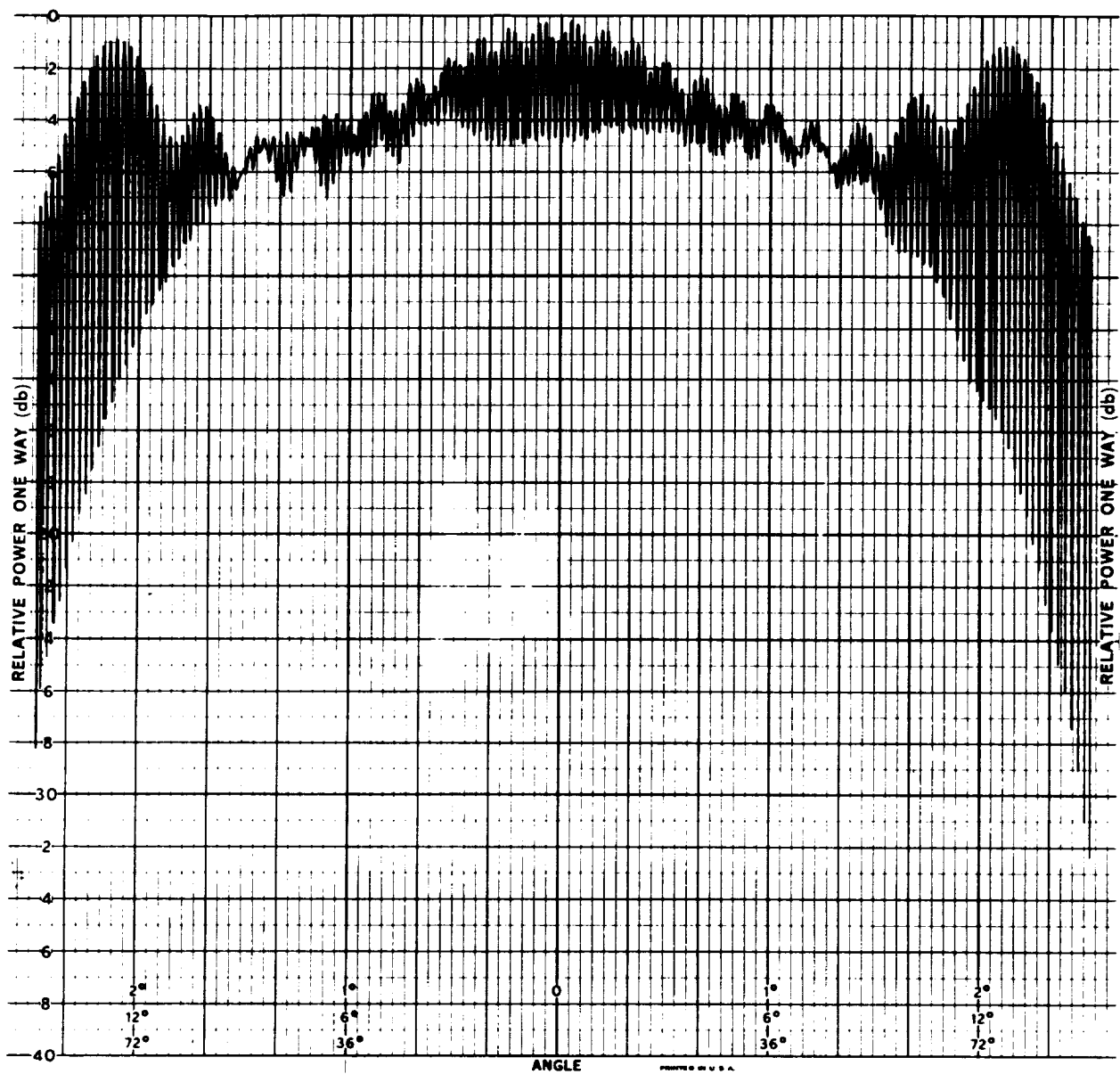
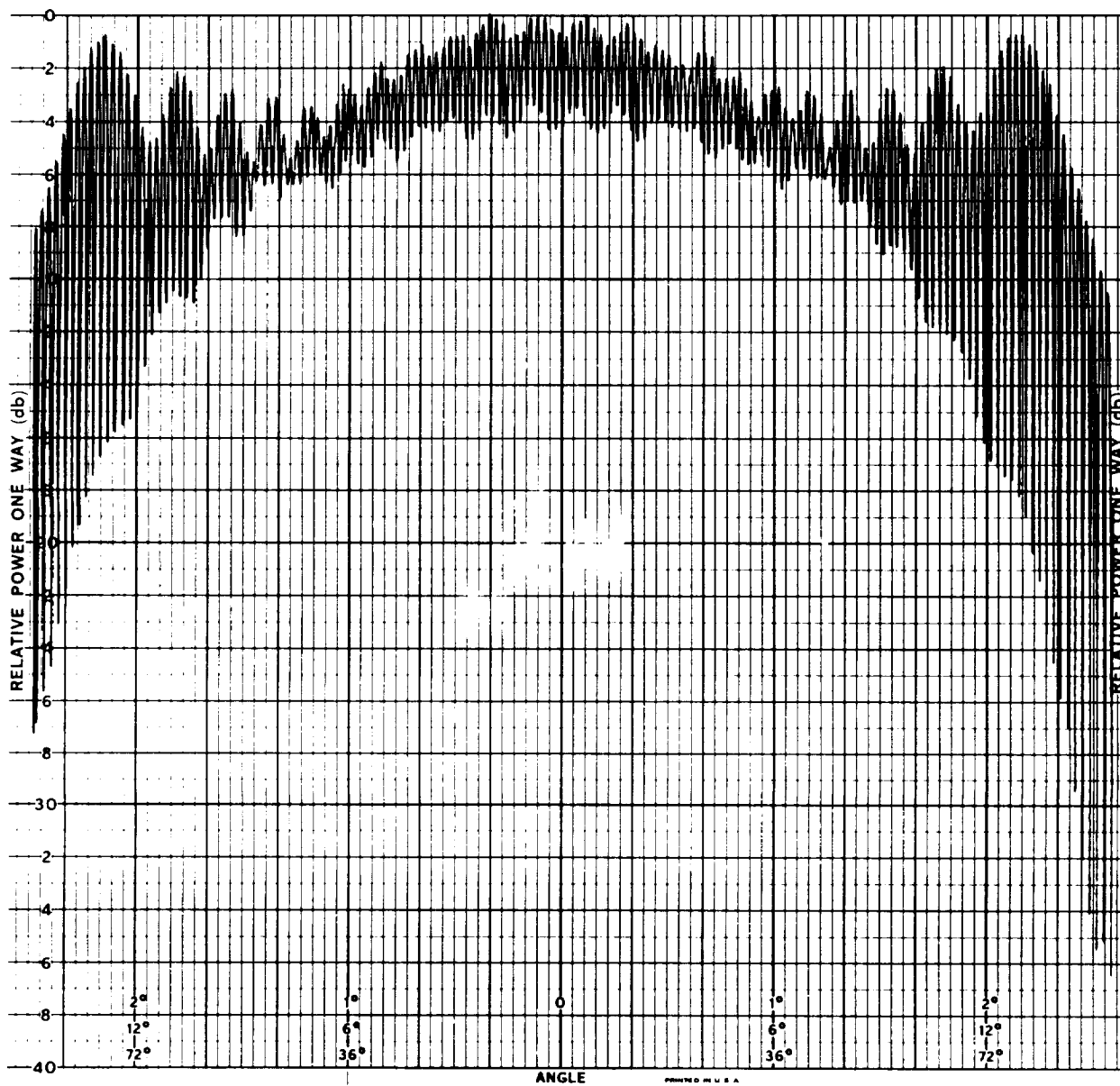


FIGURE 134 STANDARD GAIN HORN REFERENCE LEVEL - 2.1 GHz



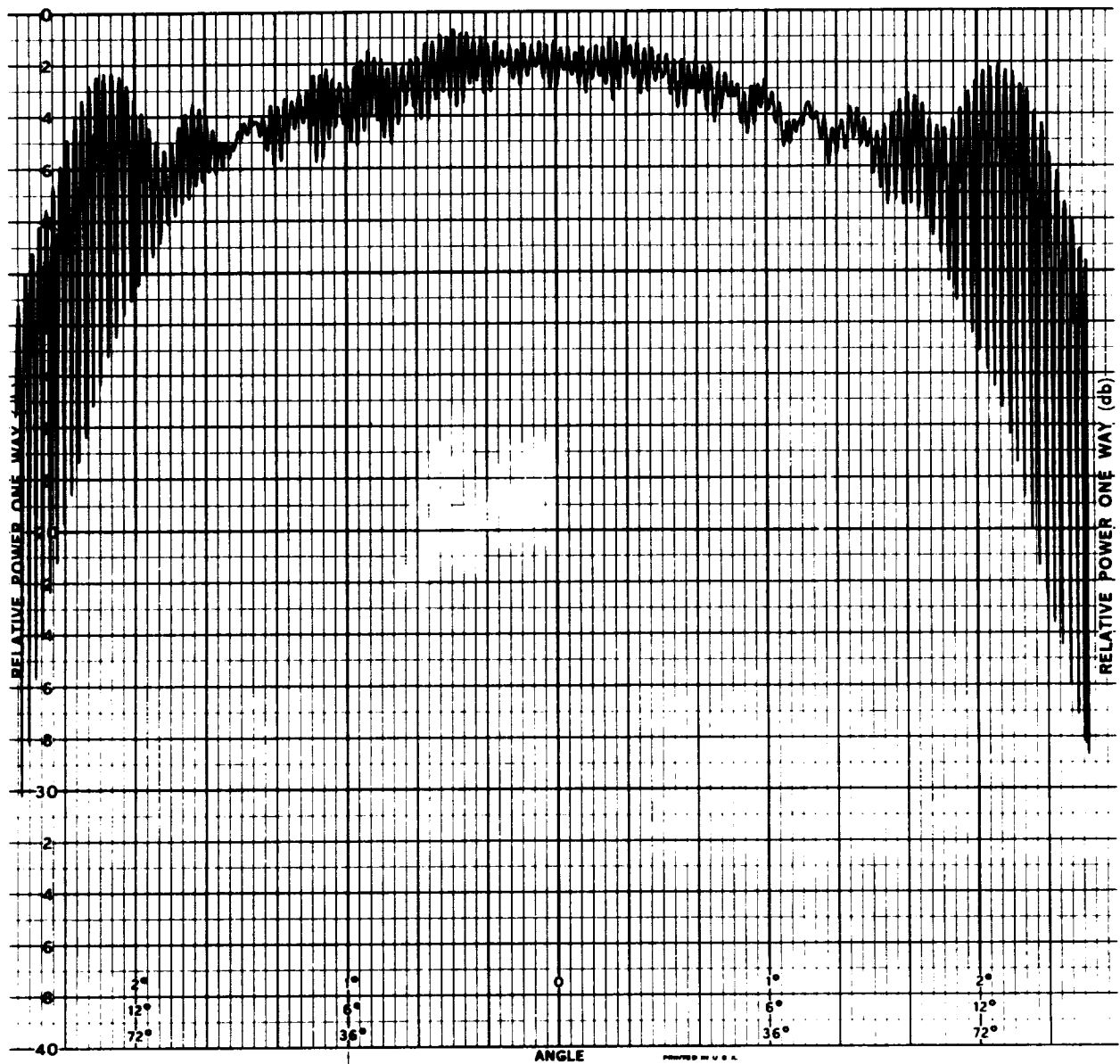
(a)  $\phi = 0^\circ$

FIGURE 135 REFERENCE RADIATION PATTERNS - 2.1 GHz



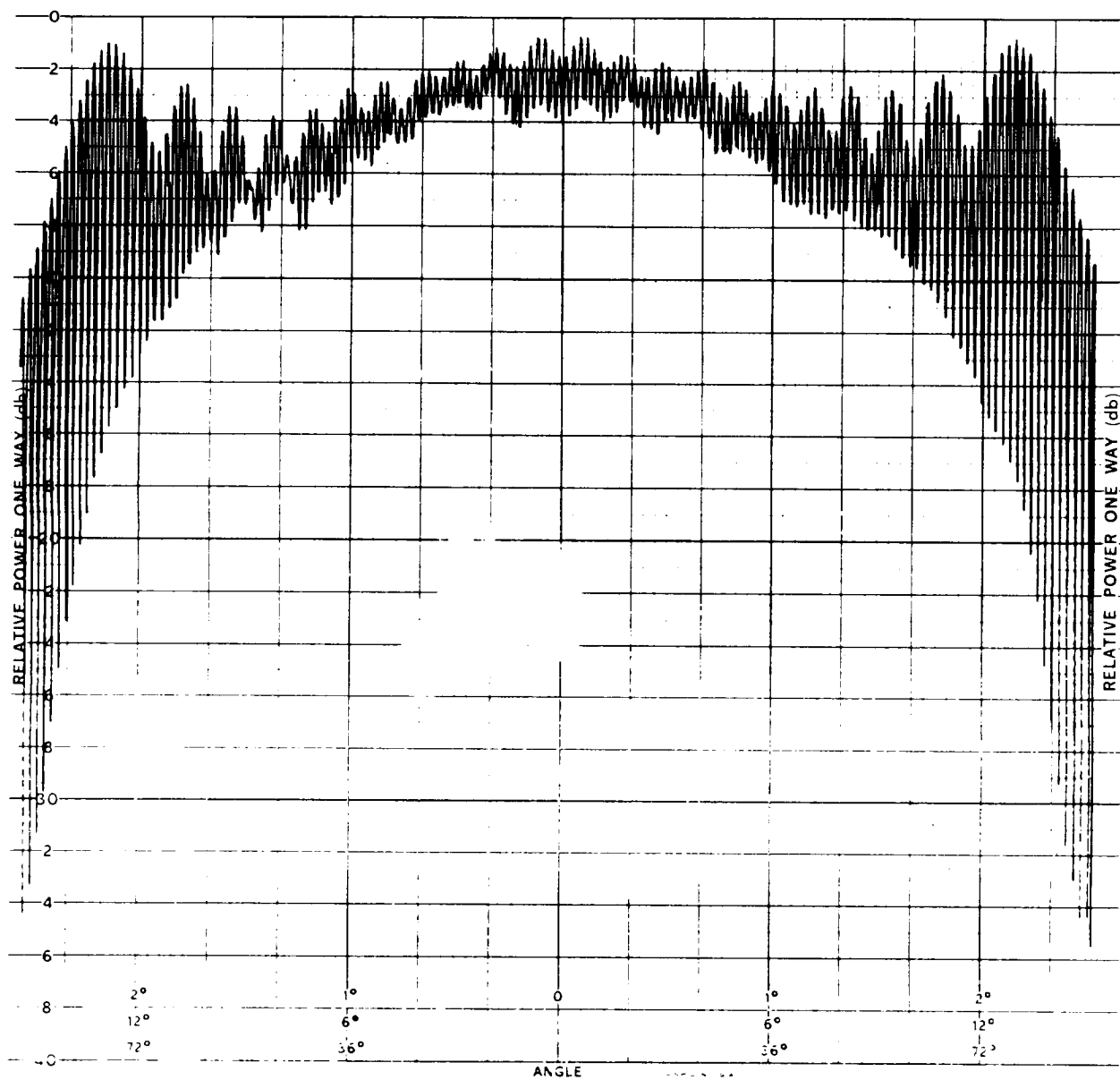
(b)  $\phi = 45^\circ$

FIGURE 135 REFERENCE RADIATION PATTERNS - 2.1 GHz (CONT)



(c)  $\phi = 90^\circ$

FIGURE 135 REFERENCE RADIATION PATTERNS - 2.1 GHz (CONT)



(d)  $\phi = 315^\circ$

FIGURE 135 REFERENCE RADIATION PATTERNS - 2.1 GHz (CONT)

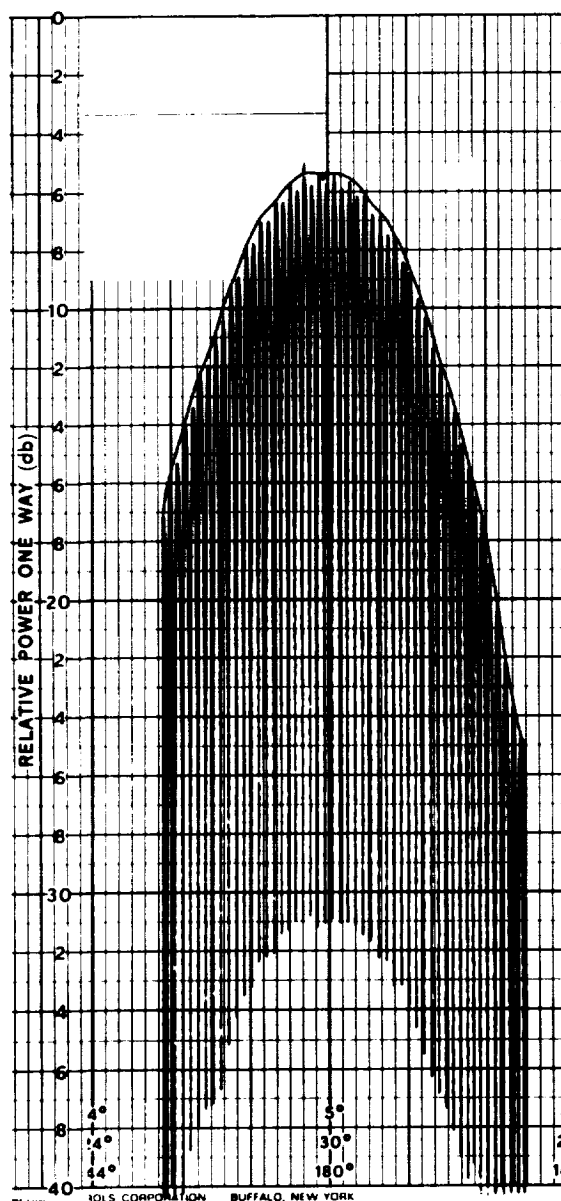
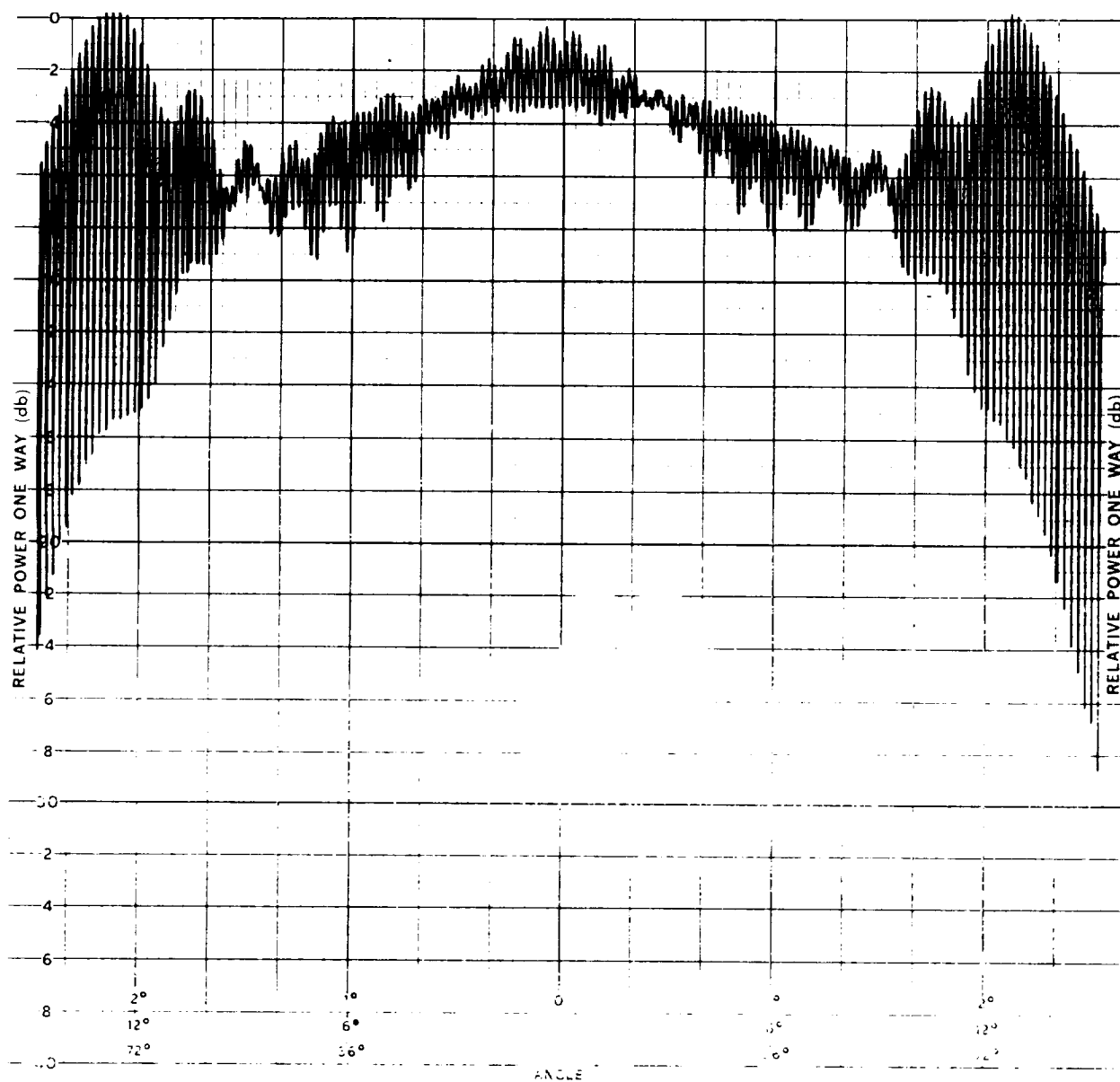


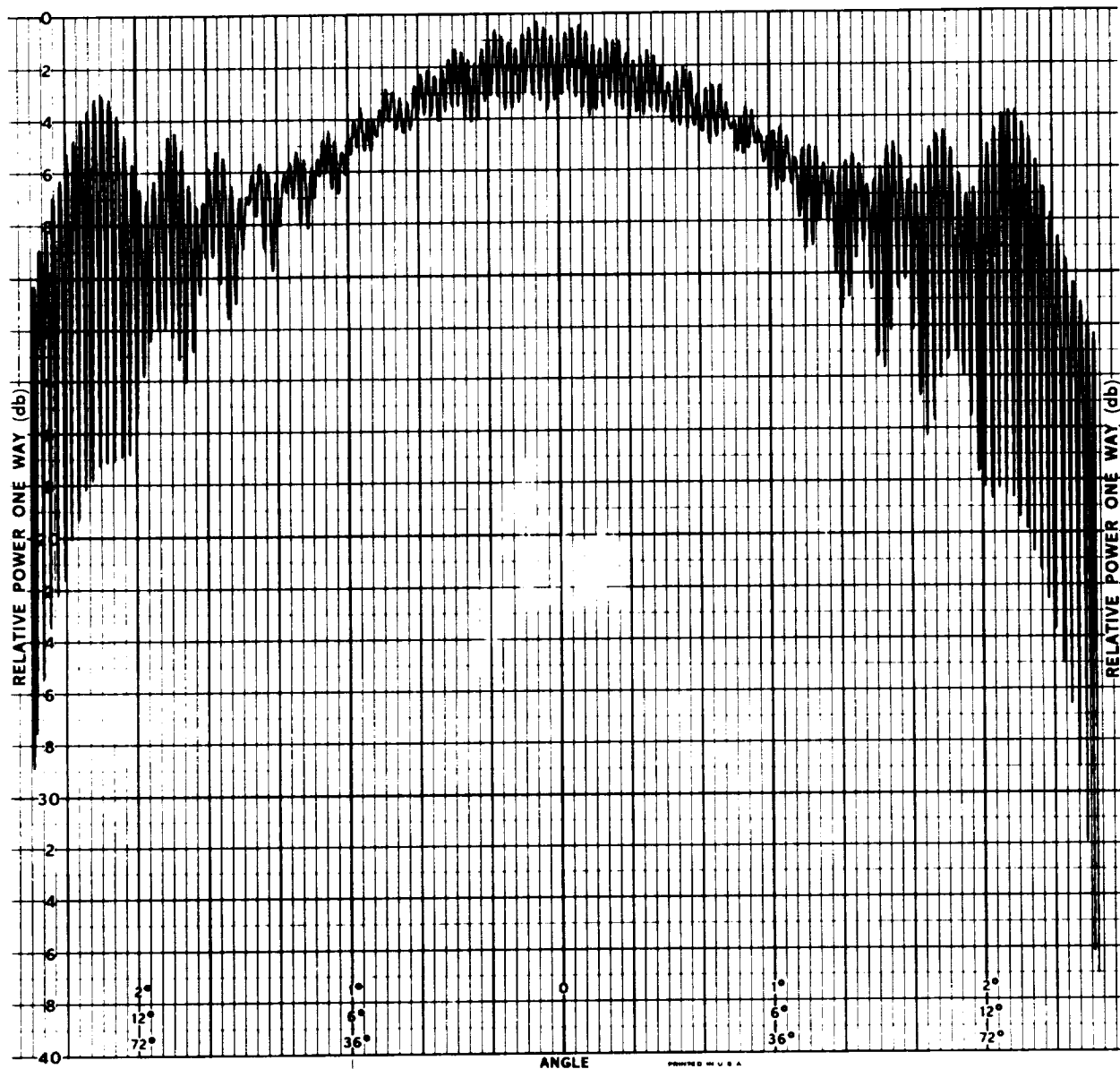
FIGURE 136 STANDARD GAIN HORN REFERENCE LEVEL - 2.3 GHz





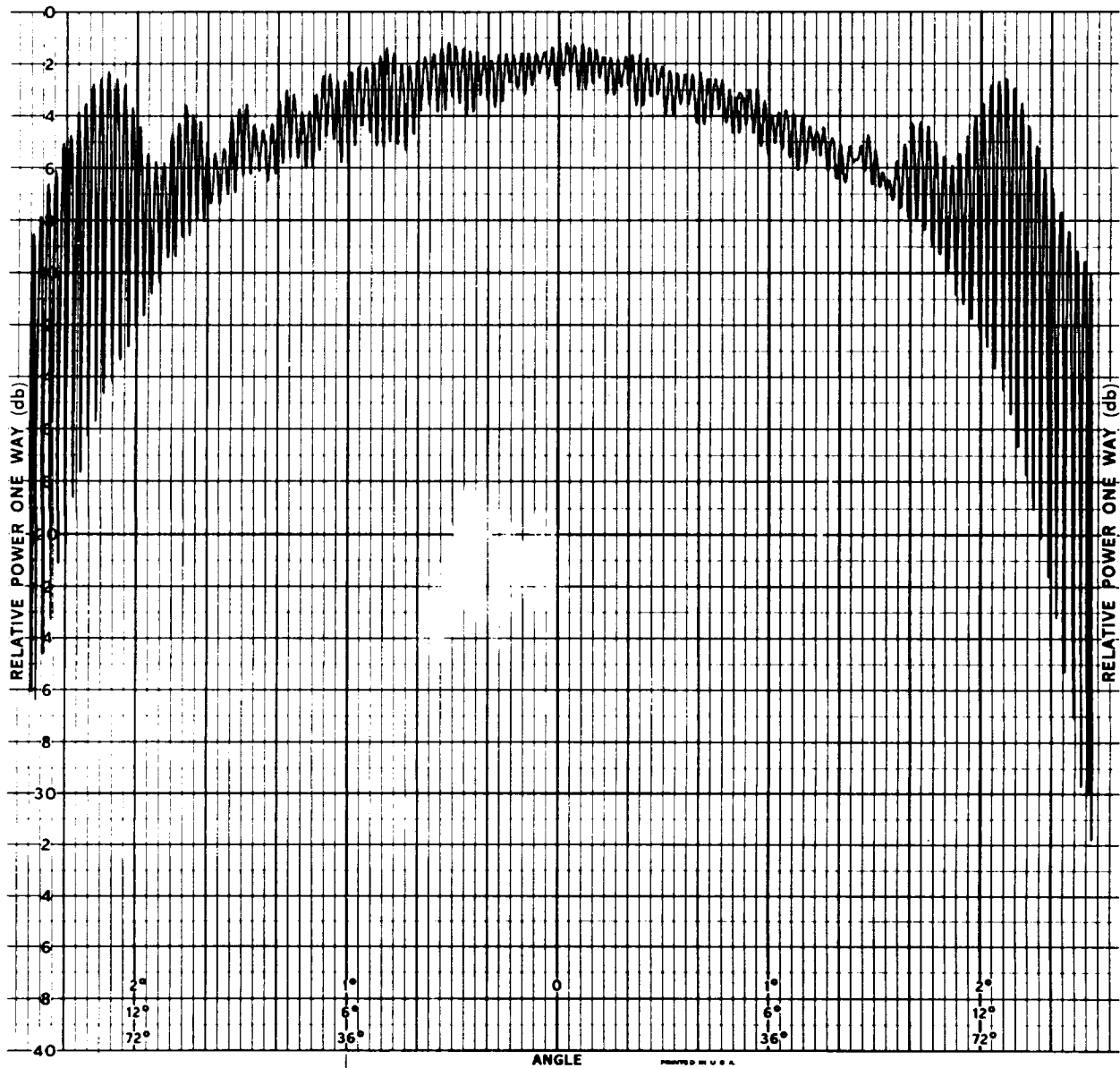
(a)  $\phi = 0^\circ$

FIGURE 137 REFERENCE RADIATION PATTERNS - 2.3 GHz



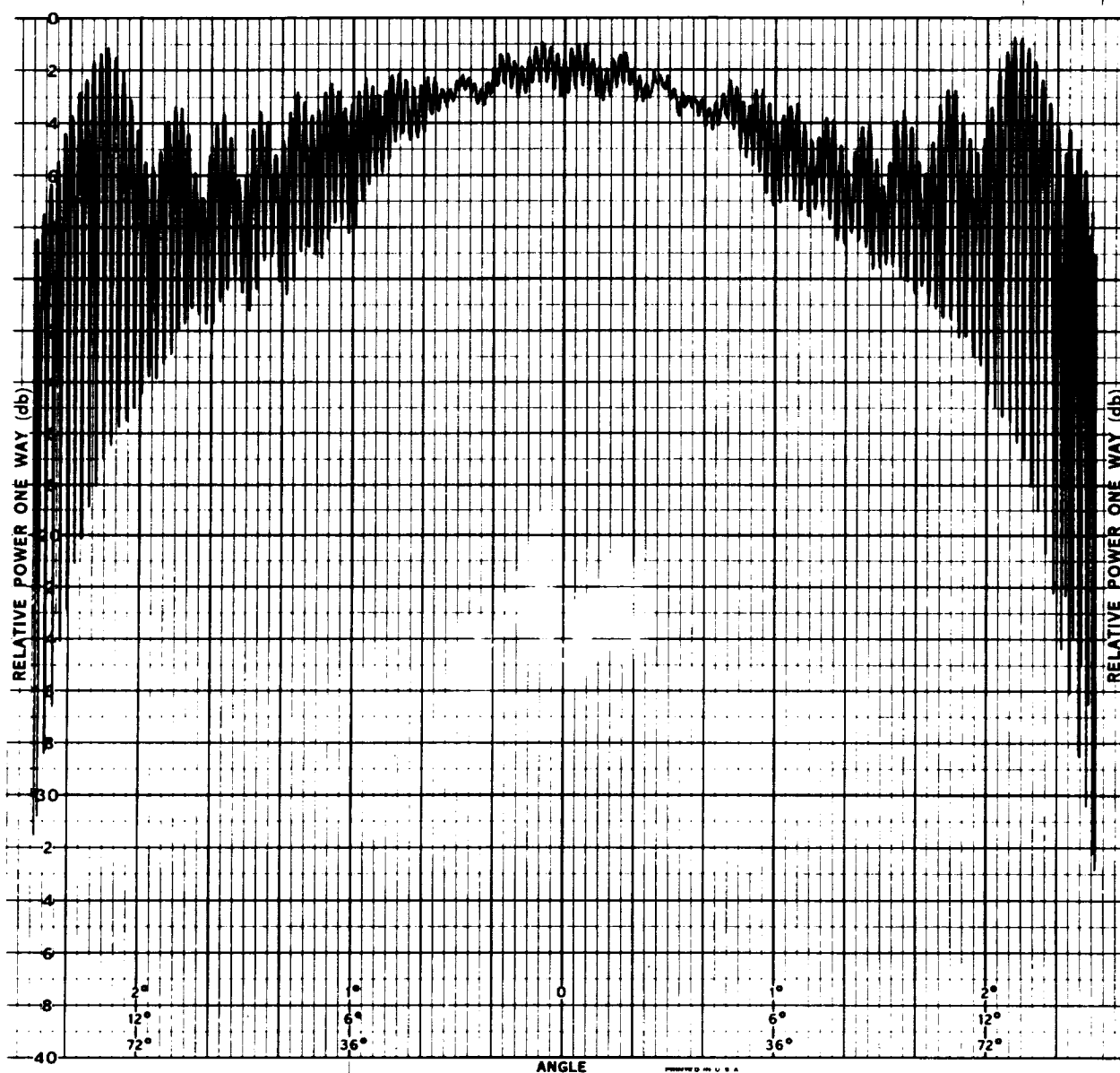
(b)  $\phi = 45^\circ$

FIGURE 137 REFERENCE RADIATION PATTERNS - 2.3 GHz (CONT)



(c)  $\phi = 90^\circ$

FIGURE 137 REFERENCE RADIATION PATTERNS - 2.3 GHz (CONT)



(d)  $\phi = 315^\circ$

FIGURE 137 REFERENCE RADIATION PATTERNS - 2.3 GHz (CONT)

**APPENDIX B**

**RADIATION PATTERNS IN RECTANGULAR COORDINATES FOR TEST 4**

The radiation patterns in rectangular coordinates given in this appendix correspond to the radiation patterns in polar coordinates given in figures 42, 43 and 44. These patterns are from Test 4 but are typical of those obtained for the other tests.

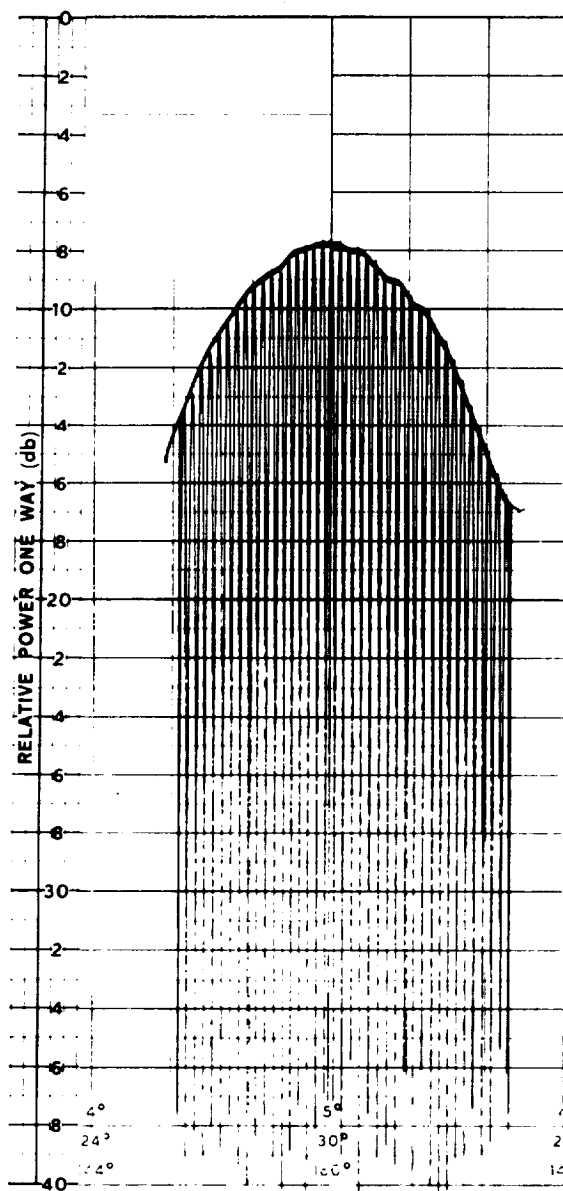
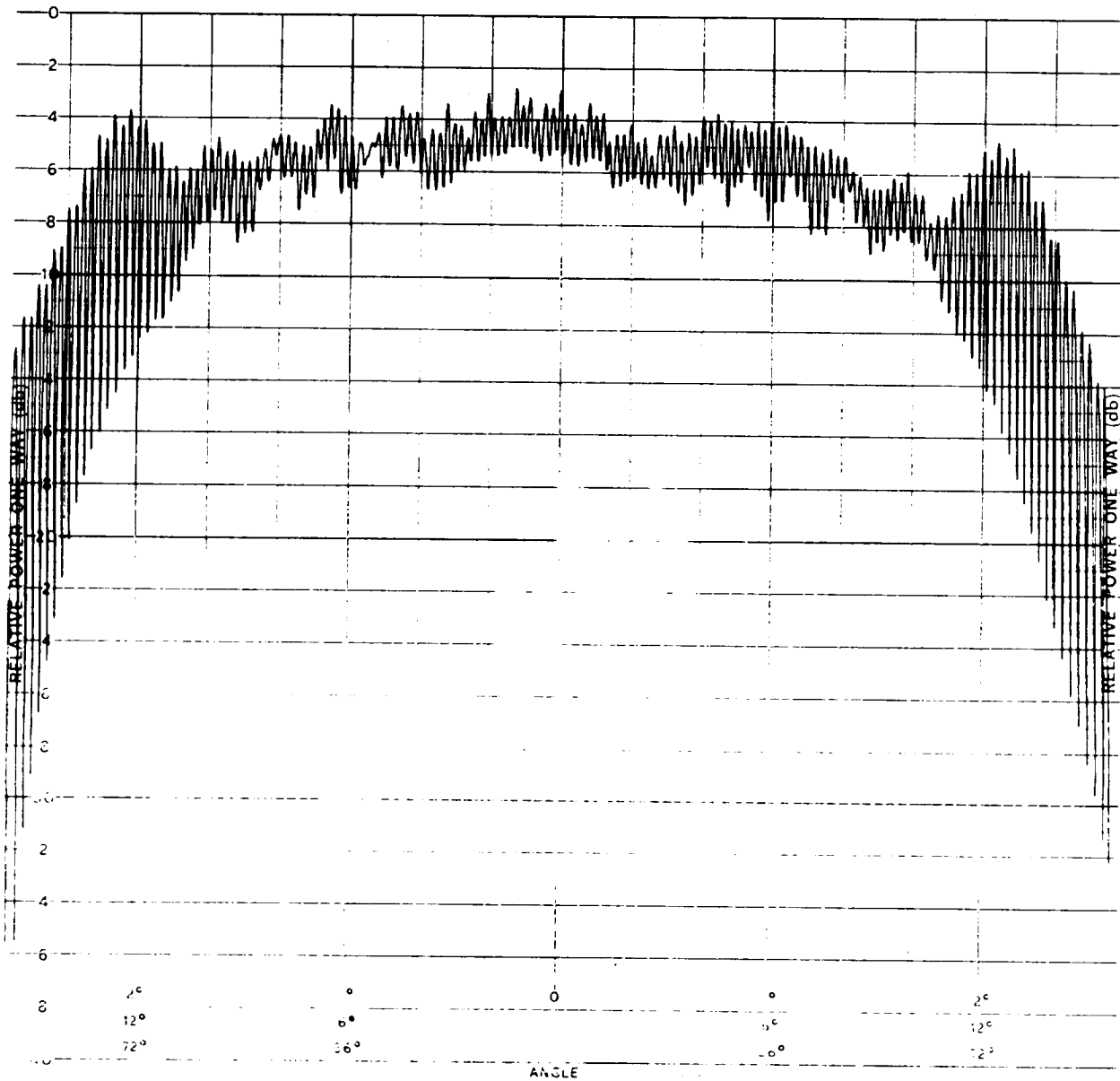
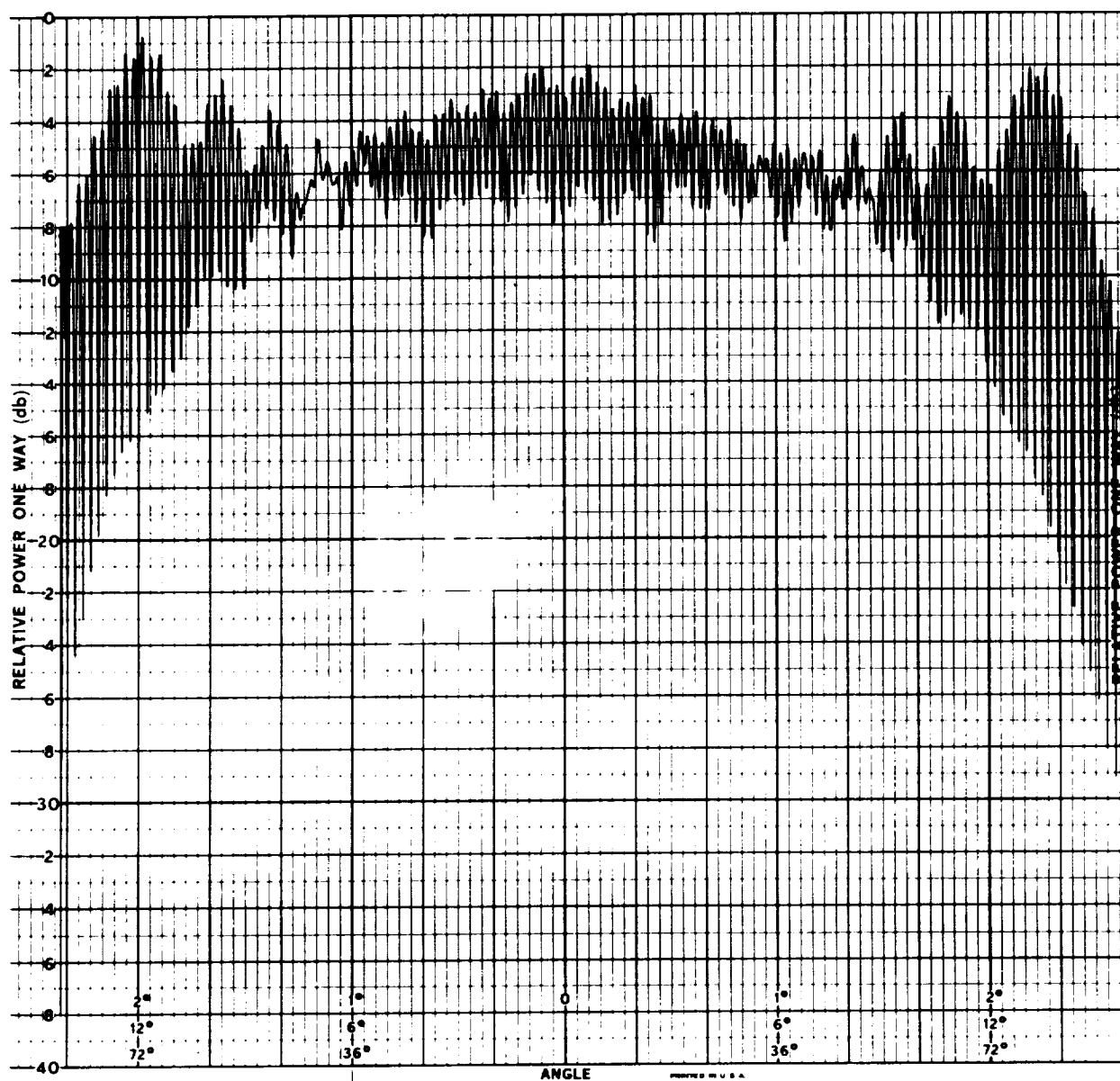


FIGURE 138 STANDARD GAIN HORN LEVEL FOR TEST 4 - 1.8 GHz



(a)  $\phi = 0^\circ$

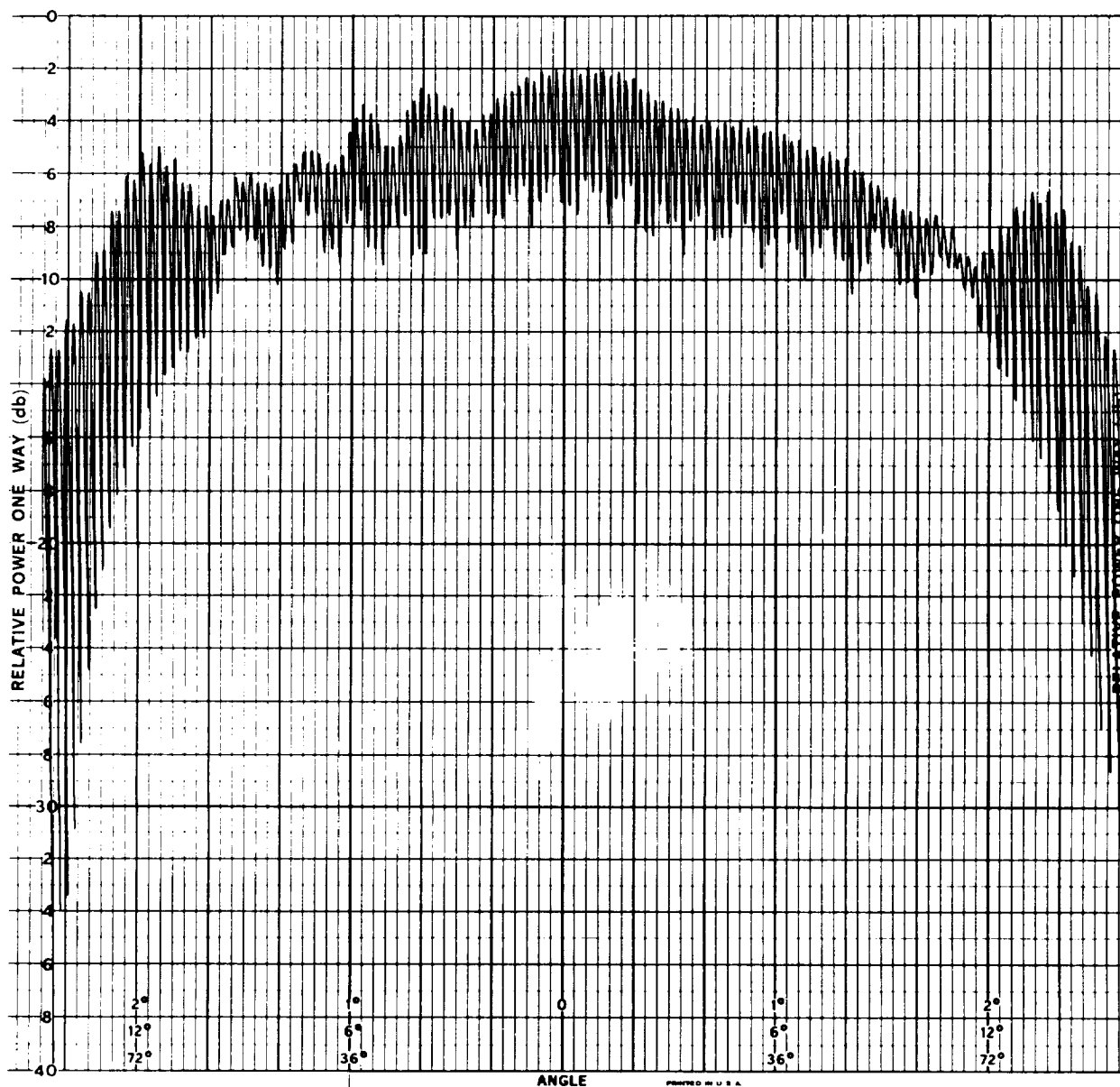
FIGURE 139 RADIATION PATTERNS FOR TEST 4 - 1.8 GHz



(b)  $\phi = 45^\circ$

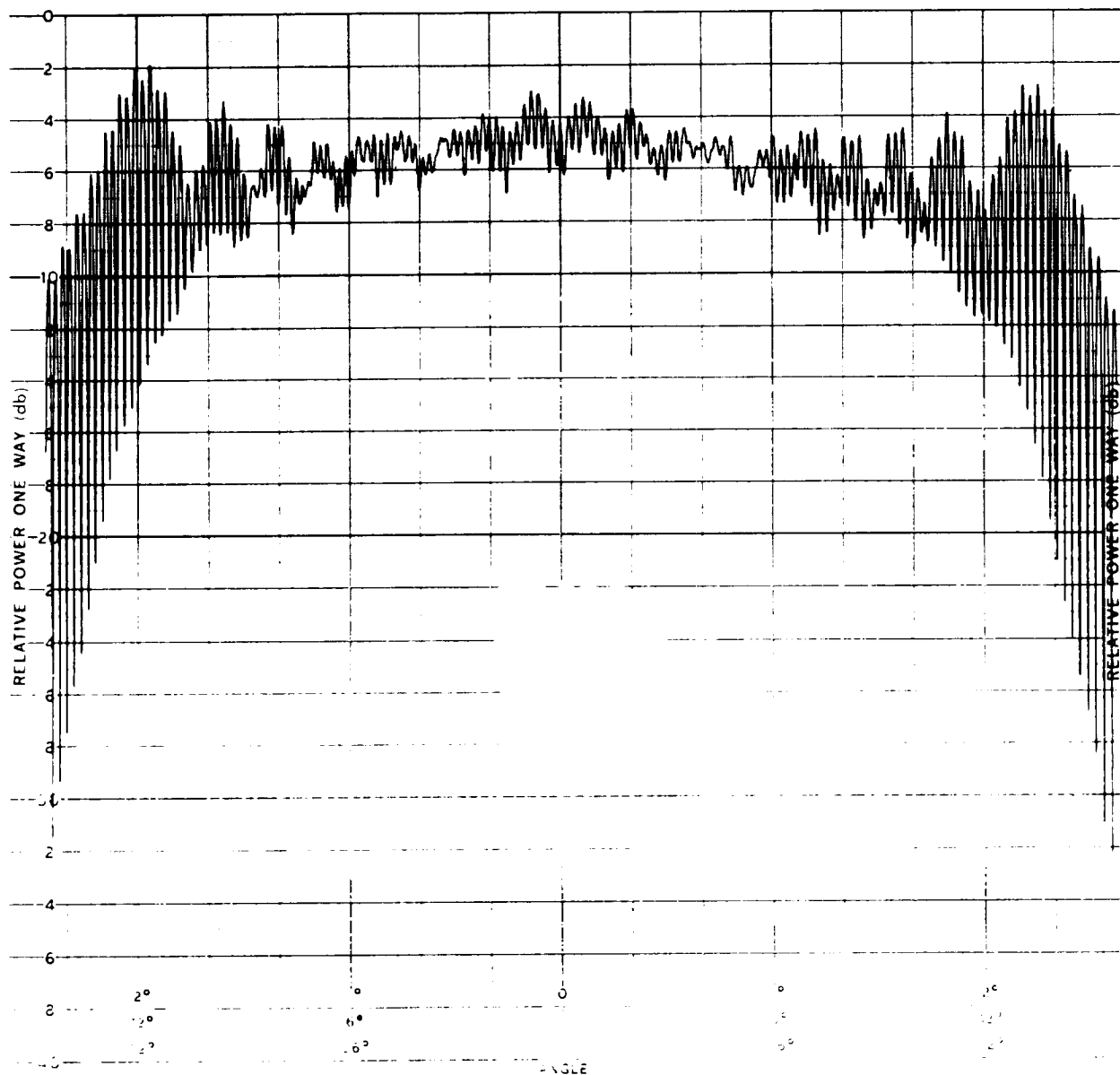
FIGURE 139 RADIATION PATTERNS FOR TEST 4 - 1.8 GHz (CONT)





(c)  $\phi = 90^\circ$

FIGURE 139 RADIATION PATTERNS FOR TEST 4 - 1.8 GHz (CONT)



(d)  $\phi = 315^\circ$

FIGURE 139 RADIATION PATTERNS FOR TEST 4 - 1.8 GHz (CONT)

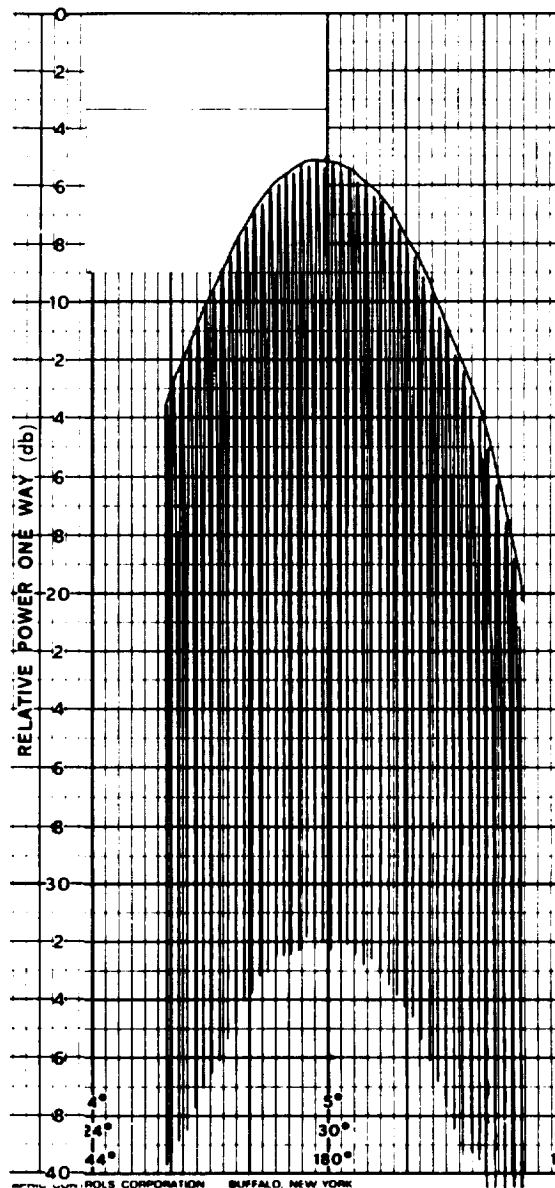
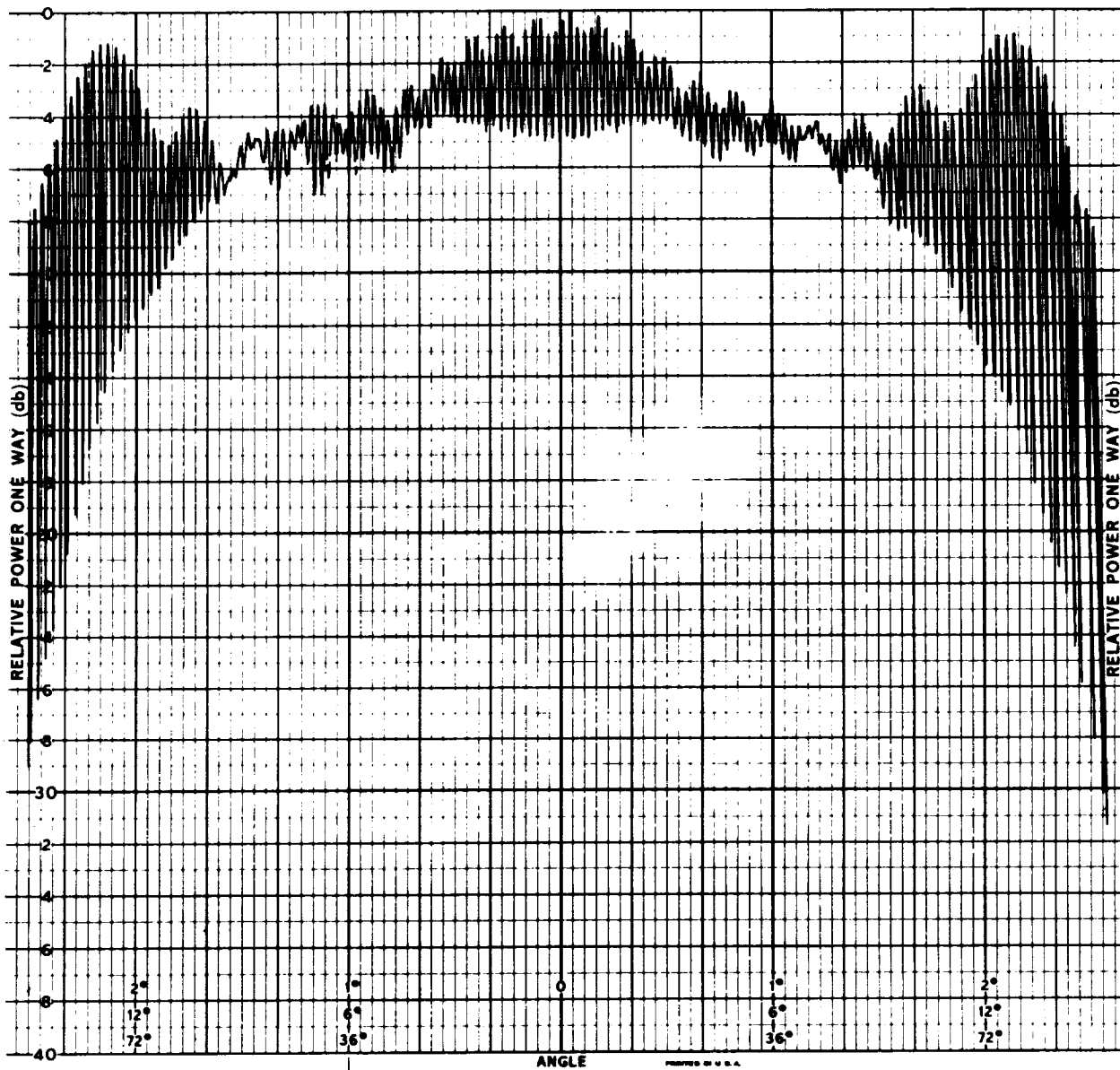
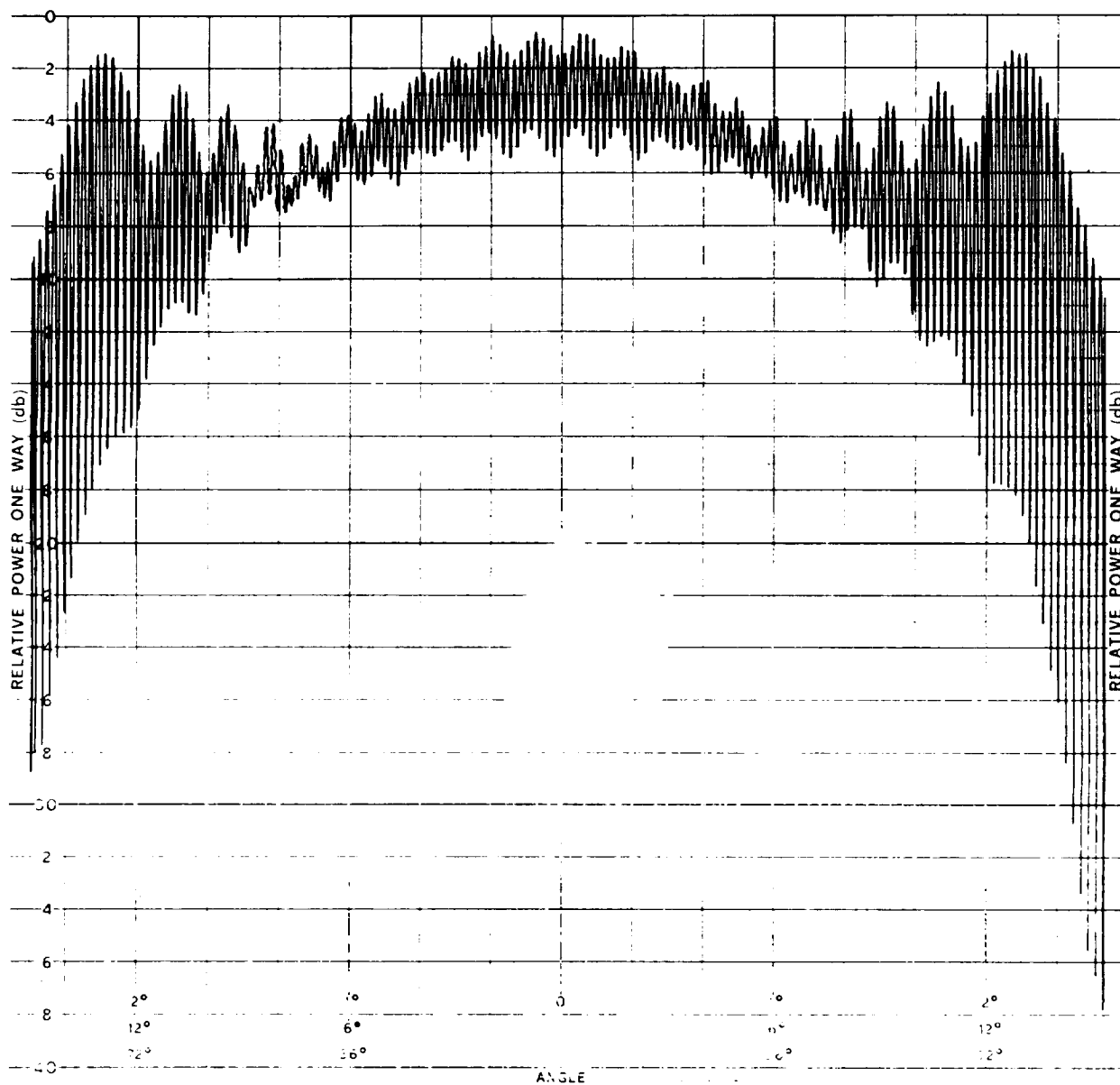


FIGURE 140 STANDARD GAIN HORN LEVEL FOR TEST 4 - 2.1 GHz



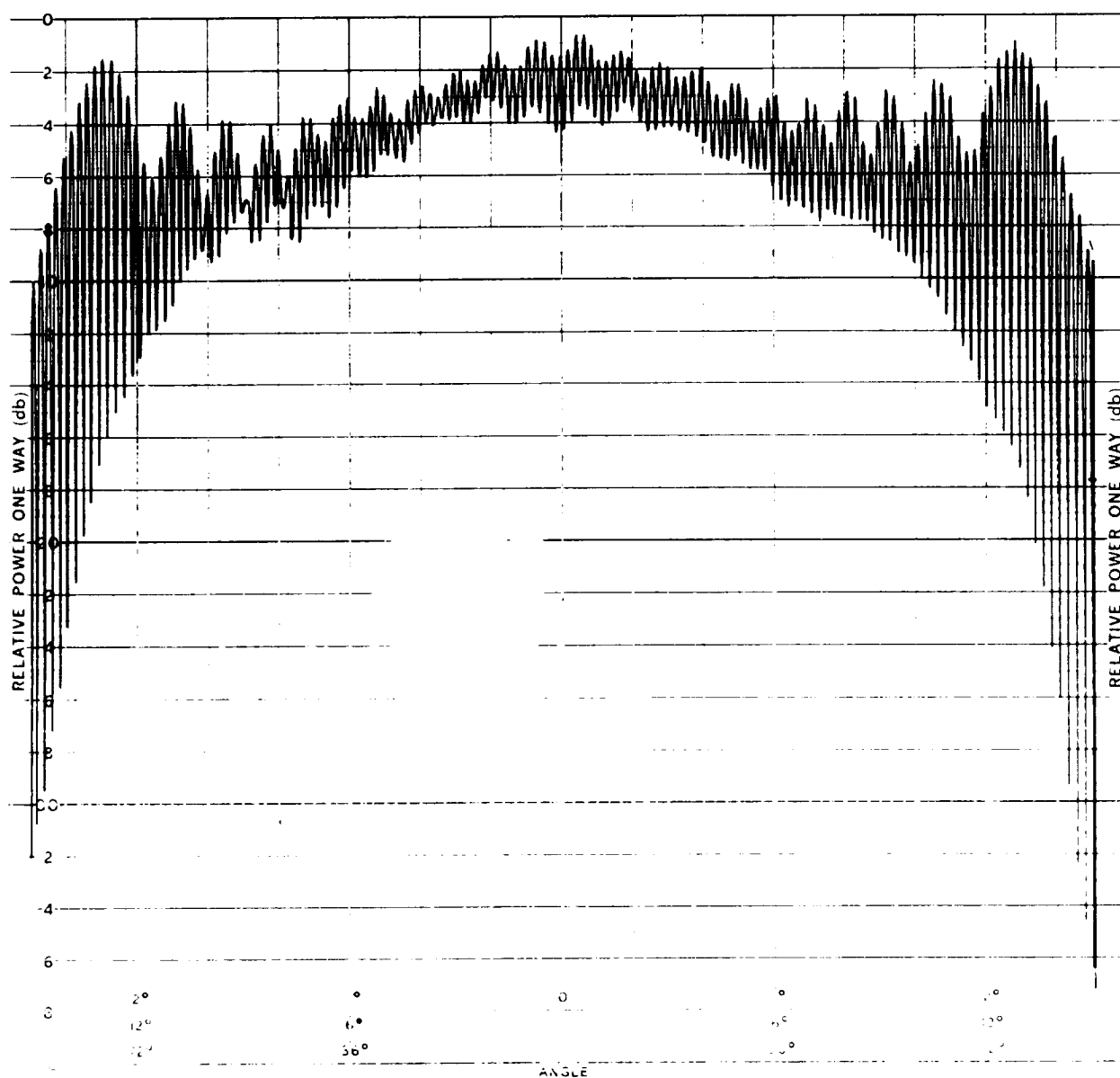
(a)  $\phi = 0^\circ$

FIGURE 141 RADIATION PATTERNS FOR TEST 4 - 2.1 GHz



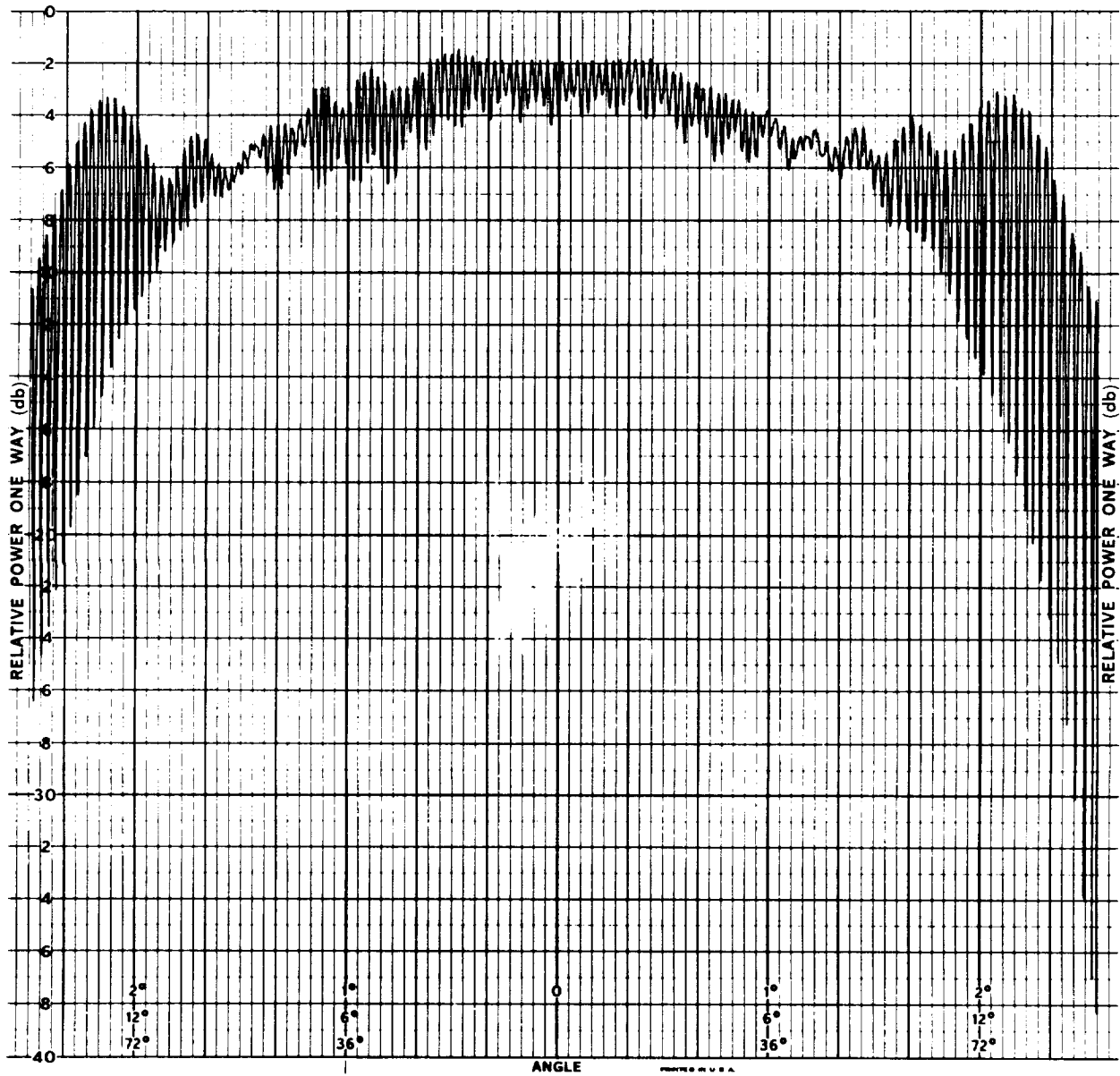
(b)  $\phi = 45^\circ$

FIGURE 141 RADIATION PATTERNS FOR TEST 4 - 2.1 GHz (CONT)



(d)  $\phi = 315^\circ$

FIGURE 141 RADIATION PATTERNS FOR TEST 4 - 2.1 GHz (CONT)



(c)  $\phi = 90^\circ$

FIGURE 141 RADIATION PATTERNS FOR TEST 4 - 2.1 GHz (CONT)

REPRODUCIBILITY OF THE  
ORIGINAL PAGE IS POOR

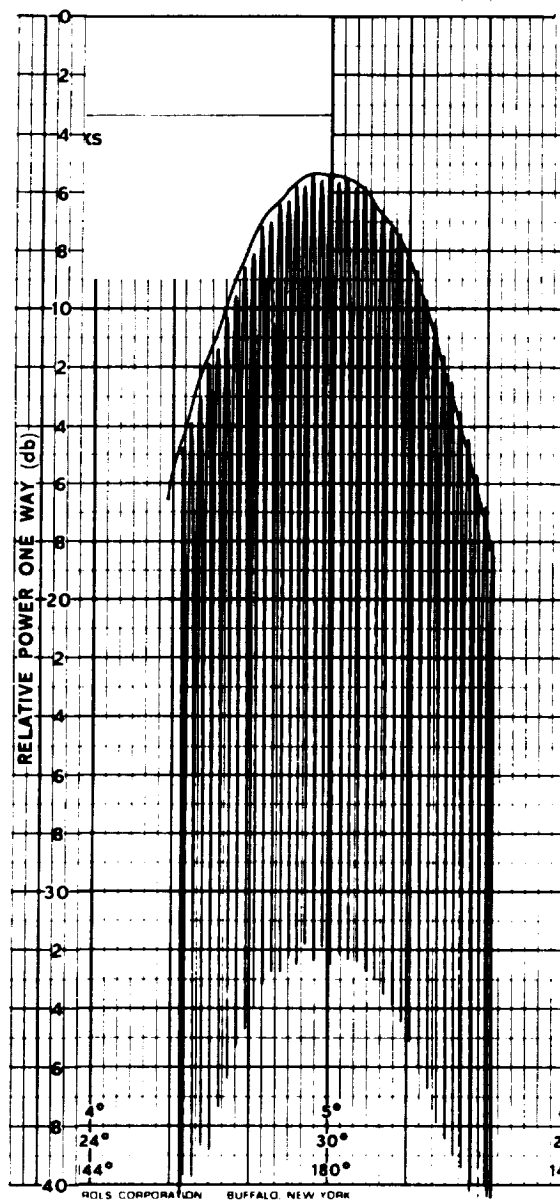
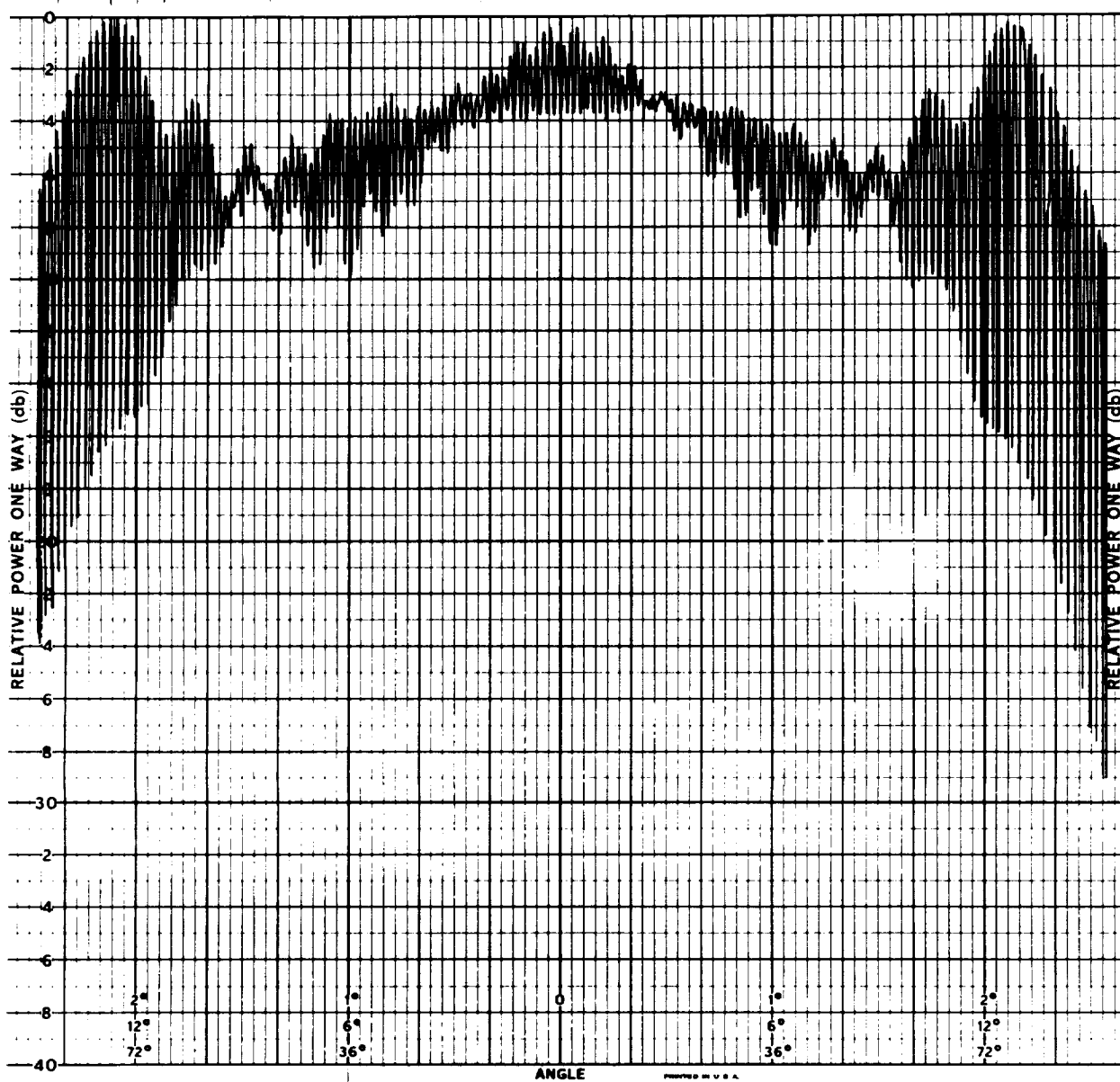


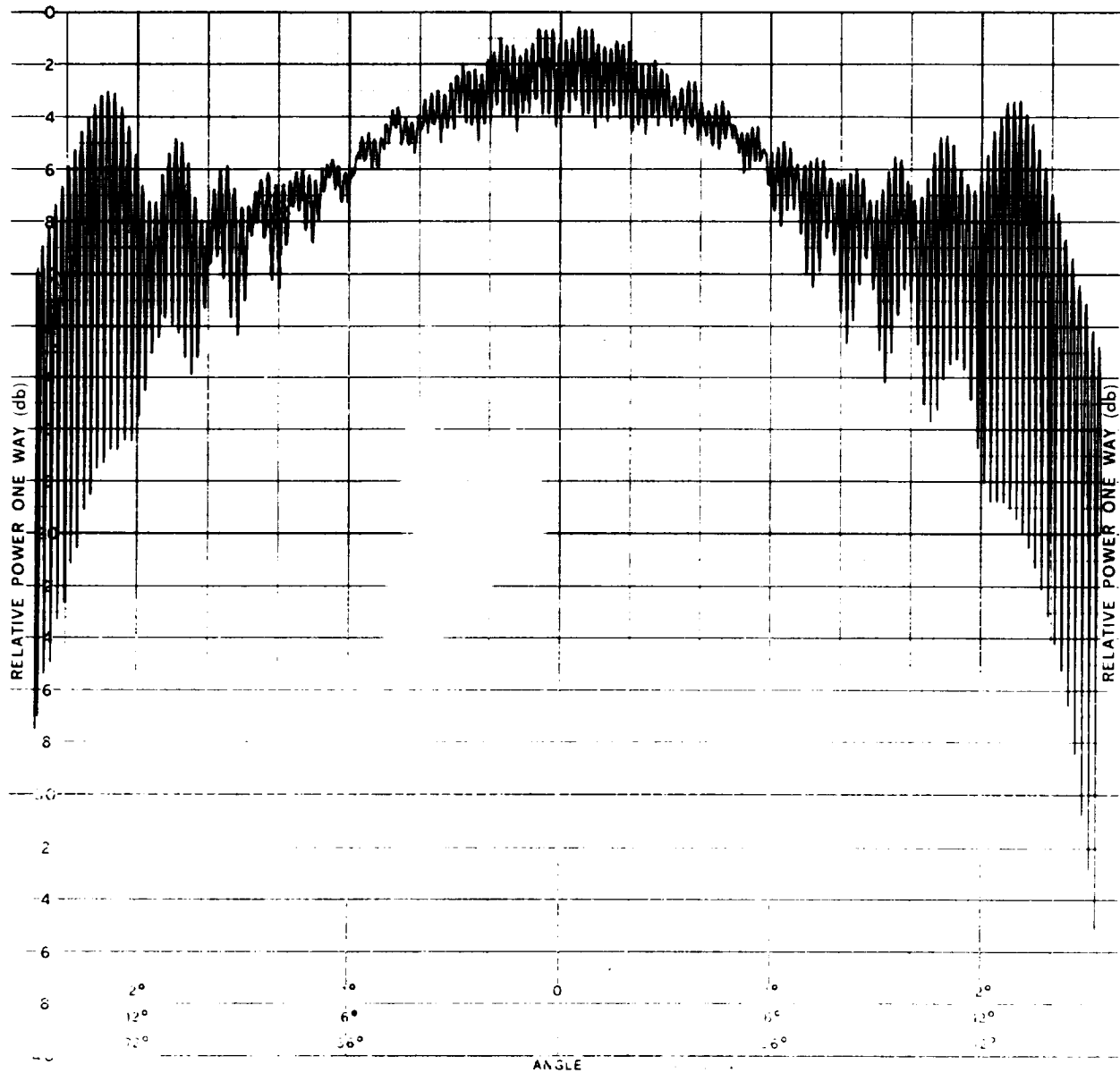
FIGURE 142 STANDARD GAIN HORN LEVEL FOR TEST 4 - 2.3 GHz





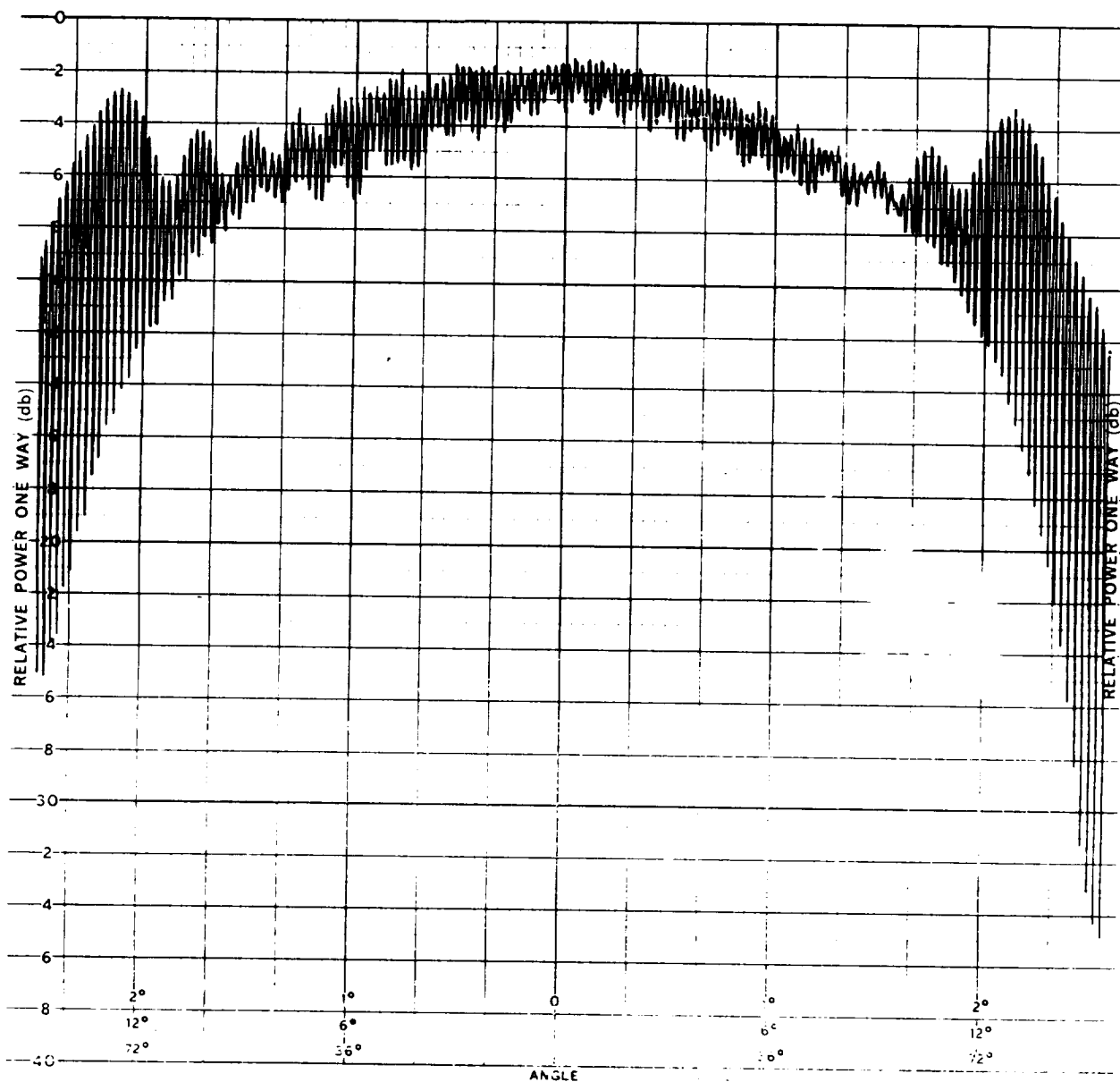
(a)  $\phi = 0^\circ$

FIGURE 143 RADIATION PATTERNS FOR TEST 4 - 2.3 GHz



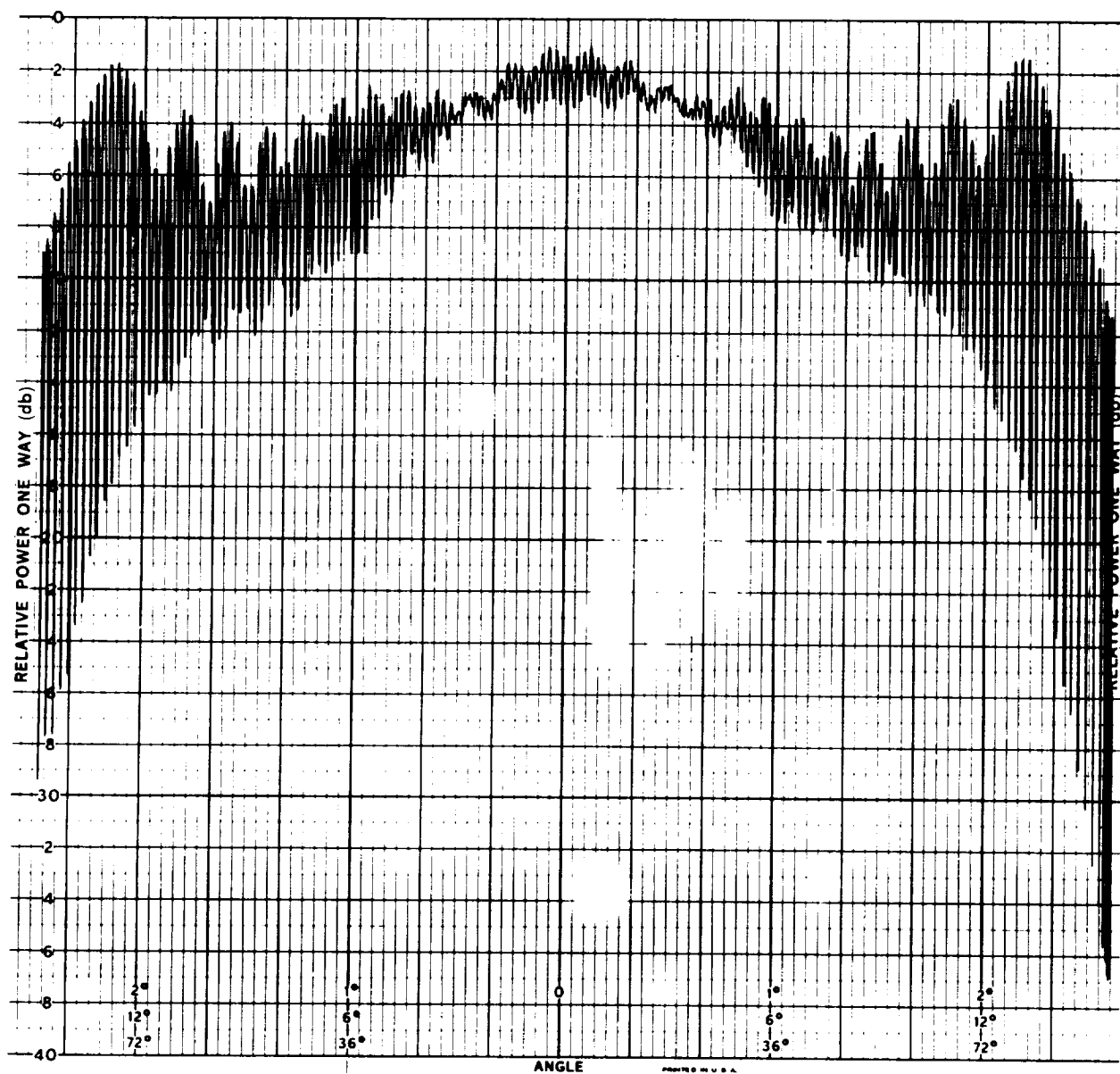
(b)  $\phi = 45^\circ$

FIGURE 143 RADIATION PATTERNS FOR TEST 4 - 2.3 GHz (CONT)



(c)  $\phi = 90^\circ$

FIGURE 143 RADIATION PATTERNS FOR TEST 4 - 2.3 GHz (CONT)



(d)  $\phi = 315^\circ$

FIGURE 143 RADIATION PATTERNS FOR TEST 4 - 2.3 GHz (CONT)



